Spring 1-1-2015

Experimental Analysis and Modeling of Robot-Tissue Contact Mechanics for In Vivo Mobility

Levin John Sliker

University of Colorado Boulder, levin.sliker@colorado.edu

Experimental Analysis and Modeling of Robot-Tissue

Contact Mechanics for *In Vivo* Mobility

by

Levin J. Sliker

B.S., University of Colorado, 2010

M.S., University of Colorado, 2012

A thesis submitted to the

Faculty of the Graduate School of the

University of Colorado in partial fulfillment

of the requirements for the degree of

Doctor of Philosophy

Department of Mechanical Engineering

2015

This thesis entitled:
Experimental Analysis and Modeling of Robot-Tissue Contact Mechanics for *In Vivo* Mobility
written by Levin J. Sliker
has been approved for the Department of Mechanical Engineering

_____

Asstistant Professor Mark E. Rentschler

_____

Assoc. Prof. Virginia Ferguson

Date _____

The final copy of this thesis has been examined by the signatories, and we find that both the content and
the form meet acceptable presentation standards of scholarly work in the above mentioned discipline.

Sliker, Levin J. (Ph.D., Mechanical Engineering)

Experimental Analysis and Modeling of Robot-Tissue Contact Mechanics for *In Vivo* Mobility

Thesis directed by Asstistant Professor Mark E. Rentschler

Robotic mobility within the gastrointestinal (GI) tract is an intriguing concept, which has received wide attention from within the research community over the past ten years. Capsule endoscopes (CEs) exist commercially, but lack an active mobility system, rendering them as passive devices. These passive devices are only capable of observational procedures, and are limited by the passive speed (dependent on intestinal peristalsis), inability to control orientation, and vulnerability to retention, requiring surgical removal in severe cases. Additionally, passive capsules take photos throughout their journey, resulting in a compilation of thousands of images, which can take the attending physician hours to review.

Due to these drawbacks, traditional endoscopes remain as the most popular intervention for GI related procedures. A traditional endoscope consists of a long flexible tube with a camera on the end of it. The tube usually has ports for tools, insufflation and irrigation. A user interface is located on the operator end of the scope, and can be manipulated to steer the tip of the scope. The scope is inserted through the oral or rectal orifice and is advanced by pushing the scope. As the scope is pushed, frictional forces can accumulate, resulting in advancement of the body of scope without advancement of the tip, termed looping. Looping results in distention of the bowel wall, pain for the patient and in rare cases perforation.

A robotic capsule endoscope (RCE) for oral endoscopies or robotic capsule colonoscope (RCC) for rectal colonoscopies is a capsular device (tethered or non-tethered) that propels itself through the GI tract. Self-propulsion could result in less looping, less pain for the patient, more ergonomic operation for the physician, control over capsule position and orientation, and the addition of diagnostic and therapeutic tools over existing passive CEs.

This work focuses on the contact mechanics of robot-tissue interaction in the GI tract with the goal of furthering the understanding of the physical problem so that more efficient and optimized mobility systems may be designed for RCEs and RCCs. This work also focuses on the design of an RCC which uses micro-patterned polydimethylsiloxane (PDMS) treads as a mobility method. The thesis is divided

into nine chapters. Chapter 1 provides an overview of capsule and flexible endoscope technology as it relates to screening, diagnostics and therapy. A thorough overview of existing mobility methods (both commercial and experimental) for RCEs is also presented along with a background on micro-patterning for friction enhancement. Chapter 2 presents the qualitative analysis of micro-patterned treads through the development and *in vivo* testing of a series of two-wheeled robots as well as a testing apparatus for quantitatively evaluating micro-patterned robotic wheels in a static environment. Chapter 3 presents the development of a novel testing apparatus for evaluating robotic wheels in a dynamic environment, and results from data collected using the apparatus. The results from this device suggested that an automated dynamic testing environment would be necessary for deeper understanding of robot-tissue interaction. Chapter 4 presents the development of an automated traction measurement (ATM) platform for evaluation of robotic wheels on synthetic or biological tissue substrates as a function of normal force, rotational velocity and linear velocity. An empirical model for predicting traction force was also developed and validated using data collected from the ATM platform. Chapter 5 presents a study on the relationship between substrate height (*i.e.*, stiffness), robot wheel tread pillar diameter, and the resulting generated traction force using the ATM platform for experimental collection and finite element modeling for validation. Chapter 6 presents the design and *in vivo* testing of an RCC which utilizes micro-patterned treads as a mobility method. The tethered prototype featured an onboard camera, and white and infrared (IR) light sources. Chapter 7 presents the development and experimental validation of an analytical model for predicting the drag force necessary to move a cylindrical capsule endoscope through the GI tract. Chapters 8 and 9 address discussion, conclusions and future work.

The work in this thesis has advanced the understanding of the contact mechanics for robot-tissue interface, especially pertaining to micro-patterned surfaces, and has resulted in several tools, both hardware and software, for measuring and modeling traction and drag force for capsule endoscope mobility methods. Additionally, this work has resulted in a novel RCC design prototype, which has the potential to evolve into a clinically viable device.

Dedication

To my family and friends, who have offered their unwavering support through my academic journey.

Acknowledgements

Thanks to all of my colleagues at the University of Colorado for the countless discussions, tips, and feedback, especially Dr. Benjamin Terry, Dr. Xin Wang, Dr. James Cezo, Madalyn Kern, Nicholas Anderson, Eric Kramer, Douglas Fankell, Micah Prendergast, Joan Ortega, Dr. Jake Dove, Dr. Jacob Segil, Greg Potts and Dr. Matthew McQueen.

Gratitude goes out to all of my colleagues at the BioRobotics Institute of Scuola Supiore Sant'Anna in Pisa, Italy. In particular, I thank Dr. Gastone Ciuti for his friendship, hospitality and discussions, and Nicodemo Funaro and Andrea Cafarelli for graciously fabricating capsule mockups and test fixtures.

Nicholas Anderson graciously machined the aluminum parts for the automated traction measurement (ATM) platform. Aleksander Stefanov collected several sets of data from the ATM platform. Xin Wang provided the finite element model presented in Chapter 2. Joan Ortega provided the finite element model presented in Chapter 5

Contents

List of Tables

Table

List of Figures

Figure

Chapter 1

Introduction

The focus of this work is around the experimental analysis, analytical modeling, and finite element modeling of the *in vivo* interaction between a robotic mobility system and tissue, specifically in the gastrointestinal (GI) tract. The work involves a combination of tissue mechanics, mechanical design, and contact mechanics. The document is organized into 6 solid chapters. Chapter 1 presents a background on flexible and capsule endoscopy for screening, diagnosis and treatment as well as a background on micro-patterning for friction enhancement. Chapter 2 presents the development of a series of two-wheeled robots for qualitatively evaluating micro-patterned treads and the results from an *in vivo* trial. Chapter 2 also presents the development of a testing apparatus for evaluating micro-patterned robotic wheels in a static environment, and the results from several experiments including the effects of micro-pattern shape on tread performance. A finite element analysis is presented with the experimental results. Chapter 3 presents the design of a testing apparatus for evaluating micro-patterned robotic wheels in a dynamic environment as an improvement over the device presented in Chapter 2. Chapter 4 presents the design of an automated traction measurement (ATM) platform for evaluating micro-patterned wheels in a dynamic environment, along with the development of an empirical model for predicting traction force. Chapter 5 presents a study on the relationship between synthetic substrate height, wheel tread pillar diameter and generated traction force. Chapter 6 presents the design and *in vivo* evaluation of a robotic capsule colonoscope (RCC) which uses micro-patterned treads for mobility. Chapter 7 presents the development and experimental validation of an analytical model for predicting the drag force necessary to move a capsule endoscope in the gastrointestinal (GI) tract. Chapter 8 discusses conclusions and a recommendation for future work.

1.1 Background

1.1.1 History of GI endoscopy

In 1868, G. Wolf and R. Schindler pioneered methodologies for inspecting the mucosa of the GI tract with semi-flexible endoscopes, paving the way to the advent of endoscopic procedures. Today, endoscopic technologies can be grouped into two categories: traditional flexible endoscopy, and wireless capsule endoscopy (WCE). Flexible scopes are considered the standard endoscopic tool, however in the past decade, several systems have been developed that have incorporated robotic control into the scopes. Traditional endoscopic techniques enable effective and reliable operation through different segments of the GI tract, *i.e.*, esophagus, stomach, large bowel or colon and part of the small bowel, with diagnostic, therapeutic and surgical capabilities. Flexible endoscopes, which are introduced into the oral or rectal orifices, consist of a steerable tip that orients the device toward the regions of interest. The rigidity of the instrument, due to the actuation mechanism and its diameter (11-13 mm for a standard colonoscope), results in limited accessibility and can increase the chances of traumatic endoscopic procedures and poor toleration by patients. Pain or problems with sedation make patients quite reluctant to undergo endoscopy and consistently limits the pervasiveness of a potential mass screening campaign. On the other hand, only mass screening could lead patients to periodically undergo endoscopy with the benefit of discovering and treating asymptomatic pathologies. A further medical drawback of flexible endoscopy is that certain areas of the GI tract cannot be reached, such as most of the small bowel.

In the past decade, capsule endoscopes (CEs) have become clinically available. Capsule endoscopy can be considered an example of a revolutionary technology since it represents an appealing alternative to traditional flexible scopes. This technology enables inspection of the digestive system with minimal discomfort for the patient or the need for sedation, thus mitigating the risks of conventional endoscopy, and potentially encouraging patients to undergo GI tract examinations. However, currently available clinical capsules are passive devices whose locomotion is driven by natural peristalsis, with drawbacks including failure to capture images of important GI tract regions, and lack of therapeutic and diagnostic capabilities, primarily due to the inability to control capsule position and orientation. To address these limitations, many research groups

are working to develop active locomotion devices that allow capsule endoscopy to be performed in a completely controlled manner. This would enable the doctor to steer the capsule towards interesting pathological areas and to accomplish medical tasks, such as screening, diagnosis (*e.g.*, biopsy) and therapy (*e.g.*, drug delivery, suturing). This review presents a research update on robotic endoscopic systems, including both flexible scope and capsule technologies, detailing the actuation methods and innovative treatment capabilities. The chapter also offers a 5-year future perspective on endoscope potential for screening, diagnostic, and therapeutic GI procedures.

1.1.2   Medical needs and clinical aspects

The ability to inspect and treat the entire GI tract with high quality diagnosis, controllability and therapy using a single device and procedure is a prominent need for gastroenterologists. The addition of the endoscope to the physician's toolbox has improved diagnostic and therapeutic capabilities, and therefore patient outcome in GI related pathologies. Medical needs that have been met by the advent of endoscopes can be broken into three categories: screening (*i.e.*, visualization or exploration), diagnostics, and therapeutics. Prior to endoscopes, the GI tract could not be inspected beyond what the clinician could see from the orifice. Endoscopes made visualization of the majority of the GI tract (except for a section of small bowel) possible, and with the recent advent of CEs, screening of the entire GI tract is now feasible. Flexible endoscopes are also a valuable tool for diagnosing GI pathologies. In addition to visual diagnoses, tools can be positioned and manipulated at the end of the scope through an operating channel to perform surgical tasks (*e.g.*, obtain biopsies). Prior to endoscopes, clinicians relied on patient symptoms (*e.g.*, pain, discharge, bleeding, etc.) or invasive (*i.e.*, open) exploratory procedures and biopsy methods to reach a definitive diagnosis for many GI pathologies. Flexible endoscopes, in combination with tools inserted through the operating channel, are capable of providing therapeutic treatment for GI pathologies. Flexible endoscopes can be used to repair (*e.g.*, perforations), treat (*e.g.*, foreign body removal and drug delivery), or perform preventative care (*e.g.*, precancerous polyp removal) in the GI tract.

One obstacle for all GI endoscopic technology is bowel preparation. Bowel preparation involves ingesting oral solutions (usually polyethylene glycol) to evacuate the bowel. Bowel preparation is often described

by patients as the worst part of a colonoscopy. Presently, there are no clinically viable options to bypass bowel preparation, however, there are several methods in development. The ClearPath^{TM} system is a supplemental device for colonoscopy, featuring two channels, one for irrigation and one for suction [1]. Early animal trials of the system has shown effective cleaning with no immediate mucosal damage or adverse effects, however, the system increases the diameter of the colonoscope by 6 mm. Alternatively, a soft-tipped catheter device for cleaning the bowel has been developed by Medjet Ltd. (Tel Aviv, Israel), and employs a supersonic two-phase jet of saline solution and CO_2 micro-droplets to break apart and clear bowel debris, which can then be suctioned through the operating channel of the endoscope [2]. Both of these solutions require traditional flexible endoscopes with operating channels and neither have moved into clinical practice.

1.1.3   Medical instruments and engineering solutions

GI endoscopes have evolved since their invention, and currently take two primary forms: traditional flexible scopes, and capsules. Traditional flexible endoscopes are usually comprised of two main modules: the shaft and the control module. The shaft is flexible and contains channels for operating tools, control cables, irrigation and insufflation. The control module is external to the patient and proximal to the clinician, and contains controls for tip steering, insufflation, irrigation, and image adjustment. As suggested by Ciuti *et al.* [3], CEs can be comprised of several modules; vision, power, localization, telemetry, locomotion, and diagnosis and tissue manipulation. This chapter mainly focuses on methods of locomotion, diagnostics and therapy.

Since a primary purpose of GI endoscopy is to visualize the GI tract, all endoscopes must feature an imaging system. Some traditional flexible endoscopes utilize coherent fiber optic bundles to transfer high quality images from the scope tip and non-coherent fiber optic bundles to transfer light from a light source (either xenon or light-emitting diode (LED)) to the scope tip for illumination. Other flexible endoscopes, as well as most CEs, utilize local solid-state imaging systems (usually a charge-coupled device (CCD) or complementary metal-oxide semiconductor (CMOS)) for visualization and LEDs for illumination. Since the GI tract is long and narrow, and therefore cannot be visualized all at once, endoscopes must also be actuated through the tract. Actuation methods can be basic, such as passive or manual locomotion, or advanced,

such as electric, hydraulic, pneumatic, or magnetic locomotion. A third, but not required, feature is the ability to actively steer the endoscope. Traditional flexible endoscopes utilize cables, which run the length of the scope and are controlled by a knob on the handle, to manipulate the tip for steering. Principles of locomotion and steering techniques (where applicable) for both flexible scopes and capsules will be reviewed in detail in the following sections of Chapter 1.

Diagnosis and therapy are secondary purposes of GI endoscopy, beyond the primary purpose of controlled visualization. There have been many clever engineering solutions for GI endoscopes to enable diagnosis and therapy. Recent innovative solutions for diagnosis and therapy, focusing on capsule endoscopy, will be reviewed in detail in the second part of Chapter 1.

1.2   Actuation means: principles for locomotion

The GI tract is a long and narrow lumen with only two natural access points, the mouth (at the start of the GI tract) and the anus (at the end of the GI tract). In order to access the majority of the GI tract, an endoscope must enter through either access point and be advanced, or actuated, to the point of interest. As such, endoscopes need to have an actuation means. For the purposes of this review, the actuation means have been divided into two broad principles of locomotion: passive and active. Furthermore, active locomotion principles have been divided into five actuation subcategories, based on the mechanism used:

- hands-on manual

- electric

- hydraulic/pneumatic

- magnetic/electromagnetic

- hybrid

Each locomotion principle will be reviewed, where applicable, with respect to traditional flexible endoscopes and CEs.

1.2.1 Passive locomotion

Passive locomotion only applies to CEs. Until the first FDA (Food and Drug Administration) approved capsule endoscope (CE) in 2001, all flexible endoscopes required active locomotion. Many CEs depend on passive locomotion for actuation. Passive locomotion is caused by the migrating myoelectric complex (MMC), which helps trigger peristaltic waves. Peristaltic waves facilitate transportation of indigestible objects through the GI tract. Due to the reliance on peristalsis for locomotion, a passive CE always travels aborally, and is either ingested orally or placed in the stomach or small intestines using a capsule delivery device (*e.g.*, AdvanCE, US Endoscopy, Mentor, OH, USA) for patients unable to swallow or pass the capsule through the pylorus.

Given Imaging Ltd. was the first company to bring capsule technology to market, with the PillCam SB (originally named M2A). The PillCam SB, and its successors, SB2 and SB3, all received FDA approval in 2001, 2007 and 2013, respectively. The PillCam SB series was designed for use in the small bowel. Given Imaging boasts a 30% increase (0.07 mm versus 0.1 mm smallest detectable object) in image resolution of the SB3 over the SB2, attributing the increase to an improved optics system and a new CMOS image sensor with increased pixel resolution [4]. Additionally, Given Imaging claims that the SB 3 is 40% more efficient than the SB2 due to the combination of adaptive frame rate technology and an improved video processing engine [4]. Adaptive frame rate detects the speed of the SB3 and increases image acquisition from 2 fps to 6 fps (exactly 1 frame per 0.18 s) when the capsule speed exceeds a threshold and vice versa. This ensures adequate tissue coverage when the capsule is traveling through areas with typically fast transit times, such as the duodenum. According to Given Imaging, the proprietary improved video processing engine utilizes their extensive library of pathologies to identify unique and clinically relevant images, while discarding similar or less significant images without sacrificing diagnostic yield. In a clinical trial (NCT01433042) involving 220 participants, 98% of SB3 images were graded by the physicians as superior in image quality to SB2 images.

Given Imaging also produces two other capsules, the PillCam ESO (version (FDA approval year): ESO (2004), ESO2 (2007), ESO3 (2011)), and the PillCam Colon (version (FDA approval year): Colon (none), Colon 2 (2014)). The PillCam ESO targets screening of esophageal mucosa, while the Colon 2

targets screening of the colon wall. Both the ESO and Colon capsules are equipped with 2 cameras (one on each end) to provide more screening coverage. Due to the relatively short distance that the ESO has to travel to screen the entire esophagus (30 min average procedure time), power consumption is less of a concern, enabling a high image acquisition rate (35 fps for the ESO3).

The PillCam Colon 2, recently cleared by the FDA (February 2014) for patients who have had an incomplete colonoscopy which was not due to poor bowel preparation, was designed for colon screening. The PillCam Colon and Colon 2 feature a third button battery for longer battery life, increasing the length from 26 mm to 31 mm when compared to SB and ESO models [5]. To conserve battery life, the PillCam Colon models feature a sleep mode, deactivating the capsule for the first 1.5 hr to allow for transit to the target area. The combination of the added battery and sleep mode enables image acquisition through the entire colon [5]. The PillCam Colon 2 offers several advances over the PillCam Colon, including a wider viewing angle (172° compared to 156°) and an adaptive frame rate algorithm [5]. The external receiver analyzes the transmitted images, and returns commands to the capsule based on the results. For example, the receiver recognizes when the capsule is in the stomach and maintains an image acquisition rate of 6 images per minute until the capsule enters the small bowel, at which point the frame rate is increased to 4 fps. If the capsule remains in the stomach for longer than 1 hr, the receiver notifies the patient to ingest a prokinetic agent. Similarly, once the capsule enters the small bowel, the receiver notifies the patient to ingest a laxative to help propel the capsule. The receiver can also detect whether the capsule is in motion or stationary. When in motion, the receiver commands the capsule to acquire images at a rate of 35 fps. Although the main advertised purpose of the PillCam Colon 2 is to screen for polyps, the capsule has also been used to lead to the diagnosis of other GI pathologies, such as Whipples disease [6]. Others have successfully used the PillCam SB to lead to the diagnosis of Whipples disease [7].

Other commercially available capsules include the MiroCam® (Intromedic Co., Seoul, Korea), the EndoCapsule series (Olympus Inc., Tokyo, Japan), OMOM® (ChongQing JinShan Science and Technology Co, Ltd., Chongqing, China), and CapsoCam (CapsoVision Inc., Saratoga, CA, USA), only one of which (Olympus EndoCapsule 1) has been approved by the FDA (2007). Of particular interest are the CapsoCam and the MicroCam®. The CapsoCam offers a 360° view out of the side of the capsule using 4 CMOS imagers.

Friedrich *et al.* reported a 70% detection rate of the duodenal papilla, the only landmark in the small bowel [8]. The MiroCam® employs a novel low-power transmission technology (electric-field propagation) to deliver data to the recorder, which increases battery life. The capsule uses the human body as a conductive medium to transmit data. In a clinical study, transmission rates of the captured images in the stomach, small bowel, and colon were 99.5%, 99.6%, and 97.2%, respectively [9]. A summary of passive capsules can be found in Table 1.1

Table 1.1: Passive capsule endoscopes.

Model	PillCam SB (M2A)	PillCam SB 2	PillCam SB 3	PillCam ESO	PillCam ESO 2	PillCam ESO 3	PillCam Colon	PillCam Colon 2	MiroCam® MC1000-W	EndoCapsule	EndoCapsule 10	OMOM®	CapsoCam SV1
Manufacturer (Location)	Given Imaging Inc. (Israel)								Intromedic Co. (Korea)	Olympus Inc. (Japan)		JinShan Science and Technology Co. (China)	CapsoVision, Inc. (USA)
Operative region	SB			ESO			Colon		SB	SB		SB	SB
Mass (g)	3.3	2.9	3.0	3.7	2.9	2.9	2.9	2.9	3.25	3.8	3.3	≤6	N/A
Dimensions (mm)	11 x 26	11 x 26	11 x 26	11 x 26	11 x 26	11 x 26	11 x 31	11 x 31	10.8 x 24.5	11 x 26	11 x 26	13 x 27.9	11 x 31
Battery (h)	7±1	≥8	≥8	0.3	0.5	0.5	9±1	10	12	8	12	8±1 (2 fps)	~15
Illumination	6 LED	4 LED	4 LED	2x6 LED	2x4 LED	2x4 LED	2x4 LED	2x4 LED	6 LED	6 LED	4 LED	6 LED	16 LED
Lighting	Standard	Automatic	Automatic	Standard	Automatic	Automatic	Automatic	Automatic	Standard	Automatic	Automatic	Standard	Automatic
Field of View (°)	140	156	156	140	169	172	156	172	170	145	160	140±10	360
Depth of Field (mm)	0-30	0-30	0-30	0-30	0-30	0-30	0-30	0-30	7-20	0-20	0-20	0-35	0-30
Image Sensor	1xCMOS	1xCMOS	1xCMOS	2xCMOS	2xCMOS	2xCMOS	2xCMOS	2xCMOS	1xCMOS	1xCCD	1xCCD	1xCMOS	4xCMOS
Imager Resolution	256x256	256x256	320x320	256x256	256x256	256x256	256x256	N/A[1]	320x320	1920x1080	1920x1080	QVGA (320x240) and VGA (640x480)	N/A
Image Sampling Rate (fps)	2	2 or 4[2]	2 or ~6	4 or 14[3]	19	35	2 per camera	4 or 35	3	2	2	2 fps (QVGA) or 0.5 fps (VGA)	3 or 5 per camera
Adaptive Frame Rate	No	No	Yes	No	No	No	No[4]	Yes	No	No	No	No	Yes
Data Transmission	RF	RF	RF	RF	RF	RF	RF	RF	HBC	RF	RF	RF	USB
Rx Antennas	8	8	8	3	3	3	8	8	9	8	8	14	0
Real-time monitor	No	Yes	Yes	No	Yes	Yes	Yes	Yes	Yes, USB and Wi-Fi	Yes	Yes	Yes	No
Localization	Yes[5]	Yes[5]	Yes[5]	No	No	No	Yes[6]	Yes[6]	No	No	3D Track	No	No
FDA Approval	Yes (2001)	Yes (2007)	Yes (2013)	Yes (2004)	Yes (2007)	Yes (2011)	No	Yes (2014)	Yes (2012)	Yes (2007)	No	No	No

CCD: Charge coupled device   CMOS: Complementary metal-oxide-semiconductor   HBC: Human Body Communication

N/A: Not Available   SB: Small bowel   ESO: Esophagus

[1] The PillCam Colon 2 features an Aptina MT9S526 CMOS image sensor with 1/6-inch optical format and 5.6 µm pixel, resolution unavailable.

[2] Two capsule versions

[3] 20 min operating time. First 10 min at 14 fps, second 10 min at 4 fps.

[4] PillCam Colon shuts off 3 minutes after activation to preserve energy, and automatically reactivates after 1:45.

[5] ±3.77 cm spatial resolution

[6] Capsule is localized to within the right (cecum to hepatic flexure), transverse (hepatic to splenic flexures), and left (splenic flexure to anus).

1.2.2   Active locomotion

Actuation of flexible endoscopes through the GI tract has always relied on active locomotion principles because passive actuation of scopes is not feasible. The most primitive actuation method for scopes depends on manual advancement by the clinician. Drawbacks of this actuation method include the possibility of looping and perforation, which can cause pain, discomfort, and life-threatening complications for the patient. Looping is a phenomenon which occurs when the scope is advanced from outside the patient, but the scope tip inside the patient does not advance (*e.g.*, it encounters a bend in the lumen). The result of this scenario is radial distension of the intestinal tract, which can be uncomfortable and painful for the patient. Shah *et al.* revealed that 79% of all pain episodes during a colonoscopy resulted from looping [10]. If the scope tip fails to advance, perforation of the intestine can result from either the tip or the looping. Perforation is difficult to repair, requiring open surgery in some cases, and can be life-threatening. The advent of steering mechanisms for flexible scopes has improved their navigation capabilities, especially concerning lumen bends, thus decreasing the occurrence of looping and perforation. In recent years, in an attempt to eliminate looping and perforation, and thus reduce patient pain, discomfort and risk, several new methods of actuating the scope have been proposed. These methods shy away from hands-on manual pushing and focus on front-end drive principles. A relatively high rigidity is needed for pushed scopes to prevent buckling, which would impede advancement of the scope. Front-end drive principles have introduced the possibility for soft-tethered scopes, an approach that has been pursued for both GI and cardiovascular applications. This section will review actuation methods for flexible scopes, including the hands-on manual approach and new front-end drive approaches, including electrical, hydraulic/pneumatic, magnetic/electromagnetic, and hybrid actuation.

Unlike flexible endoscopes, CEs are viable under passive or active locomotion. To date, all active capsules are investigational and have not been approved by the FDA. The main advantage of a passive capsule is its simplicity. Most passive capsules have only a few components; housing, image sensor, lens, circuit board, wireless transmitter, antenna, batteries, and, in some cases, diagnostic modules such as optical biopsy. Their simple design has resulted in quick development and inexpensive production. However, passive

capsules are limiting, mainly relating to lack of control. In order for the capsules to be a swallowable size, battery space, and thus power source, are limited. Since passive capsule speed is dependent on peristaltic activity it is difficult to control the rate of descent through the GI tract. With current battery size and power density, power often needs to be preserved during the capsule procedure. A reliable active actuation system could increase capsule speed. On one hand, this eliminates the need to conserve battery power due to a shorter procedure time, but on the other hand, active capsules will likely consume more power due to high frequency imaging rates and sensors (for control), and actuators (for locomotion). Additionally, controlling the capsule's orientation and position results in better visualization of the GI tract, reducing the risk of missing pathological cues. Development of actuation systems for CEs is currently a prominent topic in the research sector, and covers a variety of approach methods, which will be reviewed in the following sections.

1.2.2.1   Hands-on manual actuation

Hands-on manual actuation applies only to flexible endoscopy because there is no way to passively actuate a scope through the GI tract. This is the most basic actuation principle and involves manual advancement of the scope by the clinician.

Examples of hands-on manual actuation include traditional flexible endoscopes, balloon-assisted deep enteroscopy, Spirus overtubes, and the Cath-Cam system. The tip of a traditional endoscope (Figure 1.1, G) is manipulated using knobs on the control module which actuate steering cables. Steering the tip of the scope reduces the force against the colon wall, especially while navigating bends. The scope is manually advanced by the surgeon, and often results in prolonged awkward positions. Pain in the left thumb, right wrist, neck and back is more commonly reported by gastroenterologists than other internal medicine specialists [11]. One study reported average right-thumb peak pinch forces during left and right colon insertion of 10.4 N and 10.1 N, respectively, which exceeded the injury threshold of 10 N [11].

Balloon-assisted deep enteroscopy was the first endoscopic technique to allow real-time visualization of the entire GI tract. There are two types of balloon-assisted deep enteroscopy, single- and double-balloon enteroscopy. Each method utilizes an enteroscope and an overtube. For single-balloon enteroscopy, the end of the overtube is fitted with a balloon. For double-balloon enteroscopy, both the end of the enteroscope
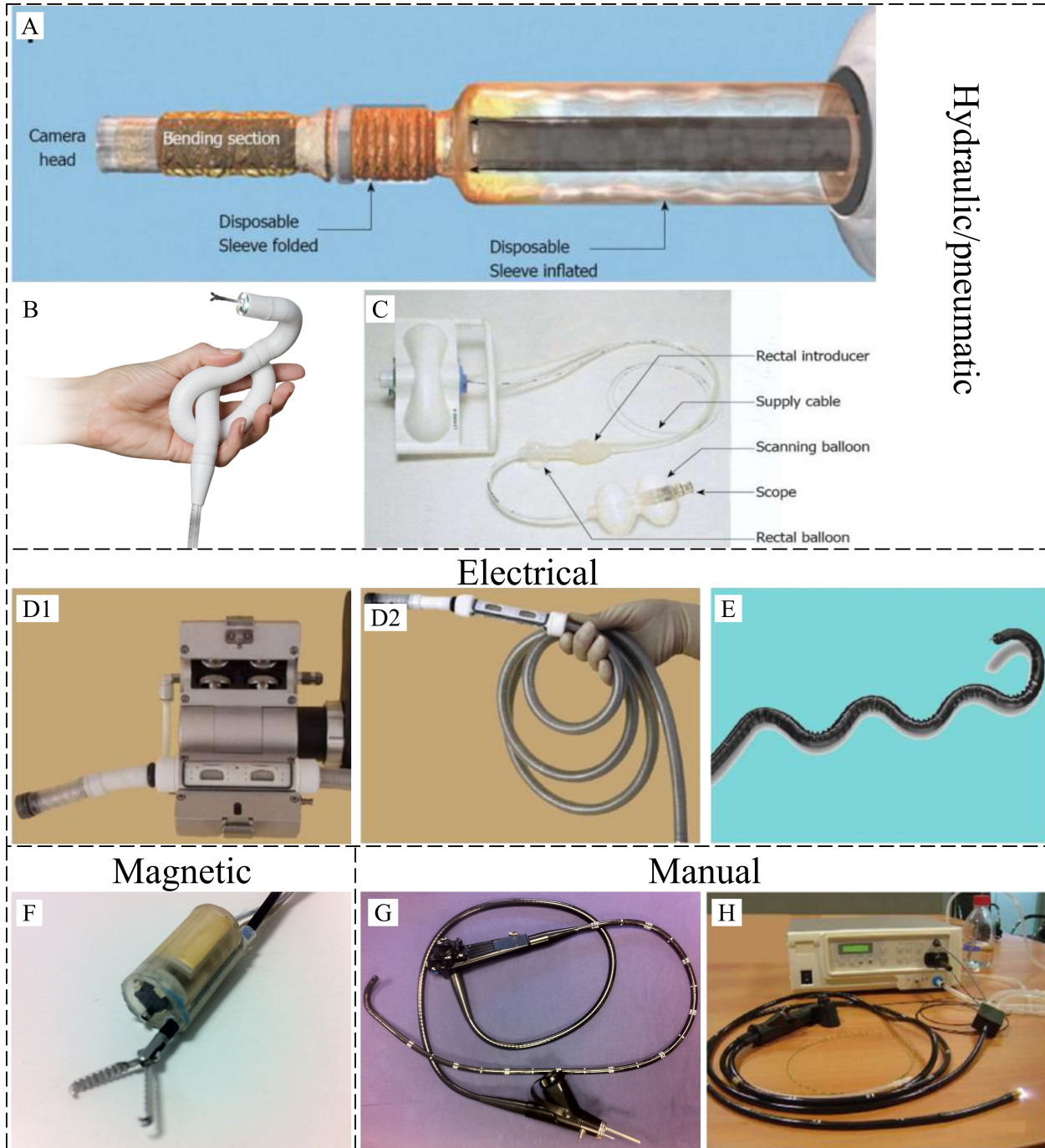
Figure 1.1: Flexible endoscopes featuring hydraulic/pneumatic actuation (top 2 rows), electrical actuation (middle row), magnetic actuation (bottom row, left), and manual actuation (bottom row, right). Examples of hydraulic/pneumatic actuation include the ColonoSight® (A), Endotics® (B, photo courtesy of S. Gorini), and Aer-O-Scope™ (C) systems. Examples of electrical actuation include the Invendoscope™ (D1 and D2), and NeoGuide™ (E) systems. An example of magnetic actuation is the MAC system (F) described in [12]. Examples of manual actuation include conventional endoscopes (G), and the CathCam system (H). Images A, C-E and H are reprinted with permission from Baishideng Publishing Group Co., Ltd.

and overtube are fitted with balloons. To advance the scope (in either anterograde or retrograde fashion), a push-pull method is used, inflating and deflating the balloon(s) while telescoping the bowel onto the overtube.

The Endo-Ease Discovery^{TM} SB and the Endo-Ease Vista^{TM} Retrograde (Spirus Medical, LLC, Bridgewater, MA, USA) are spiral overtubes for small bowel enteroscopy and colonoscopy, respectively. The overtube has a raised spiral which pleats the bowel during rotation. Advancement of the overtube is achieved by manual clockwise rotation of the spiral overtube.

The Cath-Cam system (Figure 1.1, H) consists of a catheter, guide-wire, light source, and video processor. The catheter features a 2.8 mm accessory channel, a 3 mm video camera, a 7 LED light source, air insufflation, and lens irrigation. The bend stiffness is 5 times less than that of a colonoscope. In a study comparing the push force necessary during an entire porcine colonoscopy, greater than 6.6 N was required 40%, 27%, and 12% of the time for a colonoscope, guide-wire assisted colonoscope, and Cath-Cam guide-wire combination, respectively [13]. The study also revealed no adverse effects 1 week after the procedure. Traditional flexible endoscopes, balloon-assisted enteroscopes and the Spirus Endo-Ease systems have all been cleared by the FDA, while the Cath-Cam system is an investigational device and has not been approved for clinical use.

1.2.2.2   Electric actuation

Electrically actuated flexible and capsule endoscopes are devices which employ electricity for locomotion. Usually locomotion is achieved by electrically powered actuators, but it can also include other novel uses of electricity.

Examples of electrically actuated flexible endoscopes include the Invendoscope^{TM} (Invendo Medical, Kissing, Germany), the NeoGuide Endoscopy system (NeoGuide Systems Inc., San Jose, CA, USA), and the Endo-Ease Endeavor by Spirus Medical, LLC. The Invendoscope^{TM} (Figure 1.1, D) is a single-use colonoscope (CE-marked and FDA 510(k) cleared) with a working channel that is driven in and out of the colon instead of pushed or pulled, which reduces forces against the colon wall. The system contains a motorized drive unit, steerable tip, and a double-sheathed scope. The motorized drive unit engages with the inner sheath. As the inner sheath is advanced, it inverts at the scope tip and becomes stationary once in contact with the

colon wall. The position of the steerable tip and the advancement mechanism are controlled using a joystick. Cecal intubation rate is high (98.4%) and the need for sedation is low when using the Invendoscope^{TM} [14]. The NeoGuide Endoscopy (CE-marked and FDA 510(k) cleared) system (Figure 1.1, E) consists of 16 articulated segments, which follow the geometrical path of the tip. The tip of the endoscope is controlled by the endoscopist. The scope insertion depth and tip angle are combined to create a three-dimensional (3D) map which provides accurate information regarding tip position, insertion tube position, and colonic looping [15]. Similarly, a disposable cable-actuated robot tip using two motors and gyroscopes for closed-loop position control is being developed by MIT [16]. In 2011, Olympus, Inc. acquired Spirus Medical, LLC, and since then the company has been developing a powered spiral overtube called the Endo-Ease Endeavor. The investigational device is similar to the existing manual Endo-Ease overtubes, but with the addition of motorized rotation controlled by a foot pedal.

There are many examples of electrically actuated CEs most of which employ actuators. Sliker *et al.* developed a wired CE for colonoscopy using micro-patterned treads [17]. The capsule contains one motor which simultaneously drives 8 polymer treads located on the outer surface of the capsule (Figure 1.2, A2). Valdastri *et al.* developed a legged robot (Figure 1.2, A1) which employs a novel slot-follower mechanism driven by a motor and a lead screw [18]. Another example of a legged CE was developed by Gu and Zhou, which utilizes peristalsis for forward and reverse motion [19]. Lin and Yan combine the motor driven legs and extension/retraction of the body of the CE to achieve worm-like motion [20]. Similarly, Kim *et al.* use a slotted design with a motor driven lead screw, but with paddles instead of legs for capsule locomotion [21]. De Falco *et al.* developed a four propeller swimming wireless capsule (Figure 1.2, A3) for stomach evaluation [22]. One of the most unique uses of electricity for the actuation of CEs is described by Woo *et al.*, where electrodes are embedded on the surface of the capsule to deliver electrical stimulation to the intestine [23]. Upon electrical stimulation, the intestines contract, propelling the capsule through the lumen. With the exception of the electric stimulation capsule developed by Woo *et al.*, all of these capsules contain small (and often custom) components, making them complex, difficult to manufacture, expensive and likely difficult to obtain FDA approval. The primary advantage of these capsules is their self-contained packaging, requiring little or no external equipment.
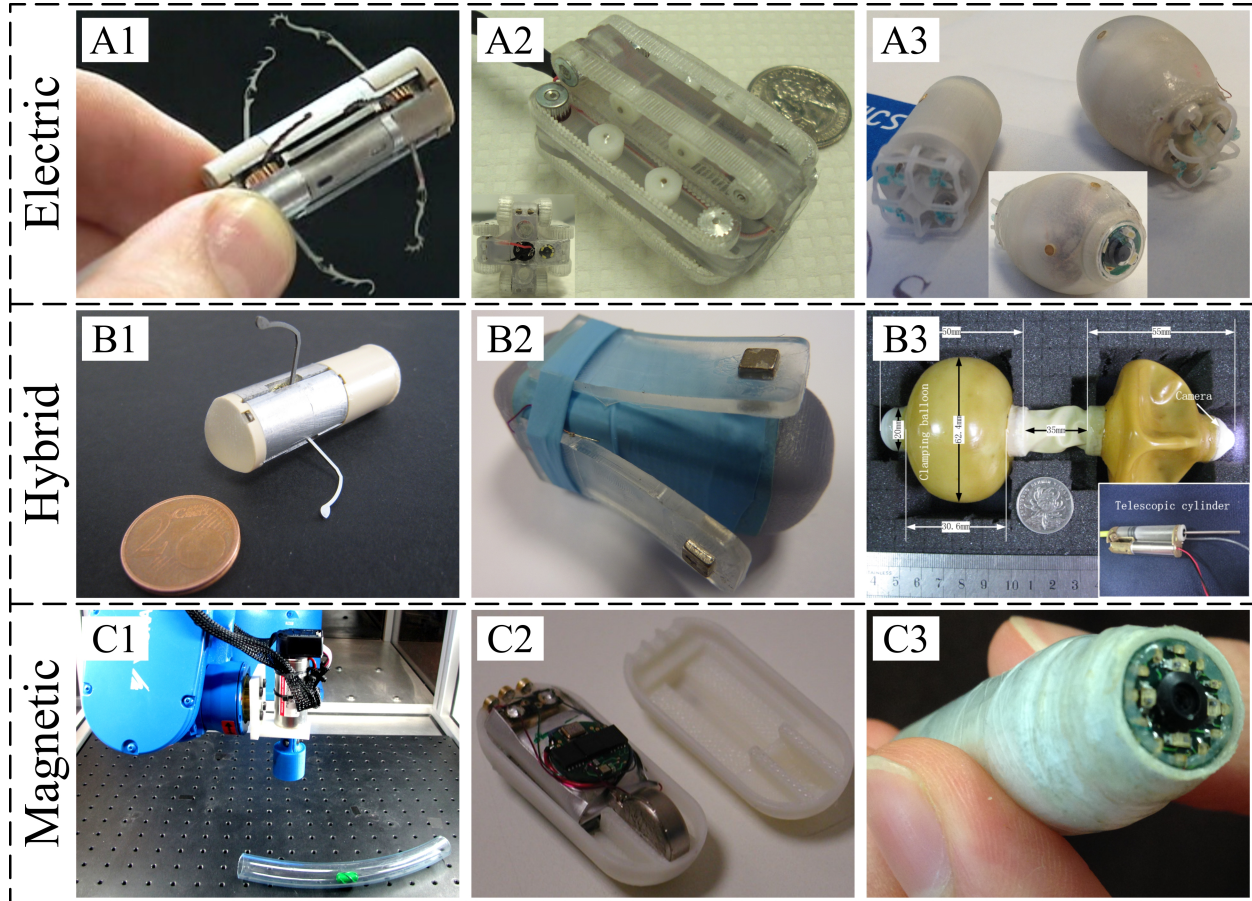
Figure 1.2: Active capsule endoscopes with electric (row A), hybrid (row B), and magnetic (row C) actuation. Examples of electric actuation include the legged capsule (A1, photo courtesy of G. Ciuti) described in [18], the treaded capsule (A2, photo courtesy of L. Sliker) described in [17], and the swimming capsule (A3, photo courtesy of I. De Falco) for a liquid filled environment (*e.g.*, stomach) described in [22]. Examples of hybrid actuation are the legged-magnetic capsule (B1, photo courtesy of M. Simi) described in [24], the jellyfish capsule (B2, photo courtesy of G. Tortora) for a liquid filled environment described in [25], and the inch-worm capsule (B3, photo courtesy of K. Wang) described in [26]. Examples of magnetically actuated capsules include a rotating capsule (C1, photo courtesy of J. Abbott) described in [27], a vibrating capsule (C2, photo courtesy of G. Ciuti) described in [28], and VECTOR (www.vector-project.com) capsule (C3, photo courtesy of G. Ciuti).

1.2.2.3 Hydraulic and pneumatic actuation

The Endotics® Endoscopy System (EES) by Era Endoscopy s.r.l. (Italy) is an example of a pneumatically driven flexible endoscope (CE-marked, not FDA approved) for painless colonoscopies and is comprised of a steerable tip, flexible body and thin tail (Figure 1.1, B). Inspired by the Geometer moth caterpillar, the EES employs two mucosal clamping devices (located at the proximal and distal ends of the probe) and an extension/retraction mechanism to achieve worm-like motion. Patients report significantly less pain with the EES when compared to traditional colonoscopes [29], and the EES demonstrates good specificity and sensitivity for the detection of polyps [30]. Additional benefits of the EES include a disposable probe to eliminate cross-infection risk, and an innovative joystick-based driving system to improve clinician ergonomics. The current EES features irrigation and insufflation/suction channels as well as a working channel.

Other examples of hydraulic and pneumatic actuated flexible endoscopes include the Aer-O-Scope and ColonoSight systems. The Aer-O-Scope system (Figure 1.1, C) is a disposable, self-propelling and self-navigating colonoscope consisting of two balloons. Both balloons are inserted into the rectum, the first is mobile, tethered and contains the imaging unit, while the second is stationary, fixed to an overtube and seals the orifice. Both balloons are inflated to create a seal against the inner lumen surface and then CO_2 is insufflated between the two balloons. The addition of CO_2 between the two balloons forces them apart. The stationary balloon is constrained by the orifice, resulting in advancement of the mobile balloon into the colon. Balloon pressure is monitored and controlled so as to maintain a seal but prevent damage. The mobile balloon is equipped with a CMOS camera with an omni-directional viewing system. Once cecal intubation is reached, CO_2 between the two balloons is vented through the rectum, and then CO_2 is insufflated between the mobile balloon and the cecum, pushing the balloon back towards the rectum while expanding haustral folds for examination. The Aer-O-Scope is equipped with suction, irrigation and insufflation, but does not have a working channel. The Aer-O-Scope is currently investigational, but a clinical trial was recently completed (November 2013), and an FDA 510(k) clearance application will soon be submitted. The ColonoSight™ (Figure 1.1, A) is an FDA approved, fully integrated colonoscope that uses air pressure to propel the steerable tip. The scope has 3 working channels and is inserted into a disposable sleeve anchored at the proximal end

of the device, protecting it from contamination and enabling propulsion. Air is pumped inside the sleeve pushing the tip forward. The maximum force generated by the ColonoSight$^{\text{TM}}$ is 4.9 N, compared to 44 N for a traditional colonoscope, and a high cecal intubation rate without complications has been shown [31].

1.2.2.4   Magnetic/electromagnetic actuation

Endoscopic capsule actuation obtained through magnetic or electromagnetic propulsion systems, *i.e.*, through an external locomotion approach, entails external magnetic fields that interact with internal magnetic components integrated into the capsule to provide propulsion by imparting forces and torques directly to the probe. The basis of this principle is that a large magnetic field is created near (but outside) the patient, either by electromagnet(s) or permanent magnet(s), while a much smaller magnetic source is embedded inside the capsule. The interaction between this small field and the large externally produced field enables active control of the endoscopic capsule with the benefit of no on-board actuators, mechanisms, and batteries, in favor of a small on-board magnetic field generator, *e.g.*, a permanent magnet. This approach provides a straightforward path to clinical and technical implementation and system integration because it does not require the incorporation of dedicated miniature actuators and mechanisms inside the endoscopic system. An additional advantage of magnetic actuation is the ability to move the capsule in both anterograde and retrograde fashions, and invert the capsule 180° to perform retrograde inspection for examining behind haustral folds. By exploiting externally generated magnetic fields, the internal available space of the capsule is increased, thus guaranteeing an easier integration of required modules in an ingestible system. Focusing on the selected magnetic approach (*i.e.*, electromagnet(s) or permanent magnet(s)), investigated by many research groups, some examples of capsules with external locomotion designed for specific districts are reported in literature. Magnetic actuation has also been exploited for other medical robotic applications, ranging from catheters (*e.g.*, the Niobe$^{\text{TM}}$ Magnetic Navigation System from Stereotaxis and Hansen Medical Magellan Robotic System) [32] to micro-scale robots [33]. Electromagnets, as external magnetic field generators, can generate well-controlled magnetic fields, although requiring bulkier equipment when compared to external permanent magnets.

A soft-tethered colonoscope with robotic magnetic steering and actuation has been developed by

Valdastri *et al.* [12]. The front-wheel magnetically driven device is composed of a capsule-like frontal unit and a compliant multi-lumen tether with a working channel (Figure 1.1, F). The device presents a trade-off between capsule and traditional colonoscopy combining benefits of a low-invasive front-wheel locomotion with the multi-functional tether for treatment.

Mahoney *et al.* have pursued permanent magnetic based actuation for helical capsules (Figure 1.2, C1) by maximizing magnetic torque while minimizing magnetic attraction [27]. A novel magnetic capsule endoscopy platform for gastric examination was developed cooperatively by Olympus Inc. (Olympus Medical Systems Corp., Tokyo, Japan) and Siemens Healthcare (Erlangen, Germany). The investigational system includes an Olympus CE (31 mm x $\varnothing$11 mm, provided with two 4 fps image sensors) and Siemens magnetic guidance equipment, composed of magnetic resonance imaging (MRI) and computer tomography (CT). The capsule can be moved by the physician in the stomach (through two control interfaces) with five independent degrees of freedom (DoF), *i.e.*, 3D translation, tilting and rotation [34].

Given Imaging Ltd. has investigated the use of a hand-held external permanent magnet to navigate a capsule in the upper GI tract using a customized version of PillCam Colon, which was half-filled with magnets as part of the European FP6 project called Nanobased Capsule-Endoscopy with Molecular Imaging and Optical Biopsy (NEMO project) [35]. Carpi *et al.* exploited a robotic magnetic navigation system (Niobe, Stereotaxis, Inc., USA), developed for cardiovascular clinical procedures, for accurate robotic steering of a magnetically modified endoscopic capsule (PillCam$^{\circledR}$, Given Imaging Ltd.). *In vivo* tests performed with 3D fluoroscopic imaging showed an accuracy of $1°$ in orientation but limited translational capabilities [36, 37]. Another approach for magnetic navigation of endoscopic capsules has been proposed by Ciuti *et al.* where active magnetic locomotion in the GI tract is achieved through a permanent magnet combined with accurate driving by an anthropomorphic robotic arm. The system combines the benefits of permanent magnets, in terms of magnetic field strength and limited encumbrance, with accurate and reliable control of the magnet through use of a robotic arm [36, 38]. This approach (Figure 1.2, C3) has been investigated in the framework of the FP6 European Project called Versatile Endoscopic Capsule for gastrointestinal TumOr Recognition and therapy (VECTOR project - www.vector-project.com). A colonoscopic spherical capsule with an internal permanent magnet and controlled through a hand-guided external electromagnetic system

supported by a passive robotic frame is under development within the European FP7 project called New cost effective and minimally invasive endoscopic device able to investigate the colonic mucosa, ensuring a high level of navigation accuracy and enhanced diagnostic capabilities (SUPCAM project - www.supcam.eu) [39]. Morita *et al.* designed a unique magnetic tail which can be attached to any 11 *mm* diameter commercial CE to obtain swimming locomotion when applying an alternating-current magnetic field [40]. Ciuti *et al.* also proposed a vibrating capsule (Figure 1.2, C2), reducing friction for magnetic locomotion [28].

A critical limitation of these external magnetic approaches is effective locomotion and lumen visualization of the capsule in the deflated lumen and mainly in the large intestine. In order to overcome this problem, several solutions for tissue distension and thus allowing reliable and accurate locomotion has been pursued and are described in Section 1.2.2.5 (hybrid locomotion capsule by Simi *et al.*) [24], and in Section 1.2.3 (wireless insufflation capsule by Gorlewicz *et al.*) [41].

1.2.2.5   Hybrid actuation

Capsules categorized by hybrid actuation are ones which combine any of the aforementioned actuation methods. For example, Simi *et al.* propose a CE (Figure 1.2, B1) which employs electrical and magnetic actuation [24]. An internal motor actuates legs, similar to the capsule described in [18] while magnetic locomotion is employed, as describe in [38]. The magnetic locomotion is primarily used with activation of the legged mechanism whenever the capsule gets lodged in collapsed areas of the GI tract. Chen *et al.* proposed a hybrid CE which employs both electrical and pneumatic actuation methods for worm-like motion (Figure 1.2, B3). The CE is comprised of two balloons, one on each end, and a middle section for extension. The balloons are individually inflated/deflated using a micro pump to hold the capsule in position against the colon wall, while the middle section is elongated/shortened using linear motors for advancement [26]. A novel approach to combining local magnetic fields with electric actuation is demonstrated by Tortora *et al.* [25]. This capsule (Figure 1.2, B2) is fitted with 4 external elastic flaps, each with a small permanent magnet embedded in the tip. Inside the capsule, an opposing magnet is rotated, which pushes each flap away from the capsule as it passes, resulting in jellyfish-like propulsion.

1.2.3   Diagnostic and therapeutic capabilities in GI endoscopy

Diagnostic and therapeutic capabilities of a traditional flexible endoscope employ tools inserted through the working channel of the scope. Common tools include biopsy forceps, saw-tooth forceps, foreign body forceps, scissors, injection and puncture instruments, polypectomy snares, retrieval devices, and cytology brushes. An example of an innovative tool for flexible endoscopy is the OTSC (Over-The-Scope Clip) system (Ovesco Endoscopy AG, Tubingen, Germany). The OTSC system features a deployable biocompatible Nitinol clip which clamps tissue to treat acute intestinal bleeding, leaking [42] and even perforations [43, 44].

There are several optical enhancement devices that have been developed to improve the screening process and diagnostic yield, including the Third Eye Retroscope (Avantis Medical, Sunnyvale, CA, USA), the Fuse^{TM} endoscope system (EndoChoice, Inc., Alpharetta, GA, USA), an extra-wide-angle-view colonoscope, and liquid lenses. The Third Eye Restroscope (CE-marked and FDA 510(k) cleared) is inserted through the working channel of a traditional colonoscope and passively forms a 180° bend as it emerges from the tip, providing a retrograde view of the colon which can improve visualization behind folds. A large study from multiple clinics showed a 23% overall increase in detection of precancerous polyps when using the Third Eye Restroscope over just the colonoscope, and a 40% increase in detection in patients with a greater risk of colorectal cancer [45]. The Fuse^{TM} endoscope system (CE-marked and FDA 510(k) cleared) utilizes multiple imagers and LEDs to obtain a wide (330° and 245° for colonoscope and gastroscope, respectively) field of view. A study comparing the Fuse^{TM} colonoscope with a traditional colonoscope demonstrated that an additional 69% more adenomas were detected by Fuse^{TM} that traditional colonoscopes missed [46]. Furthermore, an adenoma miss rate of 7% is reported for the Fuse^{TM} colonoscope [46]. The extra-wide-angle-view colonoscope developed by Uraoka *et al.* aims at providing a retrograde view for detecting lesions located behind haustral folds, flexures and rectal valves [47]. In the study, the mean detection rate was significantly higher with the extra-wide-angle-view colonoscope (68%) than a traditional colonoscope (51%) [47]. Additionally, the detection rate for polyps behind folds was higher with the extra-wide-angle-view colonoscope (61.7%) than a traditional colonoscope (46.9%) [47]. For extended depth of focus and to enable advanced vision

functions such as autofocus or zoom, a deformable liquid lens, compatible with a capsule-like device, was investigated by Cavallotti *et al.* [48] and Seo *et al.* [49]. The focal point is changed by varying the applied voltage resulting in fast responses. Furthermore, liquid lenses are inexpensive, efficient and compact.

Isolation and application of different light spectra has led to optical enhancement techniques, such as narrow band imaging (NBI) and autofluorescence imaging (AFI). NBI, developed by Olympus Medical Systems (Olympus, Japan) and implemented into some of their endoscope products, uses optical filters to isolate two bands of light; 415 *nm* (blue) and 540 *nm* (green), instead of conventional white light endoscopy which uses the entire spectrum of visible light (400-700 *nm*) to examine tissue. The shorter wavelength light (415 *nm*) only penetrates superficial layers of the mucosa and is absorbed by capillary vessels in the surface of the mucosa. This wavelength is particularly useful for detecting tumors, which are often highly vascularized. The longer wavelength light (540 *nm*) penetrates deeper and is absorbed by blood vessels located deeper within the mucosal layer, providing better visualization of the vasculature of suspect lesions [50]. A study comparing NBI to high-definition white light endoscopy (HD-WLE) for the detection of polyps concluded that NBI achieved significantly higher accuracies with good interobserver agreement once a learning curve was reached [51]. A study of 123 patients with Barretts esophagus found that NBI targeted biopsies can have the same intestinal metaplasia detection rate as a HD-WLE examination while requiring fewer biopsies, and NBI targeted biopsies can detect more areas with dysplasia [52]. For CEs, an investigational dual-mode CMOS sensor capable of acquiring one visible and one narrow band image under interillumination mode at 2 *fps* was described by Lan-Rong *et al.* [53]. In AFI, small and young malignant lesions undetectable by white-light illumination become detectable by excitation of the tissue with blue spectrum light. The autofluorescence produced by healthy tissue is stronger than collagen and other fluorescent substances in the tumor. Al-Rawhani *et al.* present an investigational AFI capsule that employs a single-photon avalanche diode for detection in combination with blue LEDs [54]. The capsule seems capable of inducing and detecting autofluorescence from mammalian intestinal tissue. Advanced image post-processing algorithms to enhance capsule diagnostic capabilities have been proposed based on texture feature, local binary pattern and multilayer perceptron neural network [55, 56, 57]. I-scan (Pentax, Ontario, Canada) and FICE (Fujifilm, Tokyo, Japan) are examples of virtual chromoendoscopy techniques

that attempt to enhance images for higher quality detection rates and diagnosis. Virtual chromoendoscopy is particularly applicable to CEs as it is a software based technology (unlike NBI which uses optical filters) and can be implemented without changing existing hardware. For example, Given Imaging Ltd. recently implemented FICE into its RAPID$^\circledR$ software for PillCam images. One of the advantages of FICE, when used with traditional endoscopes, is real-time transition between the white light and FICE images, however, this advantage is lost when used with CEs due to the post-processed static images. In the future, it is expected that FICE will work with CEs as it currently does with conventional endoscopes [58].

Valdastri *et al.* developed a therapeutic wireless endoscopic capsule able to electrically release an endoscopic clip for treating bleeding in the GI tract (Figure 1.3, A5). The therapeutic capsule navigation and positioning is controlled by means of an external permanent magnetic field source and it is provided, on the capsule front, with a single pre-loaded SMA-based endoscopic clip that can be wirelessly activated and released. Successful surgical *ex vivo* and *in vivo* experiments were performed, opening the field to a new generation of capsule devices capable of performing both diagnostic and therapeutic tasks [59].

The first example of a wireless biopsy capsule was developed in 2005 by Kong *et al.* and it consists of a rotational tissue-cutting razor fixed to a torsional spring and constrained by a paraffin block. When the paraffin block is melted by electrical heating, the razor is released and a tissue sample is collected [60]. The same author developed a more advanced biopsy device (Figure 1.3, B1) for CEs. The device consists of three modules for the complete process of biopsy, which includes monitoring the intestinal wall by a tissue monitoring module (lateral view by using a mirror reflector system), aligning onto a polyp by an anchor module (composed of four outriggers with independently connected SMA springs three of which are simultaneously activated), and sampling of the polyp tissue by a biopsy module (composed of two cylindrical razors, a spiral spring, and a trigger). The biopsy mechanism of the inner razor exploits an electrical powered mechanism: electric power, converted into heat, triggers the release of the spiral spring, and thus of the razor, by the soldering of a stopping mechanism on the chip resistor [61].

An example of wireless biopsy capsule (Figure 1.3, B2) with a reliable and effective design was developed by Simi *et al.* The biopsy device takes advantage of magnetic fields both for stabilizing the capsule during sampling and for operating the biopsy mechanism. Two couples of cylindrical diametrically magne-
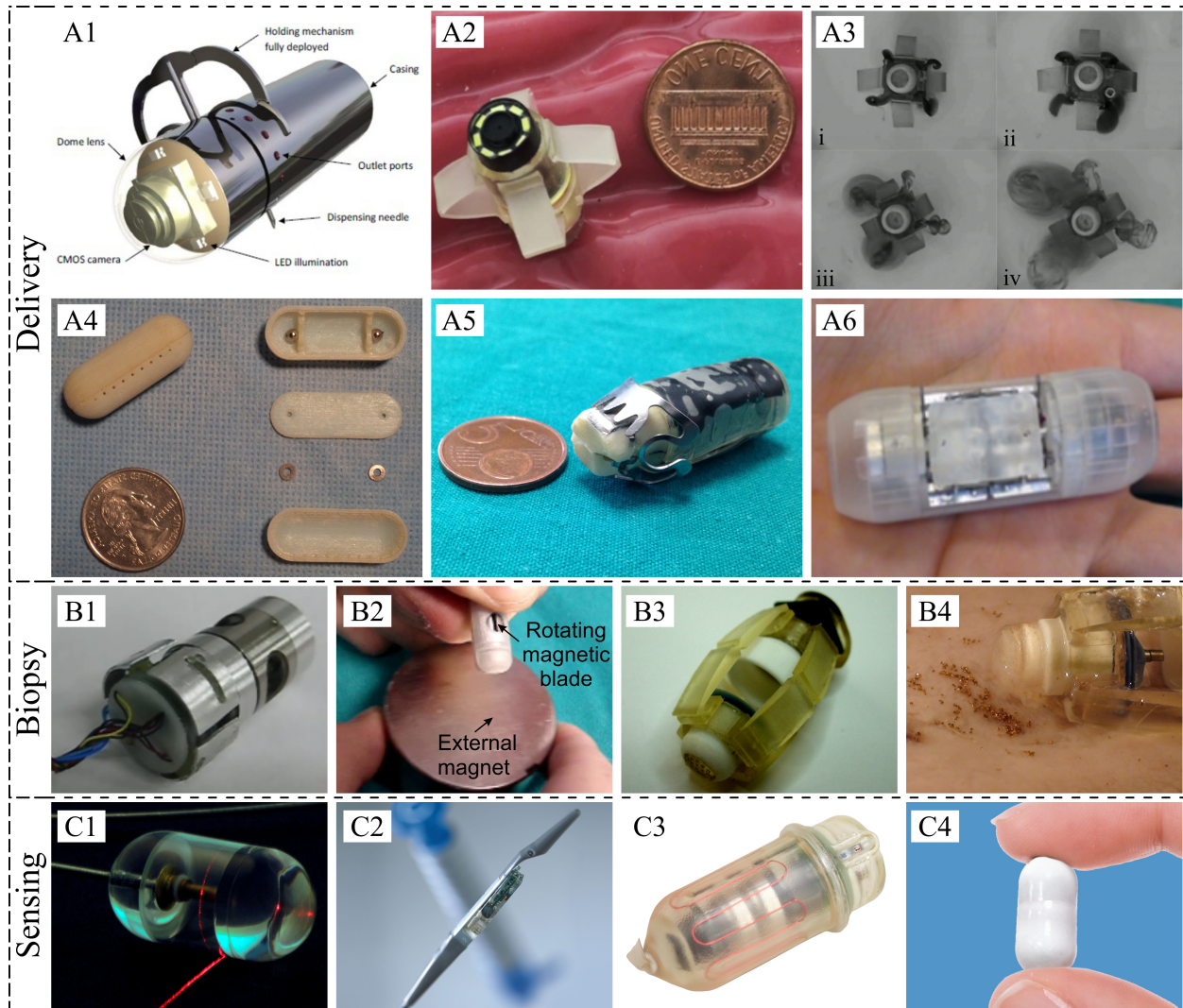
Figure 1.3: Capsule endoscopes for delivery (rows A), biopsy (row B) and sensing (row C). Delivery capsules include drug delivery (A1, photo courtesy of S. Woods and A2-A3, photo courtesy of S. Yim), insufflation (A4, photo courtesy of P. Valdastri), clip delivery for hemorrhage clamping (A5, photo courtesy of C. Quaglia), and patch delivery (A6, photo courtesy of C. Quaglia). Biopsy capsules employ rotating blades (B1, photo courtesy of S. Yim and B2, photo courtesy of G. Ciuti), and microgrippers (B3-B4, photo courtesy of S. Yim). Sensing capsules employ various technologies to obtain 3D reconstruction of the esophagus (C1, photo courtesy of G. Tearney), sense pressure (C3, SmartPill Given Imaging, Ltd. press release photo), sense pH (C2, Bravo Given Imaging, Ltd. press release photo and C3), and sense temperature (C4, photo courtesy of L. Carbonelli and C3).

tized permanent magnets embedded into the capsule act as magnetic torsional springs; the external magnetic field is modulated first for stabilization and tissue penetration inside an inner chamber and then for tissue cutting. Therefore, thanks to the innovative magnetic actuation system, actuators and batteries are not required on-board, thus allowing for a more compact size ($\varnothing 9.5\ mm$ x $17\ mm$) and potential use in pediatric patients [62].

A novel biopsy method using deployable microgrippers (Figure 1.3, B3-B4) has been developed by Yim *et al.* [63]. A large number of untethered thermo-sensitive microgrippers are released from the magnetically positioned capsule in the stomach. Triggered by body heat, the microgrippers fold, collecting small biopsies. The capsule then collects the microgrippers using a wet-adhesive patch.

A therapeutic capsule for bioadhesive patch release (Figure 1.3, A6) has been developed by Quaglia *et al.* The system exploits an SMA-based spring mechanism for unlocking a bench compressed by a super elastic structure. The bench supports a bioadhesive patch that is attached to the GI wall. The system, controlled in position by an external permanent magnetic source allows for a controlled targeted release of drugged patches [64]. A therapeutic capsule for targeted drug delivery (Figure 1.3, A1) has been developed by Woods *et al.* [65]. Although miniaturization is the primary obstacle, the device features a holding mechanism for resisting peristalsis and a micropositioning mechanism which can deliver $1\ mL$ of targeted medication. Yim *et al.* developed a magnetically actuated soft capsule for multimodal drug release [66]. The soft capsule (Figure 1.3, A2) is axially actuated using magnetic fields to squeeze drugs out of the drug chamber (Figure 1.3, A3). The drug can be gradually released with the rate dependent on the frequency of a pulsed magnetic field or released all at once using a constant strong magnetic field. There are currently no biopsy capsules approved for clinical use.

A soft-tethered capsule colonoscope developed by Valdastri *et al.* [12] features a compliant multi-lumen tether for insufflation, suction, irrigation, or access for standard endoscopic tools such as biopsy forceps, polypectomy snares, retrieval baskets, and graspers (Figure 1.1, F).

An interesting solution for obtaining tissue distension for diagnostic and therapeutic procedures was proposed by Gorlewicz *et al.* with a tetherless insufflation system which is based on a controlled phase transition of a small volume of fluid stored on-board the capsule to a large volume of gas, emitted into

the intestine [41]. The capsule prototype, depicted in Figure 1.3 (A4), is composed of an upper chamber, designed to hold an acid solution, and a lower chamber, designed to hold a powdered base. In the presence of an external magnetic field, two installed magnetic ball valves open, and the citric acid solution mixes with the potassium bicarbonate base. The CO_2 produced (375 mL) is vented through small perforated holes just under the midline of the capsule for insufflating the surrounding environment.

There are several capsules available for sensing intraluminal physiological parameters. The FDA approved Bravo® (Figure 1.3, C2) pH monitoring system (Given Imaging Ltd., Yokneam, Israel) provides a capsule-based approach for evaluating gastroesophageal reflux disease. The capsule is anchored in the esophagus for a 24-48 hr period while pH data is wirelessly sent to an external data recorder. The duration of the evaluation is debatable, but the 48 hr period is recommended by Chander *et al.* because pH data and symptom correlation is strengthened when compared to 24 hr results [67]. Another study of 66 procedures reported a 15.2% technical failure rate, attributed to poor data reception (4.5%), early dislodgement (4.5%) and capsule removal (6.1%) [68]. In a study comparing capsule- and catheter-based pH measurement Ang *et al.* determined that diagnostic yield was similar [69]. The OMOM pH monitoring system (Jinshan Science & Technology Co., Ltd, Chongqing, China) is also anchored in the esophagus and transmits pH data to an external recorder using radio frequency technology, but is not FDA approved. The SmartPill® (Figure 1.3, C3) by Given Imaging Ltd. is an example of an FDA approved capsule which measures multiple physiological parameters (*e.g.*, pressure, pH and temperature) as it travels through the GI tract for assessment of GI motility. Rao *et al.* determined that the SmartPill® was capable of detecting a generalized motility disorder in 51% of patients and influence management in 30% of patients with lower GI disorders and 88% of patients with upper GI disorders [70]. Given Imaging Ltd. was acquired by Covidien Ltd. in February 2014, which could bring exciting change to their lineup of GI capsules. CorTemp (Figure 1.3, C4) by HQ Inc. (Palmetto, FL, USA) is an example of an FDA approved capsule that measures internal body temperature accurate to ±0.1°C. After capsule ingestion, a quartz crystal in the capsule vibrates at a frequency relative to the temperature which creates a magnetic flux and sends a harmless low-frequency signal through the body. Applications for monitoring internal body temperature include sports physiology [71], firefighting, research and medicine [72, 73], occupational safety [74], and military [75].

Another group of capsules employ various methods to obtain less-invasive imaging of the GI tract. Check-Cap (Mount Carmel, Israel) is an investigational wireless capsule that images the colon using low-dose radiation which could mitigate the need for bowel preparation. A single procedure exposes the patient to as much radiation as one abdominal radiograph, and creates a 3D reconstructed image of the colon. Although still under development, a patient survey suggests that Check-Cap could be a viable option if it can provide sensitivities of 80% and 50% for cancer and large polyps, respectively [76]. Gora *et al.* developed a tethered esophageal capsule (Figure 1.3, C1) that employs optical frequency domain imaging technology to produce 3D microstructural images (30 μm (lateral) x 7 μm (axial) resolution) [77]. These technologies are very promising for both robotic control and diagnostic purposes as they provide methods for reconstructing the internal structure of the GI tract. The Check-Cap could provide an imaging method that eliminates the need for bowel preparation as X-ray can transmit through the relatively softer bowel material, but at the expense of radiation exposure to the patient.

1.3   Expert Commentary

Traditional flexible endoscopy has been a useful tool for visualizing the GI tract for over 140 years, but in recent decades, the technology has been pushed to new limits in an attempt to improve the effectiveness of the procedure and increase comfort for both the patient and clinician. Drawbacks to traditional flexible scopes can be divided in two categories; procedure comfort and effectiveness (*i.e.*, depth of screening, therapeutic and diagnostic capabilities, and device and procedure quantity).

Traditional flexible endoscopy can be uncomfortable for the patient and frequently requires sedation. Even when the patient is sedated during the procedure, pain is often felt after the procedure due to distension of the GI tract, loop formation, and, in rare cases, perforation during the procedure. An additional and often overlooked aspect of endoscopic engineering is ergonomic considerations of the gastroenterologist. Gastroenterologists are at risk for injuries such as carpel tunnel syndrome, DeQuervains tenosynovitis, and lateral epicondylitis due to repeated and prolonged awkward postures during endoscopic procedures [11]. There is a 37% to 89% prevalence of musculoskeletal complaints for endoscopists, and Shergill *et al.* showed that the prevalence is higher for endoscopists than for other medical specialists [11]. The technologies

reviewed in this chapter are focused on reducing the invasiveness of endoscopic procedures and increasing the comfort for both patients and clinicians. All of the actuation methods presented are focused on reducing the need to push the endoscope into the body, which reduces distension of the GI tract, formation of loops and, in the worst case, perforation. Additionally, the advent of capsule endoscopy has eliminated the need for sedation altogether, resulting in a virtually pain free procedure for the patient and the endoscopist. Most of the actuation methods presented here, for both flexible and CEs either reduce or completely eliminate risk factors related to overuse injuries for gastroenterologists, such as repetitive hand motions, high hand forces, and awkward wrist, shoulder, and neck positions.

The other major drawback to traditional endoscopy is procedure effectiveness. An optimal endoscopic technology would be one which can screen (*i.e.*, visualize), diagnose (*e.g.*, take biopsy) and provide therapy (*e.g.*, drug delivery) to the entire GI tract during a single procedure while minimizing pain and discomfort for the patient and the gastroenterologist. Even the longest of endoscopes can only reach a portion of the small bowel. Traditional flexible endoscopes can, at best, visualize the proximal and distal duodenum. It is possible to visualize the proximal jejunum using specialized scopes, such as pediatric colonoscopes or long enteroscopes. However, it is difficult to visualize the medial and distal jejunum, and the entire ileum using traditional flexible endoscopes. Two main design features can be addressed to expand GI tract access; scope physical design parameters (*e.g.*, length and stiffness) and scope actuation. These issues have been addressed by several of the technologies reviewed in this chapter. Flexible and soft-tethered endoscopes with novel steering and actuation techniques have paved the way for more effective endoscopic procedures. While these might not enable anesthetic-free procedures, they have high potential for decreased comfort and pain for both the patient and the clinician. Scope length has been eradicated by the advent of capsule endoscopy. By eliminating the scope, or tether, a commercially available CE is able to visualize the entire bowel with no discomfort or pain for the patient, however, a second procedure is required for therapy or diagnosis. CEs are a promising technology, but are limited by their capabilities. The challenge in this field in upcoming years is to design a CE capable of screening, diagnosis and therapy regardless of the complexity and space requirements for the necessary equipment and small volume limitation. Furthermore, a fully sensorized and controlled CE capable of screening, diagnosis and therapy would still be limited by its power supply, thus

requiring development of solutions (*e.g.*, wireless power transmission).

Many examples of treatment enabled capsules have been proposed for diagnosis and therapy. Biopsy capsules seem promising with several viable designs in development. There have been several promising capsules proposed for drug delivery, although these will likely take more effort in the FDA approval pathway. There are several FDA approved sensing capsules available to aid in the diagnosis of pH, pressure, and temperature sensitive GI pathologies.

1.4   Five-year view

The boundaries of both flexible and capsule endoscopy will be pushed within the next five years. Advancements in flexible endoscopy will continue to be motivated by increasing comfort for both the patient and clinician, working towards an easy-access mass screening campaign, *i.e.*, access to the entire GI tract, while maintaining therapeutic and diagnostic capabilities. Some of the actuated endoscopic devices (*e.g.*, Aer-O-Scope^{TM} by GI-View) have sacrificed an operating channel in order to develop a reliable actuated scope. We expect to see versions of these devices in the near future that implement operating channels, as supported by the Endotics$^{®}$ device. We will continue to see novel steering and actuation techniques which will reduce bowel wall distension, and the probability of loop formation and perforation. We also predict the emergence of new and continued development of existing soft-tethered capsules, which feature some of the benefits of wireless CEs, but bypass some of the design constraints such as the need for on-board tools and power. The soft tether is more flexible than a scope, yet still provides power for on-board electronics and a port for tools.

While capsule endoscopy is currently a decent supplement to traditional flexible endoscopy, it remains inferior and will require further development before becoming a suitable replacement for flexible endoscopy. The largest drawbacks to commercially available capsules are their passive locomotion and lack of therapeutic and diagnostic capabilities. Significant recent advancements have been made to address these two issues individually, and it is likely that convergence of solutions to both problems will emerge within the next five years. It is predicted that magnetic locomotion will be the prevailing method for actively controlling CEs. Advantages of magnetic guidance include simple capsule design (*i.e.*, the only necessary addition to existing

FDA approved capsules is an internal permanent magnet) and untethered control, which could streamline the clinical approval process. The magnetic control platform might be a large initial investment, but the individual capsule could be less expensive than capsules employing other actuation techniques requiring more expensive actuators (*e.g.*, motors). Disadvantages include large, complex external equipment, and the use of strong magnetic fields within an operating room which could interfere with other instruments and electronic equipment. Jinshan Science and Technology (OMOM Capsule Robot, Chongqing, China) and IntroMedic (MC1000-WM, Seoul, South Korea) have both developed a magnetic guidance system for a CE, neither of which has received FDA approval or a CE mark. IntroMedics non-magnetic version, the MC1000, received FDA approval in 2012, and it is predicted that approval for the magnetic guidance system will be awarded within the next 5 years upon improvement of their existing magnetic control system. Even with a CE mark or FDA approval, these existing magnetic guidance systems utilize handheld controllers, and are not automated. In a study evaluating the effectiveness of the IntroMedic magnetic system, results showed that magnetic maneuvering was possible with X-ray fluoroscopic visual data, however, real-time video from the capsule was insufficient visual feedback for the clinicians to guide the capsule through the colon [78]. An active locomotion system would ideally be radiation free, only dependent on vision and other sensor fusion in a multi-modal visualization.

Active control of capsules will advance significantly over the next five years. Speaking from a magnetic control standpoint, there are several advanced systems that have already been developed (discussed in Section 1.2.2.4) to actively and precisely control the orientation and position of CEs, however, the largest obstacle to overcome between now and a clinical application will be the implementation of a reliable automated control and risk mitigation. A magnetic link is not rigid, and therefore requires a high level of precision and feedback to close the control loop for reliable and safe control. Control precision can be increased by using multiple electromagnets, however this increases the size and complexity of the system. Control precision can also be increased by using a robotically actuated single magnet, but this method will require high sensorization to close the control loop. Sensorization will require a combination of capsule localization, image processing, force mapping, and other feedback signals to close the control loop. Building upon existing systems, it is predicted that there will be several fully-automated control systems for capsule locomotion

and immersive scenarios within the next five years. Parallel development of multi-functional capsules with integrated screening, therapeutics and diagnostics will also occur.

It is possible that within the next 5 years, an integrated magnetically actuated CE system will be developed that offers automated locomotion of the capsule throughout the GI tract with optional clinician interruption (*e.g.*, to momentarily stop and reorient the capsule, deliver therapy or perform a diagnostic activity), immediate therapeutic capabilities (*e.g.*, drug delivery, targeted radiation therapy, ablation, etc.), and diagnostic services (*e.g.*, biopsy, cell culture, stool sample, etc.), offering an immersive scenario for the clinician. Optical enhancing techniques could lead to *in situ* optical (instead of mechanical) biopsy onboard the capsule in the near future, avoiding the inconvenience of sampling, storing, conserving and analyzing several samples of tissue. Advanced diagnostic methods such as this go beyond standard endoscopic techniques, offering improved image resolution, contrast and tissue penetration, and providing biochemical and molecular information about mucosal disease through light-tissue interactions, force feedback and possible finite element modeling analysis.

In addition to the broad vision, developments within the subsystems of the CE will continue to emerge. For example, capsule power consumption continues to be a relevant challenge, which is limited by the size of the capsule and will be further limited when additional volume is consumed by magnets and feedback sensors, and mechanisms for therapy. In addition to space reduction, the feedback sensors and imaging data will also consume power. Reliable automated control or telemetry will require high frequency and quality imaging data, so compression needs to be optimized for control and diagnostic purposes. Solutions for power needs will be found through batteries or wireless power transmission. Recent advancements related to lithium ion (Li-ion) battery technology could provide an elegant solution for CEs. Pikul *et al.* report a newly developed Li-ion microbattery that offers a power density of up to 7.4 $mW \cdot cm^{-2} \cdot \mu m^{-1}$, which is 2,000 times higher than other microbatteries [79]. Additionally, Singh *et al.* have recently developed a Li-ion battery which can be painted onto a variety of surfaces, conforming to the surface shape [80]. The combination of a high power density battery which can conform to any volume would be a significant step towards an active endoscopic capsule capable of screening, diagnosis and therapy. An alternative solution lies within wireless power transmission. Yu *et al.* present a wireless power transmission system based on electromagnetic induction for

a CE, capable of delivering 150 mW of usable power [81]. The system consists of a transmitting coil ($\varnothing 400$ mm x 200 mm) external to the body and a receiving coil ($\varnothing 10$ mm x 10.5 mm) inside the capsule. The major drawbacks to this system are the additional equipment needed for electromagnetic field production, and the challenge posed by the combination of magnetic control and electromagnetic power induction, although they may be combined for providing locomotion and power. If capsule orientation is unknown, then multiple internal and/or external coils are required, which increases size, cost, and complexity. To reduce the number of coils needed, precise information about capsule orientation is required, which makes localization an even more important issue.

Other capsule subsystems that will likely be the focus of improvement include imaging, signal transmission, and lighting. We predict that capsule endoscopy video quality will improve over the next five years. Advancements in imaging sensors will likely include increased resolution and efficiency with decreased package size. Wireless signal transmission is one of the most power intensive operations for a CE. Improvements to transmission efficiency and novel transmission methods could surface over the next five years. Improvements in lighting will come in the form of hardware (*e.g.*, lighting components such as resistors and LEDs), or software (*e.g.*, efficiency and image quality improvements due to automated lighting adjustment).

Chapter 2

The Quantitative Evaluation of Micro-Patterned Robotic Wheels in a Controlled Static Environment

Despite revolutionary advances in many fields of medicine, there are no active mobile *in vivo* devices commercially available, or in use, today. Several research groups are actively investigating mobility methods in a variety of biological lumens, but little commercial work has been done. While robotic surgery is available today thanks to *ex vivo* robots such as the da Vinci surgical system, these methods are very expensive, require heavy external equipment, and are still constrained by entry incisions. An alternative approach may be to place the robot completely inside the patient. Such devices may enable non-invasive imaging and diagnostics. These devices may be significantly less expensive than current minimally invasive methods, without extensive support equipment, which may allow them to be also used routinely in the emergency room (ER)/trauma sites and remote locations. This study explores micro-patterned treads that may enable mobile capsule crawlers inside the body. Current research efforts into providing contact locomotion using micro-patterned treads are explored including initial drawbar force generation experimental results, dynamic finite element analysis with these tread designs, and *in vivo* porcine evaluation and comparison of two leading tread designs.

2.1 Introduction

The use of endoscopic devices to diagnose and treat a range of GI complications has recently grown; though minimally invasive exploratory and surgical procedures within the gastrointestinal tract are currently limited to endoscopic techniques. When utilizing an endoscopic device, the surgeon has two options of entering the gastrointestinal tract; through the oral cavity, down the esophagus, through the stomach and

into the small intestine via the duodenum, or through the anus, through the rectum, and into the colon and large intestine. A long "push" endoscope entering the oral cavity can reach mid-small intestine, while an endoscope entering the anus can only reach the distal part of the small bowel. This leaves a section of the small intestine that is inaccessible by endoscope. The PillCam is a device that contains an imaging system which is swallowed by the patient. Although the PillCam can visualize the entire GI tract, it is a passive device, and therefore cannot be maneuvered through the tract.

The focus of this research was not to further develop the endoscopic system, but rather to begin to design a locomotion system for an active mobile device that can be placed completely inside the patient and that can provide mobility in both insufflated and collapsed lumens and cavities. This *in vivo* device, equipped with cameras and other sensors, could locate the surgical site of interest after performing diagnostic scans of the region. Therapy would be provided in the form of biopsy, or tissue dissection. Such an *in vivo* robot could ultimately be swallowed, deployed off of the end of an endoscope, or injected with a syringe. The long-term objective of this work is to develop very small mobile devices for *in vivo* diagnostics and therapy. This will require:

(1) design of contact locomotion systems

(2) design and implementation of micro sensors (*e.g.*, fluid flow, pressure, vision, pH)

(3) therapy at the surgical sites.

The short-term goal of this research is to design initial contact locomotion candidate systems and implement them into a capsule device for preliminary surgical evaluation in an animal model. Here, these preliminary tread designs are discussed, and current research efforts into providing contact locomotion using micro-patterned treads are explored. Initial drawbar force generation data using such tracks are presented, dynamic numerical modeling results are described, and early *in vivo* results are discussed.

2.2   Background

2.2.1   Robot-Assisted Minimally Invasive Surgery

Minimally invasive surgery (MIS) is a broad encompassing term that includes keyhole type procedures from orthopedic joint repair to cardiac stent placement. MIS reduces collateral trauma by using tools inserted into the body through small incisions, which allows the patient to recover and resume a normal lifestyle quicker.

Laparoscopic MIS has been advanced by the introduction of the da Vinci surgical system by Intuitive Surgical, Inc. in the early 2000s. The da Vinci system is a tele-robotic system, which consists of four robotic arms (external to the patient) that hold the laparoscope camera and instruments. The advantages of such surgical robotics include hand tremor reduction, additional articulations in surgical instrument end effectors, corrections for motion reversal, and motion scaling. However, since a da Vinci system is an extension of laparoscopy, it also suffers the inherit disadvantages of laparoscopy. First, these robots are situated outside the patient and thus remain subject to the dexterity limitations imposed by the use of long tools inserted through small incisions. Most studies suggest that current externally situated robotic systems offer little or no improvement over standard laparoscopic instruments in the performance of basic skills [82, 83]. Furthermore, a limited range of motion for the robotic camera can still result in obstructed or incomplete visual feedback. Finally, a da Vinci system carries a significant price tag of approximately $1.5M (plus required inspection and scheduled maintenance costs), which limits such a system to be available only to larger hospitals. Currently, there are efforts focusing on developing next generation robots that improve mobility and sensing capability while reducing complexity and cost [84, 85, 86, 87, 88].

2.2.2   *In Vivo* Laparoscopic Robots

As shown by the da Vinci system, the use of robots in MIS offers advantages, but these are limited when situating the robot outside the body. An alternative approach is to build smaller, low-cost, robotic devices or *in vivo* robots that can be placed inside the patient and near the surgical site.

A number of research groups are working on *in vivo* robotic devices for use in minimally invasive

surgery. For example, a proof-of-concept design of an *in vivo* stereoscopic imaging system has been described by Miller *in vivo* [89]. A second generation single camera pan and tilt prototype based on this initial concept is described in Hu *in vivo* [90], and is currently being evaluated in *ex vivo* and *in vivo* tests. Finally, the HeartLander robot employs a suction-based drive to move across the surface of the beating heart [91, 92].

Others have previously developed a family of *in vivo* fixed-base and two-wheeled mobile robots (30 cm^3), and demonstrated that they can successfully operate within the insufflated abdominal cavity [93]. These robots have been used to enhance the ability of laparoscopic surgeons to visualize the surgical field [94, 95], and to obtain tissue samples during a single-port liver biopsy in a porcine model [96].

2.2.3   *In Vivo* Gastrointestinal Robots

While this work has shown that *in vivo* mobility is possible, some such designs will be ineffective in uninsufflated cavities and cylindrical lumens (*i.e.*, GI tract) where fundamentally different mobility approaches and designs are needed. In addition, insufflation in remote/trauma situations is extremely limited due to lack of equipment, and especially in cases where cavity trauma wounds may prevent proper sealing. Thus, an *in vivo* robot must also be able to traverse an uninsufflated cavity in order to be effective in remote/trauma environments.

The simplest such developed *in vivo* robotic mechanisms for the GI tract have been maneuverable endoscopes for colonoscopy and laparoscopy [97, 98]. These devices possess actuators to rotate the endoscope tip after it enters the body. Other *in vivo* robots have been developed to explore hollow cavities (*e.g.*, the colon or esophagus) with locomotion systems based on inch-worm motion that use a series of grippers and extensors [99], rolling tracks [100], rolling stents [101], or the rotational motion of a spiral-shaped body [102]. These devices apply radial pressure to the walls of the hollow cavities they explore. Dario *et al.* have recently described an endoscopic pill with an active locomotion system that uses legs to push against the gastrointestinal walls [103, 104, 18], a system that uses an external magnetic field to move the device through the intestine [38], a system that combines the two aforementioned systems [24], and a clamping system that uses shape memory alloys [105]. Additionally, Harada *et al.* have described a modular robot that enters the body in subsections through the mouth, assembles itself within the gastric cavity for a surgical task, and

then disassembles itself upon completion of the task for natural excretion [106].

2.2.4   Contact Locomotion

The current work presented here focuses on tread-tissue interaction for wheel- or tank-based locomotion devices with simple drive trains. Such results could be applicable to other contact locomotion systems (*i.e.*, wheels, tracks, inch-worms, etc.), in a multitude of cavities (abdominal, gastrointestinal, cardiac, pleural, etc.), for a variety of devices (*in vivo* robots, deployed colon and esophageal scopes, etc.).

A mobile robot moving inside a collapsed lumen or insufflated cavity can be viewed in the general context of tread-surface interaction. Tread-surface interaction has been studied extensively in the robotics and automotive communities in the context of vehicle-terrain interaction. While these passenger car tire studies can yield insight into some aspects of tread-tissue interaction, the locomotion on deformable, fragile tissue involves rather different physical phenomena which are expected to yield different tread layouts. Based on previous findings, we began this research effort by exploring novel contact methods and tread materials that could ultimately enable locomotion in uninsufflated cavities, while maintaining a small footprint to conserve onboard space.

2.3   Micro-patterned Treads

2.3.1   Introduction to Micro-patterned Treads

Researchers at Carnegie Mellon University [107, 108, 109] have developed a method for anchoring a capsule robot in the GI tract. In their work, they use polydimethylsiloxane (PDMS) to coat the legs of their anchoring device. Traction is improved further by forming micropillars on the surface of the PDMS. They showed that dry PDMS with a micropillar pattern produced 50-100% more traction than flat surfaces. They also coated the PDMS with a thin silicon oil layer, which resulted in as much as a 400% friction improvement. Thus, it was believed that if a thin layer of micro-patterned PDMS was applied to the wheels, or treads, of an *in vivo* mobile robot an increase in friction traction could result.

The preliminary PDMS tread pattern tested was derived from an optimized anchoring design [107] consisting of 140 μm pillars with less than 1:2 aspect ratio (*i.e.*, height to width) and 105 μm equidistant

spacing. In addition to testing this equally spaced circular pillar design, treads consisting of various other patterns (evenly spaced, straight rows, slanted rows) of circular and square pillars as well as a smooth surface (no pillars) were tested for a total of six tread patterns.

Two of the other five patterns included circular pillars with 140 μm diameter and a 1:2 aspect ratio (height to width). The straight row tread had rows of 245 μm spaced pillars. The rows were spaced 534 μm apart, and oriented perpendicular to the circumference of the wheel. The slanted row tread (helical pattern when wrapped around a wheel) had rows of pillars spaced 245 μm apart. The rows had a perpendicular spacing of 534 μm and were oriented 30° from a line perpendicular to the circumference of the wheel.

Square pillars were integrated into two addition tread designs. The first square pillar pattern (Fig. 2.1) had 110 μm pillars with a 1:2 aspect ratio with 102 μm vertical spacing and 135 μm horizontal spacing. The second square pillar pattern had square pillars rotated at 45° (rhombus) so that the corners of the square were facing in the direction of travel. The sides of the square were 330 μm, and the edge-to-edge spacing was 127 μm. The sixth tread tested was smooth PDMS, with no pillars.
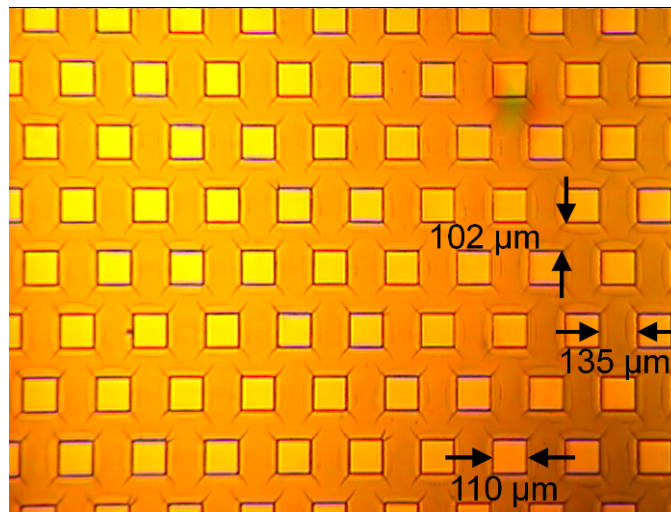
Figure 2.1: Optical microscope view of micro-tread pattern with 1:2 aspect ratio (height:width)

The PDMS treads were fabricated using a micro-mold constructed from silicon wafers (Fig. 2.2a) with SU-8 photo-resist. To make the mold, SU-8 2075 photo-resist was poured onto a 7.62 cm circular silicon wafer (Fig. 2.2b). The wafer was then spun at 500 RPM for 10 s at an acceleration of 100 RPM/s and then

ramped to 3000 RPM for 30 s at an acceleration of 255 RPM/s. The wafer was baked for 5 min at 65 °C and 9 min at 95 °C. The tread pattern was transferred from a chrome mask to the SU-8 photo-resist using a mask aligner and exposure to ultraviolet (UV) light (Fig. 2.2c). The mask had a chrome printout of the five tread patterns on it. As the SU-8 mold was exposed to UV light, the SU-8 partially cured. The pattern, which was blocked by the mask, remained uncured. After UV exposure, the wafer was baked again using the same times and temperatures above from the first bake. The wafer was submerged in SU-8 developer for 7 min. The developer washed away the uncured SU-8, producing the mold (Fig. 2.2d). Then 2.25 mL of liquid PDMS was poured into the SU-8 micro-mold to create a 0.5 mm thick sample (Fig. 2.2e). Once cured, the PDMS was peeled from the mold (Figs. 2.2f and 2.3), and cut into 6 mm wide strips. The strips were glued on 5 mm outer diameter steel hubs that were 8 mm wide using Loctite precision super glue. These micro-patterned coated hubs were then experimentally tested for drawbar force generation performance.

2.3.2   Micro-patterned Tread Testing Device

To test traction performance of a number of different tread patterns, on a number of different materials, a laboratory benchtop testing apparatus was designed and fabricated (Figs. 2.4 and 2.5). Using this apparatus, any number of different tread coated hubs could be evaluated on any number of materials by varying the normal load (*i.e.*, weight of the hub), and wheel torque while measuring the resulting generated drawbar force. The testing apparatus featured a rotational axle, 4.5 mm in diameter, to accommodate the removable PDMS coated hubs, which made contact with interchangeable surface materials. The rotational axle was driven by a belt connected to a direct-current motor (0615 C 4,5S) with a factory installed precision gearhead (06/1 from FAULHABER) that provided a 64:1 gear reduction. The rotational axle and wheel hub were on a pivoting arm to enable changes in applied normal force (*i.e.*, robot or wheel weight). The rotational axis was 12.7 cm from the pivot point. The pivoting arm was attached to a 20.3 cm lever that would apply pressure to a load cell (ESP4-1 KG, Load Cell Central) located 12.7 cm above the pivot point as drawbar force was generated. The testing apparatus was controlled by a custom software program (LabVIEW) that moved the wheel axle by setting prescribed power input while simultaneously recording drawbar force measured by a load cell, and applied current and voltage to the motor. In the initial tests
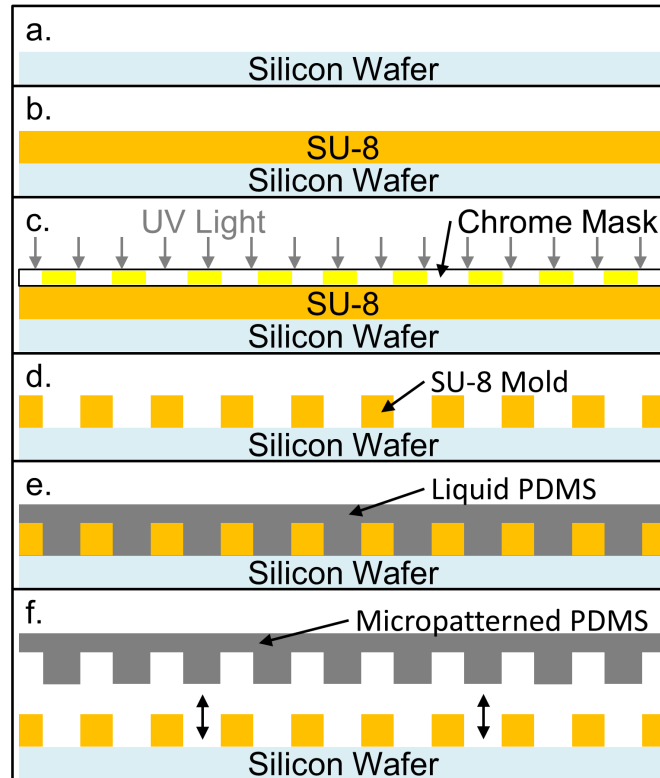
Figure 2.2: Micro-mold photolithography fabrication technique. (a) A circular (7.62 *cm* diameter) silicon wafer was used as the base for the mold. (b) SU-8 2075 photo-resist was spun onto the silicon wafer. (c) A chrome mask was aligned onto the SU-8 and exposed to ultraviolet (UV) light. (d) The wafer was submerged under developer solution to dissolve the unexposed SU-8. (e) Polydimethylsiloxane (PDMS) was poured into the mold and cured. (f) The cured PDMS was peeled from the mold to expose the micro-pattern.
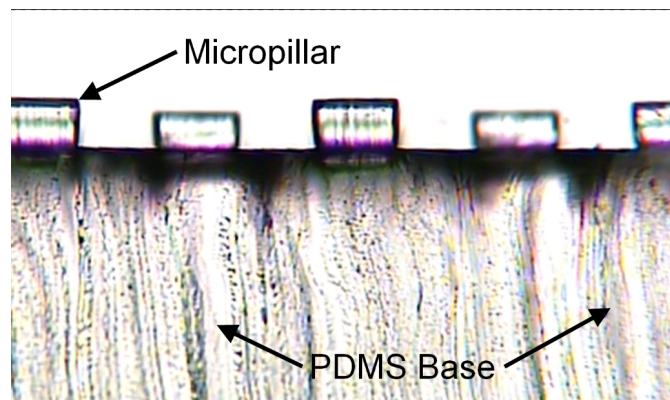
Figure 2.3: Profile view of micro-patterned PDMS with 100X magnification

presented here, focus was placed on looking at the results from static drawbar tests (*i.e.*, measured maximum drawbar force at the point of sustained slippage). Future work will include dynamic tests where the material is moved relative to the wheel to induce slip in a controlled manner as various slip ratios are studied.
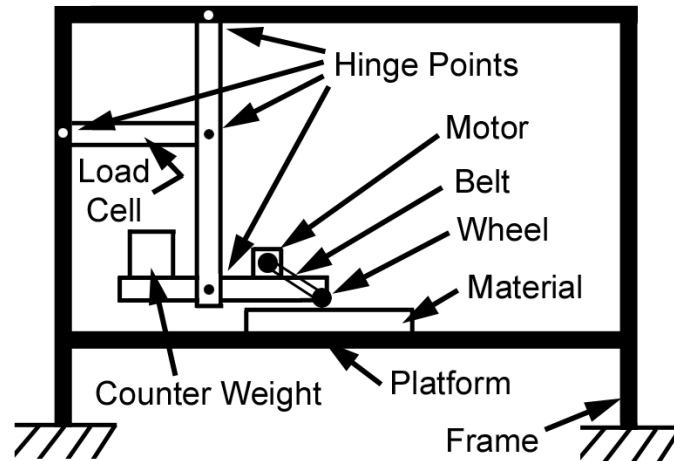
Figure 2.4: Benchtop testing platform schematic for evaluating micro-patterned treads in a static controlled environment

Test preparation included sliding the wheel hub on to the tapered axle for a frictional fit. The test material (Simulated Tissue, TSS-10, Simulab Corporation, Seattle, WA) was placed on the platform, and four normal forces (0.10 N, 0.20 N, 0.30 N, and 0.53 N) were applied sequentially to the axle by adding or removing weights from the horizontal pivoting arm (Fig. 2.4). During each test, the voltage to the motor driving the axle was ramped at a rate of 0.1 V/s. As voltage ramping occurred, the wheel would rotate slightly without slipping, and cause the soft material to deform. Upon further ramping, the wheel would momentarily slip slightly, but then immediately regain traction (Fig. 2.6). The test was terminated at the point of sustained slippage. Each test would last approximately 15 s, from voltage ramp initiation to sustained slippage. Voltage to the motor, current drawn by the motor, and drawbar force produced at the load cell were time-stamped and collected at 1 kHz by the custom software program, and the force produced at the wheel/tissue interface was calculated based on the pivot arm geometry. Each of the six tread patterns was individually tested with each weight five times on the synthetic tissue (Simulated Tissue, TSS-10, Simulab Corporation, Seattle, WA) for a total of 120 tests.
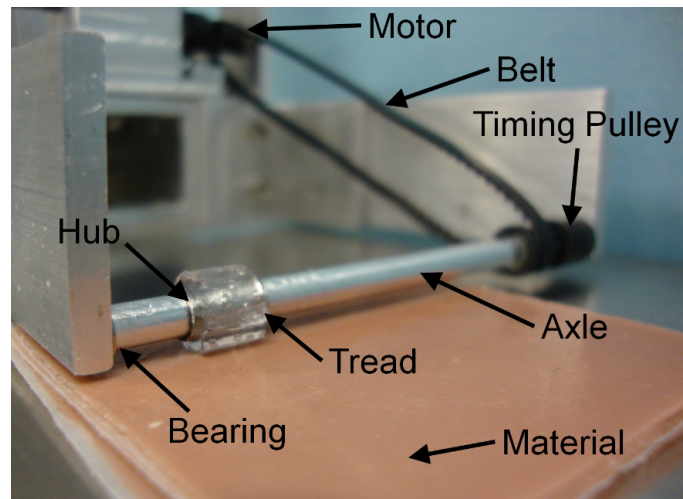
Figure 2.5: Close-up view of the laboratory benchtop testing platform
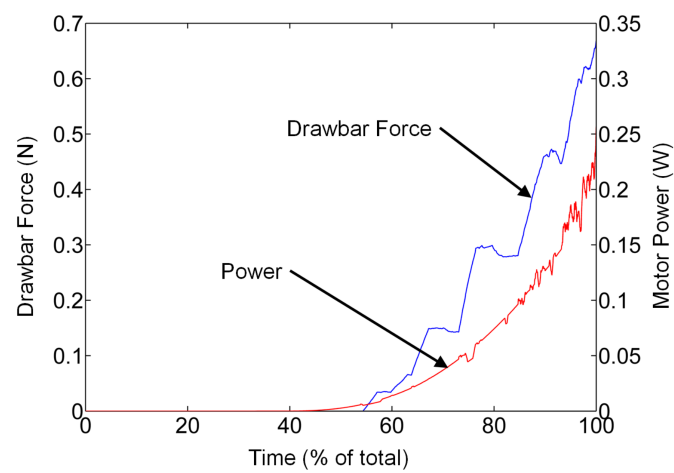
Figure 2.6: Typical trial results of micro-patterned PDMS on synthetic tissue

2.3.3   Preliminary Micro-patterned Tread Results

An example of a typical trial is shown in Fig. 2.6. The raw power and force data are plotted against a percent of the total time. As the voltage was ramped, the current to the motor increased. The first significant force recorded occurred approximately 70% into the test. As the power continued to increase, the drawbar force generated also increased. The input power signal was uniform, while the measured force signal included some noise that was filtered during data processing.

The critical point within the test was the point of sustained slippage. To find this point in the data set, the motor power was plotted against the percent of total trial time. As the wheel was holding traction, but nearing slipping, the current draw of the motor increased as well as the input power. Once the wheel reached the point of continuous slip, the motor was relieved of the resistance, and the power usage immediately decreased. To locate the point of sustained slippage, a sudden decrease in current was located in the data set. The maximum static drawbar force generated corresponds with this maximum current and power input at the wheel prior to slipping continuously. Representative drawbar test results for varying normal forces including 0.10 N, 0.20 N, 0.30 N, and 0.53 N are shown in Fig. 2.7 (equally spaced circular pillars).
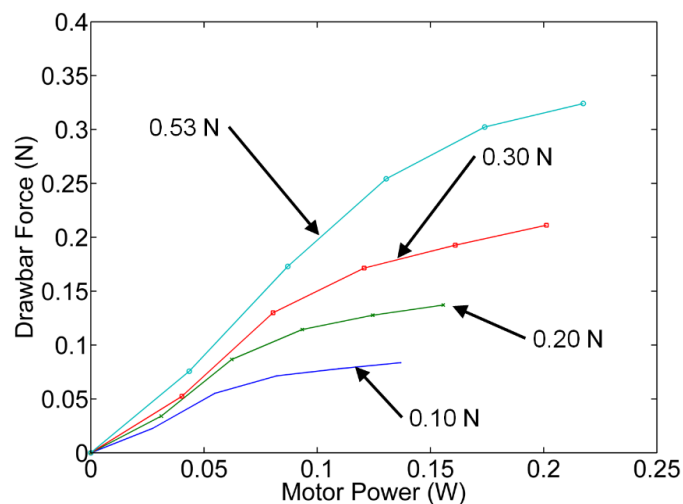
Figure 2.7: Test results for varying normal forces (equally spaced circular pillars)

Using the input voltage and current, electrical motor input power was calculated. The power and

drawbar force data for the five trials for each tread pattern were filtered, averaged, and divided into two categories: treads with circular pillars (Figs. 2.8-2.11), and treads with alternative pillar shapes (Figs. 2.12-2.15). The three types of circular treads included: (1) equally spaced (equidistant), (2) straight rows, and (3) helical rows (at 30 °C). The three types of other treads tested were: (4) square treads, (5) rhombi (or diamond shaped treads that were equivalent to square treads rotated 45 °C), and (6) flat no pattern treads. The recorded mean drawbar forces for each tread pattern were plotted against input power on two different graphs, one for each category with error bars showing maximum and minimum drawbar force values. Results are condensed in Table 2.1.
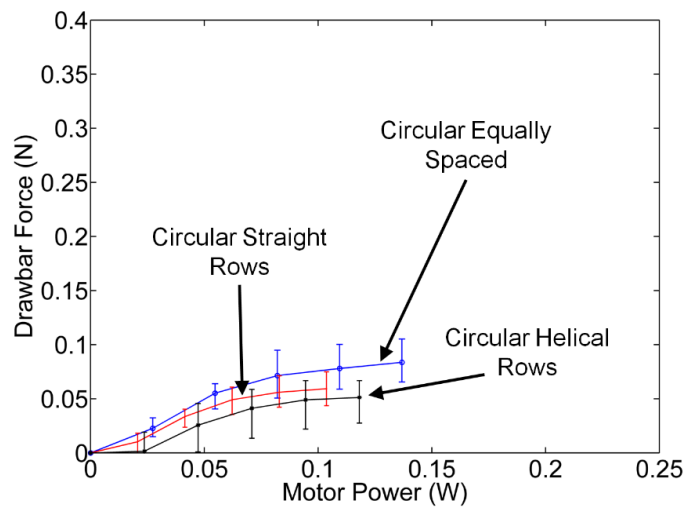
Figure 2.8: Drawbar force results for patterns of circular pillars at 0.10 N normal force

For all normal forces, the results of the circular pillar comparison revealed two trends. The equally spaced pattern produced a larger maximum drawbar force at the slipping point than both the helical and straight row patterns. Similarly, the straight row pattern produced a larger maximum drawbar force at the slipping point than the helical row pattern The maximum drawbar force to normal force ratio was compared between the three circular pillar patterns, and for each normal force, the equally spaced pattern had a higher ratio than both the helical and straight row patterns. Similarly, the straight row pattern had a higher ratio than the helical row pattern.

The square and rhombi patterned treads performed similarly to the circular helical and circular straight
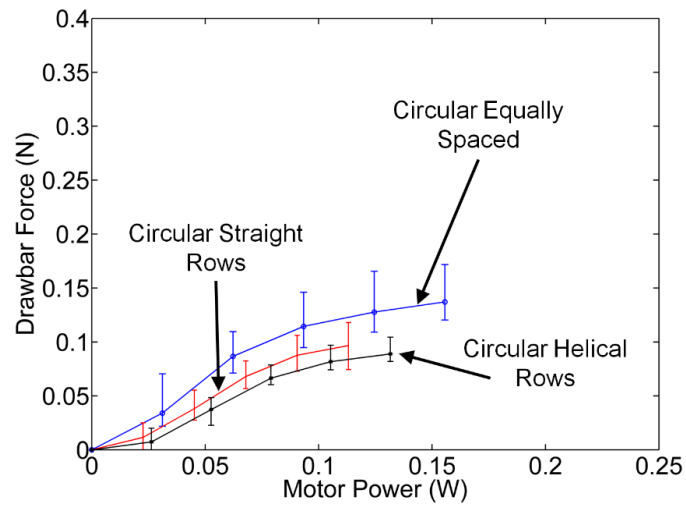
Figure 2.9: Drawbar force results for patterns of circular pillars at 0.20 N normal force
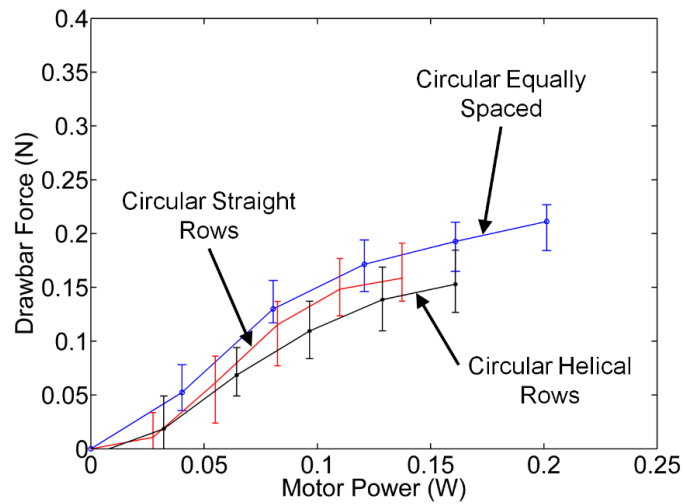
Figure 2.10: Drawbar force results for patterns of circular pillars at 0.30 N normal force
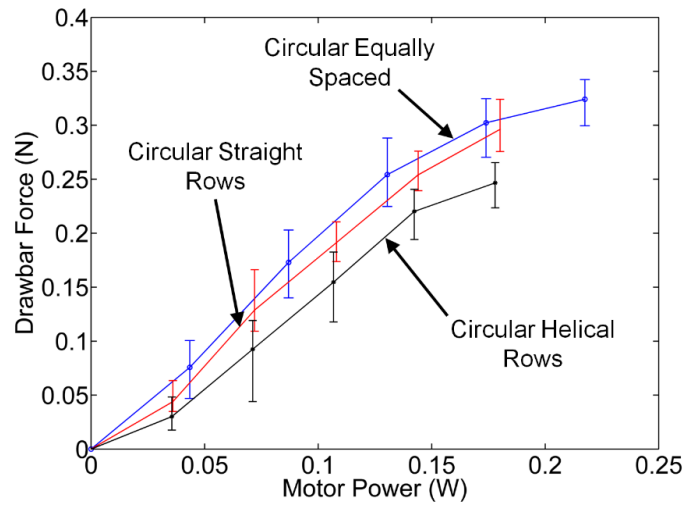
Figure 2.11: Drawbar force results for patterns of circular pillars at 0.53 N normal force
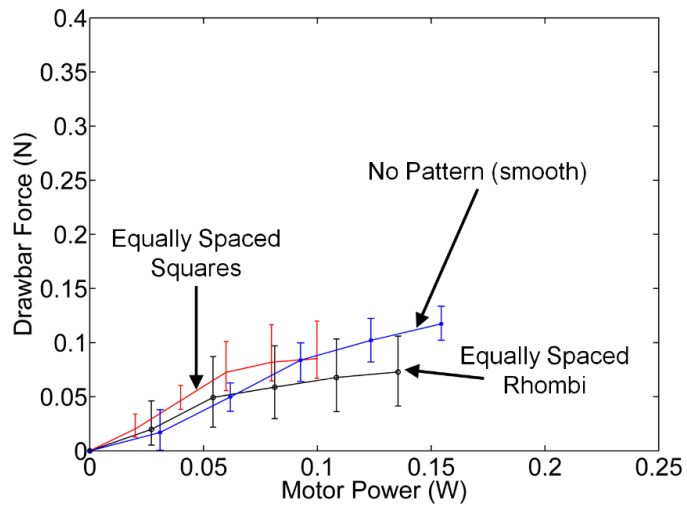
Figure 2.12: Drawbar results for alternative shaped tread patterns at 0.10 N normal force
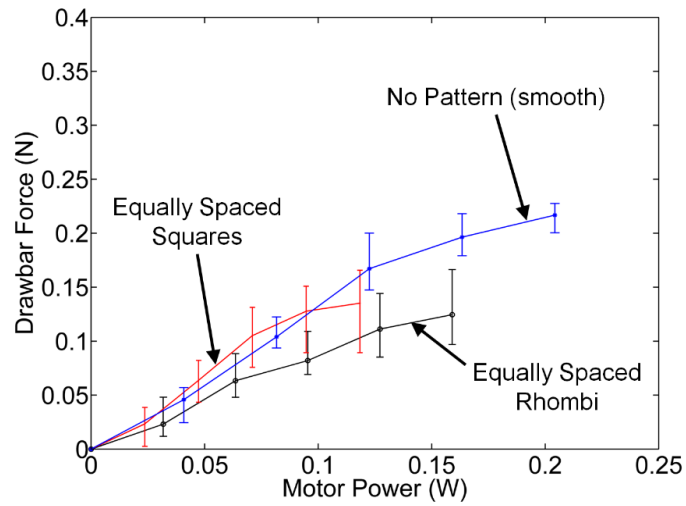
Figure 2.13: Drawbar results for alternative shaped tread patterns at $0.20\ N$ normal force
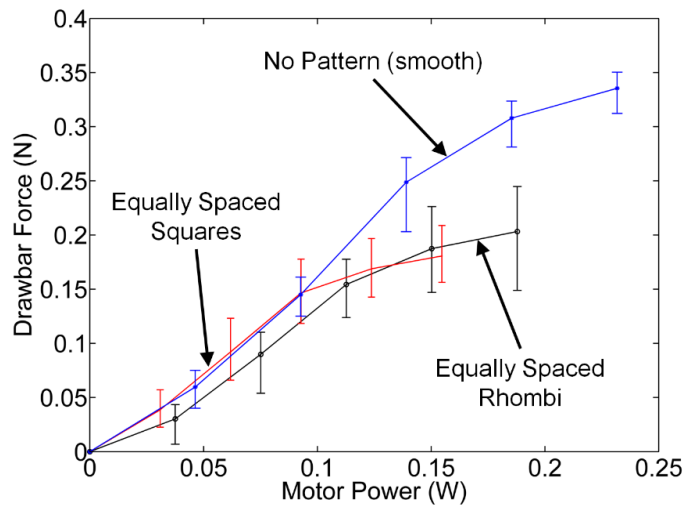
Figure 2.14: Drawbar results for alternative shaped tread patterns at $0.30\ N$ normal force
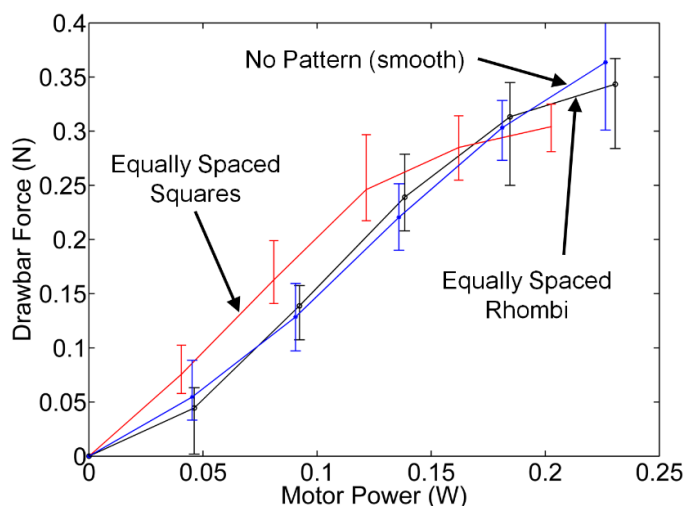
Figure 2.15: Drawbar results for alternative shaped tread patterns at 0.53 N normal force

Table 2.1: Maximum forces recorded during static testing

Tread Pattern	Maximum Drawbar Force (N)	Maximum Input Power (W)	Drawbar/ Normal Ratio
0.10 N Normal Force			
1) Equally spaced circular	0.08	0.14	84%
2) Straight rows circular	0.06	0.10	61%
3) Helical rows of circular	0.06	0.12	55%
4) Equally spaced square	0.09	0.10	85%
5) Equally spaced rhombus	0.07	0.14	75%
6) No pattern (flat)	0.12	0.15	118%
0.20 N Normal Force			
1) Equally spaced circular	0.14	0.16	69%
2) Straight rows circular	0.10	0.11	50%
3) Helical rows of circular	0.09	0.13	46%
4) Equally spaced square	0.14	0.12	69%
5) Equally spaced rhombus	0.13	0.16	64%
6) No pattern (flat)	0.22	0.20	111%
0.30 N Normal Force			
1) Equally spaced circular	0.21	0.20	71%
2) Straight rows circular	0.16	0.14	55%
3) Helical rows of circular	0.16	0.16	52%
4) Equally spaced square	0.18	0.16	61%
5) Equally spaced rhombus	0.21	0.19	69%
6) No pattern (flat)	0.34	0.23	113%
0.53 N Normal Force			
1) Equally spaced circular	0.33	0.22	62%
2) Straight rows circular	0.30	0.18	57%
3) Helical rows of circular	0.25	0.18	47%
4) Equally spaced square	0.31	0.20	58%
5) Equally spaced rhombus	0.35	0.23	65%
6) No pattern (flat) treads	0.37	0.23	70%

treads. Interestingly the smooth tread with no patterned pillars performed similar to the other treads as power was increased but it generated the largest drawbar force before slipping. This possibly suggests that an evenly distributed, or flatter tread, allows for the largest static force as the normal force is more evenly distributed and not discretized with pillars.

All treads roughly followed the same force versus power curve (Figs. 2.8-2.15), but deviated towards the top of the curve. The smooth tread was able to produce a larger drawbar force at a higher power, where as the square pillar and rhombus pillar treads started slipping at a lower power while producing less force. In addition to producing the largest drawbar force at the slipping point, the smooth tread displayed the largest maximum drawbar force to normal force ratio, indicating that it is the most efficient tread design. The success of the smooth tread could be attributed to the applied normal forces. The patterned treads may not have experienced enough normal force to make the pillars useful. With too little normal force, the patterned treads might have been bouncing on top of the tissue, instead of gaining traction. With less normal force, a larger distributed contact surface area might have been the leading factor for success. With a large contact surface area, and low normal force, the smooth tread might have had an advantage in this static testing. Additionally, the success of the smooth tread could be attributed to the material surface environment. In these tests, the synthetic tissue was dry. On a wet synthetic tissue surface, the patterned and smooth PDMS treads might perform differently.

The results presented here for the equally spaced circular pillar tread results, were compared with other results [18, 38, 24]. In those studies, a micro-patterned PDMS anchor was drug over tissue. The static force measured was approximately $0.08 \ N$ with an applied normal force of $0.50 \ N$. Thus, the results presented here show similar drawbar forces.

The maximum drawbar force to normal force ratio was compared between all tread patterns. For all tread patterns, the maximum ratio occurred at a normal force of $0.10 \ N$ (Table 2.1), indicating that all of the treads are more efficient at the lower normal force.

2.3.4   Numerical Modeling

Prior to animal surgical testing, both the treaded PDMS material and smooth PDMS material were numerically modeled using Abaqus. The micro-patterned treads were modeled as 2D-planar pillars on top of liver (Fig. 2.16). As the PDMS material is 40 to 150 times stiffer (depending on the modulus of PDMS, which ranges from 360 kPa to 870 kPa) than tissue, the PDMS treads were modeled as solid, rigid bodies, while the tissue was modeled using the viscoelastic properties of liver [110]. The pillars in the numerical model were equally spaced ($h = w = g = 100 \ \mu m$), with an edge radius of 10 μm.
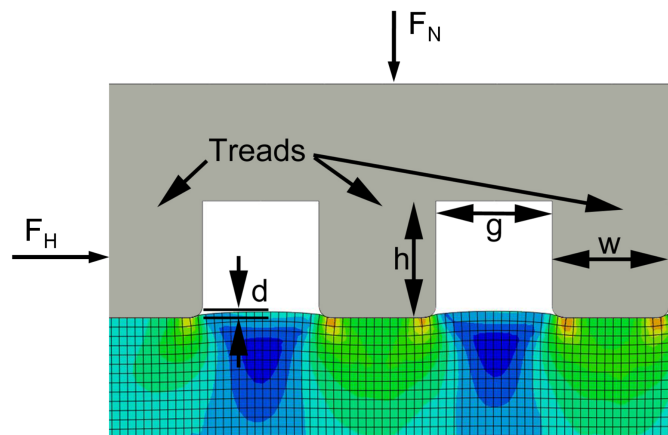
Figure 2.16: 2D-planar model of PDMS micro-patterned treads on tissue (using properties of viscoelastic liver)

Constant normal ($F_N = 0.24 \ N$) and horizontal ($F_H = 0.07 \ N$) forces were applied to the treads (Fig. 2.16) during the simulation. The output of the simulation was horizontal tread displacement as a function of time. An optimal tread would be one that has minimal horizontal movement throughout the simulation (good traction), while a poor performing tread would have significant horizontal motion throughout the simulation (poor traction). The simulation was repeated with identical normal and horizontal forces for smooth (no pillars) PDMS. The duration of each simulation was one second. The results of the two simulations are shown in Fig. 2.17.

The smooth wheel had significantly more horizontal motion during the simulation, thus indicating an inferior performance when compared to the patterned model in this dynamic simulation. The patterned
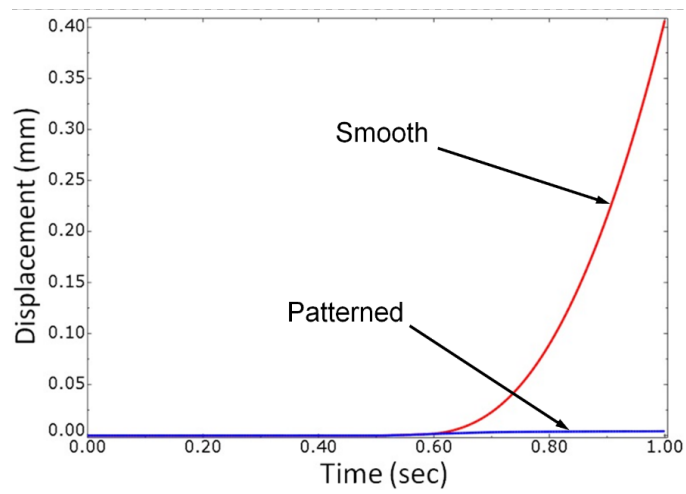
Figure 2.17: Results of the numerical simulation using Abaqus. The micro-patterned tread (bottom) performs superior to the smooth tread (top)

tread moved minimally, suggesting that the patterned wheel would perform superior to the smooth wheel on liver.

In addition to comparing the performance of smooth and patterned PDMS treads on viscoelastic liver, a simulation was performed to investigate the effect of pillar density on tread performance. A second, higher density model, with a tread size reduced by 50% ($h = w = g = 50\ \mu m$), was compared with the 100 μm spacing model. Both simulations included the same pillar surface area, lasted for 1 s, and had identical constant applied normal and horizontal forces. The results of the density simulations are shown in Fig. 2.18.
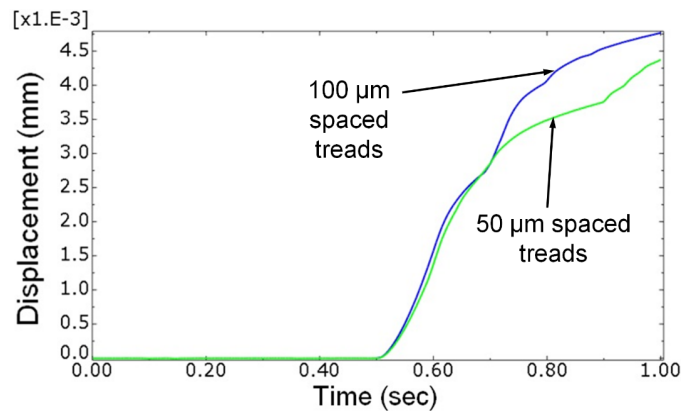
Figure 2.18: Results of the pillar density simulation. The low density pillars (top) had a larger horizontal displacement during the simulation than the high density pillars (bottom)

The high density pillars had less horizontal movement during the simulation, thus indicating a superior performance when compared to the low density pillars. The results of this test would suggest that the higher the pillar density for a given tread, the more traction that tread will provide on liver, though these results have not yet been confirmed experimentally.

2.3.5   *In Vivo* Results

The results of the dynamic numerical model on viscoelastic liver suggested that the wheels would perform differently in a dynamic, *in vivo*, environment than they had during the static benchtop tests on dry synthetic tissue. To better understand the tread performance, a simple robot was fabricated to test the theory *in vivo*. The robot, shown in Fig. 2.19, was constructed using aluminum. The robot had two

wheels, each with an identical surface area and evenly distributed weight. Each wheel was powered by an identical FAULHABER motor with a 64:1 FAULHABER gear head. Each motor was capable of clockwise and counterclockwise motion, creating a tank-like steering environment. The robot was tethered to provide power and control communications. The symmetrical robot was 19 mm in diameter, 110 mm long, and weighed 50 g. The center of mass of the robot was in its middle, so the normal force of each wheel was identical. One of the wheels was coated with smooth (no pattern) PDMS, while the other wheel was coated with patterned (equally spaced circular pillars) PDMS.
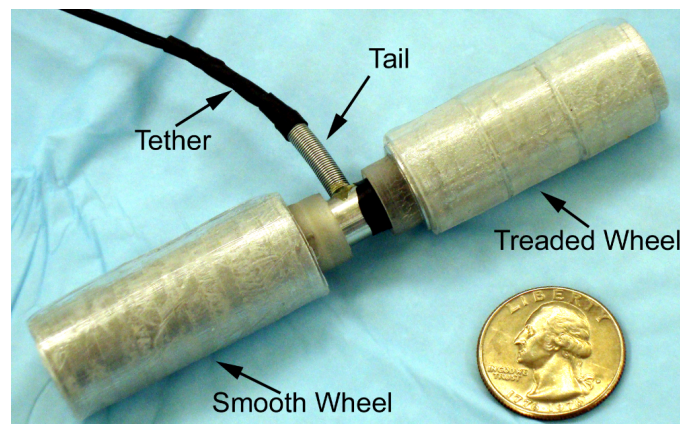
Figure 2.19: Two-wheeled robot used for *in vivo* comparison of micro-patterned versus smooth wheels

The robot was placed in an insufflated abdomen of a live anesthetized porcine (pig) model. The robot wheels were activated, and it was immediately apparent that the patterned wheel performed superior to the smooth wheel. The robot was placed on a variety of different tissues including small bowel (Fig. 2.20), stomach, and liver (Fig. 2.21). The wheels performed similarly on all tissues: the patterned wheel had sufficient traction to move the robot on all tissues, while the smooth wheel generally spun freely with no sign of traction. These mobility tests were administered for approximately 15 min on all tissues in the abdominal cavity.
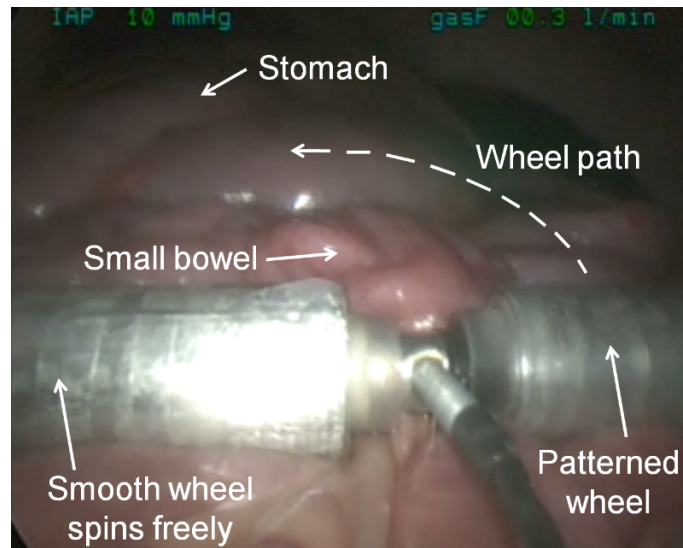
Figure 2.20: *in vivo* robot on porcine small bowel (view from laparoscope)
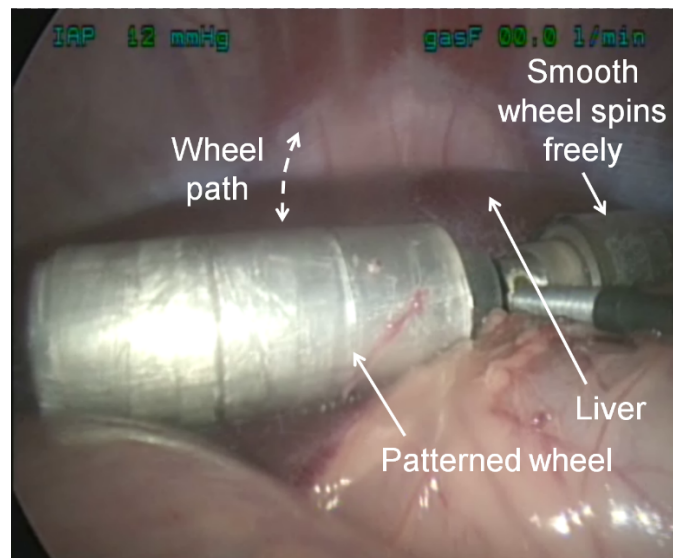
Figure 2.21: *in vivo* robot on porcine liver (view from laparoscope)

2.4   Conclusions

In this work, treads with micro-patterns of varying geometries and spacing were tested using a static open-loop testing apparatus. The treads were tested to compare their drawbar force on dry synthetic tissue as a starting point. It was found that a smooth PDMS tread outperformed all other tread patterns. There were no significant differences between the performance of square and circular pillars. Of the patterns featuring circular pillars, an equally spaced configuration performed superior to the other configurations.

Dynamic numerical modeling was also performed to further investigate the tissue-tread interaction. Treads were modeled as 2D-planar solid, rigid bodies on viscoelastic liver. The results of the simulations suggested that a patterned tread would perform superior to a smooth wheel *in vivo*.

An *in vivo* comparison of a smooth PDMS covered wheel and a patterned (equally spaced circular pillars) PDMS covered wheel was performed, and the patterned wheel outperformed the smooth wheel.

Chapter 3

The Quantitative Evaluation of Micro-Patterned Robotic Wheels in a Controlled Dynamic Environment

In this chapter, an experimental platform is developed to quantitatively measure the performance of robotic wheel treads in a dynamic environment. The platform imposes a dynamic driving condition for a single robot wheel, where the wheel is rotated on a translating substrate, thereby inducing slip. The normal force of the wheel can be adjusted mechanically, while the rotational velocity of the wheel, and the translational velocity of the substrate can be controlled using an open-loop control system. Wheel slip and translational speed can be varied autonomously while wheel traction force is measured using a load cell. The testing platform is characterized by testing one micro-patterned PDMS tread on three substrates (dry synthetic tissue, hydrated synthetic tissue and excised porcine small bowel tissue), at three normal forces (0.10 N, 0.20 N and 0.30 N), 13 slip ratios (-0.30 to 0.30 in increments of 0.05) and three translational speeds (2 mm/s, 3 mm/s and 6 mm/s). Additionally, two wheels (micro-patterned and smooth PDMS) are tested on beef liver at the same three normal forces and translational speeds for a tread comparison. An analysis of variance revealed that the platform can detect statistically significant differences between means when observing normal forces, translational speeds, slip ratios, treads and substrates. The variance due to within (platform error, $P = 1$) and between trials (human error, $P = 0.152$) is minimal when compared to the normal force ($P = 0.036$), translational speed ($P = 0.059$), slip ratio ($P = 0$), tread ($P = 0.004$) and substrate variances ($P = 0$). In conclusion, this precision testing platform can be used to determine wheel tread performance differences on the three substrates and for each of the studied parameters. Future use of the platform could lead to an optimized micro-pattern based mobility system, under given operating

conditions, for implementation on a robotic capsule endoscope.

3.1 Introduction

Currently, the most popular minimally invasive method of exploring and treating the GI tract is through the use of an endoscopic device. Traditional endoscopes (long flexible tubes) have disadvantages, such as size, surgeon disorientation due to the twisting and arduous GI tract, and the potential to perforate the bowel [111]. Recent research efforts have been focused on improving this MIS method through the use of robotics.

3.1.1 *In Vivo* Gastrointestinal Robots

Recently, there has been a move to improve endoscopic technology by moving away from the long flexible tube and towards a small, pill-sized capsule, termed CE. The most advanced CE commercially available today is the PillCam, a device that contains an imaging system, which is swallowed by the patient. Although the PillCam can visualize the GI tract, it is a passive device that relies on the slow peristaltic motion of the bowel for forward movement and therefore cannot be maneuvered. For patients with Crohns disease (an inflammatory bowel disease diagnosable by PillCam), 5% of PillCam procedures result in capsule retention [112, 113]. This results in required surgical removal of the PillCam. One way to improve this statistic would be to introduce the ability to actively maneuver the CE while inside the GI tract.

To improve the passive capsule endoscope, several research groups are attempting to implement an active locomotion component in the design. Previous research [114] has shown that wheeled robots with micro-patterned treads (Fig. 3.1) are a promising method for *in vivo* robotic mobility.

Some *in vivo* robots have been developed to explore hollow cavities (*e.g.*, the colon or esophagus) with locomotion systems based on inch-worm motion that uses a series of grippers and extensors [99], rolling tracks [100], rolling stents [101], or rotational motion of a spiral-shaped body [102]. These devices apply radial pressure to the walls of the hollow cavities they explore. Dario and co-authors describe a capsule endoscope with an active locomotion system that uses legs to push against the gastrointestinal walls [103, 18], a system that uses an external magnetic field to move the device through the intestine [38], a system that combines the
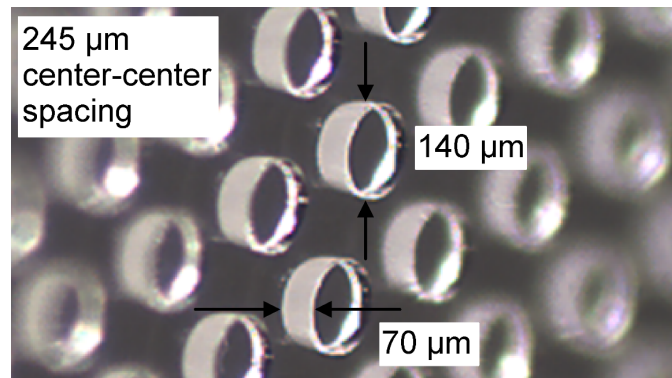
Figure 3.1: An isometric view of the micro-patterned polydimethylsiloxane (PDMS) wheel tread used in this work.

two aforementioned systems [24], and a clamping system that uses shape memory alloys [105]. Additionally, Harada *et al.* described a modular robot that enters the body in subsections through the mouth, assembles itself within the gastric cavity for a surgical task, and then disassembles itself upon completion of the task for natural excretion [106]. Our group is exploring micro-patterned treads for robotic capsule endoscopy [17].

3.1.2   Micro-patterns for Friction Enhancement

Micro-patterning for friction enhancement stems from a biological phenomenon found on the feet of various animals. Terrestrial animals have evolved to develop one of two different micro-patterns on the pads of their feet to enhance friction for locomotion on a variety of different substrates: hairy pads and smooth pads [115, 116]. Both types of pads are able to match the surface structure of their respective substrates, maximizing the contact surface area, and thus increasing the frictional and adhesive properties of the feet [117, 118]. Micro-patterned PDMS has been used as an anchoring method for a capsule robot [107, 108, 109]. Most recently, Buselli *et al.* have placed micro-patterned pads on the ends of the legs of the device in [103, 18] to enhance the friction at the leg-tissue interface [119].

The purpose of this research is to develop a testing platform capable of differentiating between the performances of various wheel treads, under various operating conditions. In this study, one micro-patterned wheel tread (based on the micro-pattern from [107]) is compared against a smooth wheel of identical material

(PDMS).

3.2   Background

To develop a capsule endoscope with wheels or rolling treads as an active mobility system, a method of measuring the relative performance between wheel treads is necessary. The purpose of this research is to develop and characterize a testing platform which will be used to quantitatively measure the performance difference between treads on various substrates and under multiple dynamic conditions by measuring a lumped traction force produced by a tread. The testing platform will investigate dynamic parameters such as normal force, translational speed, and rotational speed. In order to ensure that the platform is sensitive enough to differentiate between wheel treads on each substrate and at various dynamic parameters, an error analysis of the system will be performed.

Others have developed and used devices for physical measurements on biological tissue specimens. For example, Glass *et al.* used two devices to measure the friction force of micro-patterned PDMS on tissue [109]. The first device measured dynamic friction on a flat tissue sample while the second device measured static friction in a lumenal tissue sample. While these devices were able to detect differences in micro-patterns, they were not capable of varying slip due to the fixed tissue samples. Terry *et al.* developed a device to drag various materials across tissue samples to measure friction force [120]. Although this device was capable of varying drag speeds, it was incapable of varying slip as the tissue substrate was fixed.

A device was developed in [93] which was capable of inducing slip by both rotating and linearly translating a wheel across a fixed tissue substrate. The device was capable of detecting differences in drawbar force for wheels with large mechanical grousers. However, no results were presented for varying translational speeds.

The device presented here in this chapter is capable of inducing various slip ratios at multiple translational speeds and normal forces. The device is capable of detecting traction force differences for various micro-patterned wheel samples and biological substrates.

3.3   Design of Benchtop Testing Platform

To evaluate the performance of each of the micro-patterned wheels, a custom benchtop testing platform was designed (Fig. 3.2). The testing platform needed to evaluate each wheel on multiple substrates at various predetermined normal forces (*i.e.*, robot weight, or *in vivo* pressures), and multiple velocity profiles. In order to evaluate the micro-patterned wheels at varying velocity profiles, the testing platform needed to be both rotationally and linearly dynamic (*i.e.*, rotate the wheels while providing linear motion). In an attempt to simplify the design the testing platform was designed to rotate a fixed wheel while translating the substrate (*i.e.*, a vehicle driving on a treadmill), which is dynamically synonymous to rotating a wheel while translating it horizontally (*i.e.*, a vehicle driving on the street).

The testing platform was constructed from an aluminum frame foundation. The frame supported two main components: the linear drive system, and the rotational drive system. The linear drive system consisted of a horizontal linear sliding platform (part iii in Fig. 3.2a), a linear stepper actuator (26DBM12D2B-L, Portescap), and a linear potentiometer (LCP12B-50, ETI Systems). The driving screw of the linear actuator and the wiper on the potentiometer were fixed to the sliding platform. When the linear actuator was activated, the platform moved horizontally, which simultaneously moved the wiper on the potentiometer. The rotational drive system consisted of a vertical pivoting bar (part i in Fig. 3.2a) and a horizontal pivoting bar (part ii in Fig. 3.2a). The vertical bar was attached to the frame at point A (Fig. 3.2b) and hung freely. The horizontal bar attached to the vertical bar at point D. A wheel was attached to an axle (into the page, Fig. 3.2), on the right side of the horizontal bar. The axle also contained a timing pulley, which was driven by a timing belt and a stepper motor (STH-39C804, Shinano Kenshi). The motor shaft was also fixed to the wiper of a rotary potentiometer (132-0-0-103, Spectrol). When the rotary motor was activated, the axle/wheel and wiper of the rotary potentiometer were driven. The linear and rotary motors were driven using a stepper motor driver (ROB-10267, Sparkfun, Boulder, CO).

Upon activation of the linear actuator, the sliding platform moved with linear velocity $\dot{x}$ (mm/s) (Fig. 3.2b, solid black arrow). Upon activation of the rotary motor, the wheel moved with an angular velocity $\dot{\theta}$ (rad/s) (Fig. 3.2b, solid black arrow). The wheel had a known radius r ($9mm$). The following combination
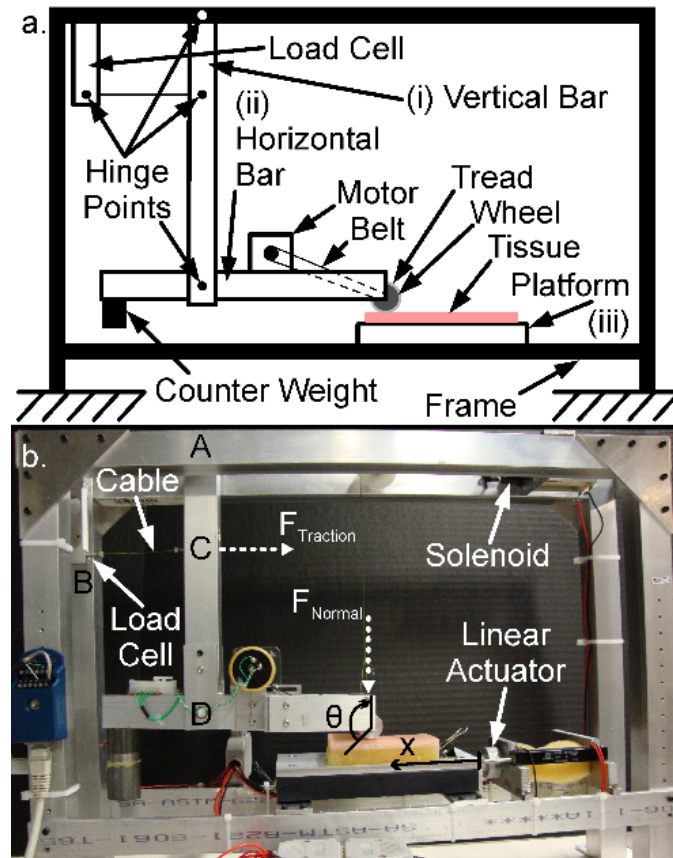
Figure 3.2: A schematic of the benchtop testing platform components (a) and a schematic of the relevant forces (dashed arrows) and displacements (solid black arrows) of the benchtop testing platform (b)

of these parameters yielded a non-dimensional value termed slip ratio (r_s).

$$r_s = 1 - \left| \frac{\dot{x}}{r\dot{\theta}} \right| \tag{3.1}$$

Slip ratio was defined as the percent slip of the wheel on the substrate. Slip ratio can theoretically vary between negative infinite and one. A slip ratio with a value of negative infinite $\left(\lim_{\dot{\theta} \to 0} r_s \right)$ is indicative of a wheel that is not rotating but translating (*i.e.*, pure sliding). A slip ratio with a value of one $(\dot{x} = 0)$ is indicative of a wheel with a finite rotational speed and no translational speed relative to the substrate (*i.e.*, a stationary vehicle performing a burnout). A slip ratio with a value of zero $\left(\dot{x} = r\dot{\theta} \right)$ indicates that the relative rotational and translational speeds of the wheel and substrate, respectively, are equivalent (*i.e.*, pure rolling).

In the test platform, wheel traction force $(F_{Traction})$ was a measured quantity, while normal force (F_{Normal}), or robot weight, was a controlled quantity (Fig. 3.2b, dashed arrows). A preliminary test value, 0.20 N, for the normal force was derived from *in vivo* GI peristaltic force measurements [120]. In the interest of understanding the behavior of the treads at higher and lower normal forces, three test weights were chosen: 0.10 N, 0.20 N, and 0.30 N. The normal force at the wheel was adjusted by the addition or removal of counterweights (Fig. 3.2a). The normal forces were calibrated by placing a load cell force sensor (ELFM-T2E-25L, Entran) under the wheel. The horizontal bar was leveled and the load cell was monitored in real-time using a custom software program (LabVIEW). Counterweights were adjusted until the desired normal forces were achieved within 0.005 N. As a wheel rotates on its substrate, it will produce a horizontal drawbar, or traction, force. The horizontal force produced by the test wheel was transferred to a load cell (ESP4-1 KG, Load Cell Central) through the rigid horizontal and vertical bars. The traction force generated at the wheel was magnified by a factor of three by the vertical lever (part i. in Fig. 3.2a). The wheel on the testing platform was driven clockwise, applying a rightward pull force on the load cell. The vertical bar was attached to the load cell using a cable, as the force it produced on the load cell was a close approximation to a point load. Attaching the vertical bar to the load cell using a rigid connection created larger variability in the data. The load cell was preloaded by tensioning the cable (pulling the vertical bar towards the load cell) in order to ensure that negative traction forces could be measured, where the wheel was being dragged.

A linear solenoid was installed at the top of the frame to automate the testing process. The solenoid was vertically connected to the horizontal bar by a string. When the solenoid was inactive, the string was slack, and the wheel rested on the substrate. When the solenoid was activated, the string became taught and lifted the wheel off of the substrate. After each trial, the testing platform was reconfigured. As the linear tray and wheel were being reset to their original positions, the solenoid was activated, lifting the wheel and preventing contact during reset. Once the platform was reset, the solenoid was deactivated which caused the wheel to regain contact with the substrate, and the test platform was ready for the next trial.

Due to variations in substrate thickness, occasionally the horizontal bar tilted, leading to offsets in applied normal force and measured traction force. To measure this tilting angle, an accelerometer (SEN-09652, Sparkfun Electronics) was installed on the horizontal bar to constantly monitor tilt. If the variation in the tilt of the bar was significant throughout the tests, these data would be used to calibrate the results.

The sliding platform had an aluminum tray fastened to the top of it to accommodate the substrate. The aluminum tray had a recessed area ($82\,mm \times 40\,mm \times 5\,mm$) to help contain a substrate sample (e.g. synthetic tissue, or porcine intestine). In the case of a synthetic tissue sample, the sample was thick enough to be placed by itself in the recessed area. In the case of a porcine intestine sample, the tissue was thin ($3\,mm$) enough that a substrate base was needed to more accurately mimic an in vivo environment, where tissues lie on multiple other tissues. To accomplish this, a custom water-filled latex bag ($82\,mm \times 40\,mm \times 4\,mm$) was fabricated and placed in the recessed area as a base substrate for porcine intestine samples (Fig. 3.3).

3.4   Experimental Setup

The treads were evaluated using large wheels (relative to tank tread size of future RCEs). The large, $18\,mm$ diameter, wheels helped to increase the signal to noise ratio of the system. The micro-patterned wheel was tested on three substrates, dry synthetic tissue (Simulab, Seattle, WA), hydrated (0.9% phosphate buffer solution) synthetic tissue, and excised porcine small bowel. An automated testing procedure was designed to induce thirteen different slip ratios (-0.30 to 0.30 in increments of 0.05) at three translational speeds ($2\,mm/s$, $3\,mm/s$ and $6\,mm/s$). The automated testing procedure was repeated 5 times at each normal force (randomized) so that human error from changing the counter weights was introduced and could be
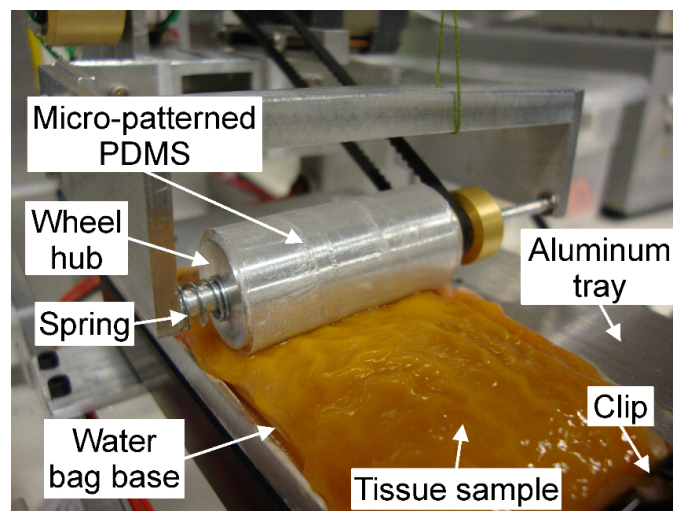
Figure 3.3: Experimental setup for the dynamic benchtop testing platform characterization (excised porcine intestine pictured)

accounted for in the error analysis. Then, one automated testing procedure at each of the three normal forces was performed with the micro-patterned and smooth PDMS wheels on previously frozen beef liver. Beef liver was used for the tread comparison due to its availability over porcine intestine and relatively similar material properties. A statistical analysis was performed to determine the largest source of error (within trials or between automated tests) and if the variance due to error was less than the variance between parameters (tread, normal force, speed, substrate, and slip ratio).

3.4.1 Automated Testing Procedure

A custom software program (LabVIEW) was designed to run the testing platform through thirteen different slip ratios (-0.30 to 0.30 in increments of 0.05). Each set of slip ratios was run at a constant linear speed (*i.e.*, the rotational speed was changed), and repeated three times at incrementing linear speeds (2 mm/s, 3 mm/s and 6 mm/s). Each slip ratio/linear speed combination was repeated consecutively for a total of five automated trials. After one automated procedure (13 slip ratios, 3 speeds and 5 trials for a total of 195 trials) the normal force was physically changed and the automated procedure was repeated. This continued until 5 automated procedures had been completed at each of the three normal forces. The above procedure was then repeated for each of the three substrates.

One single trial consisted of a combination of a tread, normal force, slip ratio, linear speed and substrate. During a trial, load cell data (1 kHz, 24-bit resolution), linear potentiometer, rotary potentiometer and accelerometer (1 kHz, 14-bit resolution) data were collected. Data from the load cell was defined as the traction force, while the linear and rotary potentiometer data were used to calculate induced slip ratio to verify during post-processing that the actual velocities were equivalent to the desired velocities. Data from the accelerometer was used to verify that the tilt on the horizontal bar remained constant throughout the entirety of the experiment. The trial duration was 5 s, and data was collected through the entirety of that time for a total of $5,000$ data points per transducer per trial.

Each time the user adjusted the platform (*i.e.*, changed the normal force, tissue sample or wheel), the preload on the normal force would be calibrated (to be subtracted from the data during post-processing). Porcine bowel and beef liver tissue samples were changed after each automated procedure. No noticeable

damage to the tissue was observed during the tests, and the order of normal force testing was randomized. Tissue samples were preheated to room temperature prior to testing, kept hydrated throughout the entirety of testing and secured to the platform using a clip to prevent lateral sliding (Fig. 3.3). Saline was periodically (approximately every 3 min) sprayed onto the sample to keep the tissue hydrated.

3.4.2 Error Analysis

The traction data was organized into six groups for statistical analysis. The six groups were substrate (dry synthetic tissue, hydrated synthetic tissue and porcine small bowel), normal force (0.10 N, 0.20 N and 0.30 N), translational speed (2 mm/s, 3 mm/s and 6 mm/s), slip ratio (-0.30 to 0.30 in 0.05 increments), trial (5 within an automated procedure), and run (5 between automated procedures). A 6-factor ANOVA was performed to reveal statistical differences between means.

Additionally, a statistical analysis was performed on two different treads (micro-patterned and smooth PDMS). The two treads were tested on beef liver at the same three normal forces and translational speeds. Each speed, normal force, tread combination was repeated for a total of 10 trials. The traction data measured was organized into five groups for statistical analysis; tread (micro-patterned and smooth PDMS), normal force (0.10 N, 0.20 N and 0.30 N), speed (2 mm/s, 3 mm/s and 6 mm/s), slip ratio (-0.30 to 0.30 in 0.05 increments) and trial (10 within an automated procedure). A 5-factor ANOVA was performed to reveal statistical differences between means.

3.5 Results

3.5.1 Benchtop Evaluation

Raw data from a typical trial is shown in Fig. 3.4. The data includes a preload force of 0.45 N explaining the relatively high value compared to the rest of the reported data (Fig. 5 and Fig. 6). Each trial contained transient and steady-state responses. Only the steady-state force was of interest for this study, so the transient data was removed from each trial by averaging the data from the settling time (t_s, Fig. 3.4) through the end of the trial ($t_f = 5$ s, Fig. 3.4), where t_s is the time required for the response curve to reach

5% of the final (steady-state) value.

$$\frac{F_{Traction}\left(t_s\right) - F_{Traction}\left(t_f\right)}{F_{Traction}\left(t_f\right)} \times 100 = 5 \tag{3.2}$$
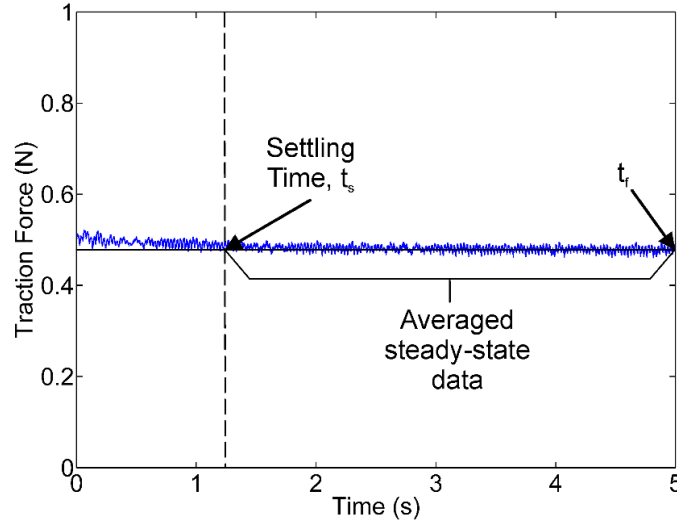
Figure 3.4: Typical raw data (with preload force) from one trial from the benchtop testing platform load cell. The data was post-processed by averaging the steady-state portion of each trial, and subtracting the preload

The preload force (measured at the beginning of each automated run) was averaged and subtracted from each trial. This force generally ranged from $0.40\ N$ to $0.50\ N$. Traction force was first plotted against all slip ratios to investigate the performance of the wheel on each substrate (Fig. 3.5). A subset of the traction force data was plotted against speed and normal force at a slightly positive slip ratio of 0.15 (Fig. 3.6) to condense the meaningful results. A slip ratio of 0.15 was chosen because it is a realistic value that might be achieved by a functional robot, and an approximate value observed in porcine surgeries with prototype RCEs [99, 108].

3.5.2   Error Analysis

The 6-factor ANOVA test revealed that with 95% confidence ($p < 0.05$) there is a statistically significant difference between means when comparing different substrates, normal forces and slip ratios. With 90% confidence ($p < 0.10$), there is a statistically significant difference between means when comparing different
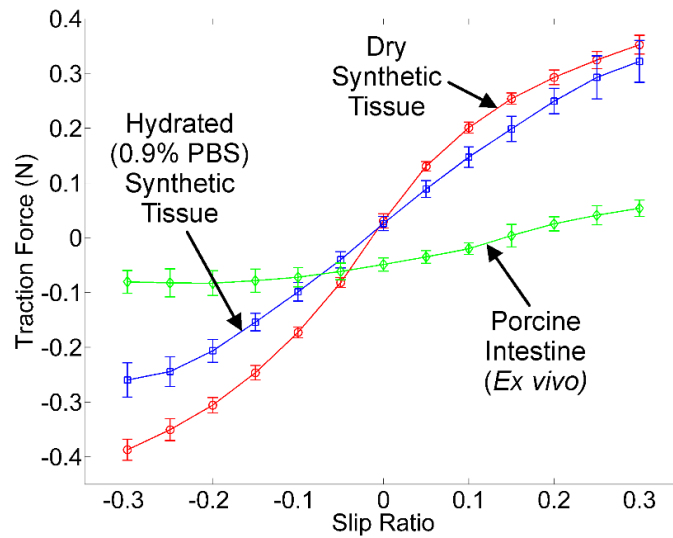
Figure 3.5: Micro-patterned PDMS wheel treads (cylindrical treads shown in Fig. 3.1) perform differently on various substrates. Traction is dramatically reduced on real tissue samples compared to synthetic tissue samples. Error bars are standard deviation. Data shown here is at a translational speed of 6 mm/s and a normal force of 0.30 N
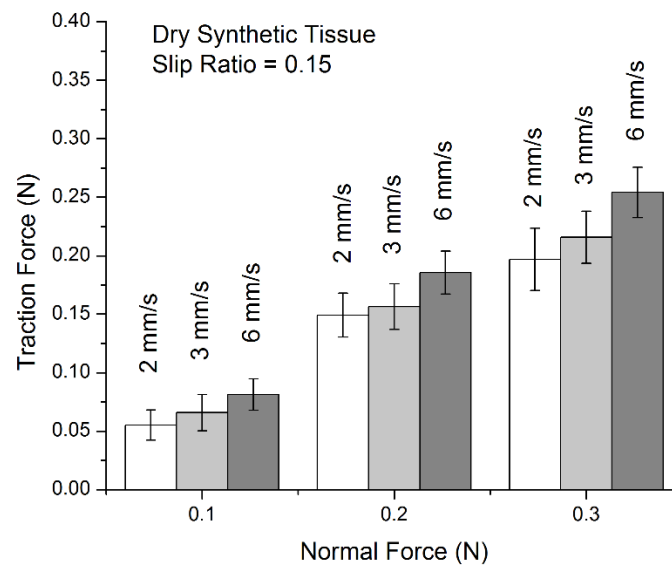
Figure 3.6: Traction force is directly proportional to robot translational speed and normal force. Data plotted here was from a micro-patterned PDMS wheel tread (cylindrical treads shown in Fig. 3.1) on a dry synthetic tissue substrate at a slip ratio of 0.15. Error bars are standard deviation.

speeds. Additionally, with 95% confidence there is no statistically significant difference between means when comparing automated trials and runs (*i.e.*, the platform and human error).

The 5-factor ANOVA test revealed that with 95% confidence, there is a statistically significant difference between means when comparing different treads, normal forces, speeds, and slip ratios. Also, there is no statistically significant difference between means when comparing the automated trials (*i.e.*, the testing platform error). P-values from both ANOVA tests are reported in Table 3.1.

Table 3.1: P-values from the 5- and 6-factor ANOVA tests

Quantity	p-Value
Tread	0.004
Substrate	0.000
Normal Force	0.036
Translational Speed	0.059
Slip Ratio	0.000
Between Automated Runs	0.152
Between Trials within an Automated Run	1.000

3.6 Discussion and Conclusions

The purpose of this study was to determine if the described novel testing platform is able to detect statistically significant differences when comparing different treads, substrates, normal forces, translational speeds, and slip ratios despite error inherent to the testing platform within automated testing procedures and error introduced by a human user from physically handling the system between automated runs (*i.e.*, changing a normal force, tread or substrate). The 6-factor ANOVA test revealed that the variance due to the lumped error in the system (within automated trials and between automated runs) was minimal when compared to the variance from the induced parameters (normal force, translational speed, substrate, and slip ratio). This is due to the relatively low P-values for substrate, normal force, translational speed and slip ratio when compared to the P-values for between automated runs and between trials within an automated run (Table 3.1). The data taken on beef liver and the subsequent 5-factor ANOVA test was used only for a tread comparison on a real viscoelastic tissue. The 5-factor ANOVA revealed that the variance due to the error inherent to the testing platform (within automated trials) was minimal when compared to the variance of different treads. This is due to the relatively low P-value for tread when compared to the P-value for

between trials within an automated run (Table 3.1). In other words, the system error is not large enough to mask difference detection for the following parameters: tread type, substrate type, normal force amount, translational speed and slip ratio.

Additionally, Fig. 3.5 and Fig. 3.6 reveal interesting preliminary trends in the data. In Fig. 3.6, it is apparent that traction force is directly proportional to normal force and translational speed. The data shown in Fig. 3.6 was taken from the micro-patterned PDMS tread (Fig. 3.1) on dry synthetic tissue at a slip ratio of 0.15. This is a representative subset of the entire dataset. From the fundamental laws of physics, it makes sense that traction force increases with normal force. However, it is interesting to note that traction force increases with translational speed. This is likely due to the viscoelastic property of the synthetic and real tissues, where the substrate modulus is strain-rate dependent. Fig. 3.5 reveals the difference in performance of a micro-patterned PDMS wheel on three difference substrates. Due to the lubricating property of the 0.9% PBS solution, it is no surprise that traction force decreases with hydration on synthetic tissue. Furthermore, due to the slippery and softer viscoelastic properties of porcine bowel, it is also no surprise that traction force is further decreased on the real tissue. Note that the traction force on viscoelastic porcine tissue is negative until a slip ratio of approximately 0.15, whereas traction force on the more elastic synthetic tissue becomes positive with positive slip ratios (Fig. 3.5). This can be explained by the differing viscous moduli of the two substrates and a resulting drag force due to substrate deformation. Porcine intestine is more viscous than the synthetic tissue and therefore absorbs more energy, inducing an added drag force on the front of the wheel. This drag force requires a larger slip ratio to be balanced ($r_s \simeq 0.15$) and overcome ($r_s > 0.15$).

The resolution of the traction force data acquisition system is 0.002 N with a mean and max standard deviation (within trials) of 0.0038 N and 0.037 N, respectively. This study has revealed that the described novel testing platform is capable of detecting statistically significant differences in means for the following five parameters: wheel tread, substrate, normal force, translational velocity, and slip ratio. Therefore, the testing platform can be used in future work to quantitatively evaluate wheel tread performance on various substrates, and at various normal forces and induced velocity profiles.

Chapter 4

The Design and Evaluation of an Automated Traction Measurement Platform for Evaluating Micro-patterned Robotic Wheels in a Dynamic Environment and Empirical Model for Predicting Traction Force

Colonoscopy is the leading preventative procedure for colorectal cancer. The traditional tool used for this procedure is an endoscope, which can cause patient discomfort, pain and fear of the procedure. There has been a movement to develop a robotic capsule colonoscope (RCC) in an attempt to mitigate these drawbacks and increase procedure popularity. An RCC is a capsule robot that propels itself through the colon as opposed to being pushed, like a traditional endoscope. In this work an overview of an *in vivo* RCC is given, followed by the introduction of a mobility method for an RCC using micro-patterned polydimethylsiloxane (PDMS). The design of a three degree-of-freedom (DoF) automated traction measurement (ATM) platform for quantitative evaluation of the mobility method is presented. An empirical model for traction force as a function of slip ratio, robot speed and weight for micro-patterned PDMS on synthetic tissue is developed using data collected from the ATM platform. The model is then used to predict traction force at different slip ratios, speeds and weights, and is verified experimentally. The average normalized root-mean-square error (NRMSE) between the empirical model and the data used to develop the model is 1.1% (min 0.0024%, max 4.2%). The average NRMSE between the traction force predicted by the model and the data used to verify the prediction is 1.8% (min 0.020%, max 8.6%). Understanding how model parameters influence tread performance will improve future RCC mobility systems and aid in the development of analytical models, leading to more optimal designs.

4.1   Introduction

Colorectal cancer (CRC) ranks third in incidence in the United States of all cancers for both men and women, resulting in approximately $140,000$ estimated new diagnoses in 2013 [121]. It is also the third deadliest cancer in the United States, accountable for approximately $50,000$ estimated deaths in 2013 [121]. The cumulative risk of CRC for people under the age of 74 is approximately 2% [122]. If detected during the earliest stage, over 93% of CRC patients can survive. Unfortunately, less than 10% of CRC cases are detected in the earliest stage [123]. To increase early detection rates, regular colon screening is highly recommended for patients older than 50 years of age or for those who have a family history of CRC [124]. Colonoscopy is the most effective method for colon screening due to the ability to visualize the colon, acquire immediate biopsies, and remove cancerous polyps [125, 126], but screening rates remain low due to fear of the procedure, patient discomfort, and invasiveness [127].

The tool used for a traditional colonoscopy is an endoscope consisting of a long, flexible scope, which is inserted into the anus, advanced through the rectum and into the colon. Looping occurs when the distal end of the scope does not advance in the colon, but the rest of the scope does, displacing the colon from its normal configuration and stretching the mesentery muscles. It has been shown that looping is responsible for 90% of the pain episodes in colonoscopy procedures and increases the chance of tissue damage and perforation [10]. In an attempt to decrease procedure invasiveness, which may decrease the patient's fear of the procedure as well as any pain caused by looping, there has been a movement away from scopes and a trend in research toward development of robotic capsule colonoscopes (RCCs).

Passive capsules for gastrointestinal (GI) exploration have been FDA approved and commercially available for almost one decade. State-of-the-art capsules include The PillCam, by Given Imaging Ltd., and the EndoCapsule, by Olympus. These pill-shaped capsules are swallowed by the patient, and their onboard imaging systems provide visual feedback to healthcare providers. The main limitation of these capsules is their passive nature and thus the inability to control their position and orientation. This drawback has led to the development of mobility systems for capsules within the research community. A capsule colonoscope with an active locomotion system is termed RCC.

This study details the mobility system of a robotic capsule colonoscope (RCC) developed by our group, and a 3 degree of freedom (DoF) automated traction measurement (ATM) platform developed to test the mobility system as the RCC design is continually improved. It is important to understand the traction force that an RCC mobility system is capable of generating, so an empirical model was developed for traction force as a function of RCC slip ratio, speed, and weight (discussed in Section 4.3.3) on synthetic tissue. The empirical model is used to predict traction force at different robot speeds and weights on synthetic tissue and is verified experimentally. This study builds upon the work published in [128], emphasizing the design and development of the ATM platform, including an analysis of the measurement signal noise which was not included in [128]. Furthermore, this work includes a modified empirical model with a more in depth explanation of the development, analysis, presentation, discussion, and a practical application of the model to a prototype previously developed in [17].

4.2   Background

The RCC developed by our group utilizes micro-patterned polydimethylsiloxane (PDMS) treads for friction enhancement within the colon. To better understand the friction enhancement capabilities of the PDMS and ultimately design more optimal tread patterns, the ATM platform was designed to evaluate tread performance on various viscoelastic substrates and under various conditions and input parameters. The automation is imperative to the study because it reduces the variability, especially for future studies in which biological tissue will be used. The use of synthetic tissue over biological tissue in this study also reduces variability.

4.2.1   *In Vivo* Robotic Capsule Colonoscopy

An RCC has the ability to self-mobilize, removing the need for a scope to be pushed manually, which mitigates significant pressure against the walls of the lumen, or removing the need to rely on passive locomotion of a capsule. Several mobility methods for RCCs have been pursued including legged [119], inchworm [107], and externally-linked magnetic [12, 129]. The legged capsules are mechanically complex, and significantly distend the colon in the radial direction, which has raised concerns regarding tissue damage.

The inch-worm capsules have been shown to be successful, but rely on a relatively long device length to operate. Although the magnetically actuated capsules provide a promising locomotion method and a simple capsule design, these systems require bulky magnetic equipment external to the patient which take up space and can interfere with other operating room equipment. Our group has had success in the past with *in vivo* wheeled robotic mobility using biologically inspired micro-patterned PDMS treads [114], which led to the design of an RCC (Fig. 4.1) utilizing the same micro-patterned treads [17]. The RCC in Fig. 4.1 consists of a plastic housing with an internally embedded direct-current (DC) motor which drives a gear train. The gear train drives timing pulleys which mate with the inside teeth of each custom tread located radially around the RCC. Each of the 8 treads is 3 mm wide (w_t) and 46 mm long (l_t). The RCC in Fig. 4.1 has a 29 mm diameter and length l_t. The PDMS treads are fabricated with a micro-pattern on the external surface which makes contact with the inner lumen colon tissue and enhances traction, while minimizing adhesion [130]. The normal force exerted on the RCC by the surrounding intestinal walls is

$$F_N = Pw_t l_t N_t N_s \tag{4.1}$$

where P is the contact pressure exerted on the RCC by the surrounding intestinal walls, N_t is the number of treads per side and N_s is the number of sides on the RCC. For the RCC to accelerate, the traction force produced by the micro-patterned treads needs to be larger than the frictional force (F_f) between the intestine and the RCC housing. Frictional force on the RCC housing can be calculated using equation (4.2),

$$F_f = Pw_h l_t N_s \mu_h \tag{4.2}$$

where w_h is the width of the housing between two treads on a side and μ_h is the coefficient of kinetic friction between the housing and intestinal tissue.

4.2.2 Micro-patterned Polymer Treads

Micro-patterning has been used in multiple fields for a vast array of purposes, ranging from microfluidics to friction enhancement. Micro-patterning for friction enhancement has been biologically inspired by insect feet. Certain terrestrial animals have evolved to develop microscopic hairs on the pads of their feet to enhance friction for locomotion on various substrates [116, 115]. The pad is able to match the surface
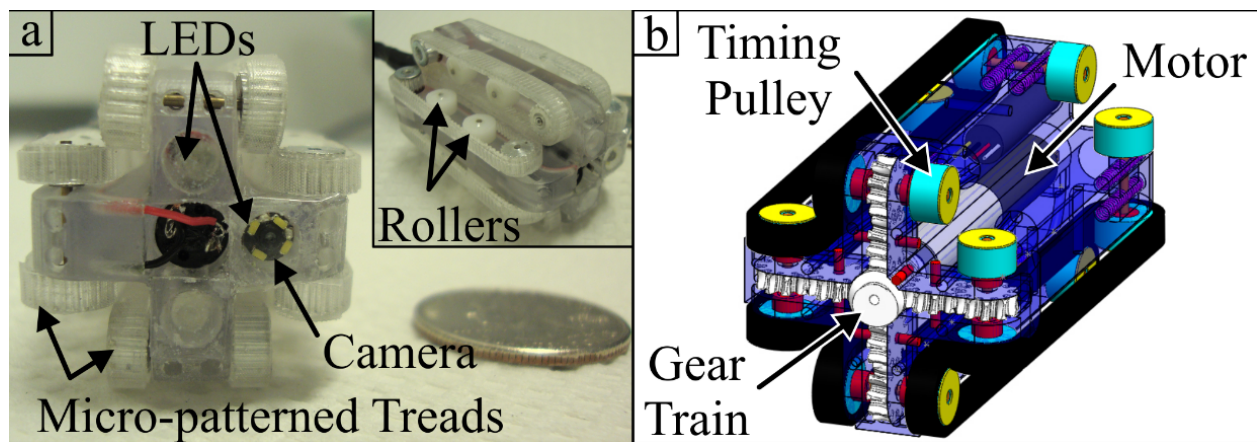
Figure 4.1: RCC prototype with micro-patterned polydimethylsiloxane (PDMS) treads as a mobility method. This prototype includes a CMOS camera, LEDs for illumination, and a small tether for power and video transmission

structure of the substrate, maximizing the contact surface area, and thus increasing the frictional and adhesive properties of the feet [117, 131, 118]. It has been shown that biological friction enhancement can be synthesized by micro-patterning polymers to mimic the microscopic features on the insect feet. In this work, one micro-pattern (Fig. 4.2) is studied and the resulting traction force produced on the synthetic tissue is examined through quantitative benchtop testing. The size and spacing of the micro-pattern used in this study was optimized by Sitti *et al.* in [132] for friction enhancement on small intestinal tissue.
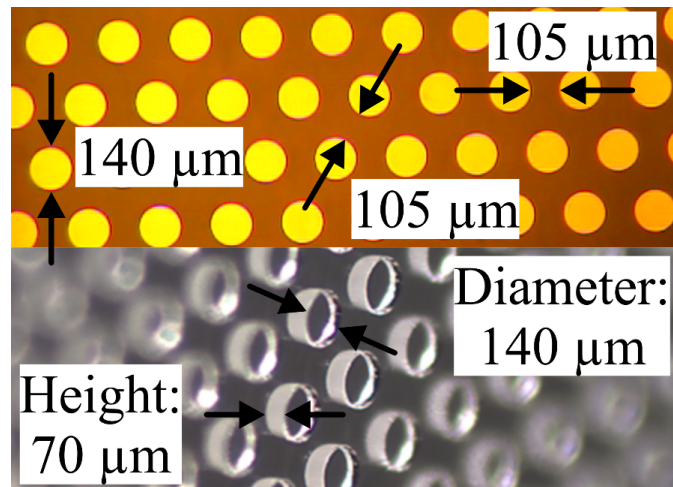
Figure 4.2: Top view (top) and isometric view (bottom) of the micro-pattern used in this study. The pattern was fabricated on the surface of a polydimethylsiloxane (PDMS) tread which was then evaluated for traction force generation.

4.2.3   Tribology Testing Platforms

Others have developed and used devices for physical measurements on biological tissue specimens. For example, Glass *et al.* used two devices to measure the friction force of micro-patterned PDMS on tissue [109]. The first device measured dynamic friction on a flat tissue sample while the second device measured static friction in a lumenal tissue sample. While these devices were able to detect differences in micro-patterns, they were not capable of varying slip due to the fixed tissue samples. Terry *et al.* developed a device to drag various materials across tissue samples to measure friction force [111, 133] at varying drag speeds, however the device was incapable of varying slip as the tissue substrate was fixed.

A device was developed in [93] which was capable of inducing slip by both rotating and linearly

translating a wheel across a fixed tissue substrate. The device was capable of detecting differences in drawbar force for wheels with large mechanical grousers. However, no results were presented for varying translational speeds.

We previously developed a device capable of inducing slip while varying translational speed [134], however it was not capable of closed-loop normal force control (*i.e.*, robot weight). It was capable of only three preset normal forces. The device presented here is capable of closed-loop control and autonomous variation of rotational speed, translational speed and normal force, while detecting traction force for various micro-patterned wheel samples and biological substrates. The automation reduces human input and error, producing a more repeatable study.

4.3   Methodology

A parametric study was performed to determine how the micro-patterned tread traction force on synthetic tissue is affected by robot translational speed, robot wheel rotational speed and robot weight (*i.e.*, normal force). An empirical model was developed to define traction force as a function of slip ratio (a normalized difference between translational and angular wheel velocities), robot translational speed and robot weight. The model was used to predict traction force at new speeds, slip ratios and weights, and then verified using additional experimental data.

Although the ultimate goal is to gain an in depth understanding of micro-patterned tread performance on biological tissue substrates, an important first step is to perform these experiments and develop models for a highly repeatable substrate such as the synthetic tissue used in this study. The substrate used was viscoelastic synthetic tissue with the following parameters for a standard linear solid (SLS) viscoelastic model: $E_1 = 16.4\ kPa$, $E_2 = 0.467\ kPa$, and $\eta = 20.3\ kPa \cdot s$. The detailed procedure used to measure these parameters can be found in [135]. The material properties of the synthetic tissue resemble typical biological tissues encountered during a colonoscopy such as intestinal tissue and the surrounding abdominal organs (*e.g.*, liver and spleen). One synthetic tissue sample was used for all tests and did not incur any damage or material alteration throughout the tests. All tests were performed in a randomized order.

4.3.1   Micro-pattern Tread Fabrication

The micro-patterned tread was fabricated from a micro-mold which was made using a standard pho-tolithography technique [114]. The pattern (Fig. 4.2) features circular pillars 140 μm in diameter and 70 μm tall. The pillars have an equal edge-to-edge spacing of 105 μm. Liquid PDMS (Sylgard 184, Dow Corning, USA) was mixed at a 10:1 base to curing agent weight ratio and poured onto the micro-mold to create a 1 mm thick tread. The mold was degassed under vacuum and heat cured. The micro-patterned tread was attached to an aluminum wheel hub using double-sided tape and the hub was fixed to the axle of the ATM platform. The following parameters for a SLS viscoelastic model of the PDMS treads were measured using the procedure in [135]: $E_1 = 1.29\ MPa$, $E_2 = 0.072\ MPa$, and $\eta = 0.11\ MPa \cdot s$. Tread stiffness is approximately twelve times that of the substrate.

4.3.2   3 DoF Automated Traction Measurement Platform

The ATM platform (Fig. 4.3) has three DoFs controlling the normal force, and rotational and trans-lational motion of a rigid wheel along a substrate. The 1st DoF provides rotation for the micro-patterned wheel. The 2nd DoF provides translation of the wheel along the substrate. The 3rd DoF adjusts the normal force of the wheel. There is a 4th actuated movement which lifts the wheel off of the substrate during a reset procedure.

4.3.2.1   ATM Design

The ATM platform consists of a base, force plate, linear slider (Del-Tron Precision, Inc., USA), linear motion drive system, horizontal pivoting arm, normal force control system, and rotational motion drive system.

The force plate is fixed to the base of the ATM platform via four horizontally oriented cantilever load cells ($0 - 300\ g$ Weighing Load Cell, Sourcing Map, China) which measure normal force on the plate. The force plate consists of two horizontal plates connected in parallel with four vertically oriented cantilever load cells ($0 - 300\ g$ Weighing Load Cell, Sourcing Map, China) which measure traction force. The top plate serves as a platform for the synthetic tissue substrate. The base of the linear slider is also fixed to the base
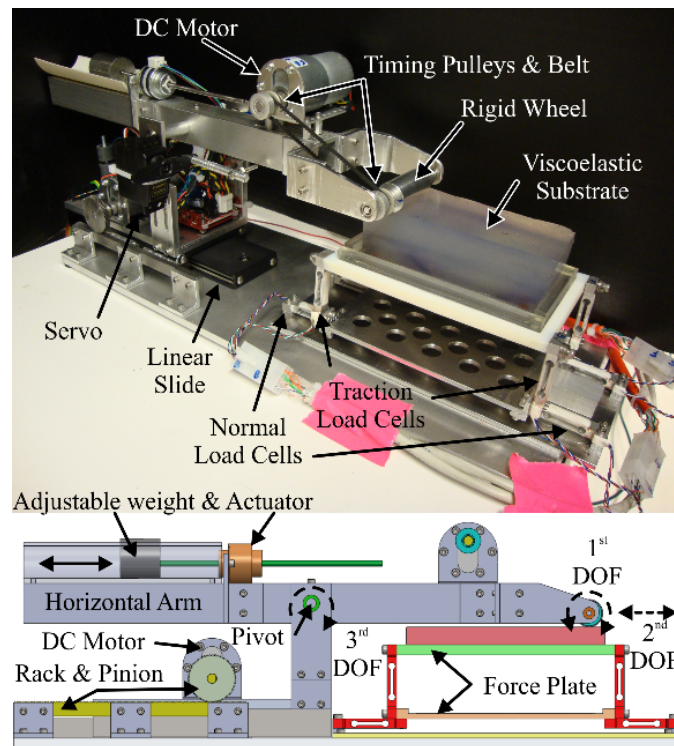
Figure 4.3: Three degree of freedom (DoF) automated traction measurement (ATM) platform for quantitative evaluation of the micro-patterned polydimethylsiloxane (PDMS) treads for robotic capsule colonoscope mobility. DoFs are labeled with dashed arrows (bottom)

of the ATM platform.

The linear motion driving system consists of a DC motor (1447, Pololu, USA), a rack (A 1C12MY 04A150, SDP/SI, USA), and a pinion (A 1Y 2MY04075, SDP/SI, USA). The rack gear is fixed to the base of the ATM platform, parallel to the sliding axis of the linear slider. The DC motor is mounted to the top of the linear slider. The pinion gear mounted to the shaft of the DC motor mates with the rack providing linear motion.

A pair of parallel vertical brackets is attached to the top of the linear slider to provide the pivot point for the horizontal arm. The normal force control and rotational motion drive systems are mounted to the horizontal pivoting arm.

The normal force control system consists of a linear stepper motor (25844-05-001ENG, Haydon-Kerk, USA) and a counter weight. The stepper motor actuates the counter weight, adjusting its distance from the fulcrum, which, in combination with the feedback from the normal load cells, controls the normal force of the wheel.

The rotational motion drive system consists of a DC motor (1447, Pololu, USA), two timing pulleys (A 6A51M017DF0306, SDP/SI, USA) and a timing belt (A 6R51M049030, SDP/SI, USA), providing rotational motion to the wheel axle. The motor is mounted to the end of the horizontal arm with a timing pulley mounted to the shaft of the motor. The second timing pulley is fixed to the wheel axle. The motor shaft and wheel axle are linked with the timing belt.

Each DC motor is equipped with an encoder providing feedback for closed-loop control in both rotation and translation. The position, velocity and acceleration of the two DC motors are controlled by a motor controller (R0403, Basic Micro, USA), which is interfaced with a custom software program (LabVIEW, National Instruments, USA) through a personal computer (PC). The normal force load cells (*i.e.*, horizontal cantilever load cells) provide feedback for closed-loop automated normal force control. The linear stepper motor position (for counter weight adjustment) is controlled by a stepper motor driver (EDE1204, E-LAB Digital Engineering, Inc., USA) and is interfaced with the same custom software program and PC.

A servo motor (S3003, Futaba, Japan) is fixed to the vertical brackets and provides lift to the horizontal arm during a reset procedure to prevent the wheel from dragging across the substrate after each trial. During

a trial, the servo motor is idle, and is not in contact with the horizontal arm, allowing the arm to rotate freely about the fulcrum.

4.3.2.2   ATM Control

The ATM platform is controlled by a custom software program and is designed to run numerous trials of programmed permutations and combinations of linear speed, rotational speed and normal force. Prior to a given trial, the wheel is placed on the substrate and the normal force is set by the linear actuator through movement of the counter weight and the feedback signal (10 kHz, 24 b). During a trial, the wheel is rotated and translated by the two DC motors. Upon activation of the motors, traction and normal force data are collected (10 kHz, 24 b) for the remainder of the trial. The travel distance of the wheel is adjustable with a range of 0 to 100 mm. The travel distance for the results presented in this work was 50 mm. The duration of a trial is dependent on the translational speed of the wheel. After each trial, the wheel is raised by the servo, and the motors reset the wheel to the initial position. This process is autonomously repeated for all programmed combinations of normal force, translational speed and rotational speed. The raw traction force data (Fig. 4.4) is post-processed by taking the mean of the steady-state (to account for acceleration and deceleration of the wheel) portion of each trial. It was determined that by taking the mean of the middle 60% of each trial, the transient data at the beginning of the trial (from wheel acceleration) and at the end of the trial (from wheel deceleration) was truncated in all cases. A representative plot of raw traction force data is shown in Fig. 4.4. Actual normal force, translational speed and slip ratio values are measured during all trials. The average errors between the set points and the measured values are 0.022 N, 0.0039 mm/s, and 6.7×10^{-4}, respectively.

A convenient way to represent the rotational speed of a wheel relative to the translational speed is through a non-dimensional value termed slip ratio, r_s,

$$r_s = 1 - \left| \frac{\dot{x}}{r\dot{\theta}} \right| \tag{4.3}$$

where $\dot{x}$ is the translational speed of the wheel (mm/s), $\dot{\theta}$ is the rotational speed of the wheel (rad/s) and r is the radius of the wheel (mm). Slip ratio has a range between negative infinity and one. A negative slip
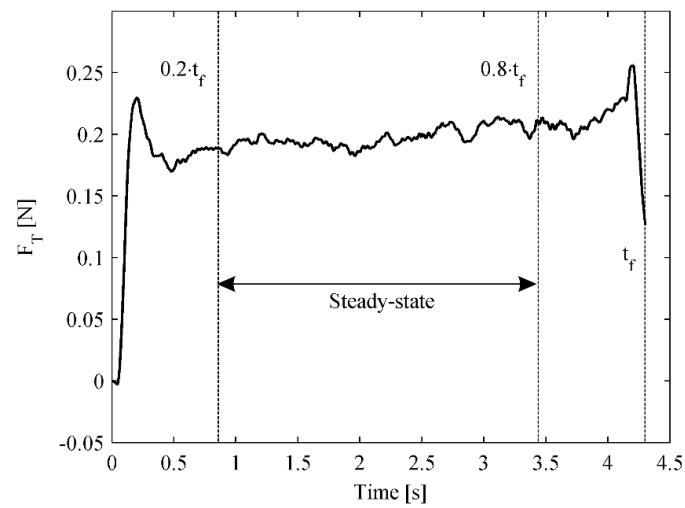
Figure 4.4: A representative plot of raw traction force data taken from the ATM platform. Data shown was produced by a wheel with a 0.30 N normal force, traveling at 8 mm/s at a slip ratio of 0.40. For post-processing, the steady-state traction force was averaged. Steady-state was determined to be the middle 60% of each trial ($0.2t_f$ to $0.8t_f$, where t_f is the trial duration)

ratio is indicative of a dragging or braking wheel $\left(\dot{x} > r\dot{\theta}\right)$. A slip ratio of zero is indicative of pure rolling $\left(\dot{x} = r\dot{\theta}\right)$. A positive slip ratio is indicative of a slipping wheel $\left(r\dot{\theta} > \dot{x}\right)$.

The force plate was characterized by applying known forces in both normal and tangential directions over multiple points of contact. No drift was observed over long periods $(> 4\ h)$ of time.

4.3.2.3   Filter Design

A 2nd order Butterworth low-pass filter was designed to mitigate the noise from the motors. To determine the cutoff frequency, raw traction force data was taken at a range of motor speeds, first with the rotational motor on, second with linear motor on, and third with both motors on (Fig. 4.5). The wheel and substrate were not engaged during these trials so that only vibration and electrical noise from the motors was measured. A typical frequency response of the raw data with both motors active (Fig. 4.5, top) showed a consistent high spectral density around $100\ Hz$ and no significant spectral density below $20\ Hz$. A typical frequency response of the raw data with wheel/substrate engagement (Fig. 4.5, middle) showed a consistent high spectral density well below $5\ Hz$. Therefore, the cutoff frequency for the filter was set to $5\ Hz$ to eliminate high frequency noise from the motors, but keep low frequency responses due to wheel/substrate engagement. Raw traction force data with both motors activated, no motors activated, and the 2nd order Butterworth filter applied is shown in Fig. 4.5 (bottom).

To determine if the filter affected the system response, data was collected at multiple sampling rates (10 kHz, $1\ kHz$, $100\ Hz$, $50\ Hz$, and $10\ Hz$), translational speeds ($2\ mm/s$, $4\ mm/s$, $6\ mm/s$, $8\ mm/s$, and 10 mm/s) and slip ratios (0, 0.1, 0.2, 0.3, and 0.4) in both filtered and unfiltered form. The mean of the steady-state raw data was compared between filtered and unfiltered data and the percent difference was calculated. The mean difference between the filtered and unfiltered data across all sampling rates, translational speeds and slip ratios was 0.64% ($\pm1.1\%$) . Filtering and then taking the mean should theoretically be equal to the mean of the unfiltered data. Since only the mean of the raw data is analyzed in this study, filtering is not necessary. However, it was important to identify the source of the noise and show that it could be filtered from the signal. Additionally, future experiments might focus on the transient traction force data, in which case filtering will be beneficial. The remaining traction and normal force data presented in this work has
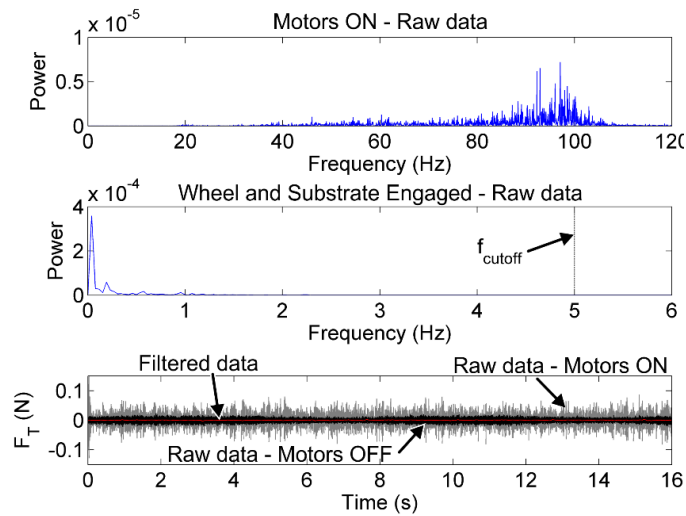
Figure 4.5: A frequency response of raw data with both motors on (top) shows a high spectral density around 100 Hz. A frequency response of raw data with the wheel and substrate engaged (middle) shows a high spectral density at frequencies less than 5 Hz. A comparison of raw data with both motors stationary and with both motors active (bottom) shows that noise is introduced to the data when at least one motor is active. A filter with a 5 Hz cutoff frequency was implemented to eliminate high frequency noise due to the motors but keep low frequency responses due to wheel/substrate engagement. Further analysis was performed to show that pre- and post-filtered data had, on average, 0.64% relative difference when the wheel and substrate were engaged.

been passed through the 2nd order Butterworth filter with a 5 Hz cutoff frequency.

4.3.3   Empirical Model Development

An empirical model was developed from a set of data collected from the ATM platform. The parameters programmed for variation were 5 normal forces (0.15 N, 0.25 N, 0.35 N, 0.45 N, 0.55 N), 5 translational speeds (2 mm/s, 4 mm/s, 6 mm/s, 8 mm/s, 10 mm/s), and 5 slip ratios (0.00, 0.10, 0.20, 0.30, 0.40). These values were selected to cushion a target robot *in vivo* speed of 6 mm/s, and a predicted pressure on an RCC from the clamping of the intestinal lumen of 0.30 N, as determined by Terry *et al.* in [136]. Although a combination of high normal force and high slip ratio is unlikely in practice, all combinations are included here in an attempt to fully understand the mechanics, even under extreme conditions. The dataset consists of 1 trial at each parameter combination for a total of 125 permutations. The wheel was made from a 9 mm radius (r_h) aluminum hub with a 1 mm thick micro-patterned PDMS layer as the tread, giving the wheel a 10 mm total radius (r_w).

To develop the model, the mean traction force (F_T) data was plotted against slip ratio (r_s) on a log-log scale which revealed a linear relationship described by

$$\log\left(F_T\right) = B\log\left(r_s\right) + \log\left(A\right) \tag{4.4}$$

where B is the slope of the log-log plot and $\log\left(A\right)$ is the $\log\left(F_T\right)$ intercept (Fig. 4.6). The average correlation coefficient between $\log\left(F_T\right)$ and $\log\left(r_s\right)$ for all cases was 0.998 with 99% confidence. The form in equation (4.4) can be contracted to

$$\log\left(F_T\right) = \log\left(Ar_s^B\right) \tag{4.5}$$

and an inverse logarithmic transform of equation (4.5) yields

$$F_T = Ar_s^B \tag{4.6}$$

which best represents the data. A nonlinear regression of the form in equation (4.6) was performed to obtain A and A constant values for all 5 translational speeds ($\dot{x}$) and normal forces (F_N).

The regressions resulted in 5×5 matrices of constants for A and B, corresponding to the 25 different combinations of normal force and translational speeds. Then, A and B were assumed to be functions of
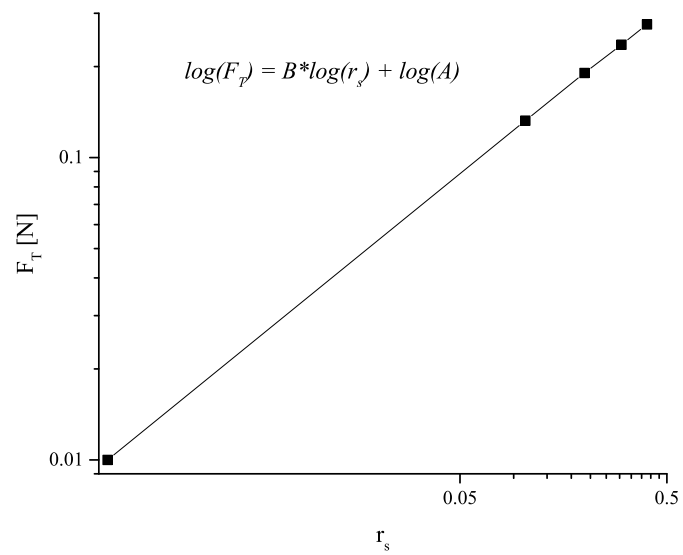
Figure 4.6: A representative logarithmic (in both mean traction force and slip ratio) plot of the micropatterned tread on synthetic tissue. Data shown is from a normal force of 0.25 N and a translational speed of 3 mm/s. The average correlation coefficient between $\log(F_T)$ and $\log(r_s)$ is 0.998

normal force and translational speed. Lastly, the data for A was fit to a 1st degree polynomial in normal

force and 2nd degree polynomial in translational speed, while the data for B was fit to a 2nd degree polynomial

in normal force and 3rd degree polynomial in translational speed. The polynomial degrees were determined

by maximizing an adjusted r-squared value. The empirical model for traction force as a function of normal

force, translational speed and slip ratio is

$$F_T = A\left(F_N, \dot{x}\right) r_s^{B(F_N, \dot{x})} \tag{4.7}$$

where

$$A\left(F_N, \dot{x}\right) = \alpha_0 + \alpha_1 F_N + \alpha_2 \dot{x} + \alpha_3 F_N \dot{x} + \alpha_4 \dot{x}^2 \tag{4.8}$$

$$B\left(F_N, \dot{x}\right) = \beta_0 + \beta_1 F_N + \beta_2 \dot{x} + \beta_3 F_N^2 + \beta_4 F_N \dot{x} + \beta_5 \dot{x}^2 + \beta_6 F_N^2 \dot{x} + \beta_7 F_N \dot{x}^2 + \beta_8 \dot{x}^3 \tag{4.9}$$

Values for the coefficients of equations (4.8) and (4.9) are reported in Table 4.1 along with the r-squared

values of the polynomials. The average normalized root-mean-square error (NRMSE) between the model

and the experimental values used to develop the model were calculated. NRMSE was used as opposed to

percentage error due to the nonlinear relationship between error severity and size. NRMSE distinguishes

this empirical model from the model presented in [128], which is less accurate due to the use of percentage

error.

Table 4.1: Polynomial degrees, coefficients and units for equations (4.8) and (4.8)

	α_0	-0.0118	N
1st-degree in F_N	α_1	0.237	$-$
2nd-degree in $\dot{x}$	α_2	0.104	$N \cdot s/mm$
$r^2 = 0.993$	α_3	0.123	s/mm
	α_4	-0.00148	$N \cdot s^2/mm^2$
	β_0	0.150	$-$
	β_1	0.0172	$1/N$
	β_2	0.165	s/mm
2nd-degree in F_N	β_3	0.726	$1/N^2$
2rd-degree in $\dot{x}$	β_4	-0.0676	$s/N \cdot mm$
$r^2 = 0.988$	β_5	-0.0187	s^2/mm^2
	β_6	-0.117	$s/N^2 \cdot mm$
	β_7	0.0113	$s^2/N \cdot mm^2$
	β_8	0.000639	

4.3.4   Empirical Model Validation

The empirical model was used to predict traction force at an additional 5 normal forces (0.20 N, 0.30 N, 0.40 N, 0.50 N, 0.60 N), translational speeds (3 mm/s, 5 mm/s, 7 mm/s, 9 mm/s, 11 mm/s) and slip ratios (0.05, 0.15, 0.25, 0.35, 0.45). It is important to note that these parameter values were not used to develop the model. A second set of data was collected for these parameters using the ATM platform. Each combination of normal force, slip ratio and translational speed was measured once for a total of 125 permutations. The predicted (from empirical model) and experimental values (from ATM platform) were compared as a validation of the model. The average NRMSE between the predicted values from the model and the experimental values measured by the ATM platform were calculated.

4.4   Results

The results are presented in two sections, Empirical Model Development and Empirical Model Validation, followed by the Discussion (Section 4.5). Each data point displayed in Figs. 4.7 and 4.8 represents 1 trial, and the error bars associated with each data point represent the in trial error. To obtain the value for each data point, the steady-state traction force from each trial was averaged, while the error bars are the standard deviation of that mean. The slip ratios and velocities reported in Figs. 4.7 and 4.8 are measured values.

4.4.1   Empirical Model Development

The developed empirical model for traction force is plotted against slip ratio with the data used to develop the model in Fig. 4.7. The data and model plotted in Fig. 4.7 is for a normal force of 0.55 N and is representative of the data found in the 4 other normal forces measured. The mean and max NRMSE between all of the data and the developed model were 1.1% and 4.2%, respectively, suggesting that traction force can be described by normal force, translational speed and slip ratio.
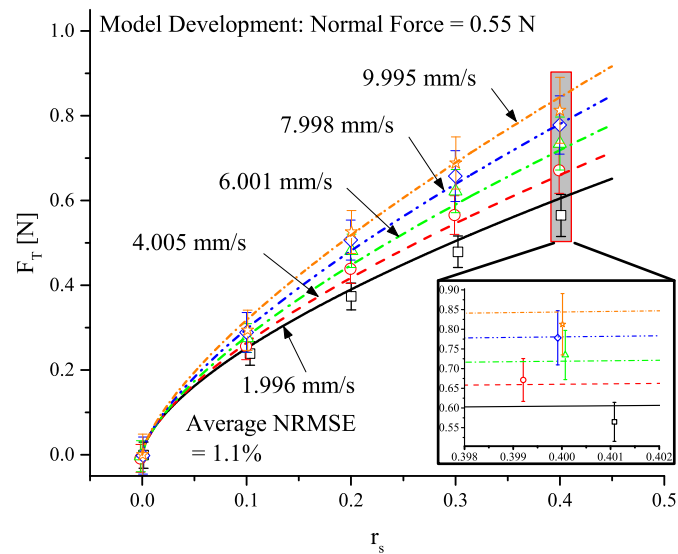
Figure 4.7: The empirical model (lines) for traction force (F_T, y-axis) as a function of slip ratio (r_s, x-axis), translational speed (line type and color) and normal force (0.55 N shown) plotted with data used to develop the model (data points, actual measured values). The average NRMSE between the developed model and data was 1.1% (min 0.0024%, max 4.2%). Error bars are standard deviation of the steady-state in trial mean.

4.4.2 Empirical Model Validation

The empirical model was used to predict traction force at additional normal forces, translational speeds and slip ratios (Fig. 4.8). The lines in Fig. 4.8 are the predicted values from the model, each line represents a new translational speed, different from the translational speeds used to develop the model. Although the data represented in Fig. 4.8 is for a normal force of 0.60 N, the data is representative of all other normal forces. The mean NRMSE between all predicted traction force and validation data was 1.8% with a maximum NRMSE of 8.6% indicating traction force can be sufficiently approximated using the empirical equation described in (4.7).
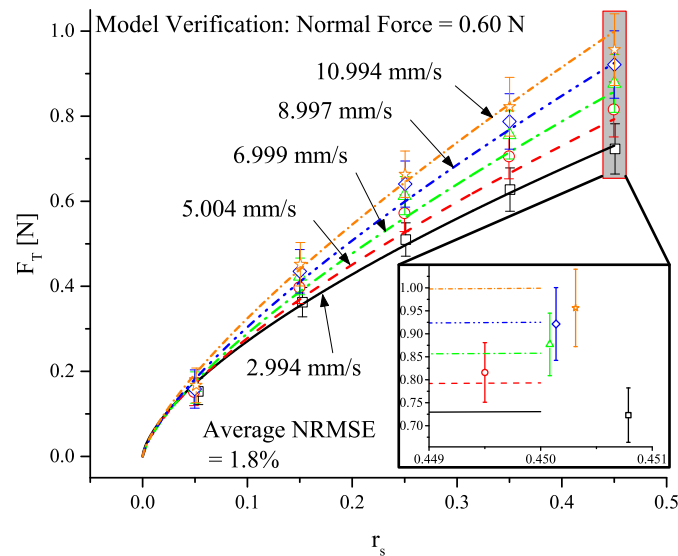
Figure 4.8: The predicted (lines) traction force (F_T, y-axis) as a function of slip ratio (r_s, x-axis), translational speed (line type and color) and normal force (0.60 N shown). Experimental data (data points) were used to verify the model at select measured slip ratios, translational speeds and normal forces. The average NRMSE between the predicted traction force and the experimental data was 1.8% (min 0.020%, max 8.6%). Error bars are standard deviation of the in trial mean.

4.5   Discussion

This empirical model builds confidence for the capabilities of the 3 DoF ATM platform. The empirical model is able to predict tread performance for the micro-patterned wheel in Fig. 4.2 on the synthetic substrate for slip ratios in the range of 0 to 0.45, RCC speeds in the range of 2 to 11 mm/s, and RCC weights in

the range of 0.15 to 0.60 N. *In vivo* dynamics of future RCC prototypes will likely fall into these ranges. It is hypothesized that the coefficients in Table 4.1 are functions of substrate material properties (*e.g.*, modulus, viscoelastic time constant, surface roughness, and hydrophobicity) and tread parameters such as geometry, spacing, aspect ratio, and tread material stiffness. A future goal will be to develop a comprehensive empirical model that can predict the performance of a micro-patterned tread on any biological tissue, given the geometrical parameters of the tread and the mechanical properties of the substrate. This model is a necessary first step as it verifies the ability to build such a model while bypassing high variability from biological tissue. An analytical model describing the contact mechanics between the micro-patterned treads and substrate is the ultimate goal of the research, but the empirical model gives insight into various physical trends.

It is observed that traction force increases with slip ratio to fit the form in equation (4.7). Traction force also increases with normal force and translational speed. The results here contradict those of Canudas *et al.* in [137], who propose dynamic tire friction models for traction on various surfaces. In [137], traction force increases with slip ratio to a point (*e.g.*, 10%) and then decreases. Additionally, Canudas *et al.* report that traction force decreases with increasing vehicle velocity. The main difference between automobile traction research and the research presented here is the mechanical properties of the substrate. Here, tests are performed on a soft, viscoelastic substrate, while the model proposed in [137] is for a rigid and elastic substrate. In addition to our findings, frictional resistance of an object in contact with a viscoelastic substrate has been shown by others [138, 139, 140, 23, 141, 142, 143] to be directly proportional to object horizontal speed, normal force and slip ratio. It is well-accepted that the positive correlation to speed is a result of the strain-rate dependent stress response of the substrate. With tissue (or in this case synthetic tissue), the substrate deformation is relatively large, so the strain rate effect is magnified.

In addition, the trends observed here with data taken using the 3 DoF ATM platform agree with the results in [134] which utilized an entirely different traction force measurement platform. The results in [134] show that traction force increases with slip ratio, normal force and speed for the same micro-pattern used in this study on dry synthetic tissue. Furthermore, the mean NRMSE between the data presented here and the data from equivalent parameter values in [134] is 1.1%.

In [136], Terry *et al.* report a mean contact force from myenteric contractions on a 2.2 cm diameter solid bolus of 1.9 ± 1.0 N/cm. Using equation (4.1), an RCC of identical diameter to the bolus in [136] would experience a summed normal force of $0.30N$. Using equations (4.1) and (4.7)-(4.9), and assuming $\dot{x} = 5$ mm/s, $r_s = 0.15$, $w_t = 3$ mm, $w_h = 6$ mm, and $l_t = 46$ mm, the RCC could produce up to a 7.0 N traction force on synthetic tissue. Using equation (4.2) and the value for μ_h reported by [133], the frictional force on the housing of the RCC by intestinal tissue would be 0.015 N. The traction force produced is larger than the frictional force which satisfies the requirement for acceleration. However, the friction coefficient reported by [133] is for polycarbonate (similar to RCC housing material) on small porcine intestine while the model predicts traction force of micro-patterned treads on synthetic tissue. For an accurate prediction of RCC mobility in the intestine, the model will need to be developed using intestinal tissue as a substrate. We predict that the traction force will reduce by an order of magnitude for real tissue, but still be larger than the frictional force, in which case a control strategy will need to be implemented so that the RCC operates within an optimal traction force to friction force ratio. It is important to note that the frictional force calculated here does not include opposing forces due to a tether. Although a 7 N traction force is much larger than the opposing friction, it is well below reported values for colonic tissue damage [144, 145].

The error bars in Figs. 4.7 and 4.8 are small considering that each data point is one trial (*e.g.*, Fig. 4.4). The error bars are expected to decrease with additional trials and further calibration of the 3 DoF ATM platform. A large percentage of the error is a result of noise produced from vibrations within the viscoelastic substrate. When traction force data is collected at a static state, the error is negligible (± 0.0056 N). Also, a general observation that the authors have noticed during the development of the ATM platform is that error increases with decreasing substrate viscoelasticity, due to the fact that there is less damping in a more elastic material.

The ATM platform is an important tool for RCC mobility as it can be used to evaluate future tread patterns and materials. The evaluation of additional micro-patterns at multiple permutations of slip ratio, translational speed and normal force on various synthetic and biological substrates will lead to additional empirical models which will in turn be used to validate future analytical models. Once the contact mechanics between the micro-pattern and substrate are well understood, an optimized micro-patterned mobility system

for an RCC will be attainable.

It is worth mentioning that the empirical model can theoretically be built upon indefinitely (*i.e.*, including other parameters such as material properties, surface properties, and geometrical parameters). The results presented here formulate a basis to build upon. A natural end point of the project is to develop a comprehensive model that can predict (to within 10%) the traction force of a micro-patterned wheel on a viscoelastic substrate, given the rotational and translational velocities, weight and micro-pattern geometrical dimensions of the wheel along with the material (*e.g.*, SLS parameters) and surface properties of the substrate. It is difficult, if not impossible, to acquire real-time information about tissue properties *in vivo*, but it might be feasible to obtain a generalized characterization of the colon (the target location for the RCC) by compiling results from the literature and supplementing them with extensive experiments. Material properties of the colon might be location dependent, in which case values from a lookup table could be queried using localization data from RCC sensors. Furthermore, it may be possible to estimate the most critical (in terms of model accuracy) material properties (*e.g.*, long- or short-term modulus, viscosity constant) using embedded onboard sensors (*e.g.*, force, pressure, displacement, ultrasonic transducer/receiver) in combination with finite element models of the tissue [146] and ultrasonography. A future addition to the ATM platform will be a sensor to measure vertical deflection of the wheel during a trial. This will be useful for validating future analytical models.

There are several challenges to moving RCCs, especially those with onboard locomotion systems, towards an FDA approval pathway. As mentioned in [147], RCCs with onboard actuation methods face challenges related to size, actuator selection and power supplies. As our prototype is intended for use in the colon, the target size is not one that is swallowable, but the size does need to be reduced for clinical use. Our vision includes a working channel for tools, irrigation and insufflation, which will require a tether. This tether could include power and video signal transmission, so onboard power considerations are not necessary. We believe that an RCC with a 5 mm diameter tether is just as practical as a 13 mm diameter colonoscope. Further considerations for FDA approval will include reliability testing and sterilization procedures. The RCC will likely need to be introduced rectally, and might not initially reduce patient fear of the procedure, but more importantly is the potential for pain reduction, which will eventually lead to wide-spread acceptance.

Future RCC prototypes will include a number of methods to track robot translational position and velocity in order to obtain slip ratio. These methods include magnetics, gyroscopes, accelerometers, and onboard imaging. With the ability to measure *in vivo* slip ratio, we will be able to further validate the empirical model. Additionally, we plan to incorporate a solid-state pressure sensor (MPXH6300A, Freescale Semiconductor, Austin, TX, USA) into the next iteration of the RCC, which has a 300 kPa sensing range and 0.005 kPa resolution (with a 16 b analog to digital converter). This will prove useful for measuring the normal force needed for the empirical model. Implementation of sensors will also enable feedback for future control algorithms using the developed empirical model. Currently, the RCC is teleoperated, but automated navigation for screening with voluntary teleoperated interruptions for diagnosis and therapy is a future goal. This will require sensorization of the RCC so that precise localization can be achieved for a feedback signal. Additionally, image processing (using the onboard camera) will be used for feature recognition and position tracking.

4.6   Conclusions

A 3 DoF automated testing device was presented for quantitative evaluation of micro-patterned treads for RCC mobility. An empirical model was developed to describe traction force as a function of slip ratio, translational speed (*i.e.*, robot speed) and normal force (*i.e.*, robot weight). The model was able to predict traction force for additional normal forces, slip ratios and translational speeds with a mean NRMSE of . Increases in slip ratio, normal force and translational speed correlate with increases in traction force.

The custom designed ATM platform presented is capable of quantitative measurement of traction force for a micro-patterned tread on a viscoelastic substrate. This device will be useful in the future for evaluating additional micro-patterns on additional substrates. The preliminary empirical model builds confidence for the capabilities of the ATM platform and will be used to develop future analytical models.

Chapter 5

The Effect of Hyperelastic Substrate Stiffness, Wheel Tread Fibrillar Structure Size, and Fibrillar Modulus on Traction Force: Experiments and Modeling

5.1   Introduction

This chapter presents a series of studies that were performed to investigate the effect of three different variables on wheel traction force. The three main variables studied were synthetic tissue substrate stiffness, wheel tread fibrillar structure size (both diameter and height), and fibrillar modulus. The study was carried out using finite element modeling, experimental analysis with the ATM platform and comparison to analytical solutions. In order to build a dependable finite element model, the synthetic tissue substrate was characterized using both a large strain hyperelastic model and a viscoelastic model. Model parameters were determined from uniaxial tensile test (for hyperelastic model) and stress-relaxation test (for viscoelastic model) data. In addition to the material models, a velocity-dependent F_T/F_N (traction force divided by normal force) and the Poisson's ratio were experimentally determined. The material characterization was used to build the finite element model, and the model was used to predict traction force generation for both a smooth wheel and a treaded wheel. The FEM results were compared to experimental results.

An interferometer distance sensor was added to the ATM platform in order to further validate the FE model. A parametric study was performed using a smooth wheel on a synthetic tissue substrate to study vertical deflection of the wheel as a function of normal force and differential velocity. These results were compared to an analytical solution for vertical deflection of a cylinder into an elastic half-space, and then the analytical model was used to predict deflection of individual pillars into the substrate.

In addition to building a reliable finite element model, experiments were performed to study the effect of tread fibrillar elastic modulus, fibrillar size, and substrate stiffness. Fibrillar modulus was varied by changing the elastomer to curing agent mixing ratio of the PDMS. Wheels with different fibrillar diameters were fabricated using a stereolithography (SLA) technique, and then coated with PDMS. Substrate stiffness was varied by changing the height of the substrate and was measured using compression tests. The effect of fibrillar modulus, fibrillar size and substrate stiffness on traction force were all evaluated using the ATM platform at a set linear speed, slip ratio, and normal force. The normal force, slip ratio and linear speed were kept constant to remove parametric complexity, and due to the fact that their relationship to traction force is well known (discussed in Chapter 4).

5.2   Background & Theory

A schematic of the wheel-substrate interface problem is shown in Fig. 5.1. The problem can be approached from a global, or macro, perspective (Fig. 5.1a) as well as a local, or micro, perspective (Fig. 5.1b). In this work, both perspectives are utilized in analyzing wheel behavior. The problem setup consists of a wheel of radius R, weight F_N, and length L resting on a substrate with height h, elastic modulus E, and Poisson's ratio ν. The elastic modulus of the substrate is a function of strain (ε) for the hyperelastic case, time (t) for the viscoelastic case, or both strain and time for a combined model. In a static state, the wheel sinks into the tissue a vertical distance (positive **z**-direction) δ, which results in a half-width contact length b. Intuitively, both δ and b are directly proportional to F_N. In a dynamic state, the wheel can have both rotational (ω) and linear (v) velocities. There are two common ways to represent the relationship between the rotational and linear velocities; 1) slip ratio (r_s, equation (5.1)), and 2) differential velocity (v_d, equation (5.2)).

$$r_s = 1 - \left| \frac{v}{R\omega} \right| \tag{5.1}$$

$$v_d = R\omega - v \tag{5.2}$$

Slip ratio is often more convenient and intuitive when approaching the problem from a global perspective (Fig. 5.1a). The limits of r_s can be determined by taking the limit of equation (5.1) as v and ω approach

zero.

$$\lim_{v \to 0} r_s = \lim_{v \to 0} \left(1 - \left|\frac{v}{R\omega}\right|\right) = 1 \tag{5.3}$$

$$\lim_{\omega \to 0} r_s = \lim_{\omega \to 0} \left(1 - \left|\frac{v}{R\omega}\right|\right) = -\infty \tag{5.4}$$

Negative and positive slip ratios are indicative of braking and slipping wheels, respectively, whereas a slip ratio of zero is indicative of pure rolling.

Differential velocity is often more convenient and intuitive when approaching the problem from a local perspective (Fig. 5.1b). The limits of v can be determined by taking the limit of equation (5.2) as v and ω approach zero.

$$\lim_{v \to 0} v_d = \lim_{v \to 0} (R\omega - v) = R\omega \tag{5.5}$$

$$\lim_{\omega \to 0} v_d = \lim_{\omega \to 0} (R\omega - v) = -v \tag{5.6}$$

Negative ($v > R\omega$) and positive ($R\omega > v$) differential velocities are indicative of braking and slipping wheels, respectively, whereas a differential velocity of zero ($R\omega = v$) is indicative of pure rolling. When v_d is positive ($R\omega > v$), the pillar in Fig. 5.1b moves in the negative **y**-direction with respect to the substrate. Similarly, when v_d is negative ($v > R\omega$), the pillar moves in the positive **y**-direction with respect to the substrate. For the remainder of this chapter, relative rotational and linear velocities of the wheel will be discussed in terms of differential velocity. The tread pattern studied in this chapter consists of equally spaced circular pillars of radius and height a and edge-to-edge spacing $3a/2$. When approaching the problem from the local perspective, one can imagine zooming into the contact area of Fig. 5.1a to focus on the contact of one tread pillar (Fig. 5.1b). Fig. 5.1b depicts the contact between a single pillar of radius and height a and the substrate. Under an applied pressure p_0 (in the positive **z**-direction), and neglecting the effects from neighboring pillars, the pillar sinks into the tissue a vertical distance (positive **z**-direction) u_z. Assuming $u_z < a$, the contact area A_c will equal the cross-sectional area of one pillar multiplied by the number of pillars in contact with the substrate. A_c can be closely approximated by multiplying the total contact area (A_t) of the cylinder in Fig. 5.1a by the pillar density γ.

$$A_c = \gamma A_t \tag{5.7}$$
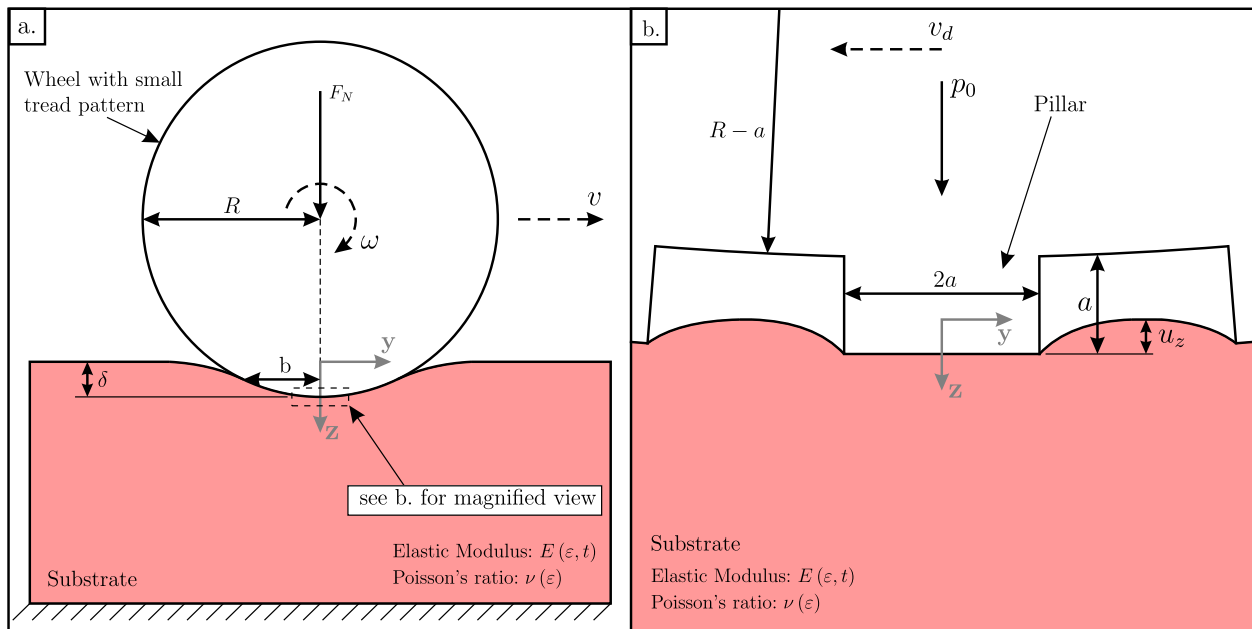
Figure 5.1: (a) A global perspective of the contact mechanics problem for a wheel with a relatively small tread pattern on a soft half-space substrate. The wheel has radius R, contact length L, weight F_N, and displaces a vertical distance δ for both static and dynamic scenarios. (b) A local perspective of the contact between a single circular tread pillar and a soft half-space substrate. The pillar has height and radius a, is acted upon by pressure p_0 and displaces a local vertical distance u_z.

where

$$\gamma = \frac{5\pi a^2}{(3a/2 + 4a)^2} = \frac{20\pi}{121} = 0.5193 \tag{5.8}$$

and

$$A_t = 2RL \sin\left(\frac{b}{R}\right). \tag{5.9}$$

Assuming that b is a function of δ, and that the presence of a small tread pattern is negligible when calculating δ (verified experimentally in Section 5.5.1.1), then the pressure p_0 can be calculated using equation (5.10).

$$p_0 = \frac{F_N}{2\gamma RL \sin(b/R)} \tag{5.10}$$

The vertical displacement of the wheel into the substrate, from both the global perspective (δ) and the local perspective (u_z) are functions of the material properties. Before elaborating on the analytical solution to δ and u_z, a discussion on the hyperelastic and viscoelastic constitutive models will be presented.

A linearly elastic material is one that exhibits a constant modulus of elasticity, E, over a wide range of strain, and can be derived by taking the ratio between stress and strain, $E = \sigma/\varepsilon$. This is an accurate model for many common materials, however, rubber-like materials and many biological materials exhibit strain and/or time dependent elastic moduli. For materials with a strain dependent elastic modulus, hyperelastic material models can be used to simulate their mechanical behavior. Examples of mechanistic hyperelastic models (derived from arguments about underlying material structure) are the Arruda-Boyce and Neo-Hookean models. Examples of phenomenological (derived from observed behavior of the material) hyperelastic models are the Fung, Mooney-Rivlin, Saint Venant-Kirchhoff and Ogden models. For materials that exhibit time dependent stress-strain relationships, viscoelastic material models can be used to simulate their mechanical behavior. Examples of viscoelastic models include the Maxwell, Kelvin-Voigt, Standard linear solid, and Generalized Maxwell models. The synthetic tissue substrate used in this study exhibits both time and strain dependent stress-strain relationships, so both hyperelastic and viscoelastic models will be used to model the mechanical behavior of the material. The Ogden model was chosen to model the hyperelasticity of the substrate due to its excellent agreement with experimental data and the recommendation for use when modeling biological materials [148]. The Generalized Maxwell model ($N = 1$) was chosen to model the viscoelasticity of the substrate due to its computational simplicity and relative good fit with the

stress-relaxation data.

5.2.1 Ogden Hyperelastic Constitutive Model

A material is considered to be hyperelastic if its stress-strain relationship is not constant over a wide range of strain. The typical method for determining hyperelasticity of a material is to perform a large strain uniaxial tensile test and fit the data of a model. The Ogden model was chosen for the substrate in this study, so a short introduction to the model is presented. The Ogden constitutive model was first presented by Ryan Ogden in 1972 [149] and is used to simulate the mechanical behavior of incompressible hyperelastic materials. The Helmholtz free energy equation for the Ogden model as a function of stretch has the following form:

$$\psi = \psi\left(\lambda_1, \lambda_2, \lambda_3\right) = \sum_{p=1}^{N} \frac{\mu_p}{\alpha_p} \left(\lambda_1^{\alpha_p} + \lambda_2^{\alpha_p} + \lambda_3^{\alpha_p} - 3\right) \tag{5.11}$$

with the following consistency condition from linear theory:

$$2\mu = \sum_{p=1}^{N} \mu_p \alpha_p \qquad \text{with} \qquad \mu_p \alpha_p > 0, \qquad p = 1, ..., N \tag{5.12}$$

With $N = 3$, the Ogden model can accurately reproduce simple tension over a very large strain range and has been suggested for use when modeling incompressible materials such as soft tissue [148]. The finite element modeling performed in this work was completed using Abaqus, where the free energy function for the Ogden material model takes the following form:

$$U = \sum_{p=1}^{N} \frac{2\mu_p}{\alpha_p^2} \left(\lambda_1^{\alpha_p} + \lambda_2^{\alpha_p} + \lambda_3^{\alpha_p} - 3\right) + \sum_{p=1}^{N} \frac{1}{D_p} \left(J_{el} - 1\right)^{2p} \tag{5.13}$$

The second summation term involving D_p is for imposing incompressibility. If $D_p = 0$, it is implied that $J_{el} = \lambda_1 \lambda_2 \lambda_3 = 1$ (incompressible), resulting in a constant second summation term. However, if the material is compressible ($D_p \neq 0$), then $J_{el} = \lambda_1 \lambda_2 \lambda_3$ where $\lambda_2 = \lambda_3 = 1 - \nu \varepsilon_1$, assuming the material is isotropic. When compressibility is imposed, then the second summation term becomes strain dependent.

5.2.2 Generalized Maxwell Constitutive Model

A material is considered to be viscoelastic if it exhibits both viscous and elastic characteristics when undergoing deformation. The typical method for determining the viscoelastic response of a material is

a uniaxial stress-relaxation test, where a material sample is subjected to a sudden and constant strain, while the stress is measured over the duration of the test. Typically, the stress in the material drops off exponentially with time. This data can then be fit to a viscoelastic material model. The Generalized Maxwell model with was chosen for the substrate used in the this study, so a brief overview of the model is presented.

The Maxwell mechanical model can be represented by a purely viscous damper and purely elastic spring connected in series, and can be mathematically represented by the following equation:

$$\frac{d\varepsilon}{dt} = \frac{d\varepsilon_{damper}}{dt} + \frac{d\varepsilon_{spring}}{dt} = \frac{\sigma}{\eta} + \frac{1}{G}\frac{d\sigma}{dt} \tag{5.14}$$

where η is the viscosity of the damper and G is the spring constant of the spring. The Generalized Maxwell model links N number of Maxwell arms in parallel with a single spring. The shear modulus $G(t)$ and bulk modulus $K(t)$ as functions of time can be represented by the following two Prony series:

$$G(t) = G_0 \left(g_\infty + \sum_{i=1}^{N} g_i e^{-t/\tau_i} \right) \tag{5.15}$$

$$K(t) = K_0 \left(g_\infty + \sum_{i=1}^{N} k_i e^{-t/\tau_i} \right) \tag{5.16}$$

where g_i and k_i are the relative moduli of terms i and $g_\infty + \sum_{i=1}^{N} g_i = k_\infty + \sum_{i=1}^{N} k_i = 1$.

5.2.3   Universal Poisson Function

A discussion about Poisson's ratio is necessary for fully characterizing the synthetic biological substrate. Isotropic, linear elasticity theory is characterized by two important constants: Young's modulus and Poisson's ratio. As was previously discussed, the stress-strain relationship (Young's modulus in linear elasticity) becomes varying once the assumptions about material behavior deviate form linear elasticity. In the case of hyperelasticity the stress-strain relationship is strain dependent, and in the case of viscoelasticity, the stress-strain relationship is time dependent. In the case of a linearly elastic, homogeneous, and isotropic material, both the Young's modulus and Poisson's ratio can be determined from the uniaxial tension test. The Poisson's ratio is determined from kinematic measurements alone, while the Young's modulus is determined from the ratio between nominal stress and strain. It is well-known that a material is considered to be incompressible when the Poisson's ratio has a value of 1/2. Similar to Young's modulus, the Poisson's ratio

becomes varying when deviations from linear elasticity are made. Beatty *et al.* derived a Poisson function for *nonlinear*, *homogeneous* and *isotropic* materials [150]:

$$\nu\left(\lambda\right) = -\frac{\varepsilon_1}{\varepsilon_3} = \frac{1-\lambda_1}{\lambda_3-1} = \frac{1-\lambda\beta\left(\lambda\right)}{\lambda-1} \tag{5.17}$$

where $\lambda_i = \varepsilon_i + 1$ and $\beta\left(\lambda\right) = \lambda_1\left(\lambda\right)/\lambda$ is a lateral contraction function. For general homogeneous and isotropic elastic solids, Poisson's ratio ν_0 is defined as the value of equation (5.17) in the undistorted, natural state where $\lambda = 1$:

$$\nu_0 = \lim_{\lambda\to 1}\nu\left(\lambda\right) = -\frac{d\lambda_1\left(\lambda\right)}{d\lambda}\bigg|_{\lambda=1}. \tag{5.18}$$

For incompressible materials under simple tension,

$$\lambda_1\left(\lambda\right) = \lambda^{-1/2} \tag{5.19}$$

By substituting equation (5.19) into equation (5.17), Beatty *et al.* define a universal Poisson function for every incompressible, nonlinear, homogeneous, and isotropic material:

$$\nu\left(\lambda\right) = \frac{1}{\lambda + \lambda^{1/2}} \tag{5.20}$$

Therefore, by equation (5.18), every incompressible, isotropic material has a Poisson's ratio $\nu_0 = 1/2$. For nonlinear, incompressible, and isotropic materials, the measured Poisson's ratio will follow equation (5.20) as strain is increased, but will have a value of $1/2$ as $\lambda \to 0$.

5.2.4   Deflections (δ and u_z) in Elastic Half-Space

Although the synthetic biological substrate material is modeled as a combination of a hyperelastic and viscoelastic material using the Ogden and Generalized Maxwell models, respectively, for the finite element model, simplifications need to be made in order to derive analytical solutions for the vertical deflections of the wheel (δ) and tread pillar (u_z).

If the substrate material is approximated as an incompressible, linear elastic solid, with Young's modulus E, and Poisson's ratio $\nu_0 = 1/2$, then the deflection δ of a rigid cylinder with weight F_N, radius R, and length L (into the page in Fig. 5.1a) into the elastic half-space substrate is [151]:

$$\delta = \frac{F_N\rho}{L}\left[1 + \ln\frac{L^3}{\rho F_N R}\right] \tag{5.21}$$

where

$$\rho = \frac{1 - \nu_0^2}{\pi E}.$$

(5.22)

Equation (5.21) is validated experimentally using the ATM platform and the results are presented in Section 5.5.1.1. Then, the half-width contact length b can be calculated using equation (5.23).

$$b = L \exp\left[\frac{1 + \ln 4}{2} + \frac{\delta L}{2 F_N \rho}\right] = \left(\frac{4 R \rho F_N}{L}\right)^{1/2}$$

(5.23)

The maximum pressure p_0 for a single tread pillar can be calculated using equation 5.10. The pressure distribution for a single pillar is [152]:

$$p(r) = p_0 \left(1 - \frac{r^2}{a^2}\right)^{-1/2}$$

(5.24)

Finally, assuming that Young's modulus of the pillar is much larger than the Young's modulus of the substrate, the local deflection of the pillar into the elastic half-space is [153]:

$$u_z = \pi^2 p_0 \rho a$$

(5.25)

Equations (5.21)-(5.25) will be used throughout the chapter to either validate experimental results or to estimate values that have not been experimentally measured.

5.3   Material Characterization

Several experiments were performed for the substrate material characterization. A simple uniaxial tensile test was performed to obtain model parameters for the Ogden hyperelastic material model and to determine the Poisson's ratio. A tensile stress-relaxation test was performed to determine the model parameters for the Generalized Maxwell model for viscoelasticity. Finally, a set of experiments were performed with the ATM platform to obtain data for a velocity dependent F_T/F_N (traction force divided by normal force).

5.3.1   Tensile Test for Ogden Hyperelastic Model

A simple tensile test was performed to obtain stress and strain data for the synthetic tissue substrate. Fig. 5.2 shows the experimental setup for the tensile test. A substrate sample with length = 112 mm,

width $= 12.25$ mm, and thickness $= 7.55$ was clamped between the base and the load cell jaws of the material testing machine (MTS, Eden Prairie, MN, USA). The sample was marked with four reference points which were recorded with a video camera during the tensile test. The sample was stretched to an elongation of 112 mm (100% strain) at a rate of 0.2 mm/s (the slowest reliable speed).

Raw data from a single tensile test trial is displayed in Fig. 5.3a-b (blue circles). Nominal stress σ_n was calculated by dividing the force by the initial cross-sectional area of the sample. Nominal strain ε_n was determined by using image processing to post-process the video tracking of the four reference points. It is apparent that the sample follows hyperelastic behavior. The stress response is initially linear, but at approximately 40% strain, the stress response increases. The material becomes stiffer at higher strains. The data was analyzed in two ways. First, a linear line was fit to the first 20% strain of the data (Fig. 5.3a, red line), and the slope of this line was taken as the Young's modulus ($E = 24.7$ kPa) for a linear elastic approximation of the substrate material. The linear elastic approximation was needed for analytical solutions to the wheel (δ) and tread pillar (u_z) vertical deflections. Second, the data in Fig. 5.3b was input into Abaqus, which generated the Ogden model parameters (listed in Table 5.1). These model parameters were used in the finite element analysis to simulate the hyperelastic behavior the substrate material.

Table 5.1: Parameters for Ogden hyperelastic material model

p	μ_p	α_p	D_p
1	3.64×10^{-4}	2.66	9.06
2	4.18×10^{-7}	19.2	0
3	1.31×10^{-2}	-9.46	0

5.3.2   Stress-Relaxation Test for Viscoelastic Model

A tensile stress-relaxation test was performed to obtain the time dependent stress strain data for the synthetic tissue substrate. Fig. 5.2 shows the experimental setup for the tensile test. A substrate sample with length $= 112$ mm, width $= 12.25$ mm, and thickness $= 7.55$ was clamped between the base and the load cell jaws of the material testing machine (MTS, Eden Prairie, MN, USA). The sample was initially swiftly stretched to an elongation of 40 mm (35% strain) at a rate of 15 mm/s and then held at that elongation for 100 s.
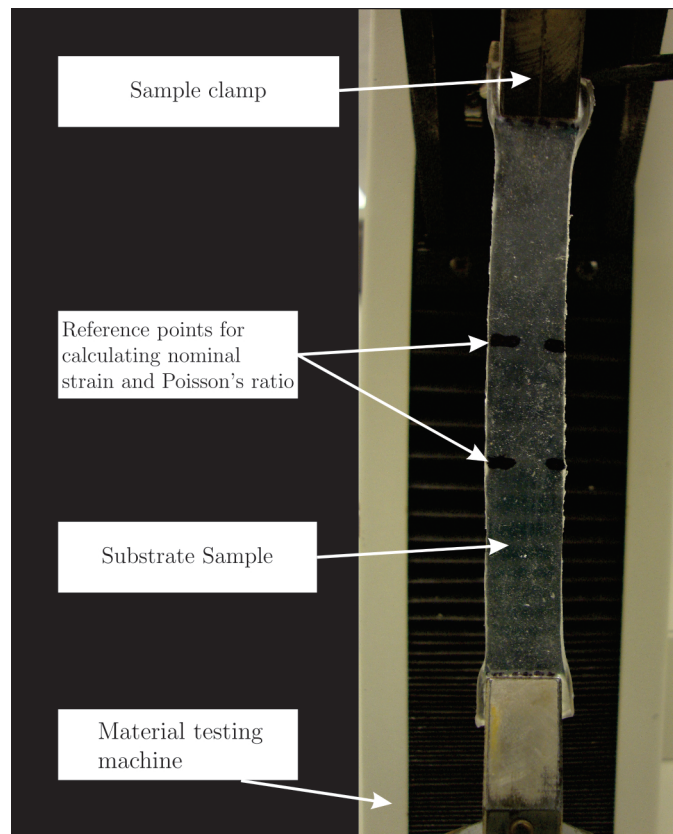
Figure 5.2: Experimental setup for simple uniaxial tensile tests and uniaxial tensile stress-relaxation tests. For both tests, a sample ($length = 112\ mm$, $width = 12.25\ mm$, and $thickness = 7.55$) was clamped between the base and the load cell of the MTS machine. The sample was marked with four reference points for calculating nominal strain and Poisson's ratio. For the simple uniaxial tensile test, the sample was stretched to an elongation of 112 mm (100% strain) at a rate of 0.2 mm/s. For the uniaxial tensile stress-relaxation tests, the sample was initially stretched at a rate of 15 mm/s to an elongation of 40 mm (35% strain) and held for 100 s.
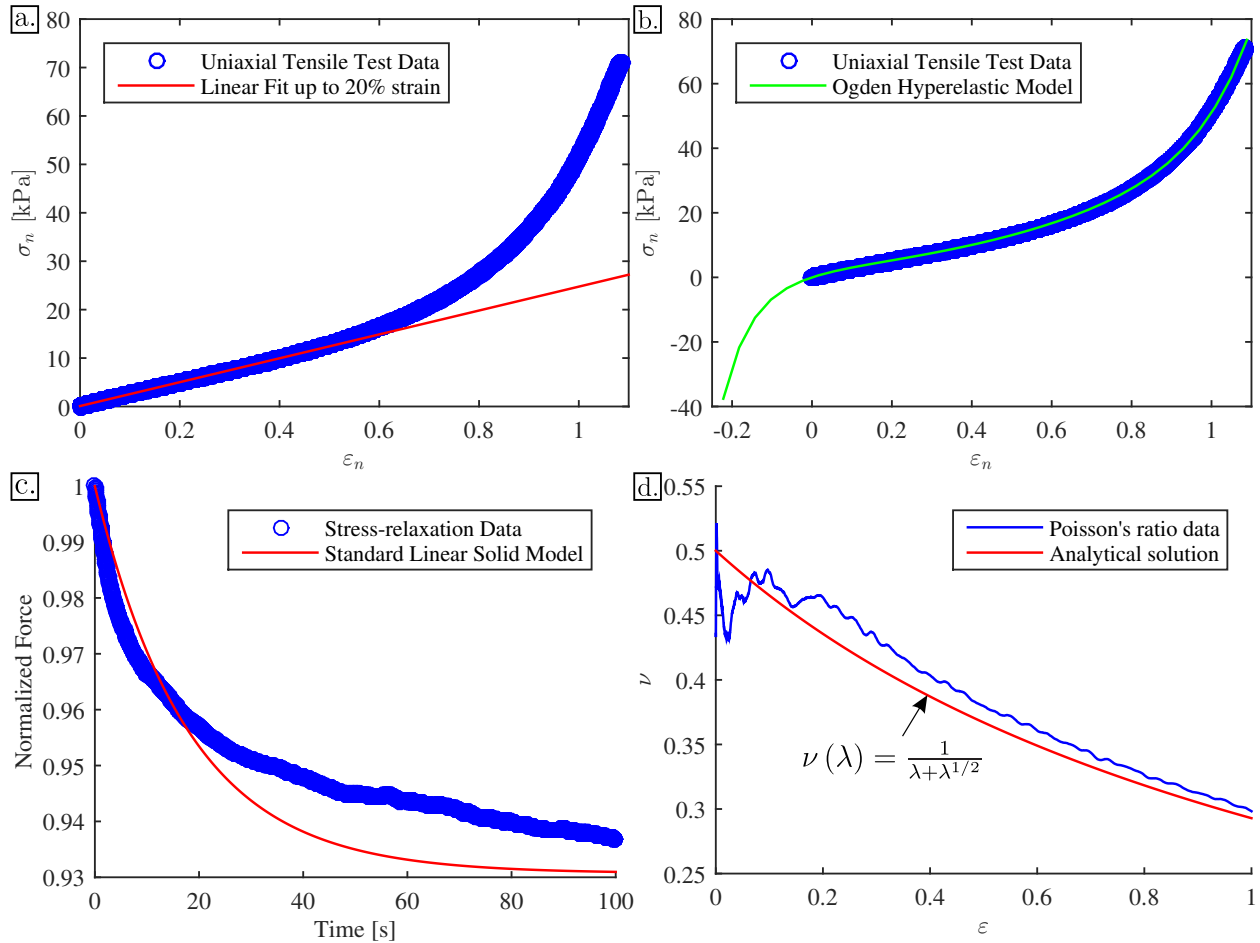
Figure 5.3: (a) Raw uniaxial tensile test data (blue) and a linear elastic approximation (red) for the first 20% strain ($E = 24.7\ kPa$), used for analytical calculations of δ and u_z. (b) Raw uniaxial tensile test data (blue) and the Ogden constitutive model (green) for hyperelasticity, used in the FE model. Parameters for the Ogden material model are listed in Table 5.1. (c) Raw uniaxial tensile stress-relaxation data (blue) and the Generalized Maxwell model with $N = 1$ (red) for viscoelasticity, used in the FE model. Parameters for the Generalized Maxwell model are listed in Table 5.2. (d) Raw Poisson's ratio data (blue), calculated from the four marked reference points on the material sample, and the universal Poisson function (red), for justification of incompressibility ($\nu_0 = 1/2$).

Raw data from a single stress-relaxation test is shown in 5.3c (blue circles). Normalized force is calculated by dividing the recorded force data by the force at $t = 0$, or the force recorded when the sample first reaches maximum strain. It is apparent that the material exhibits some viscoelastic behavior. During the stress-relaxation trial, the force immediately begins to decrease exponentially, and appears to approach a steady stress. Although the material is somewhat viscoelastic, the stress only decreases about 7% over a $100\ s$ trial. The normalized force and time data were input into Abaqus, which generated the Generalized Maxwell model ($N = 1$) parameters (listed in Table 5.2). These model parameters were used in the finite element analysis to simulate the viscoelastic behavior the substrate material.

Table 5.2: Parameters for the Generalized Maxwell ($N = 1$) model for viscoelasticity

i	g_i	k_i	τ_i
1	0.0693	0	17.95

5.3.3 Universal Poisson Function and Poisson's Ratio

During the tensile test described in Section 5.3.1, four reference points were recorded using a camera. These data were used during post-processing to calculate nominal strain, and Poisson's ratio. Fig. 5.3d (blue circles) shows experimental data for Poisson's ratio at a function of strain ε. At low strains, the experimental data is noisy and inaccurate due to low stretch in the material. However, at strains of 10% and higher, the experimental data approximately follows the universal Poisson function (Fig. 5.3d, red line) described in Section 5.2.3. It can be concluded that the Poisson's ratio ν_0 of the material is equal to 1/2, and therefore the material is incompressible, which is generally a good assumption for rubber materials. For the analytical solutions presented in this chapter, the Poisson's ratio of the substrate material will be 1/2.

5.3.4 Velocity Dependent F_T/F_N

The three laws of dry friction state:

(1) The force of friction is directly proportional to the applied load (Amonton's First Law)

(2) The force of friction is independent of the apparent contact area (Amonton's Second Law)

(3) Kinetic friction is independent of the sliding velocity (Amonton's Third Law or Coulomb's Law of Friction)

If a dry friction law is assumed, then the coefficient of friction μ_d is

$$\mu_d = F_f/F_N. \tag{5.26}$$

where F_f is the frictional force.

However, according to the data presented in Chapter 4, assuming a dry friction law is not adequate for the wheel and substrate contact mechanics. Although the first two laws of dry friction hold, the third law is violated.

In this chapter, results are often plotted with respect to F_T/F_N, which cannot accurately be termed coefficient of dry friction due to the dependence on velocity. In an attempt to characterize the material coefficient of friction μ as a function of differential velocity v_d, an experimental study was performed using the ATM platform. A smooth PDMS coated wheel ($R = 10.06 \ mm$) was actuated at various rotational velocities ω to induce differential velocities between $0.5 \ mm/s$ and $20 \ mm/s$ in increments of $0.5 \ mm/s$. The data from this experiment are displayed in Fig. 5.4a. It is apparent that F_T/F_N (*i.e.*, $\mu(v_d)$) is directly proportional to differential velocity. These data would suggest that F_T/F_N approaches an asymptote as $v_d \to \infty$. It is also interesting to compare the experimental data in Fig. 5.4a to the Stribeck curve (5.4b), which shows the dependence of the friction coefficient on velocity (viscosity$\times$velocity/normal force) for lubricated surfaces. The trend in these data strongly resembles the region of the Stribeck curve for hydrodynamic lubrication, suggesting that there is a thin lubricating layer of relatively high viscosity (since velocity and normal force are relatively low). The data presented in Fig. 5.4a was input into Abaqus as a velocity dependent coefficient of friction for PDMS on the synthetic tissue substrate.

5.4   Methodology

Methodology is separated into two section: 1) Finite element model, and experimental. With a complete characterization of the material, the experimental setup could be implemented in Abaqus. Experiments were carried out to validate the finite element model as well as study effects of pillar size, pillar elastic
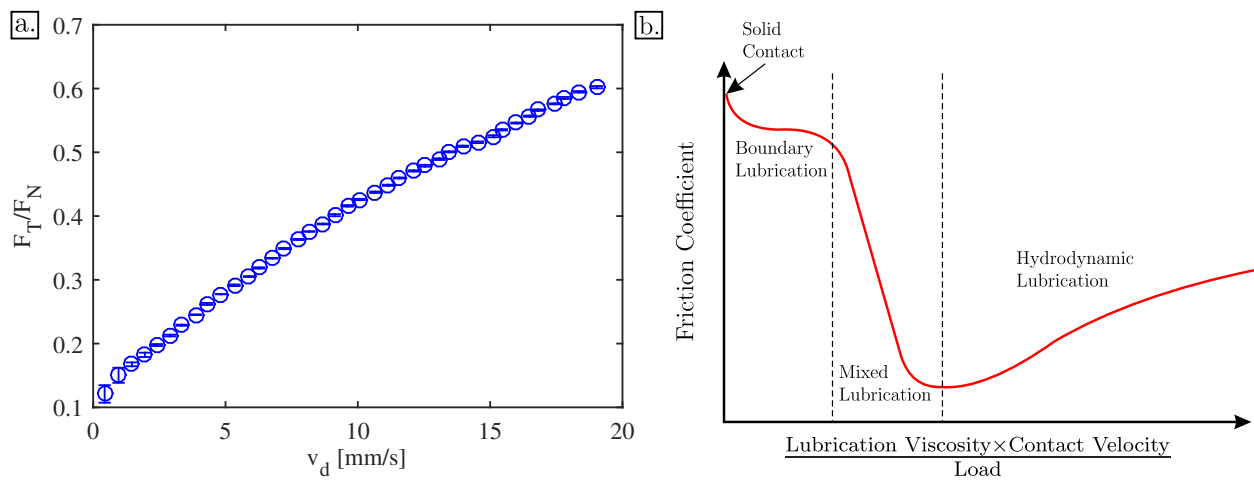
Figure 5.4: (a) F_T/F_N as a function of differential velocity v_d. Each data point represents the average of 5 trials, while the error bars represent the standard deviation of the mean. (b) A typical Stribeck curve, showing how coefficient of friction is affected by velocity throughout different lubrication regimes. The correlation between the data in (a) and the Stribeck curve suggests that the wheel-substrate contact is undergoing hydrodynamic lubrication

modulus, and substrate stiffness.

5.4.1   Finite Element Model

The finite element model was developed by modeling both the wheel and the substrate, applying material models, an interaction formulation, boundary conditions and loads.

5.4.1.1   Model Components

The goal of the finite element model was to replicate the ATM platform experimental setup. Two parts were created in Abaqus, the wheel and the synthetic tissue substrate (Fig. 5.5). The wheel was defined as an analytical solid rigid, since its Young's modulus was 3 orders of magnitude larger than the synthetic tissue (in the linear region). Both a smooth wheel and a cluster of seven rigid pillars were modeled. The rigid pillars were modeled to mimic the spatial geometry on the 3D printed wheels, and were rotated about an axis of rotation a distance away that was equal to the radius of the wheel R. The substrate was divided into different regions so that each region could be assigned its own mesh density. This allowed for a fine mesh at the region of contact, but course region through the majority of the substrate. Standard quadratic triangular elements for plane stress with quadratic interpolation were used to mesh the synthetic substrate.

5.4.1.2   Interaction Formulation

The velocity dependent coefficient data described in 5.3.4 was input into Abaqus as the interaction model.

5.4.1.3   Boundary Condition and Loads

The ATM platform has three main input control variables: 1) rotational speed of the wheel ω, 2) applied normal force F_N and 3) translational speed of the wheel v. The ATM platform measures traction force generate when the wheel slips on the tissue. Therefore, in the finite element model, the substrate will be fixed while the rotational speed of the wheel ω and applied normal force F_N will be controlled to induce a differential velocity v_d.
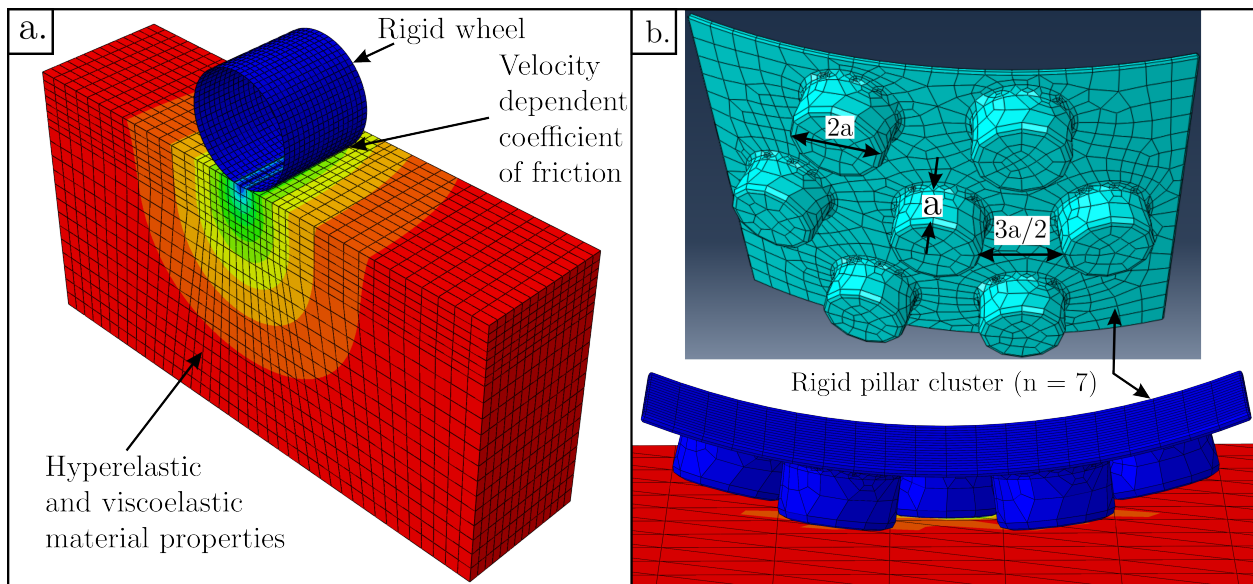
Figure 5.5: The problem setup for the 3-dimensional finite element model. (a) A rigid smooth wheel in contact with the synthetic biological substrate, modeled using both hyperelastic (Ogden, $N = 3$) and viscoelastic (Generalized Maxwell, $N = 1$) models. (b) A cluster of 7 rigid tread pillars in contact with the synthetic biological substrate.

A concentrated force was applied to the center of the wheel with a value of $0.01\ N/mm$ in the negative **z**-direction, corresponding to an experimental normal force of $F_N = 0.3\ N$ for a cylindrical wheel with length $L = 30\ mm$. The substrate was fixed (in both **y** and **z** directions) on the bottom surface, and the wheel was constrained to translational motion in the **z** (vertical) direction.

5.4.1.4 Steps

The simulation consisted of two steps. During the first (static) step ($100\ s$), the normal force is applied and enough time is allowed to lapse to ensure steady state convergence. During the second (dynamic) step, the wheel is rotated for $6 - 12\ s$ (dependent on rotation speed) on top of the substrate.

5.4.2 Experimental

Experiments were performed with the ATM platform, which the development of was thoroughly discussed in Chapter 4. The operating principle of the ATM platform is the same for this study, with the exception of an added sensor, which the implementation and calibration of will be discussed here.

5.4.3 ATM Platform with Interferometer

Fig. 5.6 shows the ATM platform with an added interferometer distance sensor. The sensor (optoN-CDT 1302-20, Micro-Epsilon, Ortenburg, Germany) has a measurement range of $20\ mm$, and a resolution of $4\ \mu m$ with a $12\ bit$ analog-to-digital converter (ADC). The sensor was aligned with the axle of the wheel and place about $10\ mm$ above the axle. The sensor reflects off of the axle end support so that it has a stationary (non-rotating) surface to measure. Measuring the distance to the rotating axle directly would have introduced noise due to the surface roughness of the axle surface. The sensor was fixed relative to the horizontal arm on the ATM platform so that any motion vertical motion of the arm would be measured by the interferometer. The sensor collects data at $750\ Hz$ and sends the data through an RS422 connection to a computer for data logging.

Example raw data of normal force F_N, traction force F_T, and wheel vertical displacement δ are displayed in Figs. 5.7a-d for a rotating wheel with finite rotational speed ω and zero linear speed ($v_d = R\omega$).
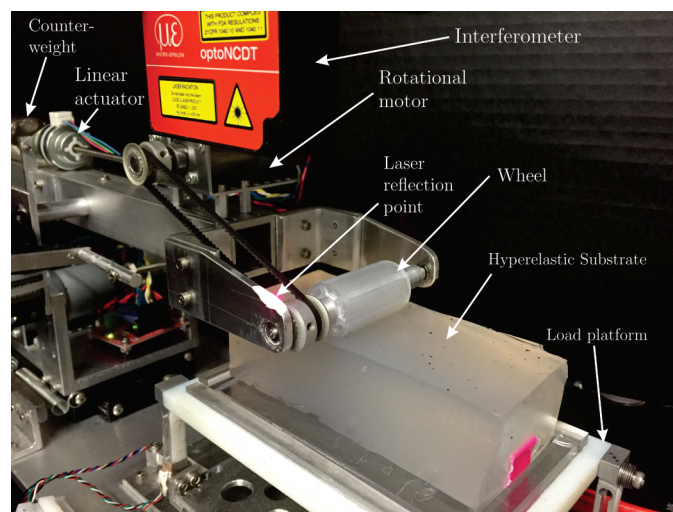
Figure 5.6: Experimental setup for measuring wheel traction force and vertical displacement. The system is the same as the ATM platform described in Chapter 4, with the exception of an added interferometer sensor for measuring vertical displacement of the wheel. The interferometer sensor (optoNCDT 1302-20, Micro-Epsilon, Ortenburg, Germany) is capable of measuring displacement with 4 μm resolution.

The horizontal axis in Figs. 5.7a-d represents trial time, which was held constant at 25 s. The left vertical axis in Figs. 5.7a-d represents wheel vertical displacement δ, while the right vertical axis represents force. Both normal force (red lines) and traction force (organe lines) are plotted on the same force scale. Fig. 5.7a shows raw data for a trial with a relatively low normal force ($F_N = 50\ mN$) and low differential velocity ($v_d = 0.5\ mm/s$). Fig. 5.7b shows raw data for a trial with a relatively low normal force ($F_N = 50\ mN$) and high differential velocity ($v_d = 20\ mm/s$). Fig. 5.7c shows raw data for a trial with a relatively high normal force ($F_N = 500\ mN$) and low differential velocity ($v_d = 0.5\ mm/s$). Fig. 5.7d shows raw data for a trail with a relatively high normal force ($F_N = 500\ mN$) and high differential velocity ($v_d = 20\ mm/s$). In general, trials with higher speeds produce noisier data. This makes sense because the wheel is rotating at a higher frequency, and vibrations don't have time to dissipate. However, these data appear to oscillate periodically about a mean, so the effect of the noise is eliminated with averaging. All of the trials feature high frequency dynamics at the start and end of each trial. This is likely due to the acceleration and deceleration of the wheel. The impulse of the wheel's initial motion likely sends a wave of vibrations through the viscoelastic substrate, causing damped oscillations. The wheel in fact visibly bounces at the start of each trial. To account for the dynamic effects of the trial, the middle 60% (from 5 s to 20 s) of the data from each trial is averaged to obtain a mean traction force.

5.4.3.1 Interferometer Calibration

It was imperative to properly calibrate the deflection data, so that data from different configuration (*e.g.*, wheel, substrate, etc.) could be compared. It is obvious that $\delta = 0$ when $F_N = 0$, however it is not practical to apply a zero normal force and accurately measure the vertical deflection. Therefore, a calibration curve was obtained by imposing a range of normal forces (between 5 mN and 50 mN in increments of 5 mN) and recording the reading from the interferometer at each normal force. Then, a 3$^{\text{rd}}$ order polynomial was fit to the data (average $R^2 = 0.99$ for all calibration curves):

$$\delta\left(F_N\right) = p_1 F_N^3 + p_2 F_N^2 + p_3 F_N + p_4 \tag{5.27}$$
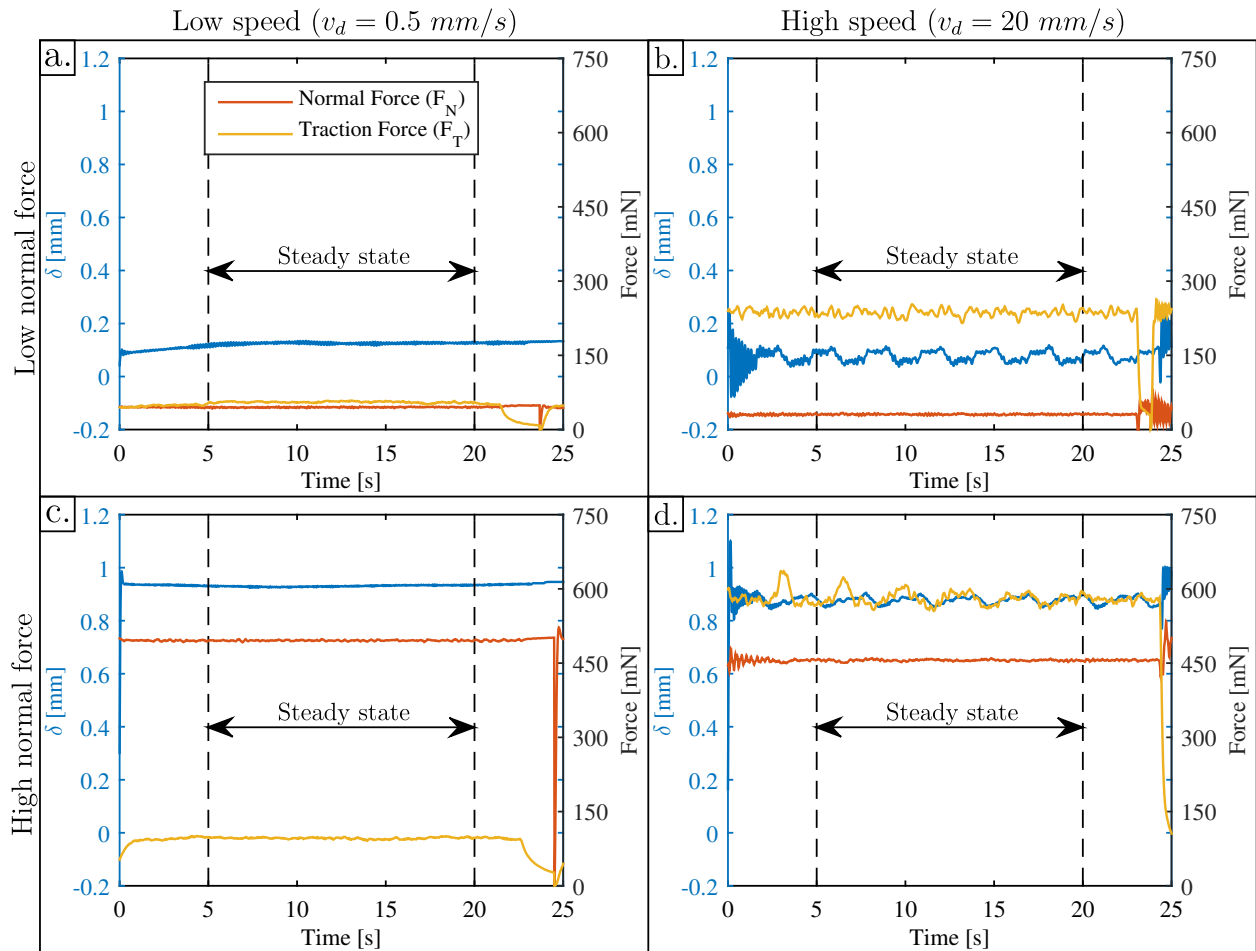
Figure 5.7: (a) Raw traction force F_T, normal force F_N, and wheel deflection δ data for a low differential speed ($v_d = 0.5\ mm/s$) and low normal force ($F_N = 50\ mN$). (b) Raw traction force F_T, normal force F_N, and wheel deflection δ data for a high differential speed ($v_d = 20\ mm/s$) and low normal force ($F_N = 50\ mN$). (c) Raw traction force F_T, normal force F_N, and wheel deflection δ data for a low differential speed ($v_d = 0.5\ mm/s$) and high normal force ($F_N = 500\ mN$). (d) Raw traction force F_T, normal force F_N, and wheel deflection δ data for a high differential speed ($v_d = 20\ mm/s$) and high normal force ($F_N = 500\ mN$).

where $\delta\left(F_N = 0\right) = p_4$. Then, p_4 was subtracted from all subsequent vertical displacement data to calibrate the data for each configuration.

In order to test that this calibration method would provide repeatable results, five calibration curves were collected, and the raw data (before offset) are displayed in Fig. 5.8a. The same data with a 3$^{\text{rd}}$ order polynomial fit are displayed in Fig. 5.8b. The five calibration curves with the offset p_4 applied are displayed in Fig. 5.8c. Fig. 5.8d shows the average of the five calibration curves after subtraction of the offset. Each data point in Fig. 5.8d represents the average of five values. The error bars (hard to see due to small size) in Fig. 5.8d represent the standard deviation of that mean. It is apparent that the calibration curves after the offset is applied are nearly identical, therefore, the proposed calibration method is appropriate for all future data sets

5.4.3.2   PDMS Modulus

To study the effect of pillar elastic modulus on traction force, seven wheel treads were fabricated out of PDMS with varying elastic modulus. The elastic modulus was varied by changing the PDMS base to cross-link ratio.

The elastic modulus of the tread was characterized with respect to the mixing ratio using indentation tests. Cylindrical samples (diameter $= 20$ mm and height $= 20$ mm) of PDMS were fabricated by mixing PDMS base to cross-linking agent ratios of 10, 11.7, 13.3, 15, 20, 25, and 30, and curing them in a vacuum (to remove air bubbles) oven at 100 $^{\circ}C$ for 1 hr. The samples were then indented with a cylindrical punch (diameter $= 3$ mm) to a depth of 2 mm to obtain the compressive stress strain relationship of each sample. The Elastic modulus for each sample was obtained from the slope of the stress-strain curve. The resulting PDMS modulus as a function of base to cross-link ratio is displayed in Fig. 5.9b. At mixing ratios lower than 10, the PDMS modulus does not increase any further due to a saturation of cross-linking agent in the polymer. For mixing ratios larger than 30, the polymer would not fully cure, and thus would remain sticky.

After characterization of the PDMS modulus, treads were fabricated using PDMS base to cross-linking agent ratios of 10, 11.7, 13.3, 15, 20, 25, and 30. Mixed PDMS was poured into a SU-8 mold, and cured in a vacuum (to remove air bubbles) oven at 100 $^{\circ}C$ for 1 hr. After curing, the PDMS tread were removed from
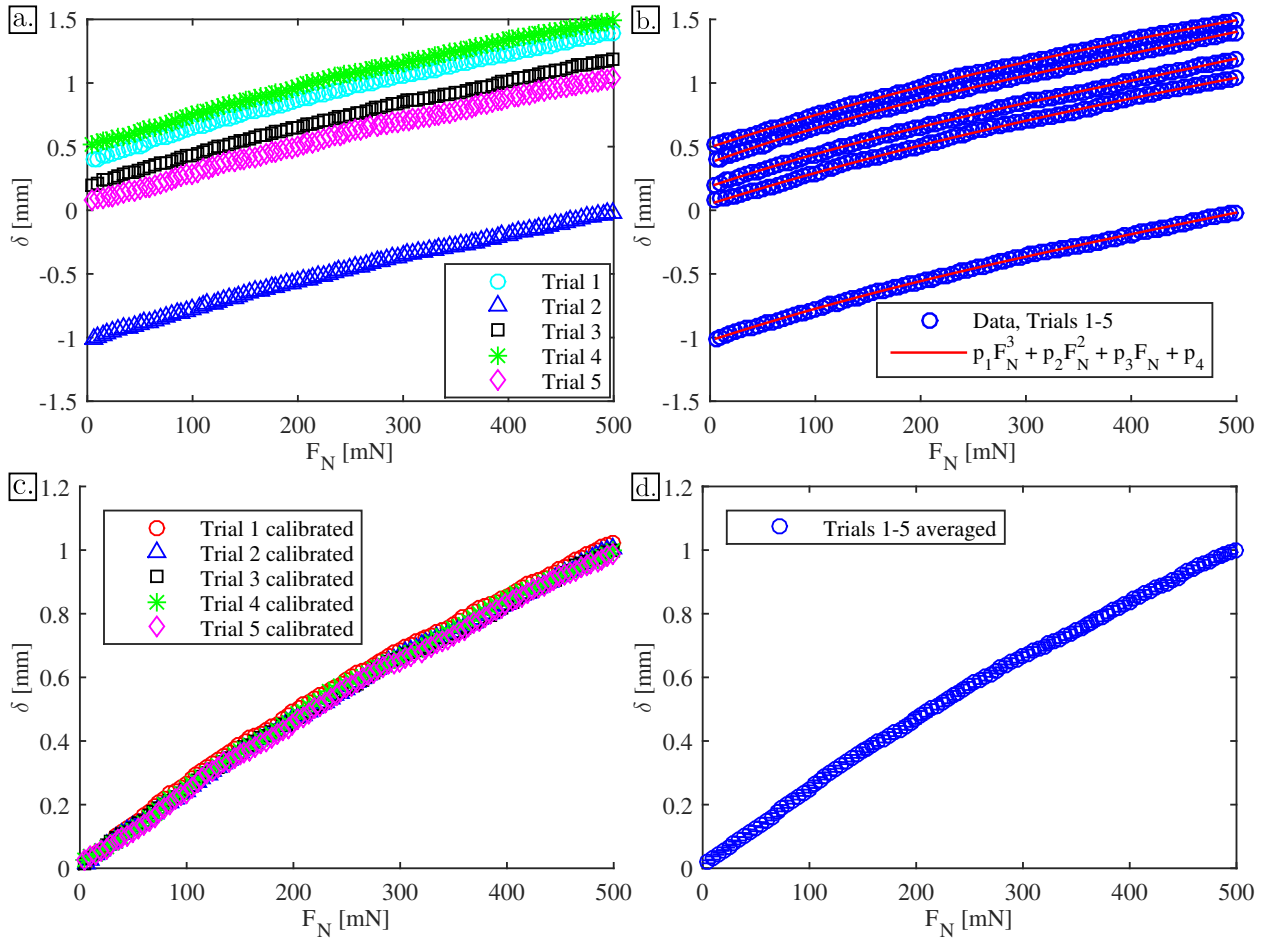
Figure 5.8: (a) Five separate calibration curves, before any offset was applied, obtained by varying the normal force F_N (between 5 and 500 mN, in increments of 5 mN) of a static, smooth PDMS coated wheel and measuring the vertical deflection of the wheel into the tissue. (b) Five calibration curves fitted to a 3rd order polynomial function. (c) Five calibration curves after the calibration offset (p_4) has been subtracted from the data. (d) The average of the five calibration curves. Each point in (d) represents the average of the five trails, while the error bars (hard to see due to small size) represent the standard deviation of the mean.

.

the mold, trimmed to size, and fixed to an aluminum wheel hub using double-sided tape. The final radius of the PDMS wheels was $R = 10\ mm$. The treads featured a micro-pattern with $a = 70\mu m$.
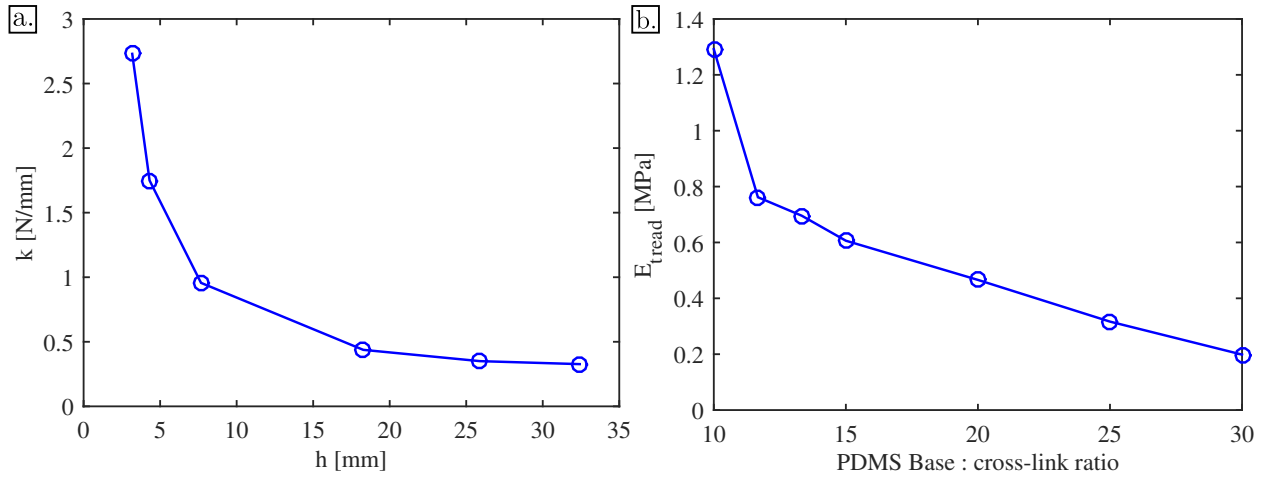
Figure 5.9: (a) Substrate stiffness k as a function of substrate height h. Stiffness was experimentally determined for each substrate height using compressive tests where the reaction force (F) was measured as a function of indentation depth (d). The ratio between reaction force and indentation depth determined $k = F/d$. (b) Elastic modulus as a function of base to cross-link ratio. PDMS tread modulus was varied to study the effect it had on traction force generation.

5.4.3.3   Pillar Diameter

To study the effect of the wheel tread size on traction force, wheels with varying size parameter a were fabricated using a stereolithography technique (Protogenic, Westminster, CO, USA). Overall wheel dimensions were radius $R = 10\ mm$ and length $L = 35\ mm$. Prior to testing on the ATM platform, the wheels were coated with PDMS (base to cross-link agent mixing ratio equal to 10) and cured in a vacuum oven at 50 °C for 8 hr. A lower temperature than previously stated was used to prevent melting of the plastic wheels. The wheels used in the study, along with the pillar radius a are displayed in Fig. 5.10a.

5.4.3.4   Substrate Stiffness

To study the effect of substrate stiffness on traction force, substrates with varying heights were fabricated. 860 mL of Super Soft Plastic (M-F Manufacturing Company, Fort Worth, TX, USA) and 215 mL (4:1 ratio) of Plastic Softener (M-F Manufacturing Company, Fort Worth, TX, USA) were measured using

a.	Smooth	$a = 0.28$ mm	$a = 0.35$ mm	$a = 0.42$ mm	$a = 0.49$ mm	$a = 0.56$ mm	$a = 0.63$ mm	$a = 0.70$ mm
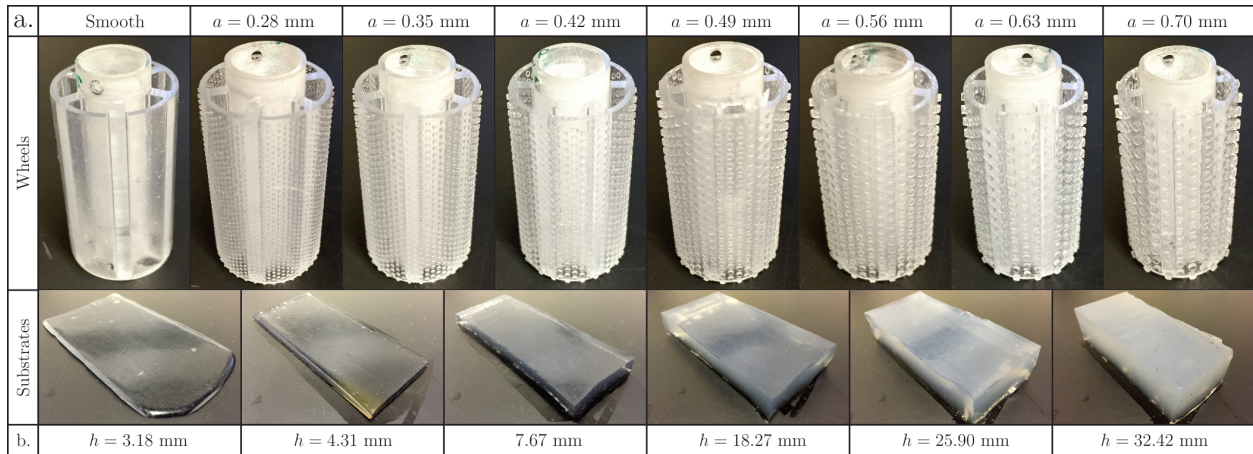
Figure 5.10: (a) Wheels used in the tread size study. Wheels were fabricated using a stereolithography (3D printing) technique with varying tread sizes and then coated with PDMS. (b) Substrates used in the substrate stiffness study.

a graduated cylinder, and poured into a 100 $mm \times 50\ mm$ Pyrex$^{\circledR}$ beaker. The solution was stirred for $\sim 30\ s$, or until thoroughly mixed, and then placed on a preheated (250 °C) hot plate in a fume hood. The mixture was constantly stirred, being careful not to introduce air bubbles, until the opaque liquid turned clear ($\sim 20\ min$). The Pyrex$^{\circledR}$ beaker was then removed from the hot plate and the hot liquid was quickly (within 5 s) poured into seven molds (width $= 50\ m$ and length $= 100\ mm$) of varying height and allowed to cool to room temperature. Once cooled, the substrates were removed from the molds. The substrates used in this study along with their heights are displayed in Fig. 5.10b.

5.5   Results

The results are divided into several categories, focusing on the effect of a single variable. Specifically, results are organized as velocity dependence, wheel deflection, PDMS modulus, pillar size, and substrate stiffness.

5.5.1   Velocity Dependence

Fig. 5.11 shows the effect of differential velocity v_d and normal force F_N on F_T/F_N (*i.e.*, $\mu\left(v_d\right)$). Fig. 5.11a shows the combined effect of differential velocity v_d and normal force F_N on F_T/F_N, while Figs. 5.11b-c show the individual effects of differential velocity v_d and normal force F_N on F_T/F_N, respectively. Fig. 5.11d shows the effect of differential velocity v_d on normal force F_N. Figs. 5.11c-d also have color bars, so that the effect with respect to v_d, F_N, and F_T/F_N, respectively, can be seen. Each data point in Figs. 5.11a-d represent the average of two trials.

Fig. 5.12 shows the effect of differential velocity v_d and normal force F_N on traction force F_T. Fig. 5.12a shows the combined effect of differential velocity v_d and normal force F_N on traction force F_T, while Figs. 5.12b-c show the individual effects of differential velocity v_d and normal force F_N on traction force F_T, respectively. Fig. 5.12d shows the effect of differential velocity v_d on normal force F_N. Figs. 5.12c-d also have color bars, so that the effect with respect to v_d, F_N, and F_T, respectively, can be seen. Each data point in Figs. 5.12a-d represent the average of two trials.

When looking at the effect of v_d on traction force, it is apparent that the two are directly proportional.
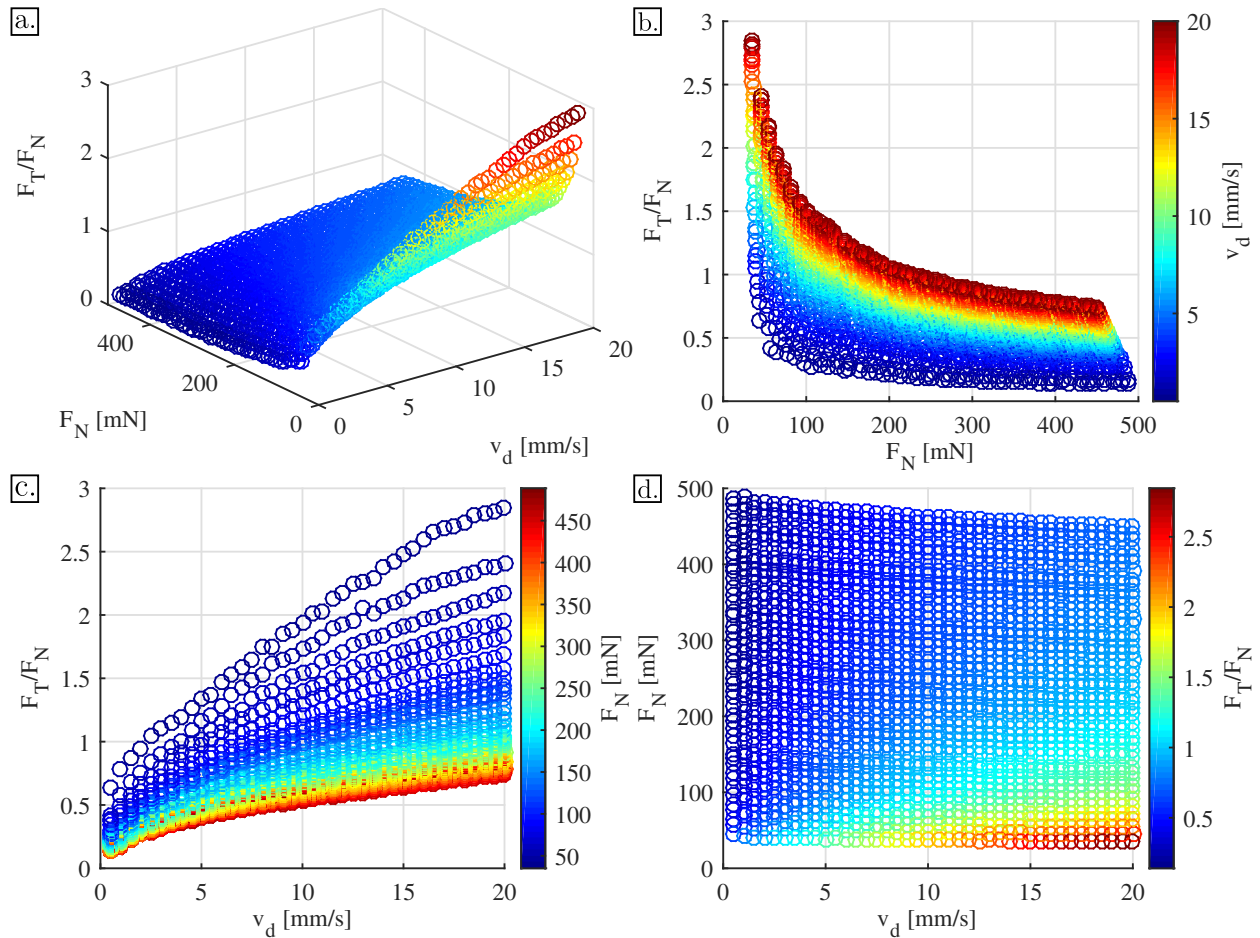
Figure 5.11: (a) The effect of differential velocity v_d and normal force F_N on F_T/F_N. (b) The effect of normal force F_N on F_T/F_N. The color bar represents differential velocity v_d. (c) The effect of differential velocity v_d on F_T/F_N. The color bar represents normal force F_N. (d) The effect of differential velocity v_d on normal force F_N. The color bar represents F_T/F_N. Each data point in (a-d) represents the average of two trials.
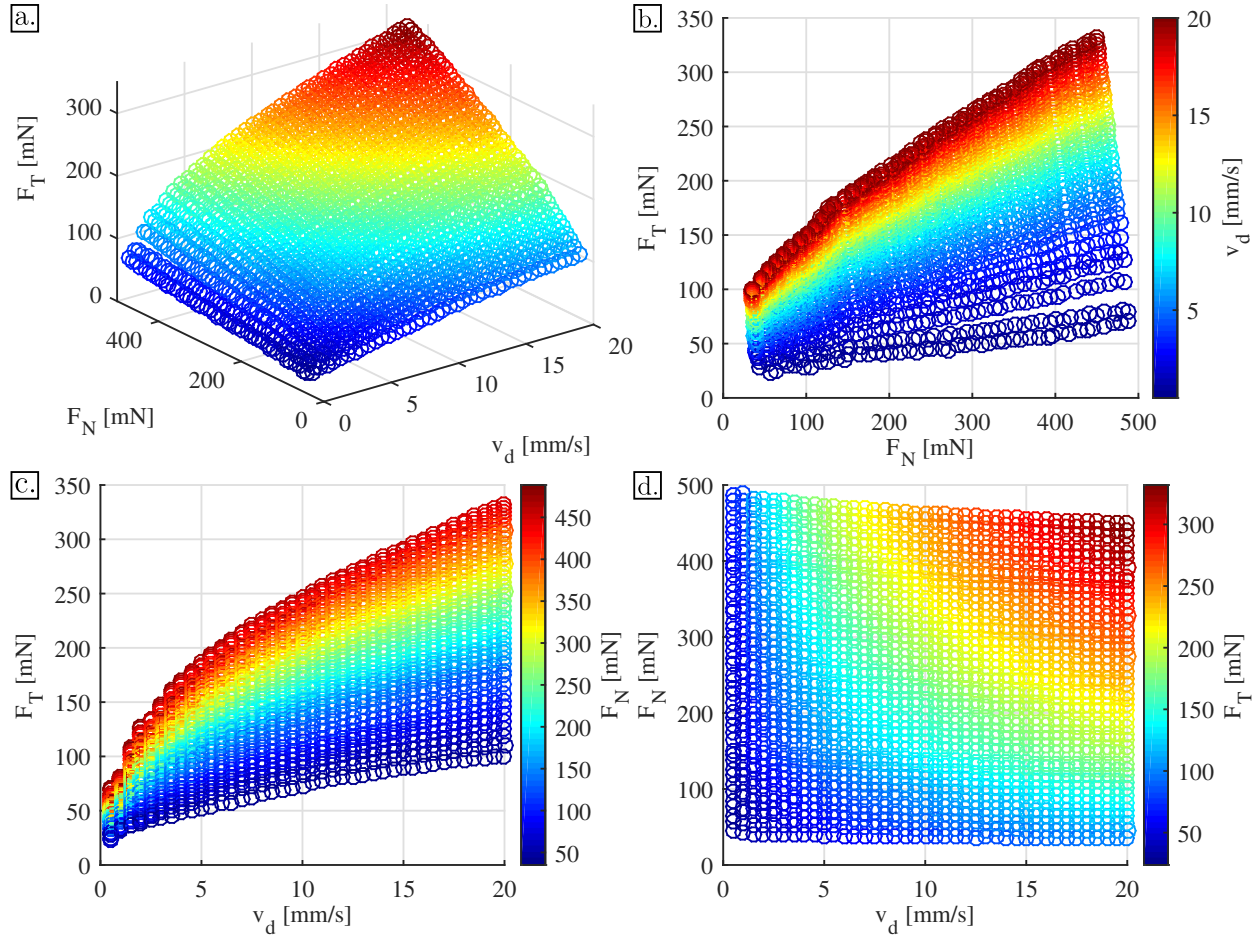
Figure 5.12: (a) The effect of differential velocity v_d and normal force F_N on traction force F_T. (b) The effect of normal force F_N on traction force F_T. The color bar represents differential velocity v_d. (c) The effect of differential velocity v_d on traction force F_T. The color bar represents normal force F_N. (d) The effect of differential velocity v_d on normal force F_N. The color bar represents traction force F_T. Each data point in (a-d) represents the average of two trials.

Traction force increases nonlinearly with differential velocity. Similarly, F_T/F_N increases nonlinearly with differential velocity. Fig. 5.13 shows a comparison between experimental traction force data (blue circles) and FEM simulation results (red x) for a smooth PDMS wheel on the synthetic tissue substrate with a weight (F_N) of 300 mN. For both the experimental setup and FEM simulations, the translational speed (v) of the wheel was set to zero, while the rotational speed (ω) of the wheel was varied to induce differential velocities (v_d) between 0.5 and 20 mm/s. The maximum difference between the experimental data and the FEM simulation results in Fig. 5.13 was 2.42%, which occurred at a differential velocity of 16.8 mm/s.
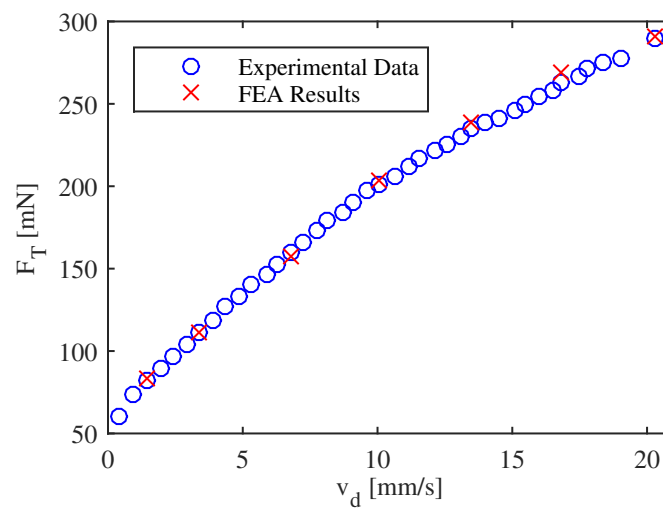
Figure 5.13: Dynamic traction experimental data (blue circles) and FEM simulation results (red x), at a normal force of 300 mN. The maximum difference between experimental and FEM results is 2.42% and occurs at $v_d = 16.8$ mm/s. In both the experimental setup and FEM simulation, the translational speed (v) was set to zero and the rotational speed (ω) was varied to obtain differential velocities (v_d) between 0.5 and 20 mm/s.

In agreement with findings in previous chapter, traction force is also directly (and nearly linearly) proportional to normal force. Contrary to Coulomb's dry friction law, F_T/F_N is nonlinearly and inversely proportional to normal force. It is interesting to note that the highest coefficients of friction are obtained at the lowest normal forces. This is probably to due the fact that adhesive force are high between the substrate and PDMS.

5.5.1.1   Wheel Deflection

Results for wheel deflection δ are displayed in Figs. 5.14-5.20. Figs. 5.14a and 5.14c show wheel vertical deflection δ as a function of normal force F_N and differential velocity v_d. Normal force and wheel deflection are positively correlated. Although at first glance, δ and v_d also appear to be correlated, a closer look at Figs. 5.12d, 5.14a and 5.14c reveal that increasing v_d decreases F_N, which in turn decreases δ. This is especially true at low normal forces ($F_N < 200 \ mN$). At higher normal forces, v_d may have an independent effect on δ. This effect can be explained by defining a pseudo-stiffness F_N/δ and examining the effect that v_d has on it (Fig. 5.14b). At low normal forces, the pseudo-stiffness is relatively constant with respect to differential velocity. However, at higher normal forces, the pseudo-stiffness increases slightly with differential velocity. An increased pseudo-stiffness would result in less vertical deflection of the wheel. This phenomenon can be explained by the viscoelastic properties of the material. Since the material has a strain-rate dependent stress response, larger impulses (larger v_d) would result in higher stiffness. Although present, this is not a dominating effect.

Figs. 5.15a-d show the effect of δ and v_d on F_T/F_N. Fig. 5.15a shows the combined effect of differential velocity and wheel vertical deflection on F_T/F_N in 3D scatter plot form, while Figs. 5.15b-c show the individual effects of δ and v_d on F_T/F_N, respectively. Fig. 5.15d shows the relationship between δ and v_d. Color bars in Figs. 5.15b-d show the effect of v_d, δ, and F_T/F_N, respectively.

Figs. 5.16a-d show the effect of δ and v_d on F_T. Fig. 5.16a shows the combined effect of differential velocity and wheel vertical deflection on traction force F_T in 3D scatter plot form, while Figs. 5.16b-c show the individual effects of δ and v_d on F_T, respectively. Fig. 5.16d shows the relationship between δ and v_d. Color bars in Figs. 5.16b-d show the effect of v_d, δ, and F_T, respectively.

Figs. 5.17a-d show the effect of wheel vertical deflection δ and normal force F_N on F_T/F_N. Fig. 5.17a shows the combined effect of normal force and wheel vertical deflection on F_T/F_N in 3D scatter plot form, while Figs. 5.17b-c show the individual effects of F_N and δ on F_T/F_N, respectively. Fig. 5.17d shows the relationship between δ and F_N. Color bars in Figs. 5.17b-d show the effect of δ, F_N, and F_T/F_N, respectively.
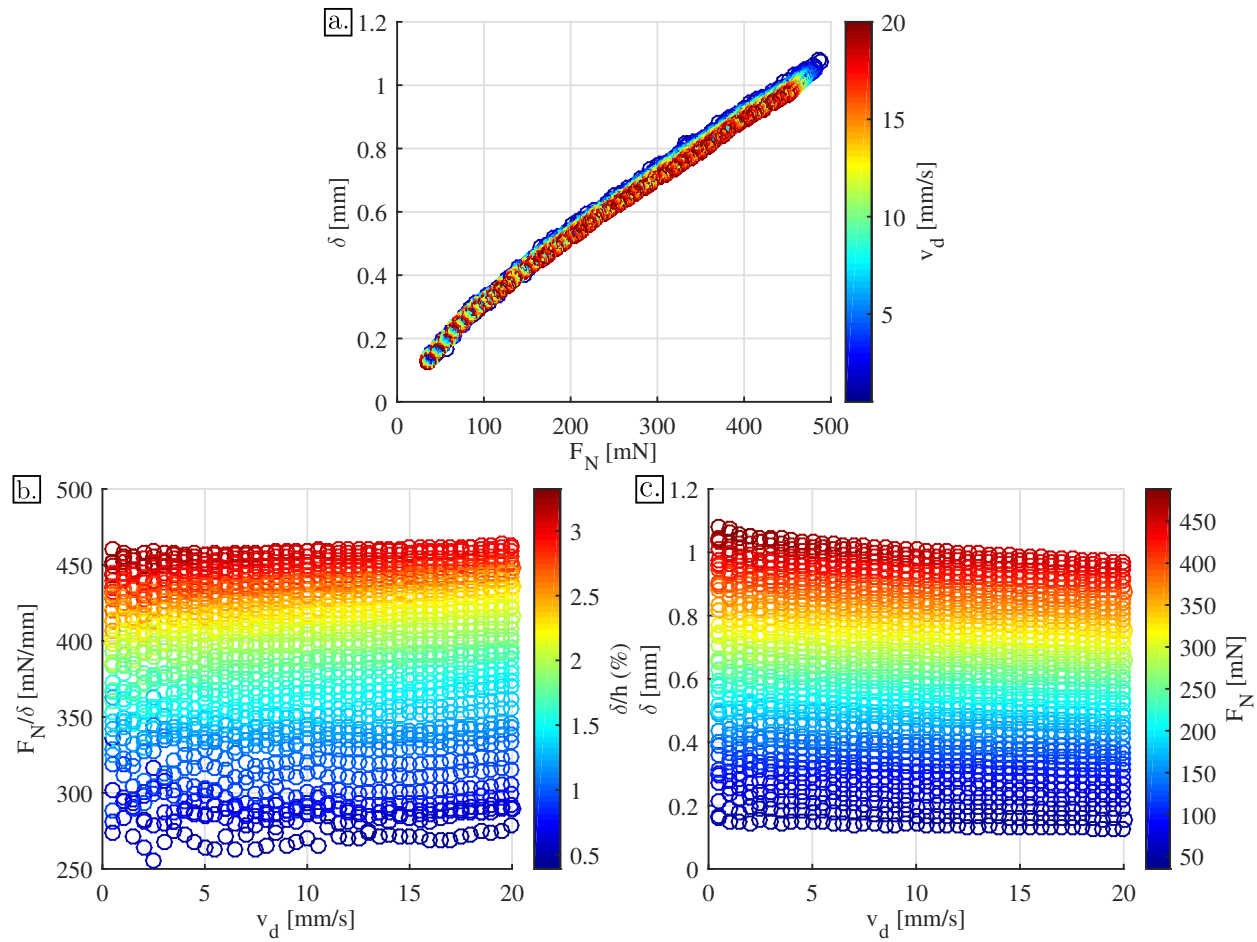
Figure 5.14: (a) The effect of normal force F_N on wheel vertical deflection δ. The color bar represents differential velocity v_d. (b) The effect of differential velocity v_d on a pseudo-stiffness F_N/δ. The color bar represents a pseudo-strain δ/h. (c) The effect of differential velocity v_d on δ. The color bar represents normal force F_N. Each data point in (a-c) represents the average of two trials.
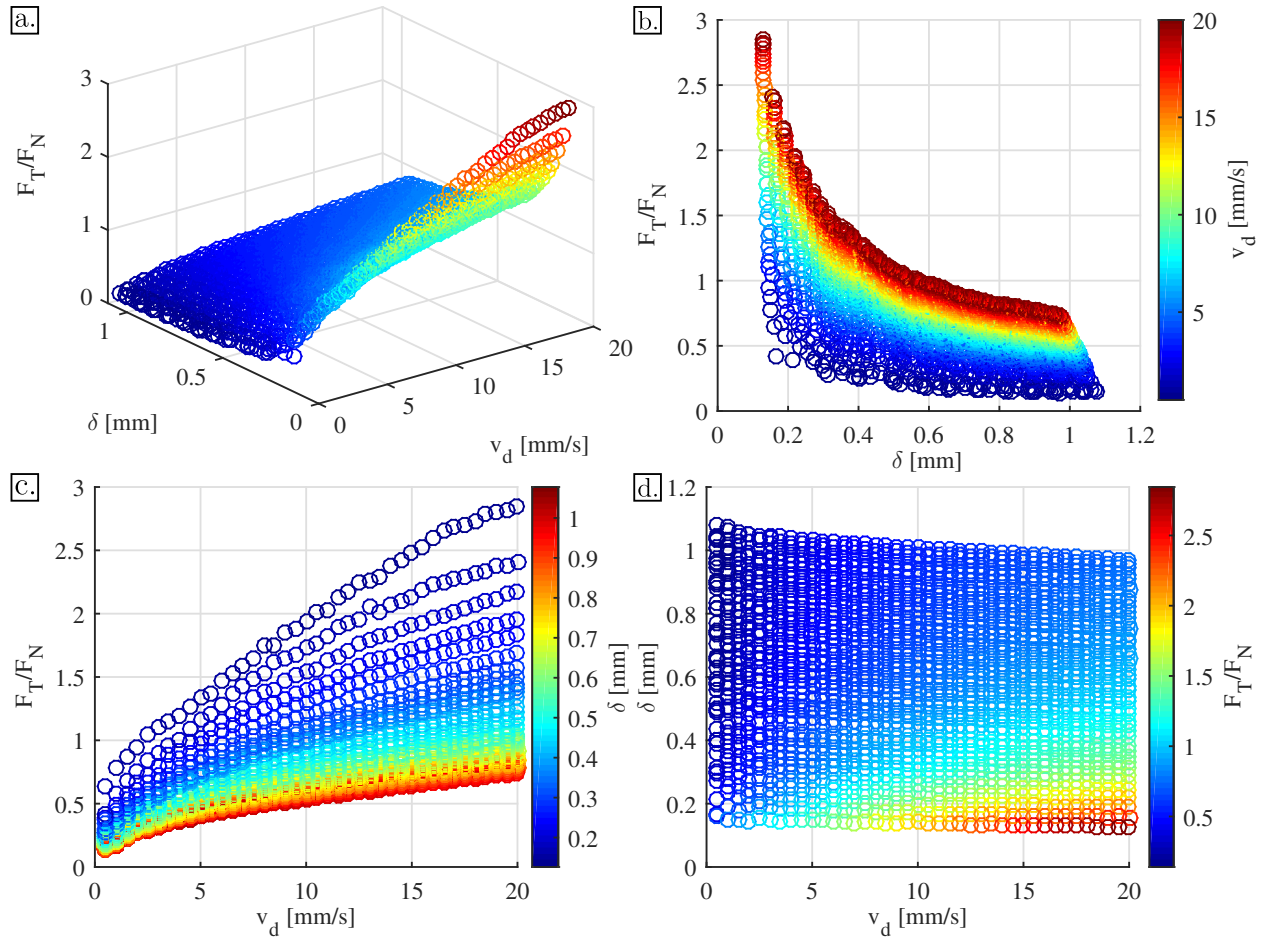
Figure 5.15: (a) The effect of wheel vertical deflection δ and differential velocity v_d on F_T/F_N. (b) The effect of wheel vertical deflection δ on F_T/F_N. The color bar represents differential velocity v_d. (c) The effect of differential velocity v_d on F_T/F_N. The color bar represents wheel vertical deflection δ. (d) The effect of differential velocity v_d on wheel vertical deflection δ. The color bar represents F_T/F_N. Each data point in (a-d) represents the average of two trials.
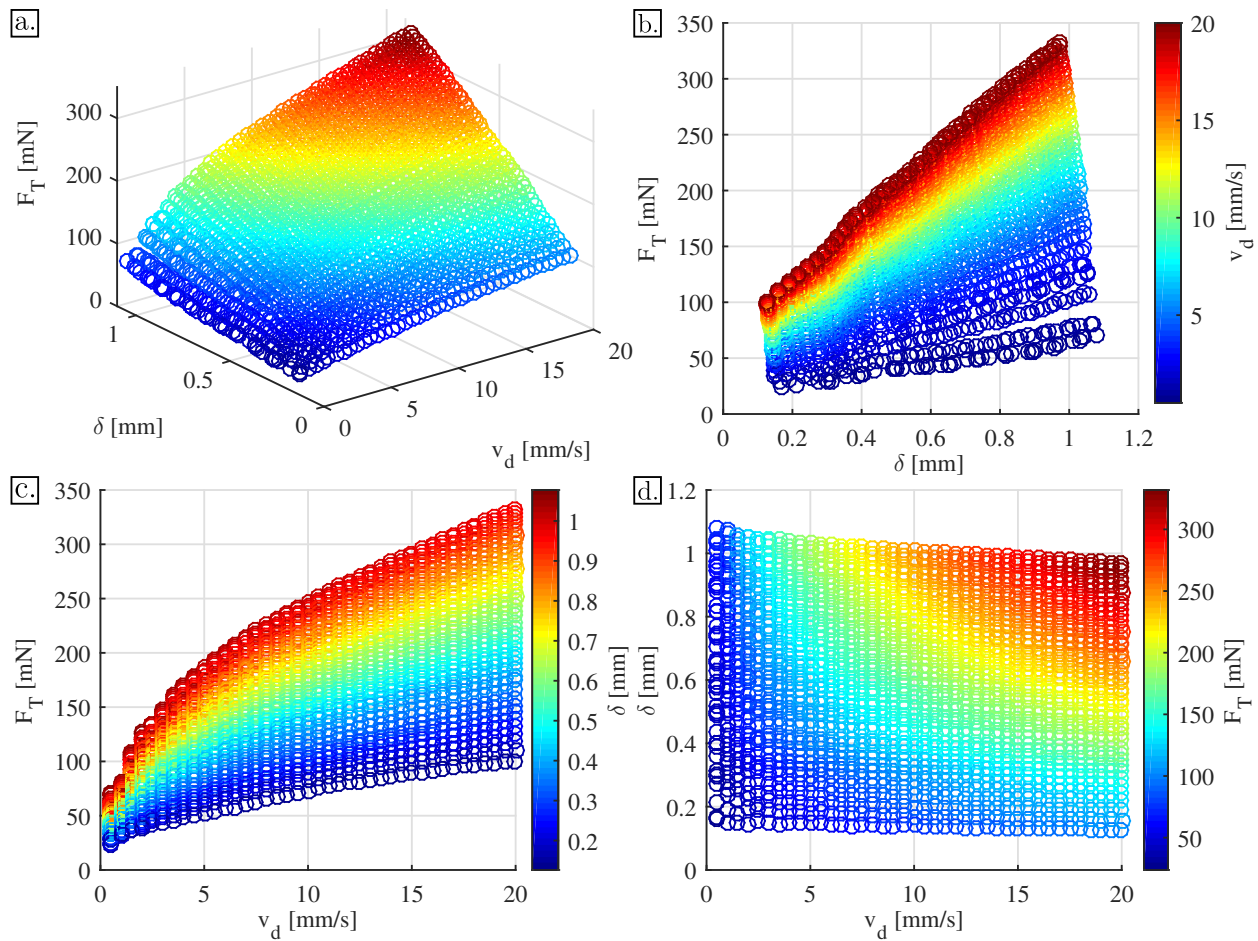
Figure 5.16: (a) The effect of differential velocity v_d and wheel vertical deflection δ on traction force F_T. (b) The effect of wheel vertical deflection δ on traction force F_T. The color bar represents differential velocity v_d. (c) The effect of differential velocity v_d on traction force F_T. The color bar represents wheel vertical deflection δ. (d) The effect of differential velocity v_d on wheel vertical deflection δ. The color bar represents traction force F_T. Each data point in (a-d) represents the average of two trials.

Figure 5.17: (a) The effect of wheel vertical deflection δ and normal force F_N on F_T/F_N. (b) The effect of normal force F_N on F_T/F_N. The color bar represents wheel vertical deflection δ. (c) The effect of wheel vertical deflection δ on F_T/F_N. The color bar represents normal force F_N. (d) The effect of normal force F_N on wheel vertical deflection δ. The color bar represents F_T/F_N. Each data point in (a-d) represents the average of two trials.

Figs. 5.18a-d show the effect of wheel vertical deflection δ and normal force F_N on F_T/F_N. Fig. 5.18a shows the combined effect of normal force and wheel vertical deflection on F_T/F_N in 3D scatter plot form, while Figs. 5.18b-c show the individual effects of F_N and δ on F_T/F_N, respectively. Fig. 5.18d shows the relationship between δ and F_N. Color bars in Figs. 5.18b-d show the effect of δ, F_N, and F_T/F_N, respectively. 5.18

Assuming that the substrate is linearly elastic and incompressible ($\nu_0 = 1/2$), and by estimating the Young's modulus from the first 20% strain of the simple tensile test, an analytical solution for the vertical deflection of a static ($\omega = v = 0$) smooth wheel can be obtained as a function of normal force using equation (5.21). Static experimental data (blue circles) the analytical solution (black line) and FEM simulation results (red x) are displayed in 5.19a for a smooth wheel. The analytical model and experiment agree with a maximum difference of 7.1% at $F_N = 500 \ mN$. The increasing deviation from theory starting at $F_N = 300 \ mN$ could be due to local strains larger than 40%, which would correlate to the hyperelastic region of the material. However, for an approximation, the linear elastic assumption provides a relatively accurate solution. The FEM results and experimental data agree with a difference of 4.0. It is important to note that the experimental and FEM results don't exhibit increasing deviation as normal force increases. This agreement most likely comes from the fact that the FEM accounts for the hyperelasticity of the material.

In order to calculate the vertical deflection of the pillar u_z, δ and b have to be know in order to calculate the contact surface area. However, the analytical solution for δ assumes that the wheel has a smooth surface. Fig. 5.19b shows experimental data for δ for wheels with pillar radius ranging from $a = 0.28 \ mm$ to $a = 0.70$ mm. Although these data deviate from the analytical solution more than the smooth wheel data, the analytical solution for a smooth wheel still provides an accurate prediction of δ for wheels that are not smooth. Therefore, the analytical solution for δ and b can be used to calculate a first-order approximation for u_z.

Fig. 5.20 shows the theoretical pillar deflection u_z as a function of normal force F_N for pillar radii ranging from $a = 0.28 \ mm$ to $a = 0.7 \ mm$ for a substrate with a constant Young's modulus E. u_z is directly proportional to both normal force and pillar radius, height, and spacing. The theory suggests that material bulging into the spaces between the pillars is minimal for the synthetic tissue substrate.
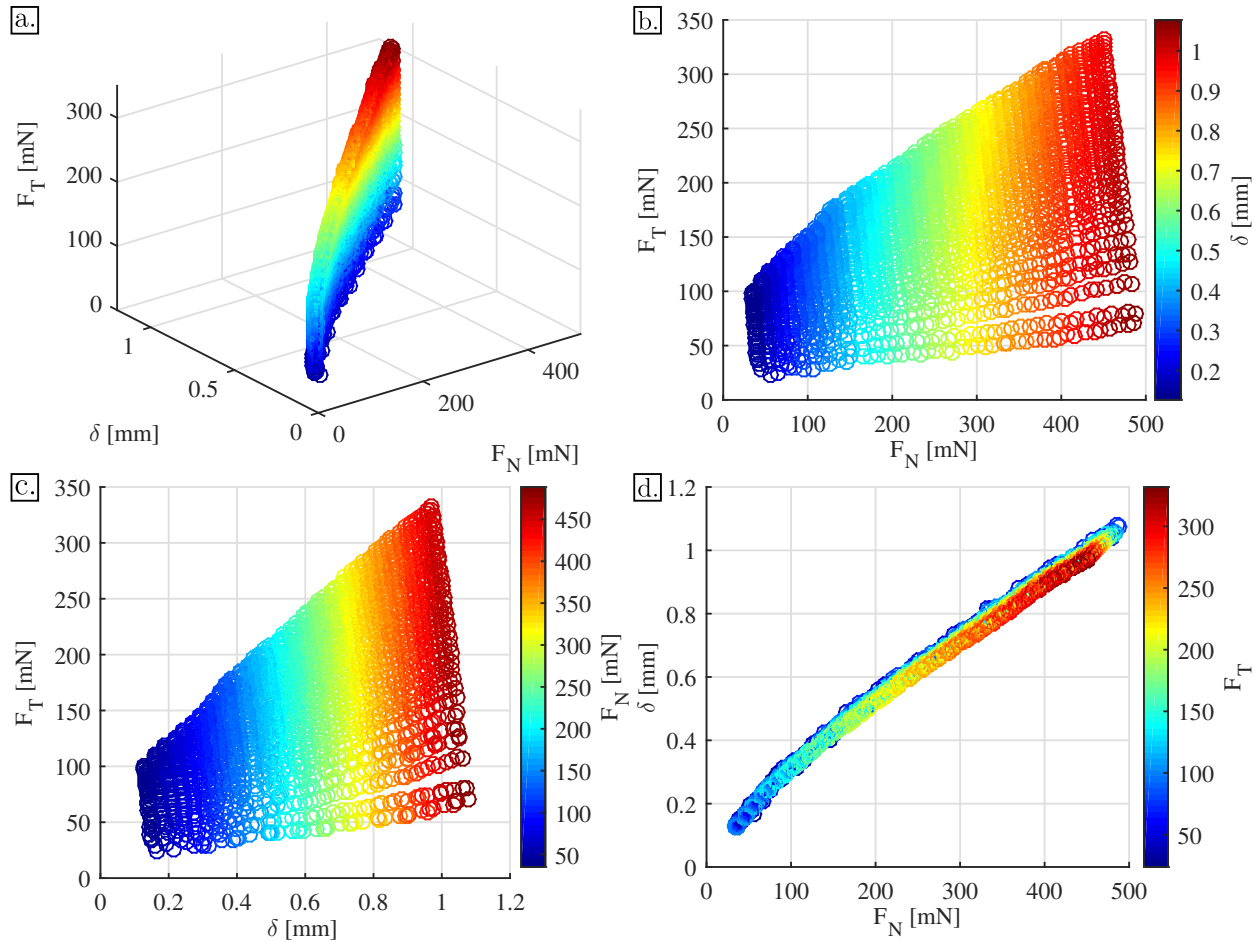
Figure 5.18: (a) The effect of wheel vertical deflection δ and normal force F_N on traction force F_T. (b) The effect of normal force F_N on traction force F_T. The color bar represents wheel vertical deflection δ. (c) The effect of wheel vertical deflection δ on traction force F_T. The color bar represents normal force F_N. (d) The effect of normal force F_N on wheel vertical deflection δ. The color bar represents traction force F_T. Each data point in (a-d) represents the average of two trials.
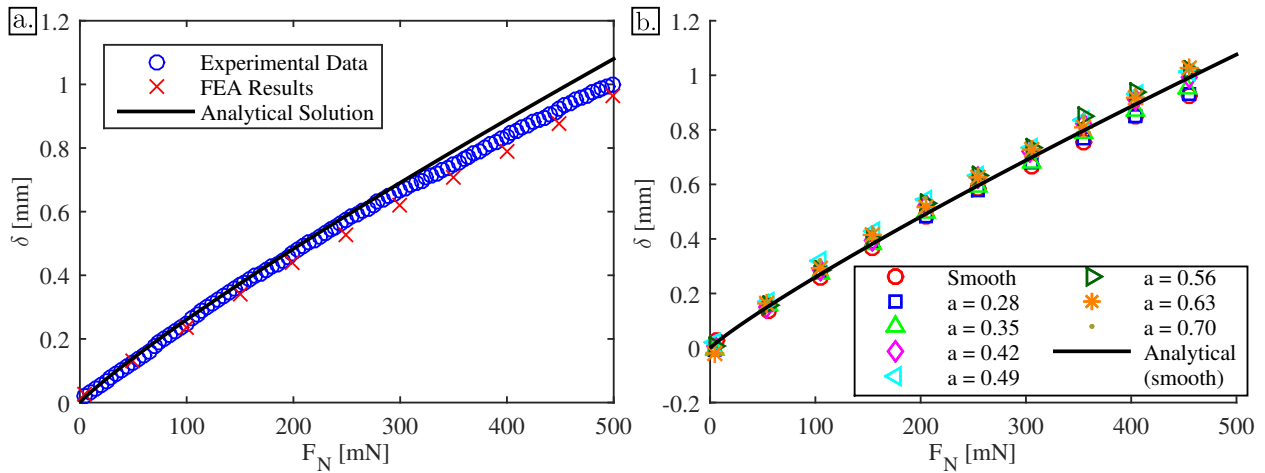
Figure 5.19: (a) Anaytical solution (black line), experimental data (blue circles), and FEA results (red x) for wheel vertical deflection δ as a function of normal force F_N in a static scenario (*i.e.*, no rotation or linear velocity) and a wheel with a smooth PDMS tread. (b) Analytical solution (black line) and experimental data (data points) for wheel vertical deflection δ as a function of normal force F_N in a static scenario for wheel with varying tread pillar size. The analytical solutions for (a) and (b) assume linear elasticity of the substrate, where Young's modulus E was approximated using the first 20% strain from the hyperelastic tensile test data (Fig. 5.3a).
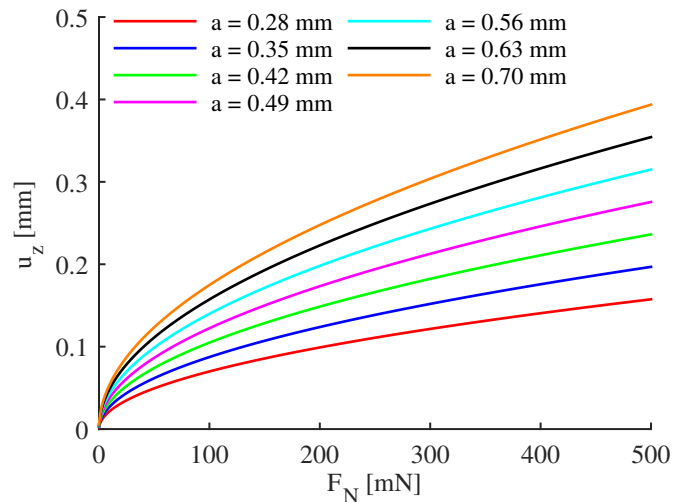
Figure 5.20: Analytical solution of the effect of normal force F_N on tread pillar vertical deflection u_z at a constant substrate Young's modulus E for varying tread pillar radii a. The Young's modulus E was approximated using the first 20% strain from the hyperelastic tensile test data (Fig. 5.3a).

5.5.1.2   PDMS Modulus

Fig. 5.21 shows the effect of relative stiffness between substrate and tread on F_T/F_N. Although the trend is not crystal clear, it suggests that there is a correlation between the traction generation and the relative stiffnesses of the materials. The data suggests that F_T/F_N increases until $k/E_{tread} = 1$, and then levels off with $k/E_{tread} = 1$. For maximum traction generation, substrate stiffness should be larger than the elastic modulus of the tread.
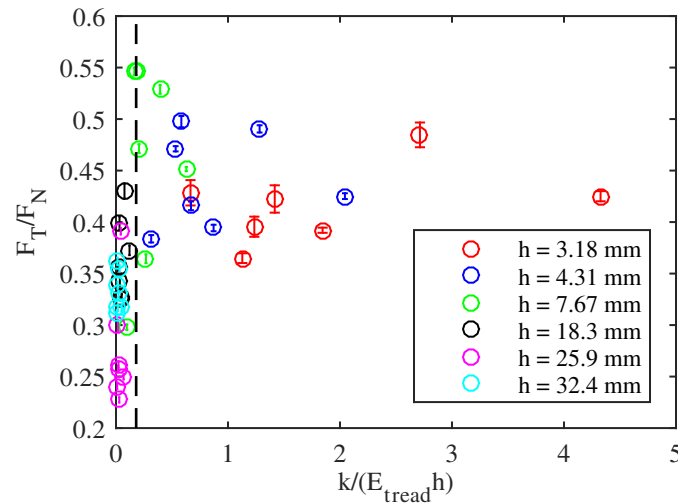
Figure 5.21: The effect of $k/E_{tread}h$ (substrate stiffness/tread elastic modulus/substrate height) on F_T/F_N. Substrate stiffness variation was obtained by varying the height of the substrate sample. Tread elastic modulus variation was obtained by adjusting the PDMS base to cross-link mixing ratio.

5.5.1.3   Pillar Size and Substrate Stiffness

The results for pillar size and substrate stiffness have been combined due to their apparent correlation. Fig. 5.22 shows the relationship between h/a and F_T/F_N, both dimensionless parameters. The substrate height is related to stiffness of the material, while the parameter a is related to the tread size. The data suggests that there is a cutoff for maximum traction force generation at around $h/a = 25$. The three substrates in group 1 ($h/a < 25$) are the shorter of the six and have relatively large stiffnesses. The three substrates in group 2 ($h/a > 25$) are the taller of the six substrates and have low and nearly equal stiffnesses. An attempt was made to fill in the gap by stacking substrates to achieve heights of 10 mm and 15 mm,

but it was determined that the effect of stacking the substrates was not negligible. In other words, stacking substrates to achieve a height of 25.94 mm produced different results than the 25.90 mm substrate
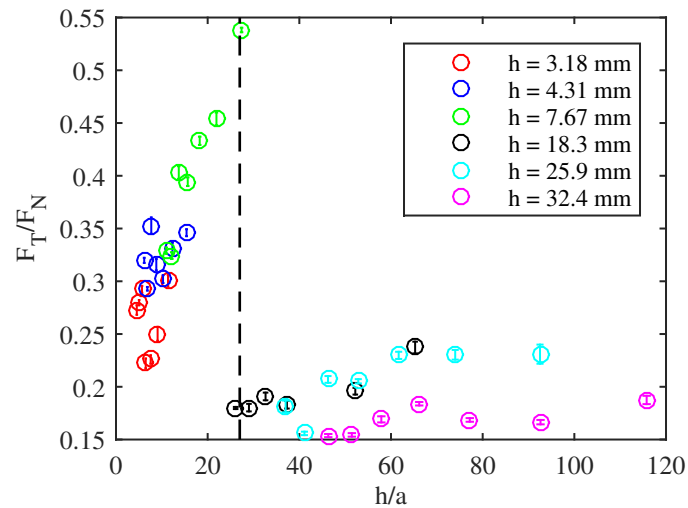
Figure 5.22: The effect of the dimensionless parameter h/a (substrate height/pillar radius) on F_T/F_N.

5.6   Conclusions

In this chapter, the synthetic tissue substrate was characterized to be modeled as both a hyperelastic and viscoelastic material. The hyperelastic material model chosen was the Ogden constitutive model with $N = 3$. The viscoelastic material model chosen was the Generalized Maxwell model with $N = 1$. In addition to the mechanical behavior characterization, a velocity dependent coefficient of friction was experimentally developed. These material parameters were implemented into a finite element model to predict traction force generation of a smooth rigid wheel on a synthetic substrate.

Experiments were performed using the ATM platform with an interferometer sensor for measuring vertical displacement of the wheel. The effects of differential velocity and normal force on traction force and wheel vertical displacement were studied. The data suggests that the stiffness of the substrate slightly increases with differential velocity, and that wheel vertical deflection and normal force are positively and strongly correlated. When assuming that the substrate is a linear elastic material, the analytical solution for δ matches closely with the experimental results. The analytical solution for δ for a smooth wheel also

holds true for wheel with small tread patterns ($a \leq 0.7$).

Chapter 6

The Design and *In Vivo* Evaluation of a Robotic Capsule Colonoscope Using Micro-patterned Treads for Mobility

The state-of-the-art technology for deep gastrointestinal (GI) tract exploration is a capsule endoscope (CE). Capsule endoscopes are pill-sized devices that provide visual feedback of the GI tract as they move passively through the patient. These passive devices could benefit from a mobility system enabling maneuverability and controllability. Potential benefits of a tethered robotic capsule endoscope (tRCE) include faster travel speeds, ability to maintain an anchored position, reaction force generation for biopsy, and decreased capsule retention. In this work, a tethered prototype CE is developed to evaluate an active tracking locomotion system for *in vivo* mobility. Micro-patterned polydimethylsiloxane (PDMS) treads are implemented onto a custom capsule housing as a mobility method. The tRCE housing contains a direct current (DC) motor and gear train to drive the treads, a video camera for visual feedback, and two light sources (infrared and visible) for illumination. The device was placed within the insufflated abdomen of a live anesthetized porcine (pig) model to evaluate mobility performance in an open cavity as well as within the cecum to evaluate mobility performance in a collapsed lumen. The tRCE was capable of forward and reverse mobility for both open and collapsed lumen tissue environments. Also, using an on-board visual system, the tRCE was capable of demonstrating visual feedback within an insufflated, anesthetized, porcine abdomen.

6.1 Introduction

Endoscopy is a current surgical method used to clinically investigate the lumen of the gastrointestinal (GI) tract. An endoscope is a long flexible scope which enters the patient through a natural orifice. The entire GI tract consists of the esophagus, gastric cavity, and small and large bowels. The small bowel itself is about 7 m long. The major limitation of the endoscope is the difficulty of viewing the entire small bowel, specifically the jejunum and ileum, the medial and distal sections of the small bowel respectively. Capsule endoscopy is a method for overcoming these limitations. Currently there are only two commercially available capsule endoscopes, the PillCam® SB (to view the small bowel) and the PillCam® ESO (to view the esophagus). These devices are pill sized capsules ($11\,mm \times 26\,mm$) that are swallowed by the patient and house a miniature video camera and light source. As the capsule endoscope (CE) passively moves through the GI tract, the camera transmits images at a rate of 2 frames/s which can be immediately downloaded and viewed by a physician [154]. Although these devices have made great strides in the pursuit of effective CEs, the devices also present some limitations. A CE is a passive device, so there is no control over the position of the device as it moves through the GI tract making it difficult to know exactly where, and at what orientation, the images are taken. Also, the image transmission rate does not give physicians a continuous, real-time, view of the GI tract during device passage. In addition, a major risk of CE devices is capsule retention. Capsule retention rates are about 5%, and primarily seen in patients with Crohns disease, at the inflammation site [112, 113]. A maneuverable CE could provide an additional force enabling the capsule to drive away from a position or traverse an occlusion that might ordinarily cause passive capsule retention.

The main focus of this research is to develop a tethered robotic capsule endoscope (tRCE) that provides video feedback at 30 frames/s, and active tracking locomotion through the bowel for endoscopic applications. The authors acknowledge that the tether is problematic and incompatible with the swallowing paradigm of traditional CEs, but is a necessary simplification for initial prototypes. Additionally, the device may be able to travel through an insufflated abdomen, demonstrating the feasibility of such a device in natural orifice translumenal endoscopic surgery (NOTES). Potential advantages of NOTES over traditional laparoscopy include the elimination of external incisions and the potential subsequent side effects such as pain, hernias,

and external wound infections. Other potential benefits of NOTES include decreased adhesions, decreased need for anesthesia, and shorter hospital stays.

The proposed method of tRCE mobility stems from a biological phenomenon found on the feet of insects. Certain terrestrial animals have evolved to develop micro-hairs on the pads of their feet to enhance friction for locomotion on various substrates [115, 116]. The pad is able to match the surface structure of the substrate, maximizing the contact surface area, and thus increasing the frictional and adhesive properties of the feet [117, 131, 118]. Other groups have attempted to enhance friction within the large bowel using micro-patterned PDMS [107, 108, 109, 119] and other friction enhancement techniques [18].

The purpose of this study is to demonstrate that the use of micro-patterned polymers as traction treads for a tRCE enables mobility on both tissue in an insufflated abdominal cavity and a collapsed lumen. The study also demonstrates a proof-of-concept of a tRCE with visual feedback.

6.2   Materials and Methods

The tRCE was designed, fabricated, and then tested *in vivo* in a live porcine (pig) model.

6.2.1   Tethered Robotic Capsule Endoscope Design and Fabrication

The following criteria were developed when designing the tRCE: 1) the ability to traverse an approximately planar tissue surface, such as the open insufflated abdominal cavity, 2) the ability to travel within a collapsed lumen, 3) capability of both forward and reverse motion, 4) sized to fit within the large bowel of a human (6 *cm* diameter), and 5) provide visual feedback to a monitor located external to the patient.

The tRCE design can be divided into four main parts, the 1) housing, 2) drivetrain, 3) micro-patterned treads, and 4) vision and illumination system.

6.2.1.1   tRCE Housing

Based on previous success with robotic mobility using micro-patterned PDMS treads, a tissue-robot interface was designed for the tRCE to address the first two design criteria [114]. In order to gain mobility within a collapsed lumen, the housing was designed to include tank-like tracking treads on the four sides of

the robot. The housing took the form of a box to produce a robot with flat sides for traversing planar tissue, while creating tread surface area on all four sides for traveling within a lumen. In order to maximize traction both in a lumen and on planar tissue, each side of the tRCE was designed to have two treads, creating a large ratio between the tread surface area and the housing surface area. For simplicity, this initial tRCE was designed for forward and reverse motion, but not left, right, up, or down. In other words, all treads could be simultaneously driven in the same direction at any given time, minimizing the number of required actuators, and thus reducing the size of the tRCE. For travel within a cylindrical lumen (the tRCEs primary goal), the design relies upon the geometry of the robot and its environment for steering. As long as the robot is longer than it is wide and there is sufficient radial pressure from the lumen, the lumen will guide the robot in the axial direction, preventing it from turning around or getting stuck within the lumen. The housing (Fig. 6.1) was designed to hold the drivetrain, 8 micro-patterned treads (two per side), a vision system, and an illumination system. The housing was prototyped (Protogenic, Westminister, CO, USA) using Protoclear 10120 (DSM Somos, Elgin, IL, USA).
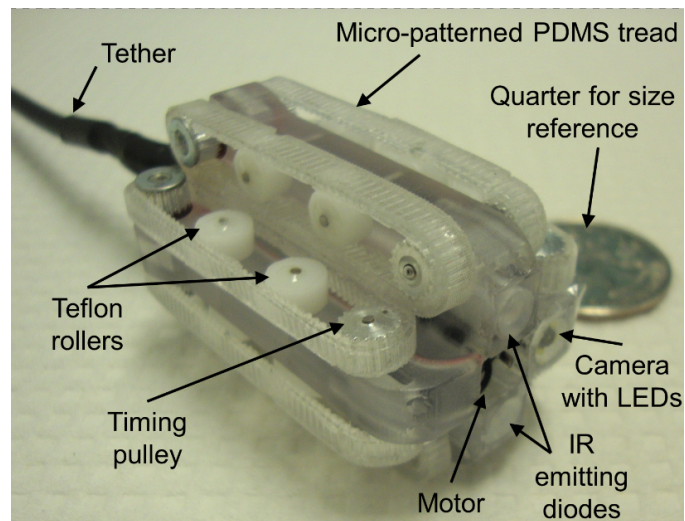
Figure 6.1: Fully assembled tethered robotic capsule endoscope (tRCE) on benchtop

6.2.1.2 tRCE Drivetrain

The drivetrain consisted of a direct current (DC) motor (FAULHABER, Croglio, Switzerland) with a 256:1 planetary gearhead reduction (FAULHABER, Croglio, Switzerland), a gear train, and timing pulleys. The DC motor was centrally located within the housing. A 0.5 modulus worm (GW0.5-01-14, Gizmoszone, Hong Kong, China) was press-fit on the shaft of the motor. Four (one per side) 0.5 modulus worm gears (GWG0.5-10-19, Gizmoszone, Hong Kong, China) were mounted to a bottom axle and driven by the worm. The ratio between the worm and worm gears provided an additional 10:1 reduction. Two 3 mm wide timing pulleys, made from timing pulley stock (A 6A15-010MXL02, Stock Drive Products/Sterling Instruments, New Hyde Park, New York, USA), were also fastened to each top axle (one on each end). Therefore, as the worm gears were driven, power was transferred to the top axles and thus the timing pulleys.

6.2.1.3 Micro-patterned PDMS Treads

Micro-patterned polydimethylsiloxane (PDMS) treads were used as the mobility method for the tRCE because they provide sufficient traction on the bowel tissue while minimizing tissue damage [114]. The purpose of the drivetrain was to transfer power from the DC motor to the timing pulleys on the end of each top axle. The timing pulleys then drove each micro-patterned tread. Each PDMS tread had custom fabricated timing belt teeth on the inside of the belt to mate with the driving timing pulley. The outside of each PDMS tread featured a micro-pattern consisting of 140 μm diameter, 70 μm high circular pillars. The pillars were equally spaced with a center-to-center distance of 245 μm. In addition to the timing pulleys, two Teflon rollers were added to each tread for support (Fig. 6.1). In order to prevent the treads from slipping off the pulleys, washers, slightly larger than the pitch diameter of the pulleys, were adhered to the outer faces of the pulleys using epoxy. The overall dimensions of the tRCE were 29 mm wide, 29 mm tall, and 46 mm long. The mass of the tRCE was 29 g. The tRCE prototype travels at a maximum speed of 3 mm/s.

Fabrication of micro-patterned treads for the robotic capsule endoscope (RCE) has progressed through multiple revisions. Each revision has either improved the functionality of the tread by increasing flexibility or reducing thickness, and/or improved the ease of fabrication. Each tread consists of two major parts: the micro-patterned polydimethylsiloxane (PDMS) treads and a driving mechanism. The micro-patterned

PDMS is on the outside surface of the tread, which interfaces with the tissue, while the driving mechanism is on the inside surface of the tread, and interfaces with the robots driving mechanism (*e.g.*, a timing pulley or roller). PDMS is inherently hydrophobic which makes it hard to bond to its self or other materials. Thus, it is a challenge to adhere the micro-patterned PDMS to the driving mechanism. Each tread is formed in the shape of a loop. Since the micro-patterned PDMS treads are fabricated in sheets, it is a challenge to transform the sheets into a loop.

Titanium coated timing belt PDMS treads The first iteration of the tread fabrication was for tRCE version 1 (tRCE v1), which employed a timing belt/timing pulley drive system. In an attempt to increase the adhesion properties of the PDMS, the non-patterned side of the PDMS was coated with 100 nm of titanium (Ti) using a standard thermal deposition procedure. Double-sided tape (3M, 3M415) was applied to the outside surface of polyurethane timing belts (SDP/SI, A 6B18M094030). The micro-patterned PDMS was trimmed to the correct size, and the Ti coated side was pressed onto the tape (Fig. 6.2). This resulted in a two-layer tread, with a polyurethane timing belt as a driving mechanism and micro-patterned PDMS outer surface. Eight of these treads were fabricated for tRCE v1. Each tread had a radius of 15 mm, a width of 3 mm and a thickness of 1.5 mm. The main problems associated with this tread were high stiffness, large thickness and seam separation.

Custom timing belt PDMS treads The second iteration of the tread fabrication was for tRCE version 2 (tRCE v2), which also employed a timing belt/timing pulley drive system. To reduce the stiffness of the treads, the polyurethane timing belts were replaced with custom PDMS timing belts (Fig. 6.3). Also, to reduce tread seam separation, a new fabrication procedure was employed. A mold for the PDMS timing belts was fabricated using polyurethane timing belts (SDP/SI, A 6B18M094030) and an aluminum mold. Trenches (3 mm wide, 95 mm long, and 1.5 mm deep) were formed in an aluminum plate. Polyurethane timing belts were cut, stretched out, and glued to the bottom of the trenches (teeth side up). Liquid PDMS was poured into the mold and cured. The PDMS was polymerized by a heat curing process (100 °C for 1 hr). The polymerized PDMS was peeled out of the mold, creating strips of PDMS with one smooth side and one side containing timing belt teeth. The micro-patterned PDMS strips and the timing belt PDMS strips were then adhered together using double-sided tape (3M, 3M415). To increase the adhesion properties of
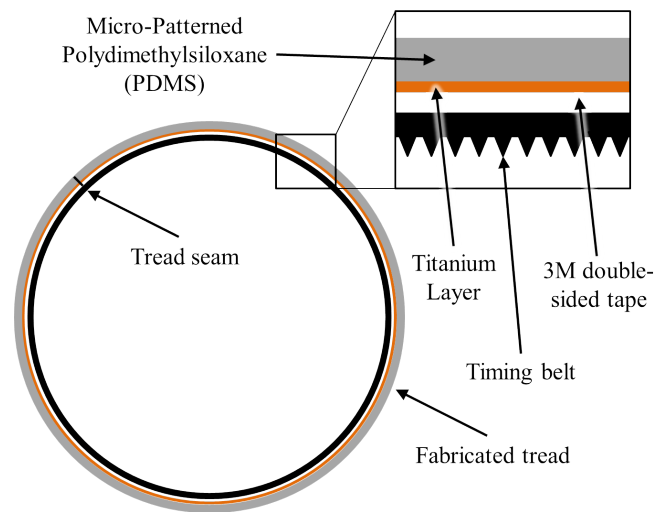
Figure 6.2: Titanium coated treads consisting of 4 layers, an outer micro-patterned PDMS layer for traction, a layer of titanium for adhesion, a layer of double-sided tape for interlayer adhesion, and an inner polyurethane timing belt layer to interface with the timing pulleys.

the PDMS, the strips were exposed to 20 W O_2 plasma for 25 s prior to contact with the double-sided tape. To form a closed loop, excess tape was used to overlap the seam (in between the two layers of PDMS). The following procedure was used to form closed loop treads using micro-patterned PDMS and custom timing belt PDMS strips:

(1) Lay out a 100 mm strip of double-sided tape with backing paper still attached to one side (sticky side up)

(2) Lay out a 95 mm strip of timing belt PDMS (smooth side up)

(3) Expose both strips to 20 W O_2 plasma for 25 s.

(4) Immediately press smooth side of timing belt PDMS to sticky side of tape.

(5) Peel off backing on tape

(6) Expose new sticky side to 20 W O_2 plasma for 25 s

(7) Immediately form closed loop, using the 5 mm excess tape to overlap the seam

(8) Expose the smooth side of a 95 mm long micro-patterned PDMS strip to 20 W O_2 plasma for 25 s

(9) Immediately press smooth side of PDMS onto tape, forming a layer of micro-patterned PDMS on the outside surface of the tread

This procedure resulted in flexible treads with minimal seam separation. The treads had custom PDMS timing belts as an inside surface for mechanical engagement with the timing pulleys on the tRCE v2. The treads also featured micro-patterned PDMS on the outside surface. Eight treads were fabricated in this manner for tRCE v2. The treads had a radius of 15 mm, a width of 3 mm, and a thickness of 1.5 mm.

Friction driven PDMS treads The third iteration of the tread fabrication was for tRCE version 3 (tRCE v3), which employed a friction drive system (Fig. 6.4). The friction drive system eliminated the need for timing belts as a mechanical engagement system, enabling a reduction in tread thickness and overall size of the tRCE. The design of the tRCE required fewer, but wider treads, decreasing the fabrication time and increasing the ease of handling. The treads were fabricated in a similar manner to tRCE v2 treads,
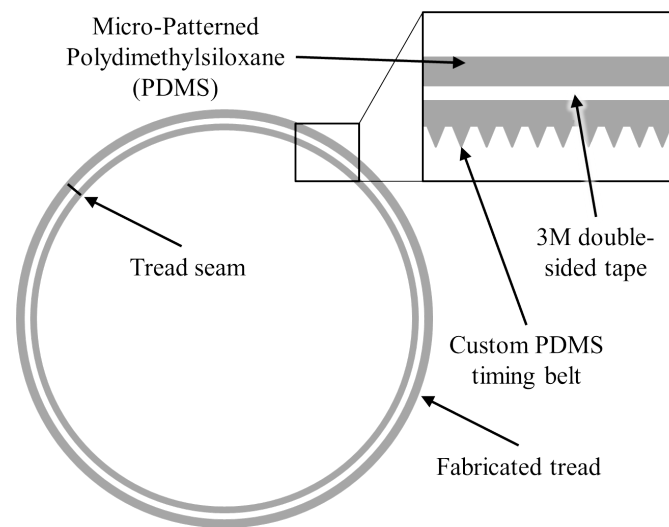
Figure 6.3: Custom PDMS timing belt treads consisting of 3 layers, an outer micro-patterned PDMS layer for traction, a middle double-sided tape layer for interlayer adhesion, and a custom PDMS timing belt inner layer to interface with the timing pulleys.

except the PDMS timing belts were replaced with a thin layer of smooth PDMS. The thin layer of PDMS was used to promote friction between the inside surface of the tread and the frictional rollers on the tRCE. The following procedure was used to fabricate closed loop treads:

(1) Lay out a 100 mm strip of double-sided tape with backing paper still attached to one side (sticky side up).

(2) Clamp the tape so that 5 mm of the tape is covered.

(3) Paint the remaining uncovered 95 mm of the sticky side with a thin layer of liquid PDMS.

(4) Heat cure the PDMS in an oven at 100 °C for 1 hr

(5) Unclamp the tape and wrap the strip around an 1.5 in diameter cylinder (PDMS side down), using the excess 5 mm to overlap the seam.

(6) Peel off the paper backing

(7) Expose the tape and the smooth side of a 95 mm long micro-patterned PDMS strip to 20 W O_2 plasma for 25 s.

(8) Immediately wrap the micro-patterned PDMS strip around the tape (smooth side to tape).

(9) Slide the tread off of the cylinder.

This procedure results in treads with a smooth PDMS inside surface for frictional engagement with the RCE rollers and a micro-patterned PDMS layer on the outside surface of the treads. Four treads were fabricated in this manner for RCE v3. The treads had a radius of 15 mm, a width of 6 mm, and thickness of 0.75 mm.

6.2.1.4   Vision and Illumination Systems

The rear of the tRCE housed the gear train for power transfer from the actuator, while the forward part of the tRCE housed the vision and illumination system, as illustrated in Fig. 6.1. Three holes were created in the housing for the imaging and illumination systems. The tRCE design integrated two different imaging
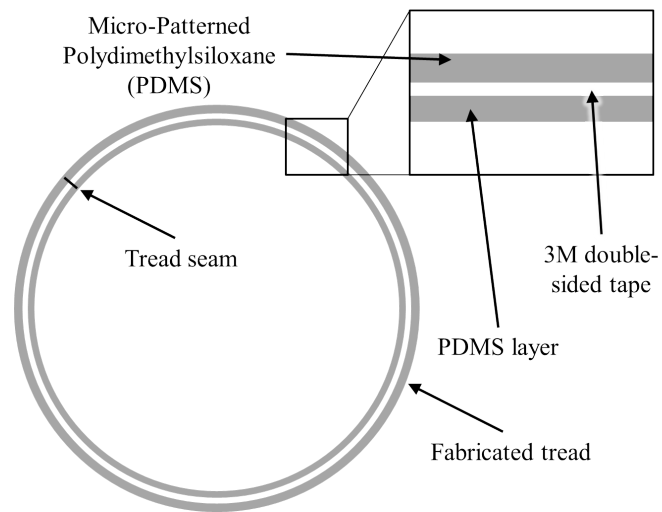
Figure 6.4: Friction PDMS treads consisting of 3 layers, an outer micro-patterned PDMS layer for traction, a middle double-sided tape layer for interlayer adhesion, and an inner layer to interface with the rollers

techniques, visible light and infrared (IR) light. IR technology has shown to be useful for distinguishing healthy and cancerous tissue [155]. IR rays emitted at the near infrared (NIR) range are ideal for imaging large organs [155]. The tissues of large organs exhibit low absorption and allows light at a safe power to penetrate the tissue [155]. When the emitter produces wavelengths in the NIR range, they are reflected off of the tissue and back to the camera, producing a greyscale image with shades dependent on the different IR absorption rates of each tissue type. A 4 mm wide analog camera with 4 integrated LEDs (RS4018A-118, Bangu Technology Development Company Limited, Guangdong, China) was placed in one of the three holes in the housing. The camera was recessed in the hole and a flat transparent cover was placed over the hole and adhered to the housing to keep tissue away from the lens and seal the camera from fluid. The two remaining holes each housed a 3 mm infrared emitting diode (LIR204X, Jameco Electronics, Belmont, CA, USA). A user-controlled system was implemented to select the type of illumination and the intensity of the light. All of the wires for the LEDs, camera, and motor were routed out of the rear (near the gear train) of the tRCE and tethered to an external control box. The control box featured controls for light selection and intensity, motor activation and direction, and camera activation. The image from the camera was displayed on a monitor, external to the porcine specimen, for real-time viewing (Fig. 6.5).

The camera is capable of detecting both visible and IR light. When the camera is placed in an environment with no visible light (*i.e.*, an insufflated abdomen), and the IR illumination is activated, a grey scale image is produced (Fig. 6.6).

6.2.2   Benchtop Performance Evaluation

Upon fabrication, the tRCE was first evaluated in a controlled laboratory setting to benchmark the performance of the device prior to *in vivo* testing. More specifically, the expected *in vivo* loads were applied to the tRCE to determine if the torque requirement had been met. Both the mobility and the imaging/illumination systems were tested. The purpose of the benchtop tests was to evaluate the torque performance of the device, and not necessarily to accurately simulate all features of an *in vivo* environment.

To test the mobility system, the device was driven across dry synthetic tissue (Simulab Corporation, Seattle, WA, USA) to evaluate mobility. Next, the device was placed in between two layers of synthetic
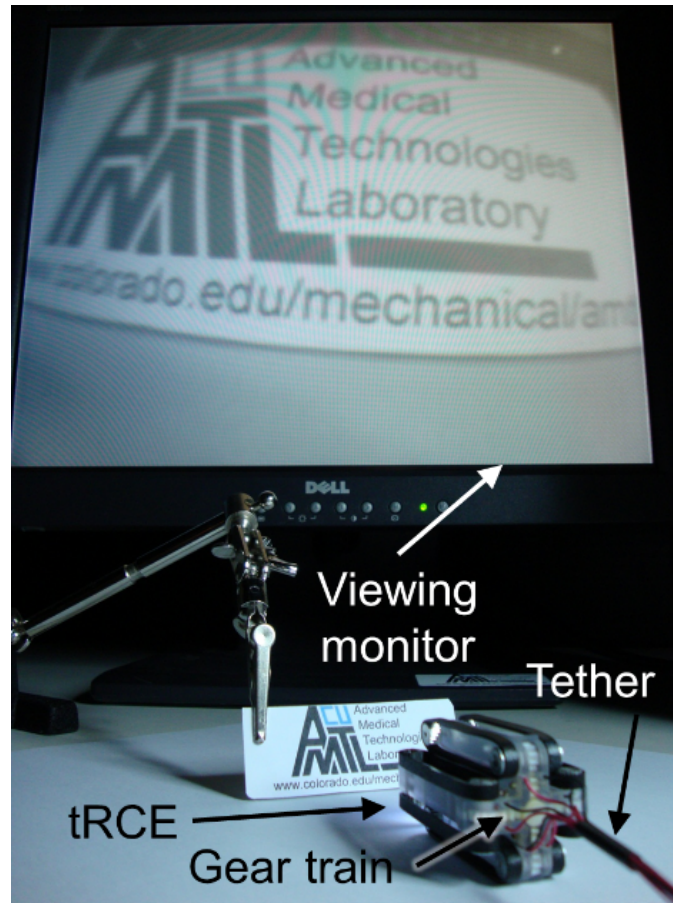
Figure 6.5: Image of tethered robotic capsule endoscope (tRCE) with vision and illumination system
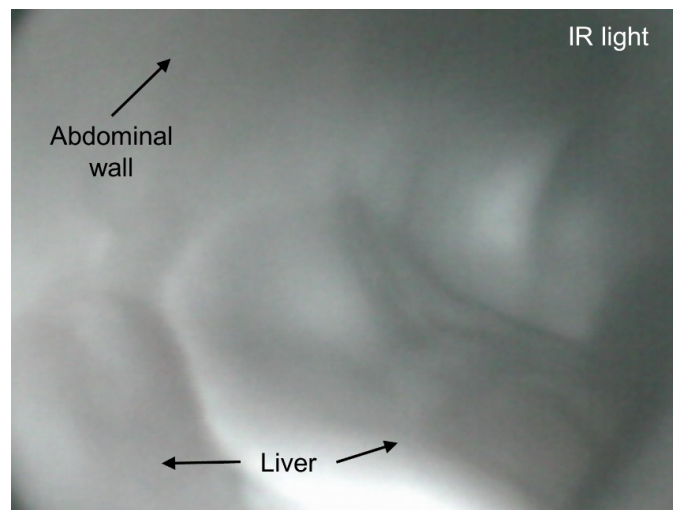
Figure 6.6: View from the tethered robotic capsule endoscope (tRCE) imaging system inside the insufflated abdomen using an IR light source.

tissue, with a 500 g mass on the top (chosen because this weight simulates a worst case scenario for loading in the GI tract), to benchmark the durability and required torque of the tRCE, to move through a collapsed lumen.

To test the vision/illumination system, the tRCE was placed in a dark box. A monitor was placed outside of the box and the camera was activated with 1) no light source, 2) visible light from the LEDs, 3) IR light, and 4) visible and IR light. Various objects (color and grey scale) were placed in the field of view at various distances from the tRCE to qualitatively evaluate the imaging system with the various illumination sources.

6.2.3   Porcine Study

The benchtop tests provided a benchmark performance level for the tRCE under various conditions. The purpose of the porcine study was to determine the level of performance relative to the benchmark performance level in various *in vivo* environments. The two primary test conditions of interest were mobility on tissue in an insufflated cavity, and mobility within a collapsed lumen. To test mobility of the tRCE in an uncollapsed environment, the device was placed within an insufflated abdomen. To test for mobility within a lumen, the tRCE was placed in the cecum (section of the large bowel).

6.2.3.1   Abdominal Mobility

During *in vivo* testing, a 5 cm long incision was made in the umbilicus of the pig and then the tRCE was inserted through the incision with approximately 30 cm of wire tether to reduce drag on the tRCE. After insertion, the incision was sutured around the wire to produce an air tight seal. Two 12 mm trocar ports were inserted in the abdominal wall using a standard technique. One trocar was used for a laparoscopic camera (model 22220130, Karl Storz, El Segundo, CA, USA) and CO2 insufflation, while the other was used as a tool port (to manipulate the tRCE). Upon abdominal insufflation, the tRCE was positioned on bowel and mesentery using laparoscopic tools. Then, the tRCE was activated to evaluate mobility on bowel and mesentery. Next, the tRCE was repositioned onto the liver/abdominal wall using laparoscopic tools. Again, the tRCE was activated to evaluate mobility on liver and abdominal wall. Throughout the test, video from

the laparoscopic camera was recorded. The imaging system from the tRCE was also recorded throughout the entire test to evaluate imaging system performance.

6.2.3.2 Imaging/Lighting

After mobility testing in the insufflated abdomen, the imaging system was tested. The light source from the laparoscope was deactivated. The visible light source on the tRCE was activated, and then deactivated. Next, the IR light source on the tRCE was activated and then deactivated. Finally, both the visible and IR light sources on the tRCE were simultaneously activated and then deactivated. Throughout the test, video from the tRCE camera was recorded for later viewing and evaluation.

6.2.3.3 Intraluminal Mobility

In order to test for mobility within a collapsed lumen, the tRCE was placed in the cecum of the porcine model. Due to size restrictions, the test could not be performed in the small bowel, though future versions of this device will likely be tested in the small bowel. The test was performed as follows. The 5 cm long incision was reopened and the tRCE was removed from the abdomen. A section of the cecum (2.5 cm in diameter) was pulled out of the abdomen and placed on the outside of the animal. A 3 cm incision was made in the cecum and then the cecum was cleaned out using suction. The incision was held open using forceps while the tRCE was inserted partially into the cecum (the cecum had to be stretched slightly around the outside of the device). The tRCE was activated to evaluate the performance of the device in the collapsed lumen.

6.3 Results

6.3.1 Device Performance

The purpose of the benchtop tests was to set a benchmark performance level for all tRCE tasks, so that performance during the *in vivo* study could be compared to a control. During benchtop mobility testing, the device successfully traversed the synthetic tissue. Also, the device travelled the maximum possible distance (length of the synthetic tissue sample, 170 mm) between two layers of synthetic tissue with a 500 g mass

on the top of it at an average speed of 3 mm/s. During the benchtop imaging system testing, an adequate picture was displayed on the monitor for each of the lighting scenarios. Common objects (*e.g.*, cord, pencil, pen, calculator, battery, coin) placed within the field of view could easily be identified on the monitor under all of the lighting scenarios, except for the scenario with no light, where none of the objects could be seen.

6.3.2 Porcine Study Results

6.3.2.1 Abdominal Mobility

During the first phase of the porcine study, the tRCE was placed in the insufflated abdomen of the porcine. First the tRCE was placed on a combination of bowel and mesentery. When the motor was activated, the tRCE moved forward approximately 5 cm with minimal slipping at an average speed of 3 mm/s. The tRCE was positioned at an angle such that two of the sides (*e.g.*, four treads) were in contact with the tissue. After 5 cm of travel, the direction of the motor was reversed, and the tRCE traveled backwards 5 cm to the starting position at an average speed of 3 mm/s. Then, the tRCE was moved to the liver using laparoscopic tools. The tRCE was positioned so that three sides of the tRCE were in contact with tissue (Fig. 6.7). Two of the sides were in contact with liver, while a third side was in contact with abdominal wall. Again, when the tRCE was activated, it traveled forward approximately 5 cm (Fig. 6.7, dashed line) with no visible slipping at an average speed of 3 mm/s. When the motor was reversed, the tRCE traveled back 5 cm to the original location at an average speed of 3 mm/s. The pitch of the tissue surfaces varied between 0° and approximately 20°.

6.3.2.2 Imaging/Lighting

Next, the imaging system was tested. The tRCE was positioned so that several organs of varying color and density were in the field of view. The image from the camera with visible light only is shown in Fig. 6.8. The image was adequate enough to identify the organs within the field of view. The image from the camera with IR light only is shown in Fig. 6.6. The IR image provides a grey scale thermal view of the organs. Although it was hard to identify the different organs, the IR light does provide a high contrast image that could be useful in diagnosing diseased or unhealthy tissue. Figs. 6.8 and 6.6 are taken from the
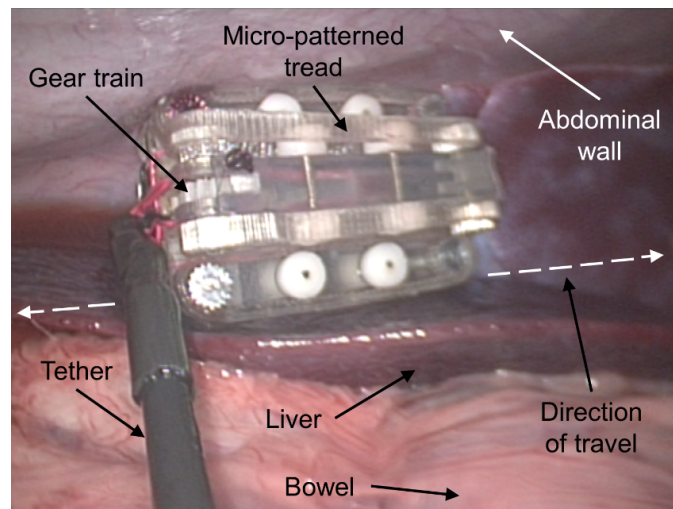
Figure 6.7: Tethered robotic capsule endoscope (tRCE) inside the insufflated abdomen of a live anesthetized porcine on liver (view from laparoscope).

same tRCE orientation, so the field of view is nearly identical. In Fig. 6.6 (showing infrared light), there is a large white spot in the bottom center of the frame. This might initially be mistaken as contrast from the tissue, but it is in fact a focused reflection from the infrared diodes. Since the visible light LEDs were integrated on the camera board, they were internal to the lens cover. Glare from the LEDs on the lens cover was noted at times which resulted in impaired vision.
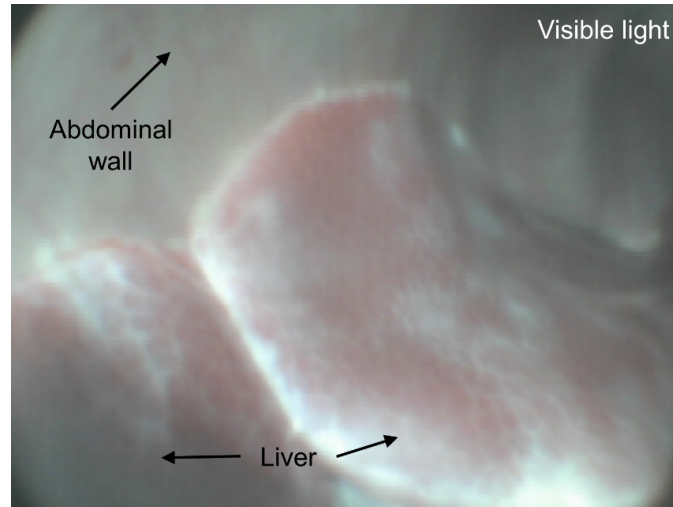
Figure 6.8: View from the tethered robotic capsule endoscope (tRCE) imaging system inside the insufflated abdomen using a visible light source.

6.3.2.3   Intraluminal Mobility

The final phase of the porcine study was the demonstration of mobility within a collapsed lumen. Due to size restrictions, the device was placed inside the cecum of the large bowel and not the small bowel. An incision was made in the cecum, and the device was placed about halfway into the incision. When the device was activated, it traveled approximately 4 cm into the cecum. When the direction of the motor was switched, the device traveled approximately 5 cm back out of the cecum, past the starting position. During reverse operation, the device was working against gravity and with the added weight of the tether. This test was repeated three times with similar results. During the travel through the cecum, minimal slippage was observed. The device crawled through the cecum at an angle of 0° (horizontal) and 90° (vertical). While the device was in the cecum, visual feedback was impaired due to the close proximity of the tissue to the

camera lens.

6.4   Discussion

The results presented here demonstrate that mobility within the GI tract using a tethered capsule type device is possible. The prototype device presented in this work is not suitable for travel through the entire GI tract due to its large size, and size reduction is a necessary next step. Size reduction will enable future devices to travel through the entire GI tract, and not only the large bowel. The device is also too slow, and speed will need to be increased. The slow speed was a direct result of creating a device with high torque. The next challenge will be to optimize speed and torque. Now that mobility has been demonstrated, the focus can now be on making smaller and faster tRCE versions. The most recent version (Fig. 6.10), not yet tested *in vivo*, was created using custom fabricated parts and has a 56% smaller cross-sectional area than the tRCE tested *in vivo* (Fig. 6.9).
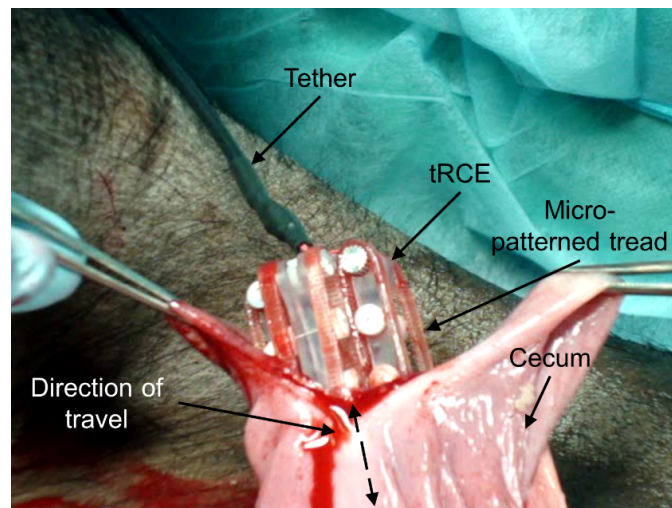
Figure 6.9: Tethered robotic capsule endoscope (tRCE) inside the cecum of a live anesthetized porcine.

This research demonstrates that a mobile tethered capsule endoscope with visual feedback is possible. The visual feedback system of the device also needs improvement. The camera used was chosen based on its small size, low cost, and easy integration. The analog camera provides a low quality picture, so future iterations of this device will explore different imaging systems in order to compete with current CE image
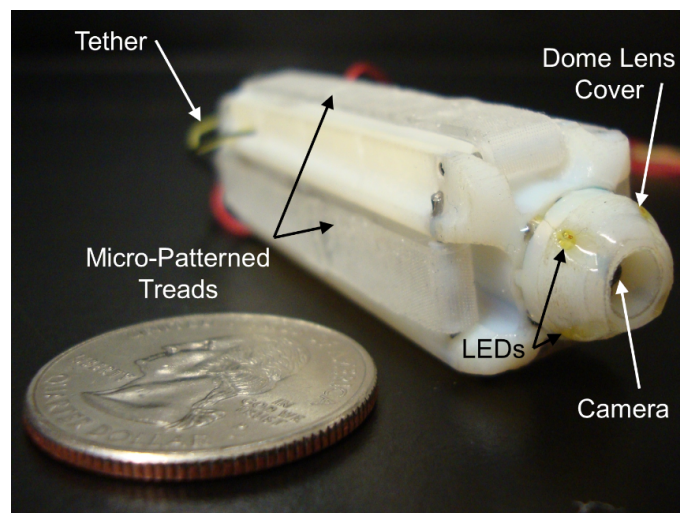
Figure 6.10: A smaller (approximately 56% decrease in cross-sectional area) tethered robotic capsule endoscope (tRCE) not yet tested *in vivo* with a dome lens cover to increase distance between the tissue and the lens, and LEDs that are external to the lens to prevent reflection off the cover.

quality. In future tRCE versions, similarly sized high-definition (HD) digital cameras will be used. However, the HD cameras require a much more complicated integration scheme and were therefore not chosen for this prototype device. The current camera is not the limiting feature for size reduction, so the tRCE can be made substantially smaller without regard to the imaging system.

When tested in the cecum, the vision feedback was impaired due to the proximity of the tissue to the lens. In an attempt to fix this visual impairment, a dome shaped lens cover has been added to the most recent tRCE version (Fig. 6.10) increasing the distance between the tissue and the camera lens. Additionally, during *in vivo* testing LED glare on the inside of the lens cover was noticed. This glare also impaired the vision at times. To eliminate glare in the most recent version, the LEDs were placed external to the lens cover. Infrared light was investigated because the IR LEDs were easy to implement and control. Since the main focus of the most recent version was size reduction and increased image quality, the IR LEDs were not integrated into the design.

The most important results of the study are the demonstration of tRCE mobility on tissue within an open abdominal cavity and within a collapsed lumen. This current device is too large to fit in the small bowel, which is why the large bowel was used for collapsed lumen testing. Although the device only traveled 5 *cm* on both abdominal tissue and in the collapsed lumen, distance was limited by the length and stiffness of the tether. In future versions the tether will be lengthened and made less stiff, and eventually eliminated so that longer travel distances will be attainable.

The results of this and previous research [115] show that *in vivo* mobility is possible in both the insufflated abdominal cavity and a collapsed lumen using micro-patterned treads in a tRCE configuration. These results suggest that the area of NOTES could possibly be advanced with future versions (smaller and faster with higher quality video, onboard tools, and no tether) of the tRCE. A future version of a tRCE would operate alone, eliminating the need for other endoscopes or laparoscopic tools. The tRCE presented here could be reconfigured to enable turning capabilities in the abdomen by configuring two tRCEs side-by-side in a tank configuration. As a maneuverable device, it could be positioned in places that a traditional laparoscopic camera cannot, thus expanding potential camera views. Additionally, the advantages of a mobile tRCE in the GI tract alone (excluding the abdomen) are numerous. With an active, cost effective,

compact tRCE, the device could provide inexpensive non-invasive diagnostic, exploratory, surgical, drug and other therapies at hard-to-reach locations within the small bowel. Of course, none of this will be possible without the elimination of the tether, as a tethered device will suffer from the same limitations as traditional enteroscopy. Furthermore, it is unlikely that a tethered RCE will develop enough traction force to drag a tether deep within the small bowel. Therefore, future elimination of the tether will be necessary for practical implementation of the tRCE.

A smaller version of the tRCE, termed tRCE v3 (Fig. 6.10) has been developed, but not yet experimentally validated. The tRCE v3 consists of an outer housing for a centrally located, planetary geared, DC motor (Faulhaber, Clearwater, FL), a custom designed geared drive train, and a series of rollers for the micro-patterned PDMS treads to pass over as the tRCE moves. A custom designed worm (pitch diameter of 0.0787 in and modulus of 0.013) is press fit and adhered to the shaft of the DC motor with a 5 Minute$^{®}$ Epoxy (ITW Devcon, Danvers, MA). The worm drives four mating worm gears (6 teeth, modulus of 0.013, and pitch diameter of 1.99 mm) that are equally spaced, radially around the worm. Four adjacent shafts also have cylindrical rollers (outer diameter of 2.30 mm and length of 8.38 mm) to drive the four PDMS treads (approximately 6 mm wide and 0.75 mm thick). The rollers along the body of the housing have various outer diameters to make the shape of the device more rounded. The shafts for the gears and rollers are made from 1 mm drill bit shanks and are approximately 12 mm long. The device also has a centrally located 4 mm diameter video camera (Bangu Technology Development Company Limited, Baoan District Shenzhen Guangdong, China) with 30 fps and four 2 mm diameter, yellow LEDs (Digi-Key Corporation, Thief River Falls, MN) embedded in a front cap to view and illuminate the bowel. A clear piece of plastic is adhered to the front cap to prevent any fluids from entering the device and damaging the internal electronic components. An end cap part is adhered to the rear of the device to protect the geared drive train. The figure below shows computer-aided design (CAD) assembly views of the tRCE v3 design with the various parts labeled.

6.4.1   Conclusions

In this work a prototype tRCE was designed and fabricated. Main features of the tRCE consist of micro-patterned PDMS tracking treads as a mobility method, forward and reverse locomotion, and an onboard analog imaging system with both visible and IR light sources. The tRCE was tested in a controlled laboratory setting as well as in a live anesthetized porcine surgery. The tRCE demonstrated mobility both in benchtop and *in vivo* environments. The tRCE was able to traverse several abdominal tissue surfaces (*i.e.*, bowel, mesentery, abdominal wall and liver) in an insufflated abdominal cavity as well as travel in and out of a collapsed lumen (*i.e.*, the cecum). The imaging system provided an adequate visual feedback in the insufflated abdomen with both visible and IR light sources, but failed to provide an adequate imaging in the cecum, due to close proximity between the tissue and imager lens.

Chapter 7

The Development and Experimental Validation of an Analytical Model for *In Vivo* Robotic Capsule Colonoscope Resistance Force

7.1   Introduction

In recent years, wireless capsule endoscopes (WCEs) have become commercially available and have been a popular topic of research in the diagnostic robotics field. State-of-the-art WCEs are gaining popularity as a screening tool within the gastrointestinal (GI) tract to aid in the diagnosis of diseases, such as colorectal cancer (CRC) and inflammatory bowel disease (IBD). Cancer is the leading cause of death worldwide, accounting for 7.6 million deaths (approximately 13% of all deaths) in 2008. Furthermore, death from cancer is projected to rise to over 13.1 million in 2030 [156, 157]. Colorectal diseases, and in particular CRC, affect a large number of people worldwide, with a strong impact on healthcare systems. It was estimated that 137,000 people will be diagnosed with CRC in 2014 (8.5%, or 3rd in incidence ranking, of all new cancers) in the U.S., resulting in approximately 50,000 deaths (8% of all cancer deaths), making it the 3rd deadliest cancer [121]. Additionally, CRC ranks fourth in terms of incidence rate among all cancers in high-income countries, accounting for 608,000 deaths worldwide in 2008 [156]. There is a 90% 5-year survival rate if CRC is detected at the earliest stage (confined to a primary site) [121]; however, the 5-year survival rate drops to 13% if CRC is detected after the cancer has metastasized [121]. Only 40% of CRC cases are detected in the earliest stage, in part due to the under-use of screening [121]. Therefore, regular screening is highly recommended for patients older than 50 years or who have a family history of CRC. An adequate screening procedure is one which allows for the detection and removal of colorectal polyps before progression to cancer

[121]. The potential benefit of cancer screening, a life-saving procedure, can be achieved if accuracy and reliability are high at every step. Screening is performed on predominantly healthy people, thus tests should be low invasive to maintain a convenient trade-off between benefit and harm. A rise in screening procedure prevalence has been linked to both incidence and death rate declinations [121]. Therefore, reliable regular screening methods are imperative to early stage CRC diagnosis.

WCEs are a promising technology for CRC screening because they are non-invasive and compact, resulting in a painless and accessible option for patients. However, there are several drawbacks to commercially available designs which render them inferior to the clinically preferred endoscopic methods. WCEs rank relatively low in diagnostic accuracy due to their passive nature. They are also limited to exploratory procedures as they do not have tools for therapeutic procedures, such as drug delivery or biopsies. One method of addressing these drawbacks is to implement an active position control method. By actively controlling WCEs, accuracy is improved due to the ability to position and orient the capsule, and return to abnormal areas for secondary diagnoses. Additional capabilities could also be added to a soft-tethered capsule [12] with a working channel, such as irrigation, insufflation, and tools for biopsies and drug delivery. The major drawback of implementing locomotion for WCEs is the increase in complexity and size of the system.

Several actuation methods for WCEs are under development, including legged [18], treaded [17], inchworm [26], magnetic [27, 28, 38] and hybrid [24] systems, all of which require dragging the capsule through the GI tract. A comprehensive discussion on capsule endoscope locomotion methods can be found in [158].

Knowing the resistance force on the capsule from the surrounding tissue is imperative for an effective, efficient and safe design. The model developed in this work provides accurate prediction of the force required to drag a WCE through the GI tract when the capsule is in partial contact with the GI wall (*e.g.*, in the insufflated colon or stomach). A typical problem setup is presented by using a magnetic actuation system as an example, followed by the model development. A pilot study is performed on excised porcine colonic tissue to validate the model with respect to each capsule design parameter (edge radius, length, diameter, normal force and velocity) and to determine which parameter affects the drag force the most, followed by an in depth study on excised colonic porcine tissue of that parameter (*i.e.*, edge radius). Finally, a study is carried out to validate the model in all regions of the GI tract (esophagus, stomach, small bowel, and colon).

7.2   Background

For the purpose of presenting a potential application for the model and for determining realistic test values, a magnetically actuated WCE system is considered. However, it is important to note that the model and experiments were designed in such a way to be applicable to any system where a cylindrical capsule is moved across a tissue substrate.

Magnetic actuation of WCEs is a promising locomotion method in development, and employs magnetic coupling between an external magnet (located outside of the patient) and an internal permanent magnet (IPM) located inside the capsule [3]. The external magnet is generally fixed to and manipulated by an external robotic arm in order to guarantee higher stability for steering, and can be either an external permanent magnet (EPM) or an electromagnet. Several groups have developed complete EPM systems [38, 159, 36] and electromagnetic systems [160, 161, 162] including a system which uses magnetic resonance imaging (MRI) to control the capsule endoscope [34]. A typical setup of a magnetic actuation system using an EPM is summarized in Fig. 7.1a. An IPM is added to a typical WCE and placed in the GI tract. The WCE is attracted to the EPM, but is constrained by the intestinal wall and surrounding organs. The EPM can be positioned and oriented to induce a magnetic field $\vec{B}$ and a magnetic field gradient $\nabla\vec{B}$ which impose forces and torques on the IPM within the capsule.

The magnetic force $\vec{F}_m$ and the magnetic torque $\vec{T}_m$ exerted on a magnetic capsule endoscope with magnetic moment $\vec{m}$ in a magnetic field $\vec{B}$, assuming that no electric current is flowing in the workspace, are given by:

$$\vec{F}_m = (\vec{m} \cdot \nabla)\,\vec{B} = \left[\frac{\partial \vec{B}}{\partial x} \quad \frac{\partial \vec{B}}{\partial y} \quad \frac{\partial \vec{B}}{\partial z}\right]^T \vec{m} \tag{7.1}$$

$$\vec{T}_m = \vec{m} \times \vec{B} \tag{7.2}$$

Locomotion is achieved when both of the following are satisfied:

$$F_M = F_{\nabla \vec{B}_y} = N \cdot F_W \qquad N \geq 1 \tag{7.3}$$

$$F_D = F_{\nabla \vec{B}_x} \geq F_R = F_x + F_A + F_f \tag{7.4}$$

where F_M is the attraction force due to the magnetic field gradient, $\nabla\vec{B}_y$, F_W is the weight of the capsule,
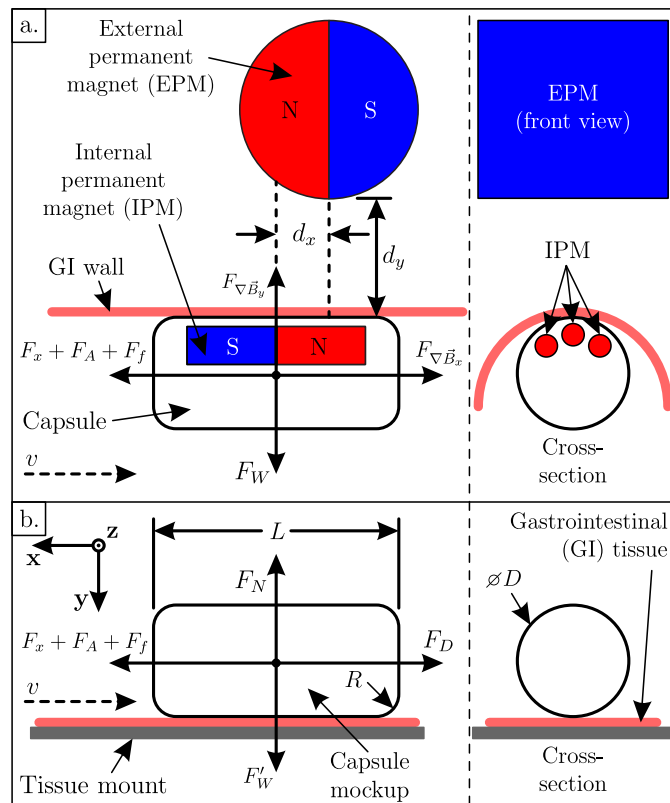
Figure 7.1: A simplified typical setup of a magnetically actuated system (a) using an external permanent magnet, and the free body diagram of the bench top tests (b).

F_D is the drag force due to the magnetic field gradient, $\nabla \vec{B}_x$, F_R is the resistance force on the capsule, and N is a design factor. N must be at least 1 to overcome the weight of the capsule. When N is larger than 1, a normal force (F_N) is introduced into the free body diagram in Fig. 7.1a. The resistance force, F_R, is a summation of forces opposing the drag force, F_D, and includes friction (F_f) and pressure on the front of the capsule due to deformation of the tissue (F_A and F_x). As long as tissue deflection (δ_{max}) is non-zero or $h > 0$, F_x exists and is equal to the integration of the horizontal component of the stress over the contact area. F_A only exists when $(h + \delta_{max}) > R$, and is due to pressure from the tissue on the flat front face of the capsule.

While it is true that F_D and F_M both increase as the operating distance (d_y) decreases, capsule actuation is not improved by minimizing d_y because the normal force (F_N) and therefore tissue deflection also increase, which increases the resistance force (F_R). Using equation (7.3), a typical magnetic system might employ $N = 2$ (see A for the derivation of N), which ensures enough attraction force to lift the capsule, maintain a magnetic link and guarantee reliable capsule locomotion and steering, but not an excessive normal force which can increase F_R and the risk of tissue damage [145].

The general magnetic setup depicted in Fig. 7.1a can be represented as the free body diagram depicted in Fig. 7.1b by assuming equivalent normal forces:

$$F_N = F'_W = F_{\nabla \vec{B}_y} - F_W = (N - 1)F_W \tag{7.5}$$

where F'_W is the adjusted weight of the capsule mockup to simulate the normal force of the magnetic capsule against the inside surface of the bowel.

F_D can be increased by either increasing the size of the EPM or increasing its proximity to the IPM; however, both of these solutions increase F_M, F_N, and therefore F_R (equations (7.4)-(7.5)). To increase the efficiency of the system, F_R needs to be reduced. By decreasing the resistance force, the force needed to move the capsule decreases (for a given operating distance) and F_D can be used to overcome obstacles and maneuver through constrictions. Additionally, the precision of the position and orientation of the capsule increases with a decrease in F_R (for a given operating distance) because the magnetic field gradient needed to drag the capsule is lowered. As long as equation (7.3) remains satisfied, a decrease in F_R can provide for

an increase in operating distance, broadening the application of the system by accommodating patients of different sizes. Decreasing the resistance force could also decrease the necessary size of the EPM, robotic manipulator and overall size of the system. A further advantage of reducing F_R is a decreased risk of tissue damage and potential to spread cancerous or otherwise infected cells. The key to reducing F_R is to identify which capsule design parameters affect the required drag force, and how severely the affecting parameters influence the drag force. The aim of this work is to develop a general model, and as such the magnetic scenario is only one example application. For this reason, some details about the magnetic system have been omitted from this work. A detailed discussion on magnetic theory and locomotion can be found in [38] and [163].

Others have evaluated various capsule parameters in GI tribology studies, but only one [164] to the authors' knowledge which addressed capsule edge radius and only provided 3 data points. Additionally, Kwon *et al.* only presented experimental results [164]. The study presented in this work offers a general model for capsule locomotion system design and an in depth analysis on the effect of edge radius. Others have extensively studied the effect of capsule diameter, length, speed, normal force, and velocity, all of which were studied to assess model validity in this work. In summary, literature reports that resistance force is directly proportional to capsule speed [1], diameter [2], length [3], and normal force [4].

7.3   Theory: Analytical Model Development

Others have developed models for predicting the resistance force on a capsule in the bowel [143, 141, 165, 139, 23], and they all rely on the assumption that the capsule distends the bowel in the radial direction, allowing for a hoop stress analysis. However, this assumption is not valid for a colonoscopy with insufflation or any other procedure where a cylindrical-shaped device is in one-sided contact with tissue (*e.g.*, insufflated GI or abdominal wall). Furthermore, the models rely on the tensile material properties of the bowel, and do not take into account surrounding tissues in the abdomen, which may often be under compression. In particular, [139] developed an analytical model based on a hoop stress analysis, and compared it to finite element model

---

[1] [138, 139, 140, 23, 141, 165, 166, 142, 143]
[2] [167, 164, 138, 139, 140, 23, 143]
[3] [167, 140, 143]
[4] [138, 140, 132]

(FEM) results. [23] developed a similar model, using a hoop stress analysis and tensile properties reported by [167], but included an empirical model for a propulsion force due to electrical stimulus of the bowel. [141, 168] presented a velocity-dependent model, based on a hoop stress analysis, which also accounted for viscous and Coulomb friction. [165] also developed a model for predicting frictional resistance at a constant velocity, using a hyperelastic material model for the bowel. [143] present an interesting model for predicting the resistance force, taking into account the peristaltic wave (modeled as a sin wave) for propulsion of the capsule, but no validation (FEM or experimental) is presented. Some of these models present response as a function of capsule diameter, length, weight and velocity, however, none of the models previously developed present the response as a function of capsule edge radius ([164] only reports experimental data). The model developed here focuses on the application where a capsule is not completely surrounded by the lumen, and thus a hoop stress analysis is not applicable, and is experimentally validated with respect to capsule diameter, length, edge radius, normal force, and velocity.

The goal of the analytical model was to provide an accurate prediction of the force necessary to drag a capsule endoscope across a tissue substrate. In the case of a colonoscopy, where the lumen is insufflated for visualization, the capsule endoscope is not completely surrounded by tissue, but rather is in contact with the tissue on a partial circumference of the capsule. This may also routinely be the case in the stomach, and could even be the case in the esophagus or small bowel if the size of the capsule is small enough. A depiction of this scenario is shown in Fig. 7.2. Even though the thickness of the lumen wall throughout the GI tract is small ($\leq 2\,mm$), the tissue substrate is modeled as a semi-infinite viscoelastic half-space, where the dimensions of the tissue in the $\mathbf{x}$ and $\mathbf{z}$ (out of the page) directions are much larger than the thickness of the tissue (H), and maximum strain of the tissue is less than 10%. This assumption is made based on the fact that the GI wall rests on other viscoelastic organs (*e.g.*, other parts of the bowel, mesentery, spleen, liver and abdominal wall). For the problem presented in this work it is not realistic to model the intestinal wall as a thin layer of tissue, but rather as a layer of tissue lying on other tissues.

The problem setup depicted in Fig. 7.2a consists of a capsule with diameter (D), length (L), weight (F_W), and edge radius (R), traveling at a constant velocity (v) on a viscoelastic semi-infinite half-space. It is important to note that in certain applications, the downward force on the capsule could include more
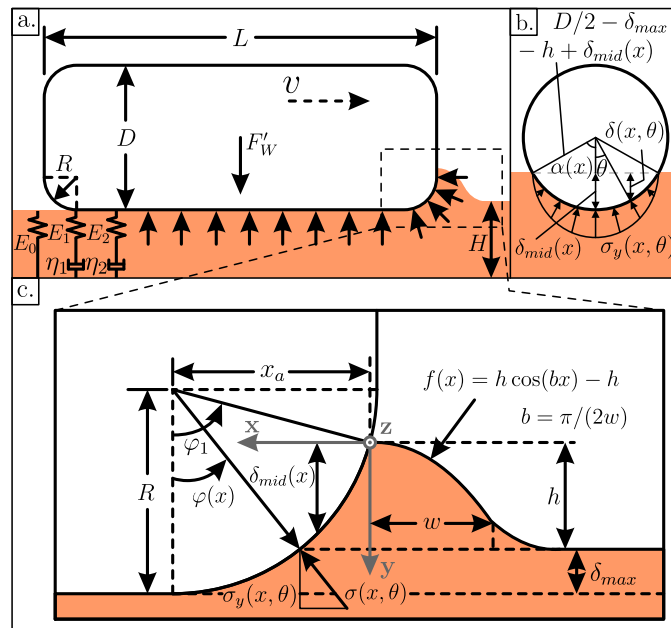
Figure 7.2: A side-view (a) and end-view (b) of a capsule endoscope in contact with a viscoelastic (represented as a 5-element Double Maxwell-arm Wiechert model) tissue substrate. A close-up view (c) of the front of the capsule encountering a tissue fold (approximated as a cos function with amplitude h and quarter period, or width, w).

than just the weight, *e.g.*, during magnetic attraction as described in equations (7.3)-(7.5). To simplify the development of the model, the following assumptions were made:

(1) The capsule body is much stiffer than the tissue and is therefore assumed to be a rigid body.

(2) The capsule's velocity is constant and motion is restricted to 2 degrees (*i.e.*, **x** and **y**, but no rotation).

(3) Once in contact with the capsule, the deformation of the tissue conforms to the shape of the capsule.

(4) The tissue is incompressible (Poisson's ratio $\nu = 0.5$) and isotropic [141, 139].

(5) The tissue behind the trailing edge of the capsule remains momentarily deformed (due to the viscous effect) and therefore does not apply stress on the capsule in the **x**-direction.

(6) The GI wall and underlying tissue substrate is modeled as a semi-infinite half-space.

Furthermore, the inside of the GI tract is not smooth, and the capsule can encounter folds, or bumps, in the tissue. The model takes these into account by implementing a tissue shape function, $f(x)$ (Fig. 7.2c).

$$f(x) = \begin{cases} h - h\cos(bx) & x \le w \\ \\ h & x > w \end{cases} \tag{7.6}$$

$$b = \frac{\pi}{2w} \tag{7.7}$$

where w is defined as the width of the fold or a quarter period of $h\cos(bx)$, and h is defined as the height of the fold or the amplitude of $h\cos(bx)$. h and w are determined experimentally, and the procedure for doing so is described in Section 7.4.1.4.

The tissue, assumed to be a semi-infinite viscoelastic half-space, is modeled using a Double Maxwell-arm Wiechert (DMW) model (5-element), as depicted in Fig. 7.5b (inset). The semi-infinite half-space is defined on $-\infty < x < \infty$, $-\infty < z < \infty$, and $0 < y < H$, where H is the thickness of the GI wall and underlying tissue. The Prony series for a generalized Maxwell-Wiechert viscoelastic model for compressive relaxation is defined in equation (7.8).

$$E(t) = E_0 - \sum_{i=1}^{N} E_i \left[1 - \exp^{\left(-\frac{tE_i}{\eta_i}\right)} \right] \tag{7.8}$$

Under constant velocity conditions and truncating the generalized Maxwell-Wiechert model to the DMW model, the stress in the tissue is defined in equation (7.9),

$$\sigma\left(x\right) = \epsilon\left(x\right)E\left(x\right) = \epsilon\left(x\right)\left[E_0 + E_1\exp^{\left(-\frac{E_1 x}{\eta_1 v}\right)} + E_2\exp^{\left(-\frac{E_2 x}{\eta_2 v}\right)}\right] \tag{7.9}$$

E_0, E_1, and E_2 are the spring constants, while η_1 and η_2 are the viscous coefficients of the dashpots in the DMW model. The parameters for the DMW model are determined using compressive stress-relaxation tests, described in Section 7.4.1.3. It is worth mentioning that the DMW (5-element) model was chosen due to a satisfactory compromise between model complexity and accuracy. The DMW model was shown to have a 35% improved model fit over the commonly used standard linear solid (SLS) viscoelastic model on porcine spleen and liver while maintaining model simplicity [135]. In order to calculate stress, the strain (ϵ) in the tissue needs to be defined.

The strain is formulated assuming that the capsule is constrained to translational (no rotation) motion in 2 dimensions, **x** and **y**. First, the contact angle, φ_1, is defined as

$$\varphi_1 = \begin{cases} 0 & R = 0 \\ \frac{\pi}{2} & R \leq (h + \delta_{max}) \\ \cos^{-1}\left(\frac{R - h - \delta_{max}}{R}\right) & R > (h + \delta_{max}). \end{cases} \tag{7.10}$$

φ_1 has a maximum value of $\pi/2$ which occurs when $(h + \delta_{max}) \geq R$. When $(h + \delta_{max}) > R$, the force on the flat front face of the capsule is accounted for with F_A, described in equations (7.27-7.29). The origin is set at the contact point, and since the purpose of the model is to predict the maximum force required to drag a capsule, it is assumed that the peak height of the tissue fold is also at the origin (Fig. 7.2c). The distance from the origin to the end of the curved capsule front is

$$x_a = R\sin\left(\varphi_1\right), \tag{7.11}$$

where x_a must be less than R, and is zero when the capsule consists of only a cylindrical body with no curved front ($R = 0$). The vertical distance from the origin to the capsule midline can be calculated using equation (7.12).

$$\delta_{mid}\left(x\right) = R - R\cos\left(\varphi\left(x\right)\right) - h - \delta_{max} \tag{7.12}$$

where δ_{max} is the maximum vertical deflection of the capsule into the tissue, and $\varphi(x)$ is a piece-wise function, defined in equation (7.13).

$$\varphi(x) = \begin{cases} \sin^{-1}\left(\frac{x_a - x}{R}\right) & x \leq x_a \\ 0 & x > x_a \\ 0 & R = 0 \end{cases} \tag{7.13}$$

Considering the geometry of the problem from a cross-sectional perspective (Fig. 7.2b), the deflection of the capsule as a function of x and θ is

$$\delta(x, \theta) = \frac{D}{2} - h - \delta_{max} - \cos(\theta)\left(\frac{D}{2} - h - \delta_{max} - \delta_{mid}(x)\right) \tag{7.14}$$

where θ is the angle from $\delta_{mid}(x)$ and is defined on $-\alpha(x) \leq \theta \leq \alpha(x)$, where $\alpha(x)$ is

$$\alpha(x) = \cos^{-1}\left(\frac{\frac{D}{2} - \delta_{max} - h - f(x)}{\frac{D}{2} - \delta_{max} - h - \delta_{mid}(x)}\right). \tag{7.15}$$

Now that the deflection of the capsule in the tissue is defined, strain can be defined as

$$\epsilon(x, \theta) = \frac{f(x) - \delta(x, \theta)}{f(x) + h + H}. \tag{7.16}$$

The stress in the tissue and therefore on the capsule as a function of x and θ is defined in equation (7.17).

$$\sigma(x, \theta) = \epsilon(x, \theta)\left[E_0 + E_1 \exp^{\left(-\frac{E_1 x}{\eta_1 v}\right)} + E_2 \exp^{\left(-\frac{E_2 x}{\eta_2 v}\right)}\right] \tag{7.17}$$

The stress can be broken up into horizontal (σ_x) and vertical (σ_y) components.

$$\sigma_x(x, \theta) = \sigma(x, \theta)\sin(\varphi(x)) \tag{7.18}$$

$$\sigma_y(x, \theta) = \sigma(x, \theta)\cos(\varphi(x))\cos(\theta) \tag{7.19}$$

δ_{max} can be numerically solved for by integrating the stress in the vertical direction and setting it equal to the weight of the capsule. However, the integration limits depend on the geometry of the tissue fold. A constant, x_h, is defined as the **x**-coordinate where the capsule midline equals the height of the tissue fold ($h = \delta_{mid}(x_h)$) and is

$$x_h = x_a - R\sqrt{1 - \left(\frac{R - \delta_{max}}{R}\right)^2}. \tag{7.20}$$

If $w < x_h$ (Fig. 7.3, left), then the integration must be divided into two parts, as described by equation (7.21),

$$F'_W = 2 \int\limits_0^{x_D} \int\limits_0^{\alpha(x)} \sigma_y(x,\theta)\,\rho(x)\,d\theta\,dx + 2 \int\limits_{x_h}^{x_a+L-2R} \int\limits_0^{\alpha(x)} \sigma_y(x,\theta)\,\rho(x)\,d\theta\,dx \tag{7.21}$$

where

$$\rho(x) = \frac{D}{2} - \delta_{max} - h - \delta_{mid}(x) \tag{7.22}$$

$$f(x_D) = \delta_{mid}(x_D) \qquad 0 < x_D < w. \tag{7.23}$$

x_D can be found by numerically solving equation (7.23). Therefore, when $w < x_h$ the numerical approximation of x_D and δ_{max} are simultaneously performed (using lsqnonlin in MATLAB). If $w \geq x_h$ (Fig. 7.3, right), then only one integration is needed, as described in equation (7.24).

$$F'_W = 2 \int\limits_0^{x_a+L-2R} \int\limits_0^{\alpha(x)} \sigma_y(x,\theta)\,\rho(x)\,d\theta\,dx \tag{7.24}$$

The integrands in (7.21) and (7.24) are multiplied by a factor of two and the integration with respect to θ is performed from zero to $\alpha(x)$ due to symmetry about the **x-y** plane.
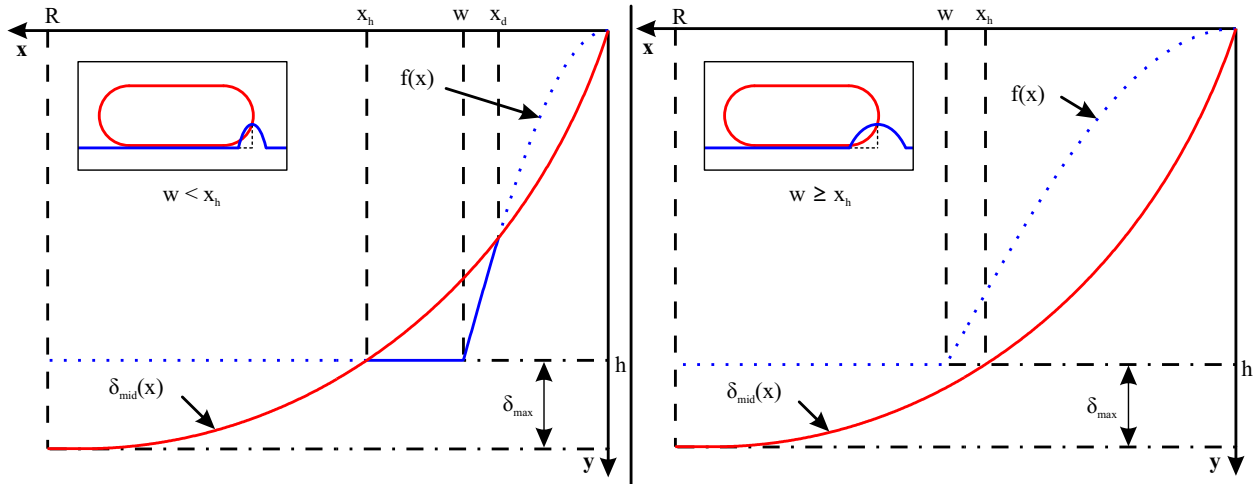
Figure 7.3: Schematics of the two different integration regimes depending on whether $w < x_h$ (left) or $w \geq x_h$ (right).

Now that δ_{max} is known, the force, F_x, due to the stress on the capsule by the tissue can be calculated by integrating the **x**-component of the stress over the surface of the capsule in contact with the tissue. Again, the integration limits are dependent on the geometry of the tissue profile. If $w < x_h$ (Fig. 7.3, left), then

the integration must be divided into two parts, as described by equation (7.25).

$$F_x = 2 \int\limits_0^{x_D} \int\limits_0^{\alpha(x)} \sigma_x\left(x, \theta\right) \rho\left(x\right) d\theta \, dx + 2 \int\limits_{x_h}^{x_a+L-2R} \int\limits_0^{\alpha(x)} \sigma_x\left(x, \theta\right) \rho\left(x\right) d\theta \, dx \tag{7.25}$$

If $w \geq x_h$ (Fig. 7.3, right), then only one integration is needed, as described by equation (7.26).

$$F_x = 2 \int\limits_0^{x_a+L-2R} \int\limits_0^{\alpha(x)} \sigma_x\left(x, \theta\right) \rho\left(x\right) d\theta \, dx \tag{7.26}$$

Similar to equations (7.21) and (7.24), the integrands in (7.25) and (7.26) are multiplied by a factor of two and the integration with respect to θ is performed from zero to $\alpha\left(x\right)$ due to symmetry about the **x-y** plane.

If $\left(\delta_{max} + h\right) > R$ and $R < D/2$, then the tissue will exert an additional horizontal stress on the front face of the capsule, which is not accounted for in equation (7.26). When this is the case, the front face of the capsule is at $x = 0$, so using equation (7.17), the stress on the face becomes

$$\sigma_x = \epsilon_A \left(E_0 + E_1 + E_2\right) \tag{7.27}$$

Then, estimating an average strain of 20%, and calculating the frontal capsule area, A, that is in contact with the tissue, the force, F_A, from the stress on the front of the capsule can be defined as

$$F_A = \epsilon_A \left(E_0 + E_1 + E_2\right) A \tag{7.28}$$

$$A = \left(D/2 - R\right)^2 \cos^{-1}\left(u\right) - \frac{\left(h + \delta_{max} - D/2\right)^2 \sqrt{1 - u^2}}{u} \tag{7.29}$$

where $u = \frac{D/2 - h - \delta_{max}}{D/2 - R}$.

In addition to the force on the capsule due to the stress of the tissue, there is a frictional force. The frictional force on the capsule is calculated using Coulomb's dry friction law. The normal force is calculated by integrating the vertical component of the stress over the contact area of the capsule, similar to equations (7.21) and (7.24), except now δ_{max} is a known parameter. The integration limits depend on the geometry of the tissue. If $w < x_h$ (Fig. 7.3, left), then the integration must be divided into two parts, as described by equation (7.30).

$$F_f = 2\mu\left(v\right) \int\limits_0^{x_D} \int\limits_0^{\alpha(x)} \sigma_y\left(x, \theta\right) \rho\left(x\right) d\theta \, dx + 2\mu\left(v\right) \int\limits_{x_h}^{x_a+L-2R} \int\limits_0^{\alpha(x)} \sigma_y\left(x, \theta\right) \rho\left(x\right) d\theta \, dx \tag{7.30}$$

where $\mu(v)$ is an experimentally determined coefficient of friction. If velocity dependence is not considered, then μ is a constant and can be experimentally determined at the velocity of interest. If velocity dependence is desired, then the coefficient of friction is defined by equation (7.31).

$$\mu(v) = qv^p + c \tag{7.31}$$

where p, q and c are experimentally determined constants. The procedure for determining μ (as well as p, q, and c in the case of velocity dependence) is described in Section 7.4.1.2. If $w \geq x_h$ (Fig. 7.3, right), then only one integration is needed, as described by equation (7.32).

$$F_f = 2\mu(v) \int\limits_0^{x_a+L-2R} \int\limits_0^{\alpha(x)} \sigma_y(x,\theta)\,\rho(x)\,d\theta\,dx \tag{7.32}$$

The total drag force (F_D) is the summation of the **x**-component of the force from the contact stress of the frictional force F_f and the resistance force (F_A when $(\delta_{max} + h) > R$ and $R < D/2$) from the flat front surface of the capsule.

$$F_D = F_x + F_f + F_A \tag{7.33}$$

The output of the model is presented in Section 7.5.1. A pilot study was performed to validate the model with respect to design input parameters (R, L, D, F_W, and v) and the results are presented in Section 7.5.2. An in depth study was then performed to further evaluate the effect of the most significant design parameter (R), and the results are presented in Section 7.5.3. The model was then validated for tissue properties of various regions in the porcine GI tract (esophagus, stomach, small bowel and colon), and the results of this study are presented in Section 7.5.4.

7.4   Materials and Methods

Methodology is divided into two main sections: Model Input (Section 7.4.1), and Tribology Experiments (Section 7.4.2). A review of similar models was presented, and the development of the authors' model was explained in Section 7.3 (Theory: Analytical Model Development). The model requires several input parameters, including tissue morphology parameters, tissue compressive properties, and coefficient of friction. The methods for obtaining these input parameters are detailed in Section 7.4.1 (Model Input). Model

validation consisted of measuring the force required to drag various capsule mockups across porcine tissue samples, and this methodology is described in Section 7.4.2 (Tribology Experiments).

7.4.1 Model Input

The model requires several inputs, which can be divided into two categories, design parameters and tissue parameters. Design parameters are subjective, and as such, need to be defined for the validation experiments. The method for defining design parameters is described in Section 7.4.1.1. Tissue parameters are beyond the control of the designer and are therefore determined experimentally for the model validation. The methods for determining the input parameters are described in the following three sections, Coefficient of Friction (μ) , Compressive Tissue Properties $(E_0, E_1, E_2, \eta_1, \text{ and } \eta_2)$, and Tissue Morphology $(h \text{ and } w)$. All parameters were determined for each tissue sample used during the tribology experiments (described in Section 7.4.2).

7.4.1.1 Design Parameter Definition

Design parameters that needed to be defined for the model validation were capsule diameter (D), length (L), edge radius (R), mockup weight (F_W) and velocity (v). The baseline parameters for the geometry of the capsule $(D, L, \text{ and } R)$ were derived from the PillCam Colon 2 (representing the gold standard for colonoscopy capsule procedures) and are summarized in Table 7.1. The baseline values were then varied in order to obtain a range of experimental values for model validation. In the case of length and diameter, the baseline values were defined as lower bounds and the upper bounds were defined as twice the baseline values. In the case of edge radius, the baseline value was defined as the upper bound, which creates a hemispherical end, and the lower bound was defined as a cylindrical capsule $(R = 0)$. The overall length (L) of the capsule mockups were kept constant while varying R.

The baseline value for velocity was defined as the *in vivo* capsule speed required to obtain a 5 *min* cecal intubation during a colonoscopy, which is slightly less than the average cecal intubation time for an experienced endoscopist [169, 170]. The lower bound velocity was defined as near-zero, and the upper bound was defined as the speed necessary for a 2.5 *min* cecal intubation, a 50% reduction in cecal intubation

Table 7.1: Design parameters for the capsule mockups which were used during the experiments to validate the model.

Parameter	Baseline Value	Boundary Values	Unit
Diameter (D)	11.6	11.6, 23.2	mm
Length (L)	31.5	31.5, 63.0	mm
Edge radius (R)	5.8	0.0, 5.8	mm
Weight (F_W)	63.2	63.2, 100.9	mN
Velocity (v)	5	0.1, 10	mm/s

when compared to experienced endoscopists [169, 170]. Speeds above $10\,mm/s$ (the upper bound of the experimental range) are not practical in a clinical setting because the physician won't have time to thoroughly examine the inside of the GI tract.

The process to determine the baseline value for the capsule mockup weight is more involved. A magnetic system, similar to the one depicted in Fig. 7.1a, is assumed to be the capsule locomotion method. It is assumed that neodymium magnets are used in a PillCam Colon capsule and that they consume 15% of the capsule volume. Using the density of neodymium $\left(\rho_{Nd} = 7500\,kg/m^3\right)$, and the volume $\left(V = 2920\,mm^3\right)$ and mass $(m = 3.22\,g)$ of the PillCam Colon 2, the weight of the magnetic capsule can be calculated using equation (7.34).

$$F_W = (m + 0.15V\rho)\,g \tag{7.34}$$

Then, using equation (7.5) and $N = 2$ (see Appendix A for derivation of N), the adjusted weight (F'_W) of the capsule mockup can be calculated, which is equal to F_W when $N = 2$. From this point forward, the capsule mockup adjusted weight will be referred to as F_W. It is important to stress that the parameters here are based on a typical magnetic capsule locomotion scenario, but can be adjusted to comply with any locomotion scenario.

In an attempt to isolate the effect of each parameter, each was varied independently, while the non-varied parameters were kept at the baseline value.

7.4.1.2   Coefficient of Friction

Drag tests were performed on each tissue sample to measure the coefficient of friction. The experimental setup for the drag tests is depicted in Fig. 7.4c, and consists of a robotic manipulator (Melfa RV-6SL,
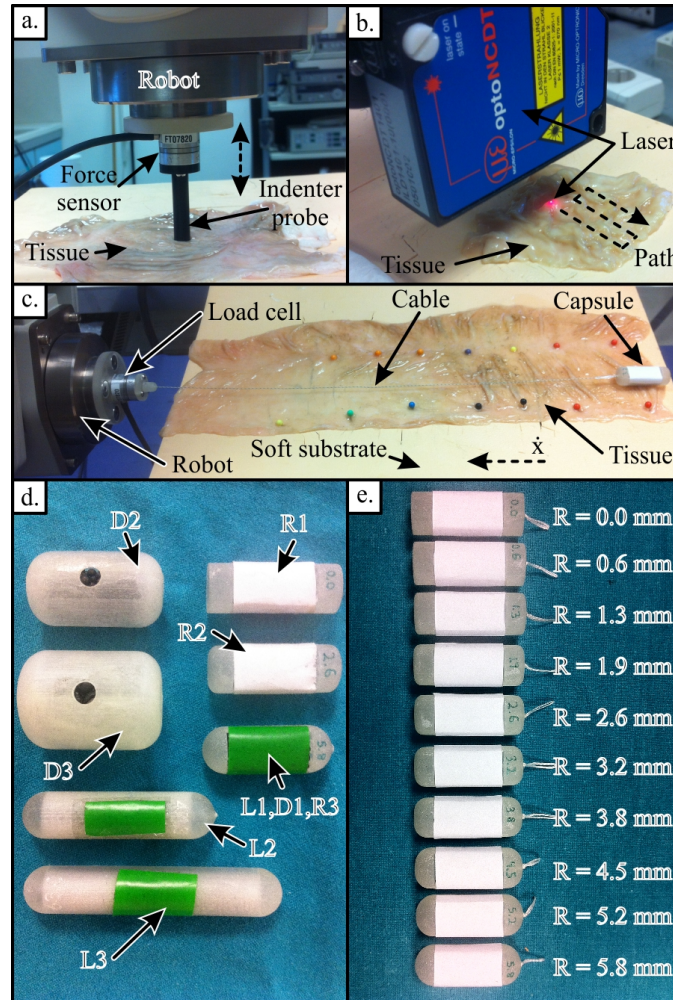
Figure 7.4: Experimental setup for stress-relaxation indentation tests (a), interferometer tests for measuring tissue morphology (b), tribology tests for measuring coefficient of friction and drag force (c), the capsule mockups used in the pilot study (d), and the capsule mockups used in the edge radius study (e).

Mitsubishi, Tokyo, Japan), load cell (Nano17, ATI Industrial Automation, Apex, NC, USA), cable, capsule mockup, tissue sample, and synthetic tissue substrate (Kyoto Kagaku, Japan). The load cell was fixed to the end effector of the robotic manipulator and connected to a computer through a data acquisition system (PCI-6220, National Instruments, Austin, TX, USA). The cable was used to connect the capsule mockup to the load cell. The end effector of the robot was positioned so that the cable was parallel to the substrate when fully extended. In an attempt to eliminate edge effects of the capsule and isolate the capsule-tissue interface, a capsule mockup with a hemispherical ($R = D/2$) end and a smooth section of tissue were used. The tissue sample was placed on the synthetic tissue substrate and the perimeter of the tissue was fixed to the substrate using pins, simulating the *in vivo* mesentery anchoring points. The capsule was pulled across the tissue at a constant velocity ($v = 5\,mm/s$) by the robotic manipulator while force data from the load cell was logged ($10\,kHz$). The drag test was repeated 10 times for each tissue sample.

Typical filtered raw data fo a single trial is shown in Fig. 7.5a. A Savitzky-Golay filter was applied to the raw data to remove spikes and high frequency signal noise. The steady-state data (middle 60%) of each trial was averaged and divided by the weight of the capsule mockup to obtain a single coefficient of friction (μ) value for each trial. The ten trials were averaged to obtain the coefficient of friction for each tissue sample. A low weight ($63.2\,mN$) was used to minimize vertical deflection into the tissue and a capsule with a large radius ($R = 5.8\,mm$ or a hemispherical end) was used to minimize any edge effects in an attempt to only measure frictional force. The measured constant velocity coefficients of friction for each tissue sample used in this study are reported in Table 7.2.

Friction between viscoelastic materials is velocity dependent. In this study, the velocity dependence of the analytical model was validated, so a velocity dependent coefficient of friction was derived for the tissue sample used during this validation. To obtain the velocity dependent coefficient of friction, 10 drag tests were performed over a range of 10 velocities (0.1, 1, 2, 3, 4, 5, 6, 7, 8, 9, and $10\,mm/s$), and the averaged raw data (divided by the normal force) was fit to equation (7.31) using the method of least squares to find q, p, and c. The values of q, p, and c are reported in Table 7.3.
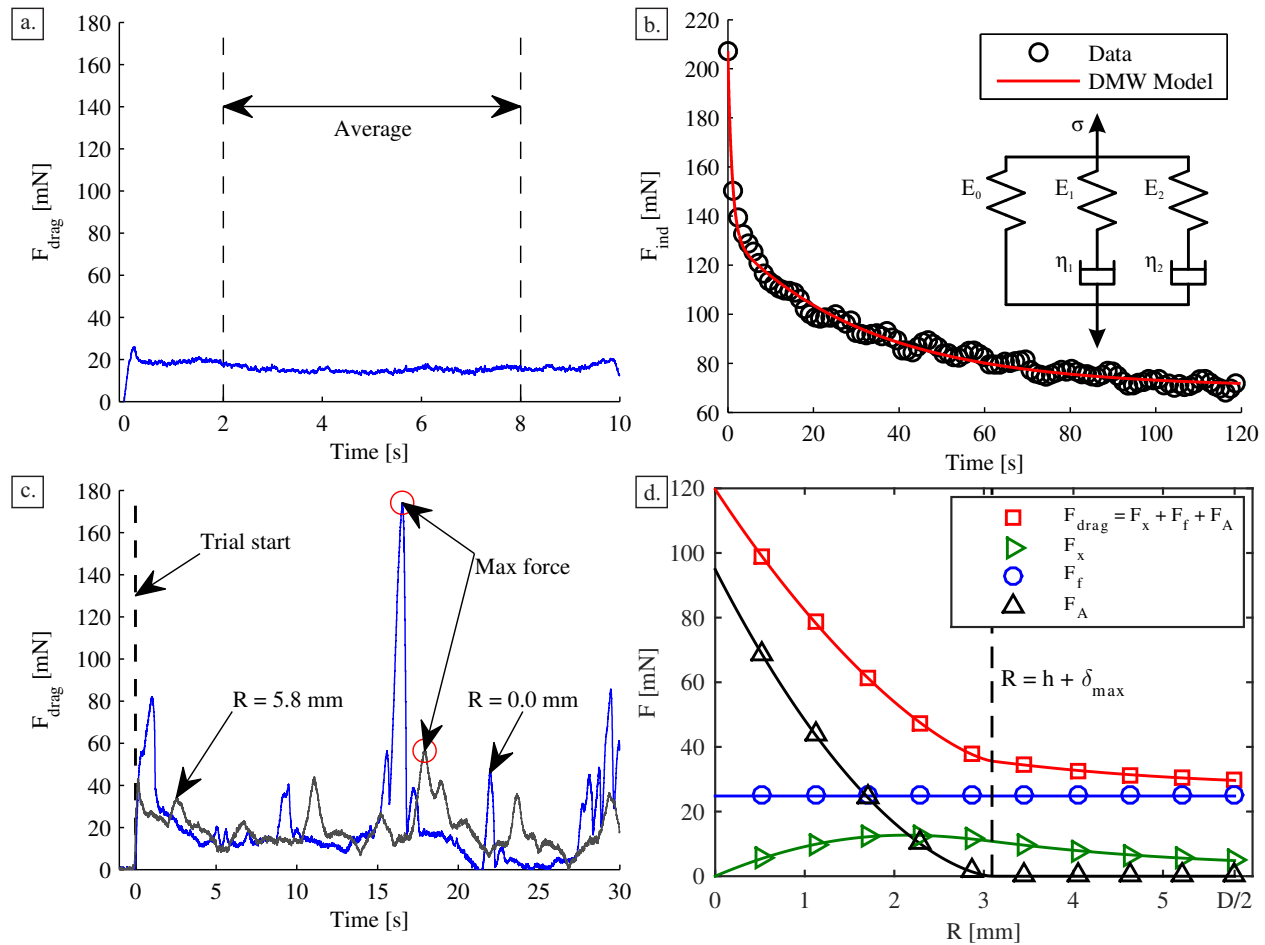
Figure 7.5: (a) Typical raw data for a friction measurement trial after the application of a Savitzky-Golay filter to remove spikes and high-frequency signal noise. The steady-state (middle 60%) force data from each trial is averaged. Ten trials were performed for each tissue sample. The coefficient of friction for a given tissue sample is calculated as the mean of the 10 trials. (b) Typical raw data (points) from indentation tests, the 5-element DMW model (inset) used to represent the tissue mechanics, and the resulting fit to the data (solid line). Five trials were performed for each tissue sample, and the mean for each parameter was used as inputs for the analytical model. Relaxation time (trial duration) and recovery time (time between trials) were 120 s. (c) Typical raw data for drag force tests after the application of a Savitzky-Golay filter to remove spikes and high-frequency signal noise. The maximum force from each trial is found and averaged across all trials for each tissue/capsule combination. A typical trial for a cylindrical capsule ($R = 0.0\ mm$, blue curve) produces a larger drag force than a capsule with hemispherical ends ($R = 5.8\ mm$, gray curve). (d) A typical analytical model output and individual components of the drag force (F_D). Force is plotted as a function of edge radius (R) at a constant capsule length ($L = 31.5\ mm$), diameter ($D = 11.6\ mm$), weight ($F_W = 63.2\ mN$), velocity ($v = 5\ mm/s$) and tissue profile ($h = 2.40\ mm$ and $w = 2.45\ mm$).

7.4.1.3   Compressive Tissue Properties

The compressive properties of the tissue were determined by performing compressive stress-relaxation tests on the tissue and underlying soft substrate (Kyoto Kagaku, Japan). It is important to note that the values reported in this work are lumped properties, representing the combined response of the tissue and underlying substrate, and should not be interpreted as compressive properties of the GI wall. This method was chosen to closely match the model assumption that the capsule is traveling through a GI tract, which rests against other tissue. Furthermore, these parameters represent reliable input to validate the model.

The experimental setup for the stress-relaxation tests is shown in Fig. 7.4a, and consists of an indenter probe ($7\,mm$ radius), a robotic manipulator (Melfa RV-6SL, Mitsubishi, Tokyo, Japan), load cell (Nano17, ATI Industrial Automation, Apex, NC, USA), cable, capsule mockup, tissue sample, and synthetic tissue substrate (Kyoto Kagaku, Japan). The load cell was fixed to the end effector of the robot and the probe was fixed to the load cell. The GI tissue sample was fixed to the synthetic tissue substrate using pins, and the indenter probe was oriented so that it was centered on and perpendicular to a relatively smooth section of tissue. The vertical position of the probe was calibrated to the surface of the tissue, and then five consecutive indentation tests were performed. The relaxation (trial duration) and recovery (between trial) times were 120 s. Indentation depths (measured from tissue surface to probe end depth) varied between $0.7\,mm$ and $2\,mm$ in an attempt to induce a maximum load cell force of $200\,mN$ (the approximate expected maximum *in vivo* force on a capsule based on preliminary measurements). Force data from the load cell were collected ($1\,kHz$) during the trials for post-processing.

Typical raw data for a single trial is shown in Fig. 7.5b (data points). A 5-element DMW model (Fig. 7.5b, inset) was used to model the compressive properties of the tissue. The stress-strain relationship for the DMW model is described by equation 7.9. The parameters $E_0, E_1, E_2, \eta_1,$ and η_2 were determined for each trial using the procedure described in [135]. The five trials are then averaged to produce a single value for each tissue sample.

7.4.1.4   Tissue Morphology

The tissue shape function used in the model is described by equations (7.6)-(7.7), and requires two experimentally determined inputs, h and w. h is the height of a tissue fold, or the amplitude of the *cos* function in equation (7.6) (Fig. 7.2c), while w is a quarter period of the *cos* function in equation (7.6) (Fig. 7.2c).

To determine h and w, an interferometer (optoNCDT 1401-10, Micro-Epsilon, Ortenburg, Germany) was used, as shown in Fig. 7.4b. The interferometer was attached to the end effector of the robotic arm (Melfa RV-6SL, Mitsubishi, Tokyo, Japan) and oriented above the tissue at a distance within the measurement range of the interferometer (between 20 and 30 mm). The end effector was then programmed to perform a zig-zag scanning pattern above the surface of the tissue used during the drag tests (approximately 100 mm long and 25 mm wide). The long axis of the scan was aligned with the capsule's direction of travel during the drag tests. The location of the robot in the x-y plane was recorded (500 μm resolution), while interferometer data in the z-direction was recorded (5 μm resolution) for post-processing.

Robot position and interferometer data were combined in a post-processing algorithm to produce a surface plot. Interpolation between point was performed to obtain a 3-dimensional (3D) representation of the tissue surface Fig. 7.6a. The surface map was then broken into slices (1 slice every 500 μm), as in Fig. 7.6b, and a peak finding algorithm was used to find the height and width of each local maximum. The heights and widths were then averaged across the entire surface map to obtain the average fold height (h) and width (w).
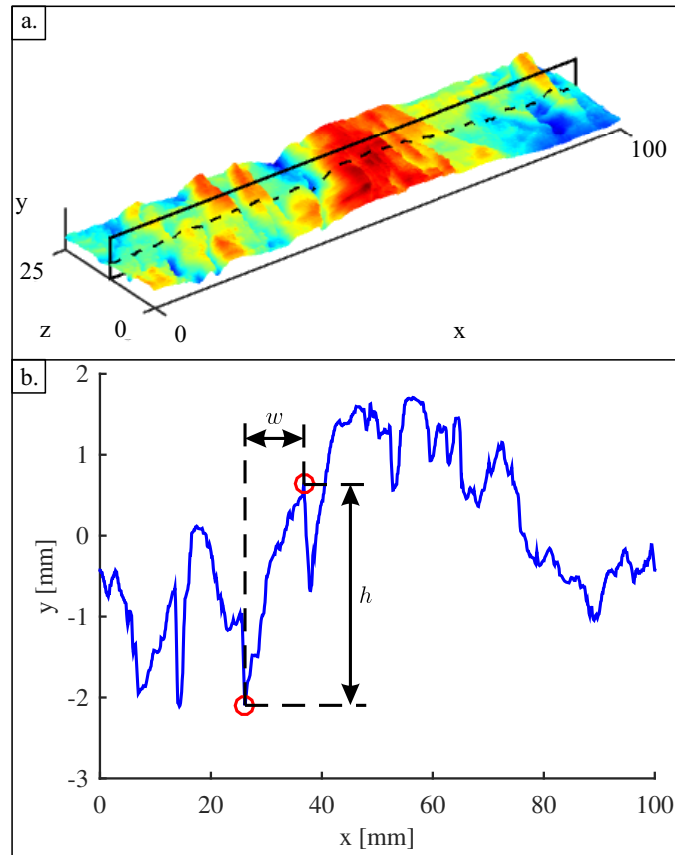
Figure 7.6: A typical 3-dimensional (3D) map of the tissue surface (a), and the cross-sectional profile of a single slice of the surface map in the direction of capsule travel (b).

Table 7.2: Measured mean material properties (model inputs) for each tissue sample used throughout the study. The prefix "P-" indicates that the tissue sample was used for the pilot study. All capsules in Fig. 7.4d were used on "P-" tissue samples. The prefix "v-" indicates that the tissue sample was used for the velocity dependence validation. Capsule R3 in Fig. 7.4d with $F_W = 63.2\ mN$ was used on the "v-" tissue sample. The prefix "ER-" indicates that the tissue sample was used for the in-depth edge radius study. All capsules in Fig. 7.4e were used on "ER-" tissue samples. No prefix indicates that the tissue was used for the GI region validation. Tissue region abbreviations are "ESO", "S", "SB", and "C" for porcine esophagus, stomach, small bowel, and colon, respectively. Capsule R3 in Fig. 7.4d with $F_W = 63.2\ mN$ was used on all "ESO", "S", "SB", and "C" tissue samples. Three porcine colon tissue samples were used for both the pilot study and edge radius study. Three porcine tissue samples from each region of the GI tract were used for the GI region validation study. One porcine tissue sample was used for the velocity dependence validation. q, p, and c (Table 7.3) are determined using velocity dependent drag force data and the method of least squares.

Sample ID	Property							
	μ	E_0 (kPa)	E_1 (kPa)	E_2 (kPa)	η_1 (kPa·s)	η_2 (kPa·s)	h (mm)	w (mm)
P-C1	0.2005	4.837	6.177	4.044	4.337	120.6	2.930	3.009
P-C2	0.6198	4.993	5.525	2.996	4.579	98.34	3.383	2.732
P-C3	0.1022	3.847	3.655	2.000	3.364	71.20	2.339	2.965
v-C1	$qv^p + c$	16.61	8.606	4.475	5.218	93.31	0.053	2.957
ER-C1	0.2915	26.96	16.55	7.877	11.30	228.2	2.165	3.860
ER-C2	0.3496	14.41	7.916	4.274	6.140	135.7	3.078	5.264
ER-C3	0.1839	12.96	13.08	8.783	13.28	313.2	0.013	3.952
ESO1	0.7818	14.24	7.497	4.098	5.366	108.1	0.7774	2.755
ESO2	0.7289	6.218	4.442	1.782	3.684	55.47	1.663	1.272
ESO3	0.7923	5.027	3.929	1.922	2.881	58.63	2.916	1.280
S1	0.3427	6.794	5.929	3.816	4.859	124.3	1.892	2.186
S2	0.3276	16.25	8.623	4.158	6.187	121.4	3.132	1.969
S3	0.3709	8.630	5.746	3.073	4.913	105.8	1.838	3.163
SB1	0.2017	2.668	8.552	6.982	7.103	$7.84 \cdot 10^5$	0.8190	1.734
SB2	0.3248	11.52	8.642	6.744	7.259	243.2	1.074	1.496
SB3	0.3145	3.674	6.611	3.994	5.132	$9.28 \cdot 10^5$	0.8067	2.688
C1	0.3037	9.562	8.186	4.777	5.455	160.3	2.270	3.566
C2	0.3191	16.29	12.65	7.700	8.854	251.5	3.104	2.377
C3	0.3083	15.68	9.932	5.358	7.123	179.9	1.246	3.360

Table 7.3: Measured parameters for the velocity dependent coefficient of friction, $\mu(v) = qv^p + c$. One porcine colon (v-C1) tissue sample was used to validate the velocity dependence in the model.

Sample ID	Parameter		
	q	p	c
v-C1	0.8766	-0.05506	-0.9221

7.4.2 Tribology Experiments

Tribology experiments were performed for the Pilot Study, the Edge Radius Evaluation, and the GI Tract Region study. The methodology for the tribology experiments is similar to the process described for the coefficient of friction measurements in Section 7.4.1, but is repeated here for completeness. All tribology experiments were performed using a synthetic tissue substrate (Kyoto Kagaku, Japan), a tissue sample, a capsule mockup, a 6 DoF robotic arm (Melfa RV-6SL, Mitsubishi, Tokyo, Japan), and a load cell (Nano17, ATI Industrial Automation, Apex, NC, USA). For all tests, the load cell was attached to the end effector of the robotic arm, the tissue sample was placed on the synthetic tissue substrate, and the capsule mockup was attached to the load cell with a light-weight cable. A single drag test consisted of pulling a capsule across the tissue at a set speed while measuring the drag force (10 kHz). All of the capsule mockups were fabricated using the same 3D printer (ProJet HD3000, 3D Systems, Rock Hill, SC, USA) and material (VisiJet EX200, 3D Systems, Rock Hill, SC, USA). All capsules were sanded using 200 grit sand paper to obtain a smooth finish. Typical trials of a cylindrical capsule and a capsule with hemispherical ends are shown in Fig. 7.5c.

7.4.2.1 Pilot Study

A pilot study was carried out to validate the model response with respect to all of the inputs. Controllable inputs were varied by changing design parameters (R, D, L, F_W) and testing conditions (v) while uncontrollable inputs were varied by using multiple porcine colon tissue samples (P-C1, P-C2, P-C3 in Table 7.2 and v-C1 in Table 7.3).

Controllable design parameters for the pilot study were varied independently with the capsules pictured in Fig. 7.4d using values from Table 7.1. Specifically, R was varied 3 times ($R1 = 0.0\,mm$, $R2 = 2.9\,mm$, $R3 = 5.8\,mm$), while D, L, and F_W were kept at their baseline values ($D = 11.6\,mm$,

$L = 31.5\,mm$, and $F_W = 63.2\,mN$). Similarly, D was varied 3 times ($D1 = 11.6\,mm$, $D2 = 17.4\,mm$, $D3 = 23.2\,mm$), while R, L, and F_W were kept at their baseline values ($R = 5.8\,mm$, $L = 31.5\,mm$, and $F_W = 63.2\,mN$). Then L was varied 3 times ($L1 = 31.5\,mm$, $L2 = 47.3\,mm$, $L3 = 63.0\,mm$), while R, D, and F_W were kept at their baseline values ($R = 5.8\,mm$, $D = 11.6\,mm$, and $F_W = 63.2\,mN$). Lastly, F_W was varied 3 times ($F_{W1} = 63.2\,mN$, $F_{W2} = 82.1\,mN$, $F_{W3} = 100.94\,mN$), while R, D, and L were kept at their baseline values ($R = 5.8\,mm$, $D = 11.6\,mm$, and $L = 31.5\,mm$). F_{W1}, F_{W2}, and F_{W3} were created by adding weight to capsule "L1,D1,R3" in Fig. 7.4d. Ten drag tests at a velocity of 5 mm/s (the speed necessary for a 5 min cecal intubation, which is the average time [169, 170] for experienced endoscopists) were performed for each parameter combination on three separate porcine colon samples (P-C1, P-C2, and P-C3 in Table 7.2). The maximum force from all 10 drag tests were averaged to obtain a single value for each tissue sample and parameter combination (9 parameter combinations and 3 tissue samples for a total of 27 values).

The velocity dependence of the model was validated using a single capsule with baseline design parameter values ($R = 5.8\,mm$, $D = 11.6\,mm$, $L = 31.5\,mm$, and $F_W = 63.2\,mN$) on one sample of porcine colon tissue (v-C1). A velocity-dependent coefficient of friction was determined using the procedure described in Section 7.4.1.2, and then 10 drag tests were performed at 10 different velocities (0.1, 1, 2, 3, 4, 5, 6, 7, 8, 9, and 10 mm/s) for a total of 100 trials. The maximum force from all 10 drag tests at each velocity were averaged to obtain a single value for each velocity (10 values).

7.4.2.2   Edge Radius Evaluation

It was determined that the most influential parameter on drag force magnitude was edge radius R (see Section 7.5.2), so an in depth study of that parameter was performed. Ten capsules (pictured in Fig. 7.4e) were fabricated with varying edge radius ($R = 0.0\,mm$ to $R = 5.8\,mm$) and baseline values for D, L, and F_W. Ten drag tests were performed at each edge radius on three separate porcine colon tissue samples (ER-C1, ER-C2, and ER-C3 in Table 7.2). The maximum force from all 10 drag tests at each edge radius and tissue sample were averaged to obtain a single value for each edge radius and tissue sample (10 edge radii and 3 tissue samples for a total of 30 values).

Three porcine colon samples were used for the edge radius study. An attempt was made to choose two relatively rough tissue samples ($h_{ER\text{-}C1} = 2.165\ mm$ and $h_{ER\text{-}C2} = 3.078\ mm$), and one relatively smooth tissue sample ($h_{ER\text{-}C3} = 0.013\ mm$) to further confirm the validity of the analytical model.

7.4.2.3   GI Tract Region

To evaluate the validity of the model throughout all regions of the GI tract, drag tests were performed on 3 tissue samples from porcine esophagus (ESO1, ESO2, and ESO3 in Table 7.2), stomach (S1, S2, and S3 in Table 7.2), small bowel (SB1, SB2, and SB3 in Table 7.2) and colon (C1, C2, and C3 in Table 7.2). Ten drag tests were performed on each tissue sample using a capsule with baseline design parameters ($R = 5.8\ mm$, $D = 11.6\ mm$, $L = 31.5\ mm$, and $F_W = 63.2\ mN$). The maximum force from all 10 trials were averaged to obtain a single value for each tissue sample (12 values total).

7.5   Results and Discussion

The results of the study are divided into 4 sections: in Section 7.5.1, the general response of the model with respect to all of the inputs is presented; in Section 7.5.2, the validation of the model with respect to R, D, L, F_W, and v is presented from the results of the pilot study; in Section 7.5.3, the in depth evaluation of edge radius is presented; Section 7.5.4 presents the results of the GI tract region study.

7.5.1   Model Output

Given a set of inputs, the analytical model described in Section 7.3 outputs a drag force. To exemplify the effect that each input parameter had on the output of the model, each input was varied according to the "Range" column in Table 7.4 while holding all other inputs at the baseline value. Compressive material properties (E_0, E_1, E_2, η_1, and η_2) were not varied, but were set equal to the values in Table 7.4, which are a mean of the material properties measured in all of the tissue samples used throughout the study. The response of the model is presented in Figs. 7.5d and 7.7-7.10 without any experimental data. The separate components and typical response of the entire model is shown in Fig. 7.5d. The model response in terms of drag force (F_D) is shown in Figs. 7.7-7.8, while the model response in terms of maximum vertical deflection

of the capsule (δ_{max}) is shown in Figs. 7.9-7.10, which is useful to look at when dissecting the underlying physics of the problem.

Table 7.4: Input parameters used for Figs. 7.5d and 7.7-7.10. Capsule edge radius, length, diameter, weight, velocity, tissue fold height and tissue fold width were independently varied to exemplify their effect on the model output. Compressive tissue properties were not varied, and were defined at typical values observed in the tissue samples used throughout the study.

Parameter	Baseline Value	Range	Unit
E_0	10.6	–	kPa
E_1	8.01	–	kPa
E_2	4.68	–	kPa
η_1	6.16	–	kPa·s
η_2	145	–	kPa·s
μ	0.393	–	–
Length (L)	31.5	[31.5, 63]	mm
Diameter (D)	11.6	[11.6, 23.2]	mm
Edge Radius (R)	5.80	[0, 5.8]	mm
Weight (F_W)	63.2	[60, 105]	mN
Velocity (v)	5.00	[0, 10]	mm/s
Max fold height (h)	2.40	[0, 4.8]	mm
Max fold spacing (w)	2.45	[0.1, 6]	mm

The first step to analyzing the model output is to understand the contributions of the individual components of the drag force, as described in equation (7.33). There are three components to the model output as defined in equation (7.4); the horizontal component of the stress induced on the capsule by the tissue integrated over the contact area (F_x), the frictional force (F_f), and the horizontal force induced by contact between tissue and the vertical leading end of the capsule (F_A). The total model output along with the individual components is presented in Fig. 7.5d. The model output in Fig. 7.5d is shown as a function of edge radius (R) at a constant capsule length ($L = 31.5\ mm$), diameter ($D = 11.6\ mm$), weight ($63.2\ mN$), velocity ($5\ mm/s$) and tissue profile ($2.40\ mm$ and $w = 2.45\ mm$). The most obvious and intuitive source of resistance is frictional force (F_f), which is constant in Fig. 7.5d because capsule weight and velocity are constant. It is important to note that F_x is nonzero when there is an edge radius because F_x only comes from the curved surface of the edge radius. It is also important to note that, in general, the largest source of resistance force is F_A, which is only present when $R > h + \delta_{max}$. When $R < h + \delta_{max}$, the tissue is only in contact with the curved surface of the edge radius, and therefore only F_f and F_x are present. However, when $R > h + \delta_{max}$, the tissue is also in contact with the vertical leading capsule end, which results in a

nonzero F_A.

Drag force (F_D) as a function of edge radius (R) and tissue fold height (h) at a constant capsule length ($L = 31.5 \ mm$), diameter ($D = 11.6 \ mm$), weight ($63.2 \ mN$), velocity ($v = 5 \ mm/s$) and tissue fold width ($w = 2.45 \ mm$) is shown in Fig. 7.7a. Drag force is inversely proportional to edge radius and directly proportional to tissue fold height regardless of edge radius magnitude. As the tissue fold height increases, the resistance that the capsule encounters will also increase. Similarly, as the edge radius decreases, or becomes more abrupt, the leading edge of the capsule will engage with the tissue more, resulting in an increase in resistance. When the fold height is larger than the edge radius ($h + \delta_{max} > R$), the drag force drastically increases. On the contrary, when the fold height is less than the edge radius ($h + \delta_{max} < R$), the drag force becomes less dependent on edge radius. For example, when $h = 2.40 \ mm$ (Fig. 7.7a, red line or square data points), drag force is at its highest when $R = 0 \ mm$. Drag force decreases significantly with increasing radius, but levels off once $R > h + \delta_{max} = 3.10$. This follows intuition because when the fold height is larger than the edge radius and the edge radius is less than the overall radius of the capsule ($R < D/2$), a portion of the vertical leading capsule end will be in contact with the tissue. This type of contact, with forward motion, produces the largest amount of horizontal resistance force (F_A), when compared to the horizontal resistance force created by the curved surface of the edge radius (F_x). Similarly, when the fold height is less than the edge radius, no tissue is in contact with the vertical leading capsule end, so horizontal resistance force from this interface is absent.

Drag force as a function of edge radius and tissue fold width (w) at a constant capsule length ($L = 31.5 \ mm$), diameter ($D = 11.6 \ mm$), weight ($63.2 \ mN$), velocity ($v = 5 \ mm/s$) and tissue fold height ($h = 2.40 \ mm$) is shown in Fig. 7.7b. Drag force is inversely proportional to tissue fold width when the edge radius is small ($R < h$), but directly proportional to tissue fold width when the edge radius is large ($R > h + \delta_{max}$). This is an interesting phenomenon, but can be explained by assessing the effective slope of the tissue fold along with the geometry of the capsule-tissue interface. At a given tissue fold height ($h = 2.40 \ mm$ in Fig. 7.7b), the effective slope of the fold increases with decreasing tissue fold width (w). At small radii, the capsule will fully interact with the tissue fold (as in Fig. 7.3, right), and the magnitude of the drag force will be dependent on the apparent steepness of the fold. In other words, slope of the tissue fold and therefore
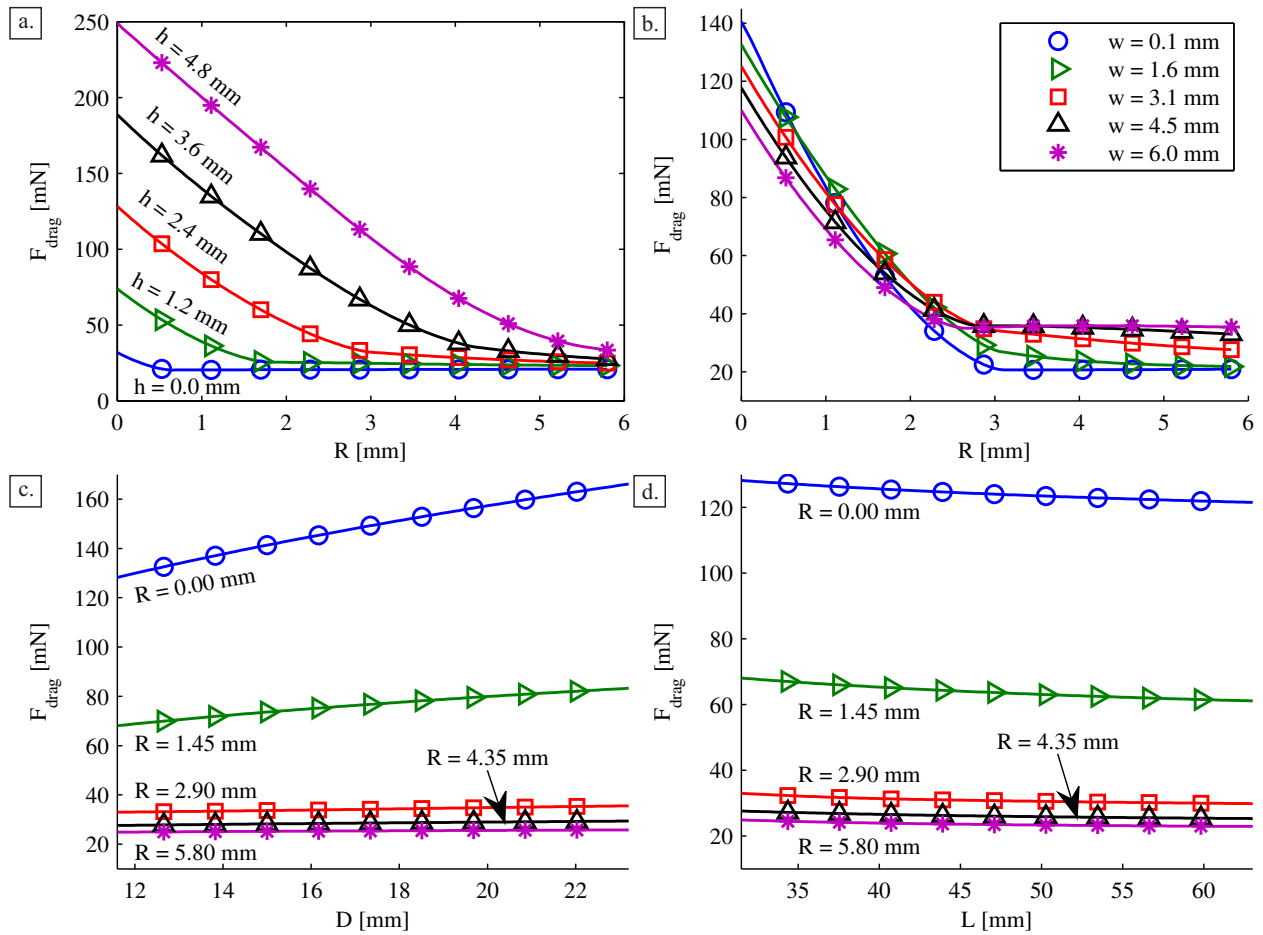
Figure 7.7: Analytical model solution for F_D as a function of R and h (a), R and w (b), D and R (c), and L and R (d). Non-varied parameters are held at the "baseline value", as defined in Table 7.4.

drag force increase with decreasing w, which is apparent at small R in Fig. 7.7b. On the other hand, for large radii, the drag force is influenced less by the tissue fold slope due to the force distribution over the curved surface of the edge radius. In this case, the drag force is dependent on the amount of contact that capsule has with the tissue. As the tissue fold width decreases, the frontal contact area also decreases, and therefore drag force decreases. These two scenarios are depicted in Fig. 7.3. For a large radius, there will be less frontal contact with decreasing w (Fig. 7.3, left), and more frontal contact with increasing w (Fig. 7.3, right). It is apparent that drag force decreases with decreasing w in Fig. 7.7b for large radii.

Drag force as a function of capsule diameter and edge radius at a constant capsule length ($L = 31.5$ mm), weight (63.2 mN), velocity ($v = 5$ mm/s) and with a constant tissue profile ($h = 2.40$ mm and $w = 2.45$ mm) is shown in Fig. 7.7c. Drag force is directly proportional to capsule diameter regardless of edge radius magnitude, but capsule diameter has a significantly larger effect (*i.e.*, steeper slope in Fig. 7.7c) at smaller edge radii ($R < h + \delta_{max}$). There are two major effects to consider when the diameter of the capsule is increased. First, the contact surface area and therefore distribution of the capsule weight increase. Distributing the weight of the capsule over a larger area decreases the vertical deflection of the capsule into the tissue (as evidenced by Fig. 7.9c). With less vertical deflection, there is less frontal contact, and therefore less horizontal resistance. On the other hand, increasing capsule diameter also increases the cross-sectional area of the capsule, which increases resistance force. These two effects can be used to explain Fig. 7.7c. In general, drag force increases with increasing diameter, which suggests that the second phenomenon trumps the first phenomenon. In other words, the increase in cross-sectional area of the capsule has more of an effect than the decrease in vertical deflection and therefore frontal contact area of the capsule. This is further confirmed by studying the slopes of the lines in Fig. 7.7c as a function of edge radius. At large radii ($R > h + \delta_{max}$), increasing D and therefore cross-sectional area has little effect on drag force because the horizontal resistance force is distributed over the curved surface of the edge radius. However, for small radii ($R < h + \delta_{max}$) the vertical leading end of the capsule will be in contact with the tissue, which is the largest source (F_A) of horizontal resistance, so increasing D and therefore cross-sectional area will have more of an effect on the drag force necessary to overcome the resistance force. This is evidenced by increasing slope as edge radius decreases when $R < h + \delta_{max}$ in Fig. 7.7c.

Drag force as a function of capsule length and edge radius at a constant capsule diameter ($D = 11.6$ mm), weight ($63.2\ mN$), velocity ($v = 5\ mm/s$) and with a constant tissue profile ($h = 2.40\ mm$ and $w = 2.45\ mm$) is shown in Fig. 7.7d. Drag force is inversely proportional to capsule length regardless of edge radius magnitude. Additionally, this effect is larger (*i.e.*, steeper slope in Fig. 7.7d) at small edge radii ($R < h + \delta_{max}$). Contrary to increasing diameter, only one phenomenon is occurring when length is varied. As length increases, the contact surface area and therefore distribution of the capsule weight increase. Distributing the capsule weight over a larger area decreases the vertical deflection of the capsule into the tissue, which in turn decreases the resistance force on the front of the capsule. Therefore, as length increases, the resistance force and drag force decrease, regardless of edge radius magnitude. However, this effect is slightly more prevalent at small radii ($R < h + \delta_{max}$) due to the fact that the vertical leading capsule end will be in contact with the tissue, which is the largest source (F_A) of horizontal resistance. As such, when length is increased, the vertical deflection is decreased, the frontal contact area is decreased, and therefore the horizontal force (F_A) and drag forces are decreased. This phenomenon is evidenced by increasing slope as edge radius decreases when $R < h + \delta_{max}$ in Fig. 7.7d.

Drag force as a function capsule weight (or normal force) and edge radius at a constant capsule length ($L = 31.5\ mm$), diameter ($D = 11.6\ mm$), velocity ($v = 5\ mm$) and with a constant tissue profile ($h = 2.40$ mm and $w = 2.45\ mm$) is shown in Fig. 7.8a. Drag force is directly proportional to normal force regardless of edge radius. This follows the Coulomb dry friction law, $F_f = \mu F_W$. Although it is hard to discern in Fig. 7.8a, the slopes of the lines are slightly steeper for $R < h + \delta_{max}$. As weight is increased, vertical deflection into the tissue is also increased, which increases the resistance force. This effect is magnified for $R < h + \delta_{max}$ due to the interaction of tissue on the vertical leading end of the capsule.

Drag force as a function of capsule velocity and edge radius at a constant capsule length ($L = 31.5$ mm), diameter ($D = 11.6\ mm$), weight ($F_W = 63.2\ mN$), and with a constant tissue profile ($h = 2.40\ mm$ and $w = 2.45\ mm$) is shown in Fig. 7.8b. Drag force is inversely proportional to velocity at larger radii ($R > h + \delta_{max}$), but is not affected by velocity at small radii ($R < h + \delta_{max}$). There is a larger effect on drag force at low velocities ($v < 1\ mm/s$), and the effect is magnified as edge radius approaches zero. Drag force as a function of velocity and tissue fold height at a constant capsule edge radius ($R = 0$), length ($L = 31.5$

Figure 7.8: Analytical model solution for F_D as a function of F_W and R (a), v and R (b), v and h (c), and v and w (d). Non-varied parameters are held at the "baseline value", as defined in Table 7.4, except for edge radius in (c) and (d), which are defined as $R = 0$.

mm), diameter ($D = 11.6$ mm), weight ($F_W = 63.2$ mN), and tissue fold width ($w = 2.45$ mm) is shown in Fig. 7.8c. Drag force is inversely proportional to velocity regardless of fold height, but velocity has a larger effect on drag force at low values ($v < 1$ mm/s). Drag force as a function of velocity and tissue fold width at 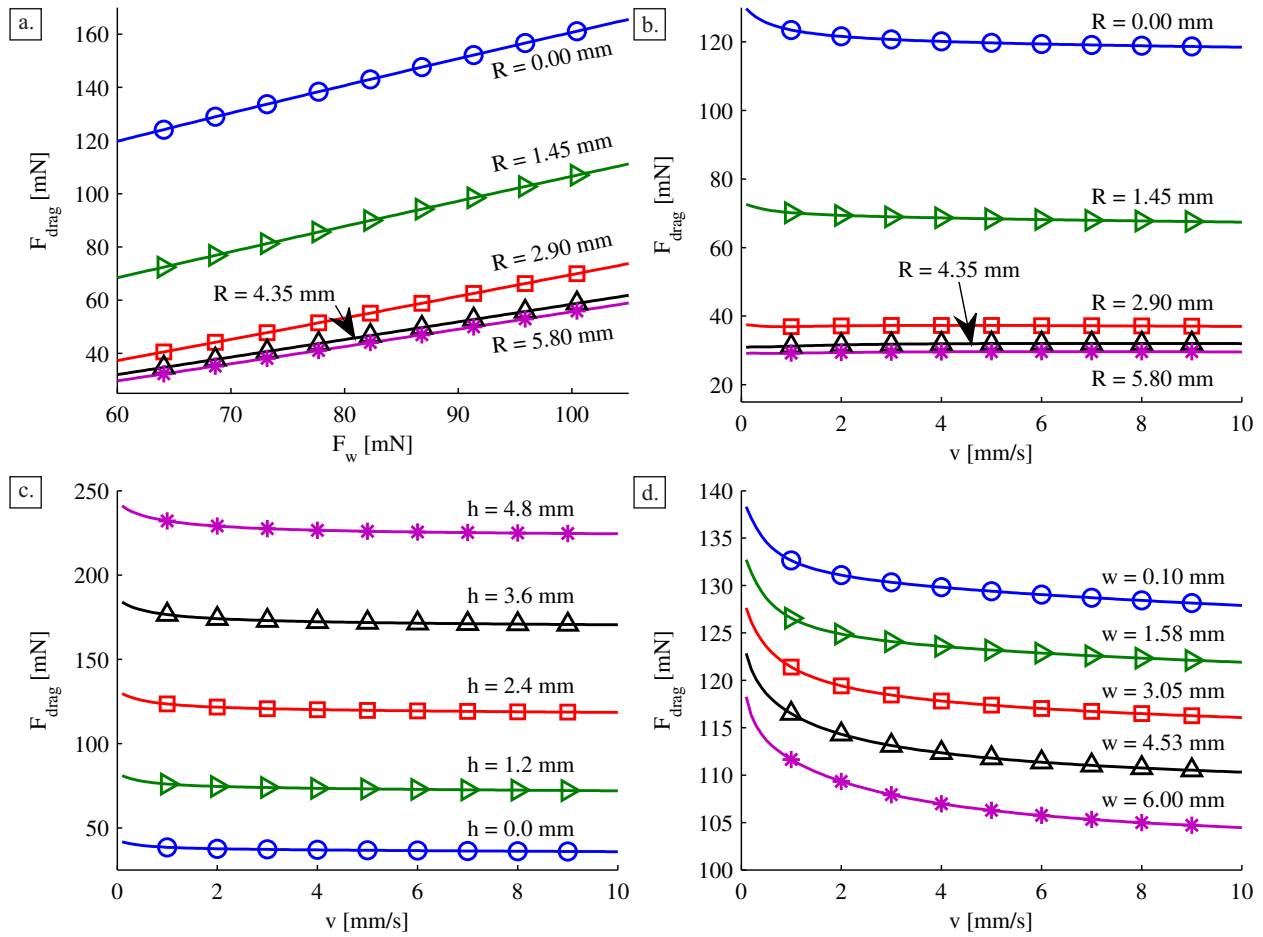a constant capsule edge radius ($R = 0$), length ($L = 31.5$ mm), diameter ($D = 11.6$ mm), weight ($F_W = 63.2$ mN), and tissue fold height ($h = 2.40$ mm) is shown in Fig. 7.8d. Drag force is inversely proportional to velocity regardless of fold width, but velocity has a larger effect on drag force at low values ($v < 2$ mm/s). The effect of velocity can be attributed to viscoelastic nature of the tissue substrate. The stress in the tissue is strain-rate dependent and therefore dependent on the velocity that the force is applied. It is also important to note that only dynamic friction is being considered as the capsule is assumed to be moving at a constant velocity.

It is also interesting to look at the maximum vertical deflection of the capsule into the tissue (δ_{max}) to gain insight about the underlying physics of the contact problem. δ_{max} as a function of edge radius and tissue fold height at a constant capsule length ($L = 31.5$ mm), diameter ($D = 11.6$ mm), weight ($F_W = 63.2$ mN), velocity ($v = 5$ mm/s) and tissue fold width ($w = 2.45$ mm) is shown in Fig. 7.9a. δ_{max} is directly proportional to edge radius regardless of tissue fold height, however, edge radius has a larger effect (*i.e.*, steeper slope) on δ_{max} as tissue fold height increases. δ_{max} is inversely proportional to fold height regardless of edge radius. Considering that δ_{max} is defined as the vertical deflection of the capsule into the tissue substrate relative to the original position of the level tissue (not relative to the tissue fold height), δ_{max} decreases as h increases due to added support from the tissue fold. This is probably not physically accurate due to the rotational constraint in the model. In reality, the capsule would most likely rotate (about the z-axis in Fig. 7.2) as h increases. δ_{max} also increases as R increases. Considering that the overall length of the capsule remains constant as R is varied, the contact length of the capsule decreases as R increases, so the weight of the capsule is distributed over a smaller area, resulting in more vertical deflection into the tissue.

δ_{max} as a function of edge radius and tissue fold width at a constant capsule length ($L = 31.5$ mm), diameter ($D = 11.6$ mm), weight ($F_W = 63.2$ mN), velocity ($v = 5$ mm/s) and tissue fold height ($h = 2.40$ mm) is shown in Fig. 7.9b. δ_{max} is directly proportional to edge radius regardless of tissue fold width,
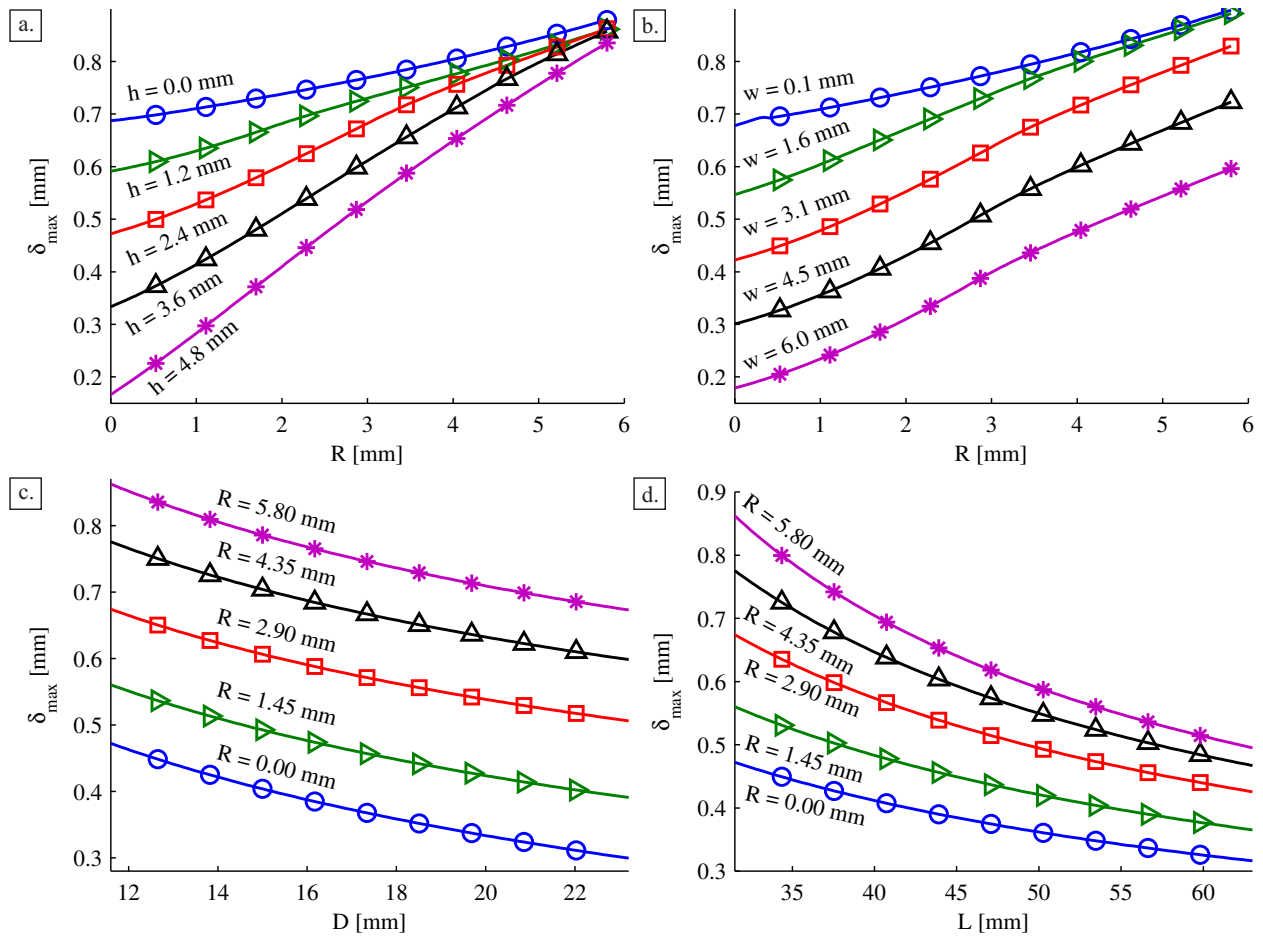
Figure 7.9: Analytical model solution for δ_{max} as a function of R and h (a), R and w (b), D and R (c), and L and R (d). Non-varied parameters are held at the "baseline value", as defined in Table 7.4. See Fig. 7.2 for the location of δ_{max}.

however, edge radius has a larger effect (*i.e.*, steeper slope) on δ_{max} for large fold widths ($w > 0.1\ mm$). Drag force is inversely proportional to fold width regardless of edge radius magnitude. Similar to the logic behind h, increasing w also provides more support for the tissue, which decreases δ_{max}, especially considering the rotational constraint of the model. In reality, the capsule would most likely rotate (about the z-axis in Fig. 7.2) as w is varied.

δ_{max} as a function of capsule diameter and edge radius at a constant capsule length ($L = 31.5\ mm$), weight ($F_W = 63.2\ mN$), velocity ($v = 5\ mm/s$), and tissue fold profile ($h = 2.40\ mm$ and $w = 2.45\ mm$) is shown in Fig. 7.9c. δ_{max} is inversely proportional to capsule diameter, regardless of edge radius and directly proportional to edge radius regardless of capsule diameter. When capsule diameter increases, the weight is distributed over a larger area, which decreases δ_{max}. Similarly, as R increases, the weight is distributed over a smaller contact surface area (due to constant overall length), and δ_{max} increases.

δ_{max} as a function of capsule length and edge radius at a constant diameter ($D = 11.6\ mm$), weight ($F_W = 63.2\ mN$), velocity ($v = 5\ mm/s$), and tissue fold profile ($h = 2.40\ mm$ and $w = 2.45\ mm$) is shown in Fig. 7.9d. δ_{max} is inversely proportional to capsule length regardless of edge radius, while directly proportional to edge radius regardless of capsule length. Again, increasing the length of the capsule distributes the weight over a larger contact surface area, resulting in less vertical deflection into the tissue.

δ_{max} as a function of capsule weight (or normal force) and edge radius at a constant length ($L = 31.5\ mm$), diameter ($D = 11.6\ mm$), velocity ($v = 5\ mm/s$) and tissue fold profile ($h = 2.40\ mm$ and $w = 2.45\ mm$) is shown in Fig. 7.10a. δ_{max} is directly proportional to capsule weight regardless of edge radius and directly proportional to edge radius regardless of capsule weight. As the weight of the capsule is increased, a larger force is distributed over the same contact area, resulting in larger vertical deflection into the tissue substrate. As edge radius increases, the weight of the capsule is distributed over a smaller contact area, also resulting in larger vertical deflection into the tissue.

δ_{max} as a function of velocity and edge radius at a constant length ($L = 31.5\ mm$), diameter ($D = 11.6\ mm$), weight ($F_W = 63.2\ mN$) and tissue fold profile ($h = 2.40\ mm$ and $w = 2.45\ mm$) is shown in Fig. 7.10b. δ_{max} is inversely proportional to velocity regardless of edge radius, but velocity has a larger effect on δ_{max} at low values ($v < 2\ mm/s$). δ_{max} as a function of velocity and tissue fold height at a constant
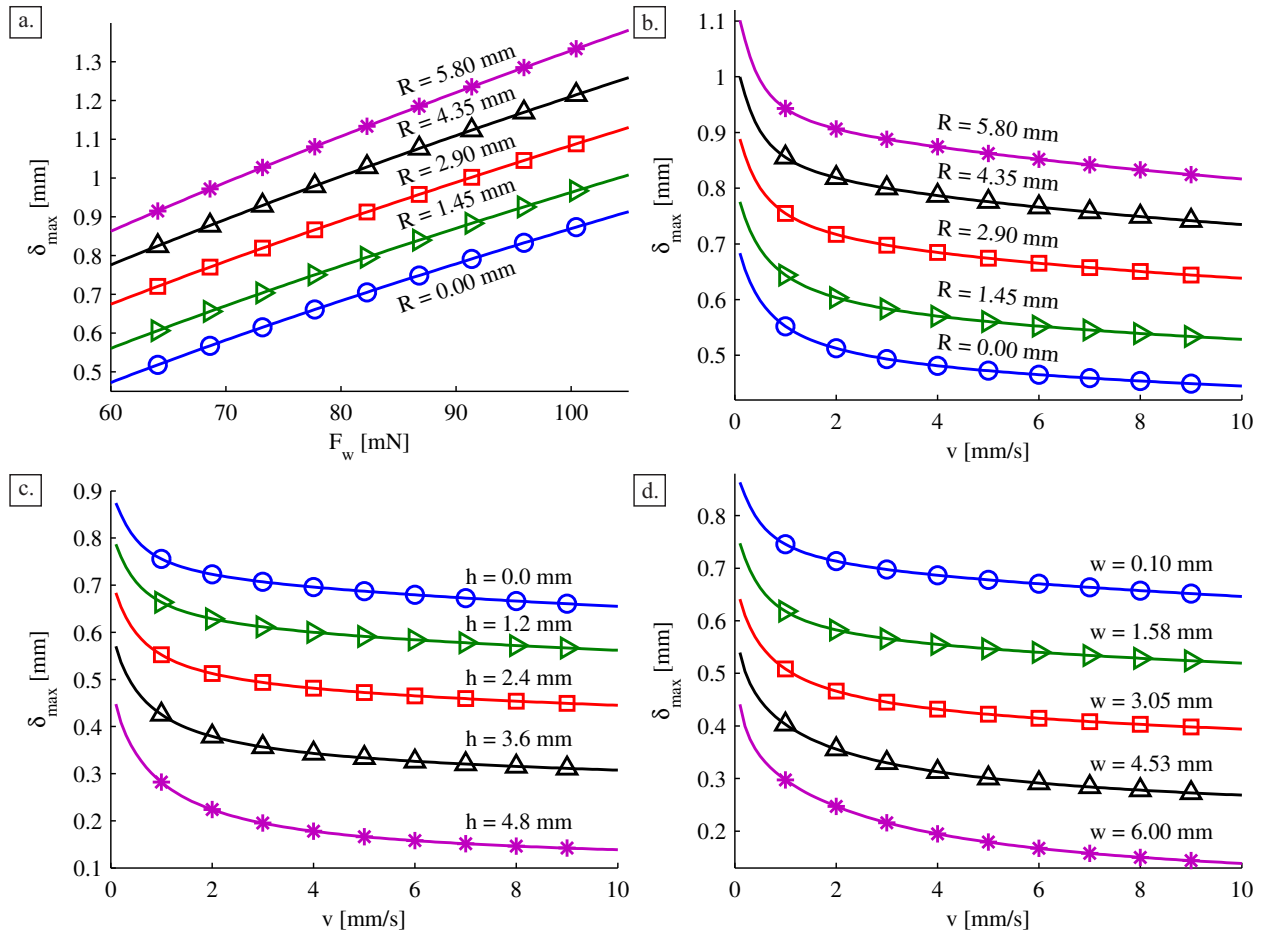
Figure 7.10: Analytical model solution for δ_{max} as a function of F_W and R (a), v and R (b), v and h (c), and v and w (d). Non-varied parameters are held at the "baseline value", as defined in Table 7.4, except for edge radius in (c) and (d), which are defined as $R = 0$. See Fig. 7.2 for the location of δ_{max}.

edge radius ($R = 0$ mm), length ($L = 31.5$ mm), diameter ($D = 11.6$ mm), weight ($F_W = 63.2$ mN) and tissue fold width ($w = 2.45$ mm) is shown in Fig. 7.10c. δ_{max} is inversely proportional to velocity regardless of fold height, and velocity has a larger effect on δ_{max} at low values ($v < 2$ mm/s). δ_{max} as a function of velocity and tissue fold width at a constant edge radius ($R = 0$ mm), length ($L = 31.5$ mm), diameter ($D = 11.6$ mm), weight ($F_W = 63.2$ mN) and tissue fold height ($h = 2.40$ mm) is shown in Fig. 7.10d. δ_{max} is inversely proportional to velocity regardless of fold width, and velocity has a larger effect on δ_{max} at low values ($v < 2$ mm/s). The behavior in Figs. 7.10b-d can be explained by studying the viscoelastic properties of the tissue. The stress in the tissue is strain-rate dependent, and is therefore dependent on the velocity of the capsule. At low speeds, force is applied on the tissue at a low rate, and the tissue is effectively softer. This results in more capsule "sinkage" into the tissue. As velocity increases, force is applied to the tissue at higher rates, and the tissue responds as a stiffer material, resulting in a decrease in δ_{max}. This also explains the drag force response in Figs. 7.8b-d. It might be expected that the drag force would increase with capsule velocity, due to the strain-rate dependency of the tissue. However, the decrease in δ_{max} with increasing velocity accounts for the decrease in drag force.

7.5.2   Pilot Study

The purpose of the pilot study was to validate the model with respect to each individual parameter on porcine colon tissue. The model response and experimental data for capsule design parameters on various tissue samples are shown in Figs. 7.11-7.14. The model response and the experimental data for validation of capsule velocity are shown in Fig. 7.15a.

Figs. 7.11a-d show both the model response and experimental data for capsule edge radius, length, diameter, and weight, respectively, on porcine colon sample P-C1. The normalized root-mean-square error (NRMSE) between the model and experiments is 5.99%, 7.64%, 4.19%, and 6.76% for edge radius, length, diameter, and weight, respectively. The overall NRMSE for P-C1 is 6.28% (Table 7.5). Each data point in Fig. 7.11 represents the average of 10 trials while the error bars represent the standard deviation of that mean.

Figs. 7.12a-d show both the model response and experimental data for capsule edge radius, length,

Figure 7.11: Modeled (solid blue line) and experimental (black circular data points) drag force as a function of capsule edge radius (a), length (b), diameter (c), and weight (d) for colon sample P-C1 (Table 7.2). The NRMSE between the model and experiments is 5.99%, 7.64%, 4.19%, 6.76%, and 6.28% for R, L, D, F_W, and combined, respectively. Each data point represents an average of the maximum drag force from 10 trials while the error bars represent the standard deviation of that mean.

diameter, and weight, respectively, on porcine colon sample P-C2. The NRMSE between the model and experiments is 22.6%, 3.46%, 3.70%, and 4.66% for edge radius, length, diameter, and weight, respectively. The overall NRMSE for P-C2 is 11.8% (Table 7.5). The larger NRMSE for P-C2 can be attributed to the discrepancy between the data and the model for the $R = 0$ data point in Fig. 7.12a. Each data point in Fig. 7.12 represents the average of 10 trials while the error bars represent the standard deviation of that mean.

Figs. 7.13a-d show both the model response and experimental data for capsule edge radius, length, diameter, and weight, respectively, on porcine colon sample P-C3. The NRMSE between the model and experiments is 11.0%, 6.25%, 4.09%, and 6.01% for edge radius, length, diameter, and weight, respectively. The overall NRMSE for P-C3 is 7.30% (Table 7.5). Each data point in Fig. 7.13 represents the average of 10 trials while the error bars represent the standard deviation of that mean.

Fig. 7.14 shows the model output and averaged experimental data for porcine colon samples P-C1, P-C2, and P-C3. Measured material properties (E_0, E_1, E_2, η_1, η_2, μ, h, and w) for P-C1, P-C2, and P-C3 were averaged and then used as model inputs. The experimental data from all three tissue samples were averaged for each parameter to produce each data point in Fig. 7.14 (for a total of 30 trials per data point). The error bars in Fig. 7.14 represent the propagation of error from the standard deviations of each individual tissue sample.

It is apparent from Figs. 7.11-7.14 that edge radius is the parameter with the largest effect on drag force. This is consistent through the multiple colon samples that were used. It is important to note that the effects of capsule length and diameter are negligible when compared to the effect of edge radius. The effect of weight on drag force is non-negligible, but is not as effective as edge radius. For all three colon samples, the trends that the model predict are consistently captured by the experimental results for edge radius and normal force, but not always captured for length and diameter. This can be attributed to the resolution of the measurement system (± 3 mN; from data sheet, and therefore is the best case) and the variability of the tissue samples. It is also important to note that the error bars for $R = 0$ in Figs. 7.11-7.14 are significantly larger than the rest of the error bars. Since the capsule with a cylindrical end ($R = 0$) is more sensitive to tissue morphology resulting in larger drag force, it is intuitive that the capsule will produce results with higher variability.
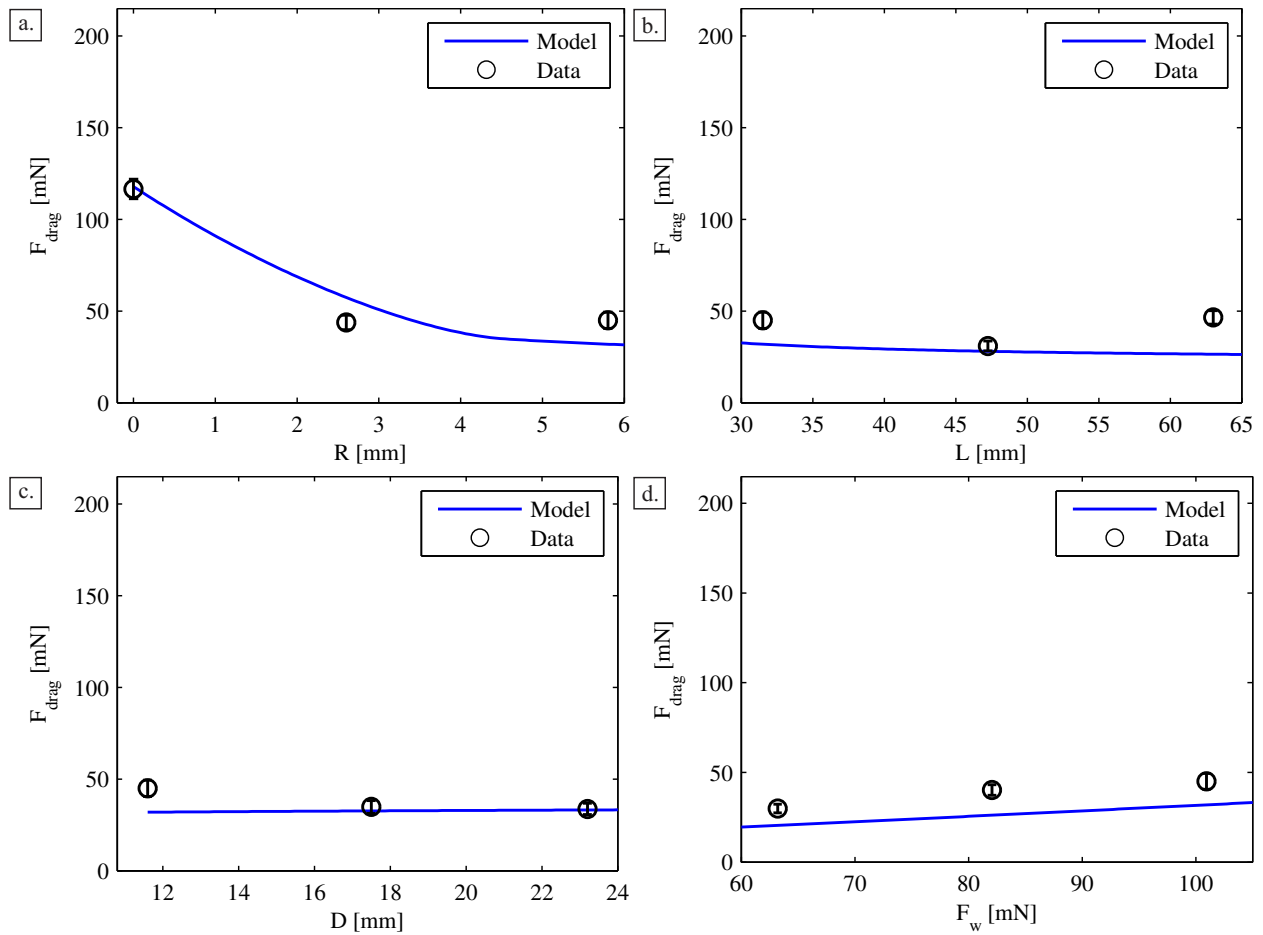
Figure 7.12: Modeled (solid blue line) and experimental (black circular data points) drag force as a function of capsule edge radius (a), length (b), diameter (c), and weight (d) for colon sample P-C2 (Table 7.2). The NRMSE between the model and experiments is 22.6%, 3.46%, 3.70%, 4.66%, and 11.8% for R, L, D, F_W, and combined, respectively. Each data point represents an average of the maximum drag force from 10 trials while the error bars represent the standard deviation of that mean.

Figure 7.13: Modeled (solid blue line) and experimental (black circular data points) drag force as a function of capsule edge radius (a), length (b), diameter (c), and weight (d) for colon sample P-C3 (Table 7.2). The NRMSE between the model and experiments is 11.0%, 6.25%, 4.09%, 6.01%, and 7.30% for R, L, D, F_W, and combined, respectively. Each data point represents an average of the maximum drag force from 10 trials while the error bars represent the standard deviation of that mean.

Figure 7.14: Average modeled (solid blue line) and experimental (black circular data points) drag force as a function of capsule edge radius (a), length (b), diameter (c), and weight (d) for colon samples P-C1, P-C2, and P-C3 (Table 7.2). The NRMSE between the averaged model and experiments is 8.81%. Each data point represents an average of the maximum drag force from 30 trials while the error bars represent the propagation of error from the standard deviations of P-C1, P-C2, and P-C3 means.

Fig. 7.15b shows the model output and experimental results from the velocity pilot study, which was only performed on one porcine colon sample (v-C1). The NRMSE between the experiments and model is 1.36% (Table 7.5). Each data point represents the average of 10 trials while the error bars represent the standard deviation of that mean. Again, compared to the effect that edge radius has on drag force, velocity is far less effective, but non-negligible. The trend that the model predicts is captured well by the experimental data. The decrease in drag force as velocity increases can most likely be attributed to a decrease in δ_{max}, which is not a measured in the experimental studies.

7.5.3   Edge Radius Evaluation

In general, the model and experimental results from the pilot study matched well, with an overall NRMSE of 8.81% (Table 7.5). More specifically, it was observed (in both the model and experimentally) that capsule length, diameter, weight and velocity had a minor effect on drag force when compared to the effect that edge radius had on drag force. To more closely examine the effect of edge radius, an in depth study was performed using 10 capsules (Fig. 7.4e) with equal length, diameter, weight and velocity, but varying edge radius, from 0 mm (*i.e.*, cylindrical end) to 5.8 mm (*i.e.*, hemispherical end).

Analysis of the model output and the pilot study indicated that the most influential parameter on drag force was edge radius, so an in depth study of edge radius was performed. The results of the study are summarized in Fig. 7.15 (b-d).

Fig. 7.15b-d shows the results of the edge radius study for porcine colon samples ER-C1, ER-C2, and ER-C3, respectively. The NRMSE between the model and experimental results for ER-C1, ER-C2, and ER-C3 were 6.47%, 3.31%, and 2.86%, respectively. The overall NRMSE for the edge radius study was 4.51% (Table 7.5). Each data point in Fig. 7.15 (b-d) represents the average of 10 trials, while the error bars represent the standard deviation of that mean. Colon samples ER-C1 ($h = 2.17 \ mm$) and ER-C2 ($h = 3.08 \ mm$) were relatively more rough than the ER-C3 sample ($h = 0.013 \ mm$).

Similar to the pilot study, the error bars are largest for data collected using a capsule with $R = 0$. It makes sense that the cylindrical capsule with the sharpest edge is more sensitive to changes in the tissue structure and therefore more susceptible to variability. It is important to note that the effect of edge radius
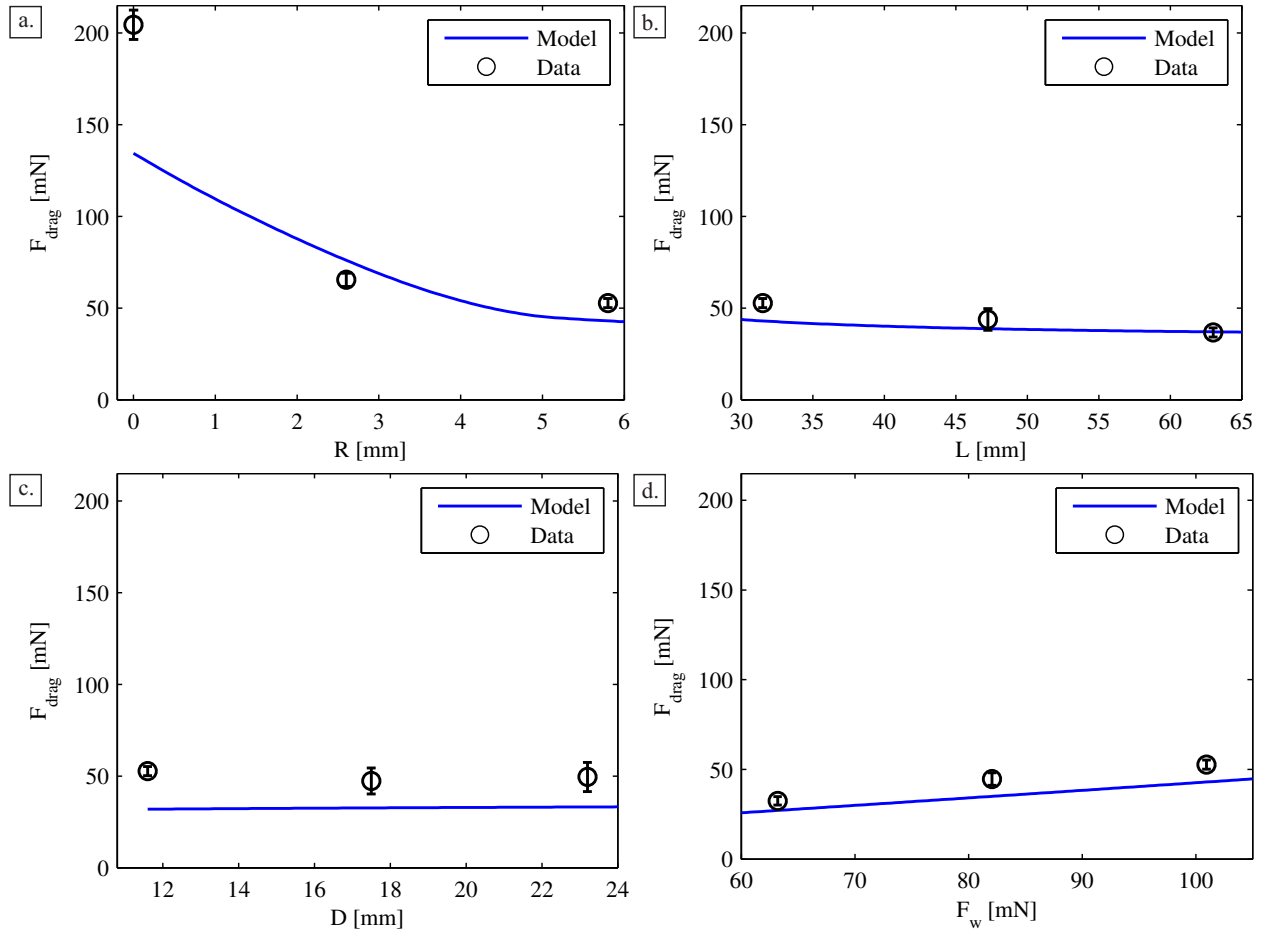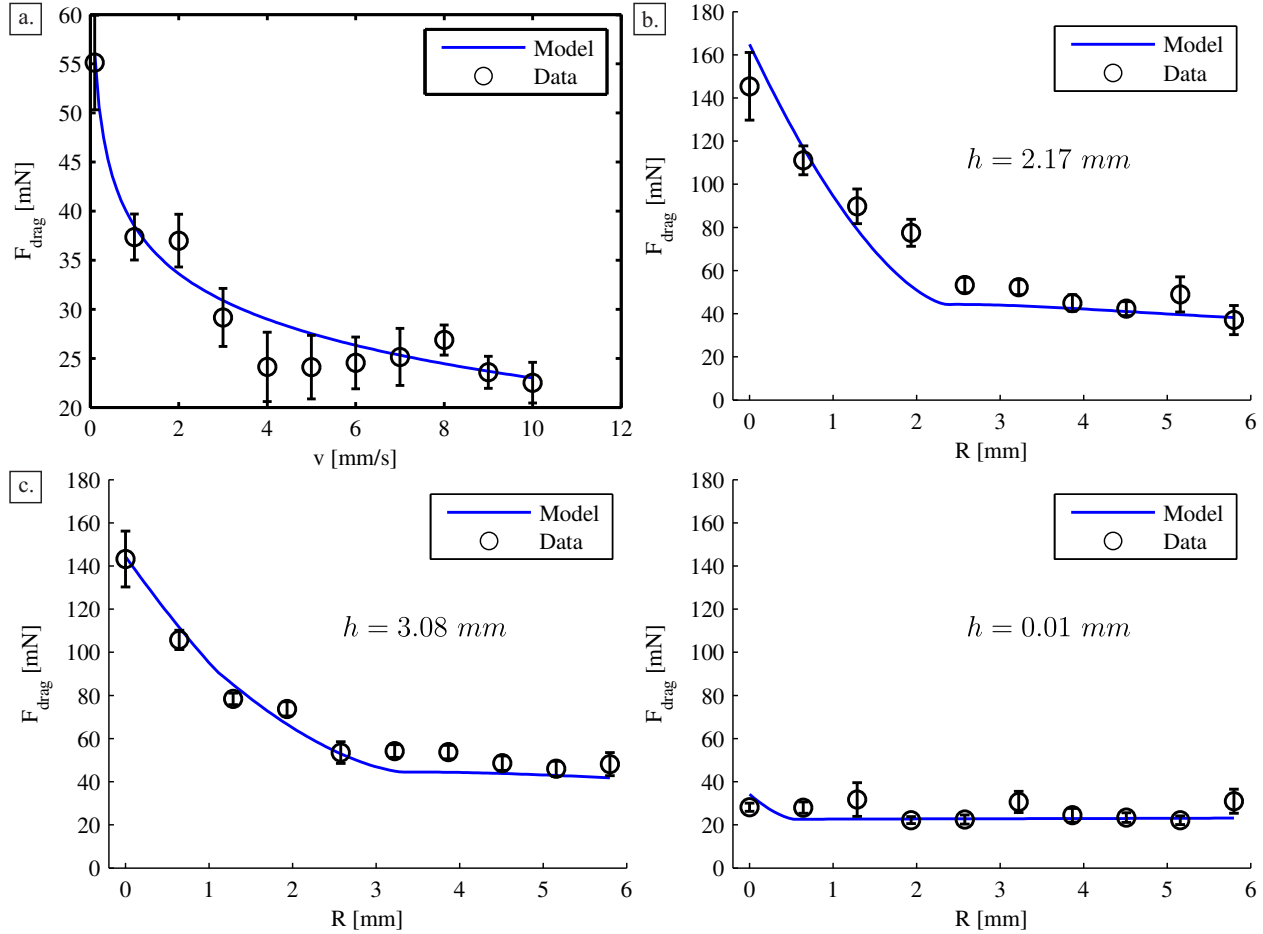
Figure 7.15: (a) Modeled (solid blue line) and experimental (black circular data points) drag force as a function of capsule velocity on one porcine colon tissue sample (v-C1 in Table 7.2). The average NRMSE between the model and experiments is 1.36%. Each data point represents an average of the maximum drag force from 10 trials while t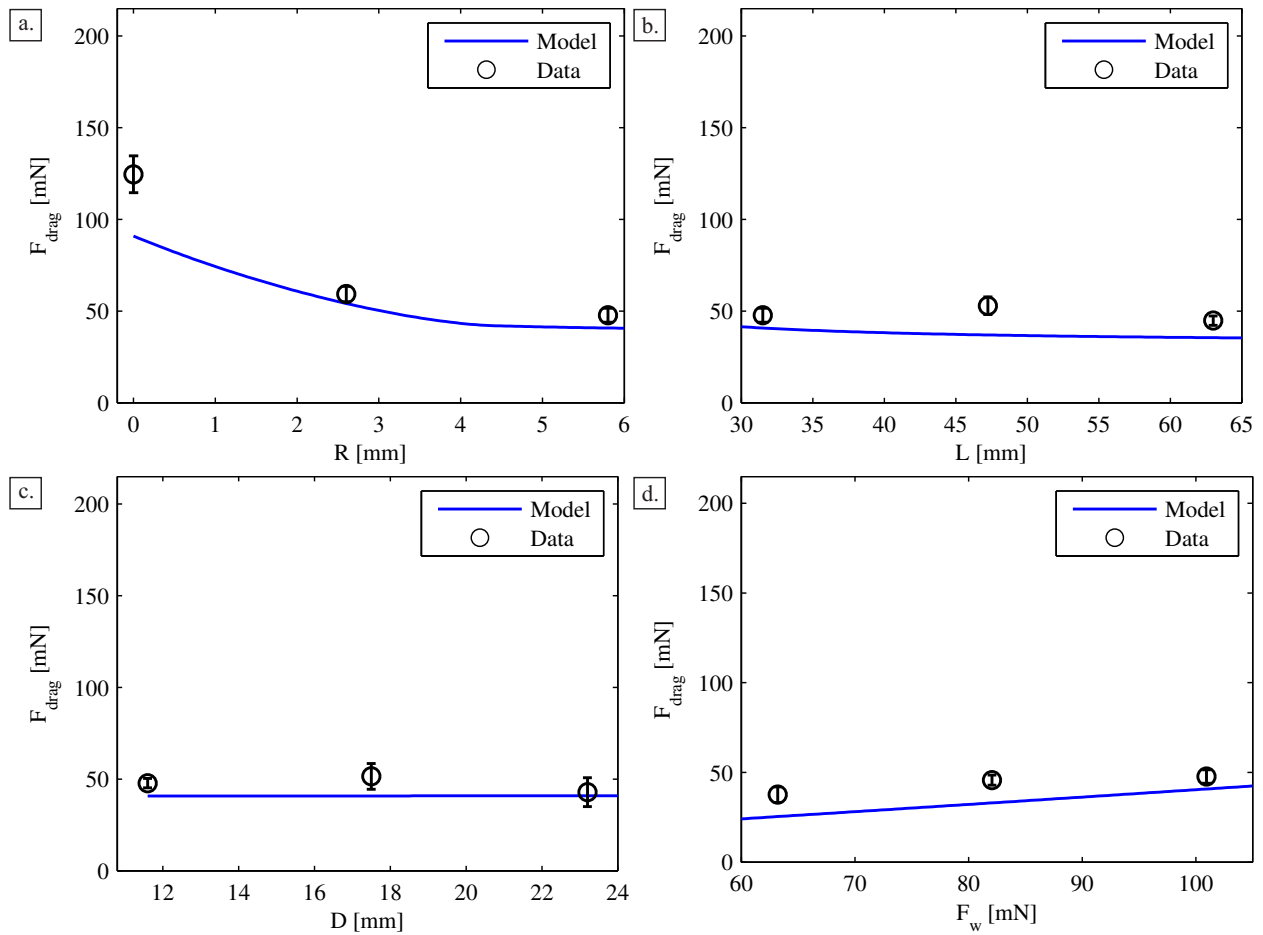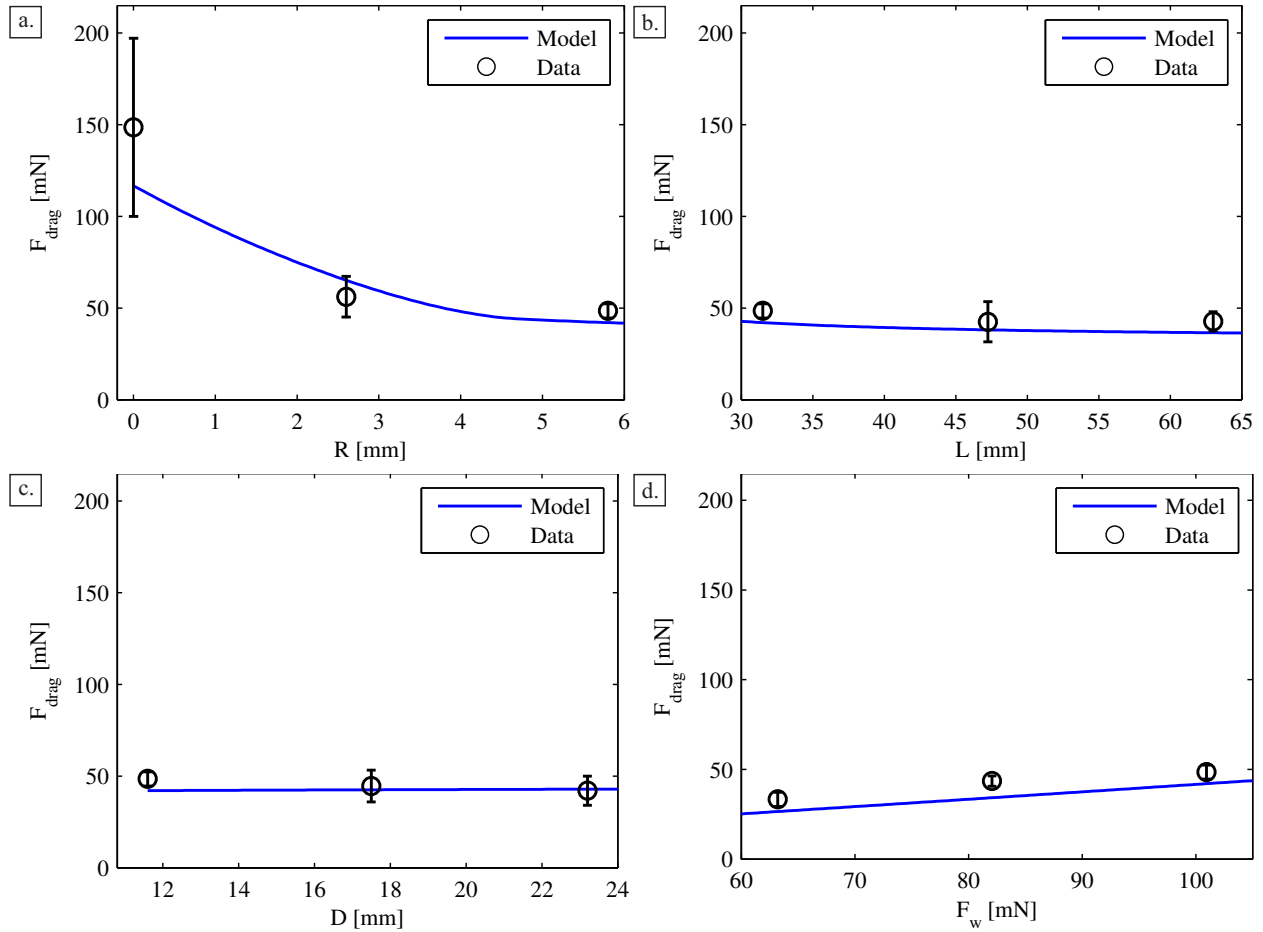he error bars represent the standard deviation of that mean. (b-d) Modeled (solid blue line) and experimental (black circular data points) drag force as a function of capsule edge radius (R) on three porcine colon samples. The colon samples used in (b) and (c) were significantly more rough (larger h) when compared to the colon sample used in (d). The average NRMSE between the model and experiments is 6.47%, 3.31%, 2.86% and 4.51% for ER-C1 (b), ER-C2 (c), ER-C3 (d), and combined, respectively. Each data point represents an average of the maximum drag force from 10 trials while the error bars represent the standard deviation of that mean.

becomes negligible for smooth tissue (*i.e.*, small h). Also, the effect of increasing edge radius becomes less effective in reducing drag force once the edge radius is larger than the height of the tissue fold and the maximum deflection into the tissue (*i.e.*, $R > h + \delta_{max}$). This becomes important when designing a cylindrical probe for use in the GI tract to maximize the payload capacity of the capsule. As edge radius increases, the force required to drag the capsule decreases, but the payload capacity also decreases (overall length, L, remains constant). If the maximum fold height is known, then the capsule can be designed such that the edge radius is large enough to reduce drag force, but small enough to maximize payload capacity. For example, if the maximum fold height of the colon is known to be $h + \delta_{max} = 2.4\ mm$, then the capsule could be designed to have an edge radius of $R = 2.5\ mm$. For a capsule with $L = 31.5\ mm$ and $D = 11.6\ mm$, an edge radius of $2.4\ mm$ amounts to a 11% increase in payload capacity over a capsule with a hemispherical end ($R = D/2$) which could be used for extra onboard sensors, batteries, or other modules (*e.g.*, diagnostic, therapeutic, etc.).

7.5.4   GI Tract Region

The final objective of the study was to validate the model in all regions of the GI tract. This was accomplished by performing drag tests on multiple tissue samples from various regions of the porcine GI tract using a single capsule (R3 from Fig. 7.4d with $F_W = 63.2\ mN$). The results of the study are presented in Fig. 7.16. The horizontal axis in Fig. 7.16 distinguishes between tissue samples. The prefixes "C-", "ESO-", "SB-", and "S-" denote colon, esophagus, small bowel and stomach, respectively. The numbered suffixes (*e.g.*, 1, 2, or 3) denote sample number, where each data point is an average of 10 trials and the error bars are the standard deviation of each mean. The suffix "Avg" indicates that the data point is an average of the three samples (30 trials total), and the error bar is the propagation of error from the standard deviations of each individual tissue sample.

The NRMSE error between the experimental results and model output for C-1, C-2, and C-3 colon samples are 14.2%, 11.3%, and 7.56%, respectively. The overall NRMSE for the colon region is 13.0%. The NRMSE error between the experimental results and model output for ESO-1, ESO-2, and ESO-3 esophagus samples are 24.0%, 0.89%, and 8.06%, respectively. The overall NRMSE for the esophagus region is 10.9%.
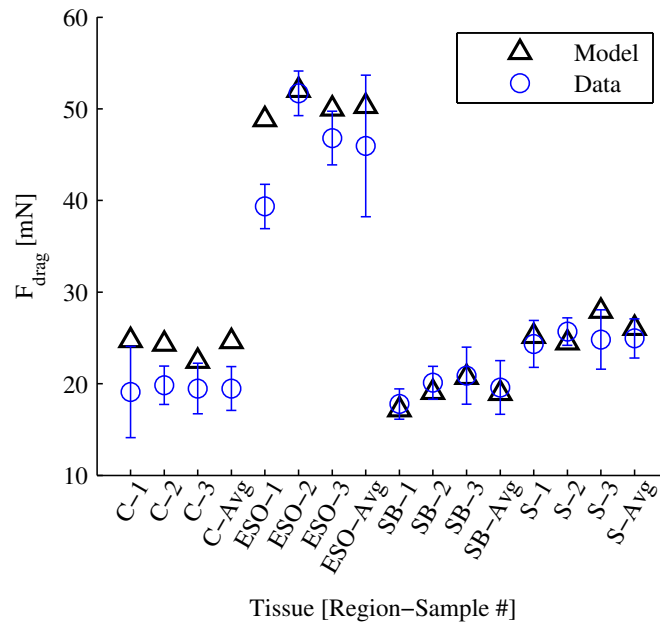
Figure 7.16: Results from the GI tract region study. The model (black triangles) and data (blue circles) fit with an average NRMSE of 9.62%. The prefixes "ESO-", "S-", "SB-", and "C-" indicate esophagus, stomach, small bowel, and colon GI regions, respectively. The number following the prefix indicates tissue sample. Each experimental data point for the numbered samples represents the average of the maximum drag force from 10 trials, while the error bars represent the standard deviation of that mean. The suffix "Avg" indicates an average of the three tissue samples from the same region. The capsule used in these tests was R3 from Fig. 7.4d with $F_W = 63.2 \ mN$

The NRMSE error between the experimental results and model output for SB-1, SB-2, and SB-3 small bowel samples are 1.58%, 2.62%, and 0.48%, respectively. The overall NRMSE for the small bowel region is 1.62%. The NRMSE error between the experimental results and model output for S-1, S-2, and S-3 stomach samples are 2.10%, 3.03%, and 7.81%, respectively. The overall NRMSE for the stomach region is 2.78%. See Table 7.5 for a summary of NRMSE.

In general, the agreement between model and experimental data was better for the stomach and small bowel tissue samples over the colon and esophagus samples. The small bowel and stomach tissue samples were smoother than the colon and esophagus samples, suggesting that most of the error comes from the tissue morphology. A potential source of error in the model could be that rotation of the capsule (about the z-axis) is not accounted for in the model. The ESO-1 tissue sample was the only outlier in the sample group. This discrepancy is most likely due to measurement error.

A graphical user interface (GUI) was developed using MATLAB to be used as a design tool. The GUI is self-contained and includes sample data for coefficient of friction drag tests, interferometer measurement, and indentation tests. The main window of the GUI presents a graphical depiction of the problem setup in the top left corner. In the top middle of the window are design parameter inputs, including capsule edge radius (R), length (L), diameter (D), weight (F_W), and velocity (v), one of which can be varied at a time. The varied parameter can be selected using the radio buttons in the top middle of the window. The selected parameter for variation is then highlighted in red in the problem setup figure. The upper and lower limits of the range, and the number of data points (capsules) desired need to be entered. Once the design parameters have been set, the user can click the "Build Capsules" button to obtain capsule profile shape functions, volume, surface area, and 3D renderings. Tissue properties are entered in the bottom half of the window. Tissue properties can either be manually entered or data files can be chosen by clicking on "Choose file(s)". The GUI is described in more detail in Appendix B. Once tissue properties are entered, the "Compile Model" button will execute solution computation. After computation, the results are displayed in graphical format. Results include stress profile on the capsule, tissue deformation, drag force (F_D), friction force (F_f), horizontal components of the stress integrated over the contact area (F_x), and horizontal force due to the contact with the vertical leading end of the capsule (F_A), if any. Results can be exported to a

MATLAB data file and figure files.

Table 7.5: The normalized root-mean-square error (NRMSE) of each study, reported as a percentage. The maximum NRMSE throughout the entire study was 24%, and the minumum was 0.48% with an overall NRMSE of 6.25%. The prefix "P-" indicates that the tissue sample was used for the pilot study. The prefix "v-" indicates that the tissue sample was used for the velocity dependence validation. The prefix "ER-" indicates that the tissue sample was used for the in-depth edge radius study. No prefix indicates that the tissue was used for the GI region validation. Tissue region abbreviations are "ESO", "S", "SB", and "C" for porcine esophagus, stomach, small bowel, and colon, respectively

Pilot Study			Edge Radius Study		Region Study	
Sample	Parameter	NRMSE (%)	Sample	NRMSE (%)	Sample	NRMSE (%)
P-C1	R	5.99	ER-C1	6.47	ESO1	24.0
P-C1	L	7.64	ER-C2	3.31	ESO2	0.89
P-C1	D	4.19	ER-C3	2.86	ESO3	8.06
P-C1	F_W	6.76			All ESO samples	10.9
All P-C1 parameters		6.28			S1	2.10
P-C2	R	22.6			S2	3.03
P-C2	L	3.46			S3	7.81
P-C2	D	3.70			All S samples	2.78
P-C2	F_W	4.66			SB1	1.58
All P-C2 parameters		11.8			SB2	2.62
P-C3	R	11.0			SB3	0.48
P-C3	L	6.25			All SB samples	1.62
P-C3	D	4.09			C1	14.2
P-C3	F_W	6.01			C2	11.3
All P-C3 parameters		7.30			C3	7.56
v-C1	v	1.29			All C samples	13.0
All pilot samples		**8.81**	**All edge radius samples**	**4.51**	**All region samples**	**9.62**
					Overall NRMSE (%)	**6.25**

7.6   Conclusions

The analytical model presented here can be used to predict the drag force necessary to move a cylindrical capsule through all regions GI tract at a constant velocity with an average NRMSE of 6.25%. The model accounts for several capsule design parameters, including capsule edge radius (R), length (L), diameter (D), contact normal force (F_W), and travel velocity (v) as well as tissue parameters, such as compressive material properties (E_0, E_1, E_2, η_1, and η_2), coefficient of friction (μ), and surface roughness (h and w). The analytical model was developed theoretically, and does not rely on empirical development. The model requires several inputs, some of which are determined experimentally, while the remaining are design parameters.

Drag tests were performed on excised porcine GI tract tissue samples to validate the model with respect to tissue material properties (E_0, E_1, E_2, η_1, η_2, μ, h, and w) and capsule design parameters (R, L, D, F_W, v). The compressive properties of each tissue sample were determined using indentation-relaxation tests. The coefficient of friction for each tissue sample was determined through drag tests on a smooth part of the sample and a capsule with a low weight (to minimize vertical deflection into the tissue sample) and large edge radius (to minimize the edge effect). The surface roughness was determined by using an interferometer-based approach. A pilot study was carried out to validate the model with respect to all of the capsule design parameters. Edge radius was the most influential parameter on the drag force, so an in depth study of edge radius was performed. Finally, drag tests on tissue samples from all regions of the GI tract were performed to validate the model with respect to uncontrollable tissue parameters. The majority of the drag force is due to the interaction between the leading edge of the capsule and the tissue, and therefore is largely influenced by the edge radius (R) and the tissue fold height (h).

A GUI (see Appendix B) was developed using MATLAB as a design tool for the end user, which is publicly available for capsule design studies. Within the GUI, capsule design parameters can be set by the user. Then, material properties of the tissue can either be manually entered or raw data can be loaded for processing. A single parameter can be varied by entering a range of values. The program then executes the model, solving for all variations of the parameter. The GUI outputs several solutions, including stress

and strain on the capsule (and in the tissue), predicted drag force, capsule surface area, capsule volume and shape functions for the deflection of the tissue. Graphs and data can be exported.

The average computation time per solution of the model is 2 s (2.27 GHz processor), and therefore could potentially be applied to a real-time scenario for control algorithms. Future work will include refining the model (*e.g.*, fast numerical integration methods) to be more computationally efficient. With a faster algorithm, real-time control of a capsule will be more achievable, especially with systems that enable wireless *in vivo* measurement of resistance properties of the gastrointestinal tract [171]. Another drawback to the model is the rotational constraint. Future work will include removing this constraint and accounting for capsule rotation, which will likely increase accuracy. Furthermore, the model could be expanded to include contact from both sides of the capsule (*i.e.*, in an uninsufflated environment). It is important to stress that several defined parameters were required to develop and experimentally validate the model, and as such a magnetic example was used. However, this model could be applied to other systems where a cylindrical probe is dragged across a tissue substrate (*e.g.*, electric, pneumatic, and hybrid locomotion systems). The model presented is a reliable design tool for those interested in knowing the maximum drag force required to move a cylindrical capsule through the GI tract.

Chapter 8

Summary and Conclusions

8.1 The Quantitative Evaluation of Micro-Patterned Robotic Wheels in a Controlled Static Environment

In Chapter 2 (The Quantitative Evaluation of Micro-Patterned Robotic Wheels in a Controlled Static Environment), a device was developed to quantitatively evaluate micro-patterned robotic wheels in a controlled static environment. The device consisted of a grounded frame with a static platform for the substrate. A wheel, attached to the end of a horizontal arm, rested on the substrate. The wheel was driven by an actuator to induce rotational motion. The horizontal arm passively pivoted about a single point, and the normal force of the wheel could be adjusted by using preset counterweights. As the wheel rotated on the substrate, traction force and motor power were measured. The static benchtop tests suggested that all of the treads perform most efficiently at the lowest normal force tested (0.10 N). In future tests, the range of varied normal forces will be increased to include even lower normal forces (lighter mobile robots) to determine if the efficiency trend continues for these lower normal forces.

The results from Chapter 2 motivated future work which included more benchtop testing using a dynamic system, where the effects of slip ratio, additional materials (including excised tissues), and pillar density could be investigated experimentally. Furthermore, numerical modeling will continue to be used to predict the performance of new treads, coupled with benchtop tests, and candidate tread designs will be evaluated *in vivo*.

8.2 The Quantitative Evaluation of Micro-Patterned Robotic Wheels in a Controlled Dynamic Environment

In Chapter 3 (The Quantitative Evaluation of Micro-Patterned Robotic Wheels in a Controlled Dynamic Environment), a device was developed to quantitatively evaluate micro-patterned robotic wheels in a controlled dynamic environment. The device consisted of a grounded frame, with single degree-of-freedom (DoF) mobile platform for the substrate. The substrate platform was driven by a linear actuator to induce translational velocities. A wheel, attached to the end of a horizontal arm, rested on the substrate. The wheel was driven by an actuator to induce rotational motion. The wheel was much larger than the wheel in Chapter 2 to increase the signal-to-noise ratio. The horizontal arm passively pivoted about a single point, and the normal force of the wheel could be adjusted by using preset counterweights. As the wheel rotated and translated on the substrate, traction force was measured. Results showed a consistent nonlinear and directly proportional response for traction force with respect to slip ratio regardless of substrate or wheel tread pattern. Additionally, traction force was directly proportional to both translational speed (nonlinear) and normal force (nearly linear) regardless of substrate or wheel tread pattern. Micro-patterned polydimethylsiloxane (PDMS) treads only enhance traction (when compared to smooth PDMS wheels) on biological tissue (*e.g.*, liver, intestines, etc.), but not on synthetic tissue.

The results from Chapter 3 motivated future work, which included the study of tread-tissue interactions through modeling and experimentation, as well as RCE prototype design. Furthermore, it would be desirable to develop an analytical model to predict experimental results. Experimentally, changes to the mechanical properties of the PDMS will be studied, including PDMS surface properties and tread modulus. Additionally, variations in the micro-pattern will be investigated. Furthermore, the testing platform will be used to thoroughly investigate the relationship between traction force and normal force as well as translational speed. Using this and future data, optimized tread patterns (based on a set of operating conditions) will be used in RCE prototypes for *in vivo* testing. An optimized tread pattern is one that will create the largest amount of traction force on a biological substrate given a robot weight and speed. We envision an optimum tread pattern as one with a certain set (or range) of material and design parameters, such as tread

geometry, size, spacing, modulus and hydrophobicity. The device was only capable of a set number of slip ratios, linear speeds, and normal forces due to the open-loop control of the stepper motors and discrete counterweight settings. This motivated future work to include the design of a device which featured closed-loop velocity/position control for both rotational and translational motion as well as closed-loop normal force control.

8.3   Automated Traction Measurement (ATM) Platform

Chapter 4 (The Design and Evaluation of an Automated Traction Measurement Platform for Evaluating Micro-patterned Robotic Wheels in a Dynamic Environment and Empirical Model for Predicting Traction Force) presented the design and evaluation of an automated traction measurement (ATM) platform for evaluating micro-patterned robotic wheels in a dynamic environment, and an empirical model for predicting traction force. The device consisted of a load platform, which measured both traction force and normal force (for closed-loop feedback of normal force control), an actuated single DoF translating sled for inducing wheel translational speed, a horizontal arm with an actuated counterweight for controlling normal force, and an actuated single DoF wheel for inducing rotational speed. A filter was designed to mitigate noise associated with motor vibration. An empirical model was developed to predict traction force as a function of translational speed, slip ratio, and normal force for a micro-patterned PDMS wheel (circular pillars) on a synthetic tissue substrate (32 mm height).

The average normalized root-mean-square error (NRMSE) between the empirical model and the data used to develop the model was 1.1% (min 0.0024%, max 4.2%). The average NRMSE between the traction force predicted by the model and the data used to verify the prediction was 1.8% (min 0.020%, max 8.6%). Although the error between predicted and actual traction force was low, the model has some limitations. Firstly, it is only valid for a single tread on a single substrate. This limits the ability to predict traction force for new tread patterns and substrates. Secondly, the model has only been validated for interpolated values, and not extrapolated inputs. Therefore, the model is only valid for predicting traction force at normal forces between 0.1 and 0.6 N, translational speeds between 2 and 11 mm/s, and slip ratios between 0 and 0.45.

The limitations of the model motivated future work, including the development of a more robust model.

Chapter 5 describes a finite element modeling approach which sets out to model the interaction between a patterned wheel and a substrate. With proper validation and characterization of the FEM, traction force could be predicted for various tread patterns, and on various substrates with an adequate material model.

8.4 The Effect of Hyperelastic Substrate Stiffness, Wheel Tread Fibrillar Structure Size, and Fibrillar Modulus on Traction Force: Experiments and Modeling

Chapter 5 (The Effect of Hyperelastic Substrate Stiffness, Wheel Tread Fibrillar Structure Size, and Fibrillar Modulus on Traction Force: Experiments and Modeling) presents the development of a finite element model (FEM) for predicting traction force of a patterned wheel on a synthetic biological substrate, and the experimental examination of the effect of substrate stiffness, tread modulus, and tread size on traction force. The FEM required a full characterization of the synthetic tissue substrate, including simple tensile tests for determining the hyperelasticity and Poisson's ratio of the material, stress-relaxation tests for determining the viscoelasticity of the material, and drag tests for determining the velocity dependent coefficient of friction. The hyperelasticity of the material was modeled using a 5-parameter Ogden model. The viscoelasticity of the material was modeled using a generalized Maxwell model ($n = 1$). The displacement (δ) due to the static loading of a smooth PDMS wheel were determined experimentally, analytically, and with FEM simulations, and were compared, resulting in a maximum difference of 4% between experimental and FEM results. The global and local displacements due to the static loading of a patterned PDMS wheel were determined analytically and with the FEM, and were compared. The dynamic traction of a smooth PDMS wheel was determined experimentally and with the FEM, and were compared, resulting in a maximum difference of 2.42%.

The effect of substrate stiffness, tread modulus, and tread size on traction force was also experimentally studied. Data suggests that there is a critical ratio ($k/(E_{tread}h) > 0.18$) between the substrate stiffess and tread modulus where traction force can be optimized. The data also suggests that there is a critical ratio ($h/a = 24$) between substrate height (*i.e.*, stiffness) and tread size which divides traction force into two different regimes. It is recommended to operated close to the ratio, but slightly under for optimal traction

force generation.

Future work from Chapter 5 includes validating the FEM with respect to substrate height, developing an analytical model for the dynamic (but constant differential velocity, v_d) sliding contact of a single pillar, and then performing a parametric study with the FEM so that it can be verified with respect to substrate height and pillar size.

8.5   The Design and In Vivo Evaluation of a Robotic Capsule Colonoscope Using Micro-patterned Treads for Mobility

Chapter 6 (The Design and In Vivo Evaluation of a Robotic Capsule Colonoscope Using Micro-patterned Treads for Mobility) presented the design and *in vivo* evaluation of a tethered robotic capsule endoscope (tRCE) using micro-patterned treads for mobility. The tRCE consisted of a housing (fabricated using a stereolithography technique), a centrally-located DC motor, 8 micro-patterned treads, and a gear-train to transfer motion from the motor shaft to the treads. The micro-patterned treads were custom fabricated to have micro-pattern on the outside surface (tissue interface) and timing teeth on the inside surface, which interfaced with timing pulleys. The tRCE was capable of speeds up to 3 mm/s in the cecum of an anesthetized porcine.

Immediate future research for the tRCE will focus primarily on further size reduction and faster speeds. Future tRCE versions will feature multiple travel speeds. Additional future work will be focused on producing a higher quality video while inside of a collapsed lumen, and decreasing the rigidity and weight of the tether. To increase image quality, the distance between the lens and the tissue must be increased.

Long-term future work will focus on further size reduction, the addition of surgical tools, a higher quality imaging system, and wireless capability. The ideal dimensions for a tRCE will be approximately 12 mm in diameter and 25 mm in length to be competitive with the leading passive CE designs. The analog imaging system will eventually be replaced with an equivalently sized high definition digital system. Eventually, the tRCE will need to be untethered. To do this, the device will need to be wirelessly controlled and have an onboard power supply.

8.6 The Development and Experimental Validation of an Analytical Model for In Vivo Robotic Capsule Colonoscope Resistance Force

Chapter 7 (The Development and Experimental Validation of an Analytical Model for In Vivo Robotic Capsule Colonoscope Resistance Force) presents the development and experimental validation of an analytical model for *in vivo* predicting the force needed to drag a capsule endoscope through an insufflated gastrointestinal (GI) tract. The work in this chapter was performed under the guidance of Dr. Gastone Ciuti, Dr. Arianna Menciassi, and Dr. Paolo Dario at the BioRobotics Institute of Scuola Superiore Sant'Anna in Pisa, Italy. The analytical model was a contact model, which assumes the stress distribution on the capsule is due to the capsule geometry and tissue topology (from haustral folds) when the capsule is undergoing constant velocity motion. The model calculates a drag force resulting from the horizontal component of the stress distribution, the frictional force, and contact with the flat front face of the capsule (for edge radius less than the haustral fold height). The model was validated experimentally with four studies: 1) a pilot study, 2) an in depth edge radius study, 3) a GI region study, and 4) a velocity-dependence study. The pilot study validated the model with respect to capsule length, diameter, edge radius and weight. It was noted that capsule edge radius contributes most to overall drag force, so an in depth study was performed to validate the model with respect to this parameter. Then, the model was validated with respect to various regions of the GI tract (*i.e.*, esophagus, stomach, small intestine, and large intestine). Finally, the model was validated with respect to capsule velocity. The model and experimental results matched with an overall average NRMSE of 6.25%. In addition to the model development and validation, a capsule endoscope design tool was developed as a MATLAB graphical user interface (GUI). The GUI enables the user to input capsule design parameters (*e.g.*, weight, length, diameter, edge radius, and velocity), tissue properties (*e.g.*, compressive material properties, coefficient of friction, and surface topology), and calculates a maximum drag force needed to move the capsule through the GI tract.

Future work includes improving the model to accommodate both hyperelastic and viscoelastic material properties (the model currently only accounts of viscoelasticity), and to account for rotation of the capsule as it encounters haustral folds. Furthermore, it is hypothesized that the model would be accurate in predicting

the drag force needed to move a cylindrical probe across the wall of an insufflated abdomen, however, experiments need to be performed to validate this hypothesis.

Chapter 9

Discussion

This chapter is dedicated to a general discussion about the work presented throughout this dissertation. The work was performed over the course of seven years, from 2008 to 2015. The chapter will first provide a general discussion about the project, and then conclude with future recommendations.

9.1   General Discussion

The overarching goal of this project was to develop robot prototypes that were capable of traveling within a collapsed lumen (*i.e.*, gastrointestinal tract). Although the first prototypes (c. 2008) were not successful from a mobility standpoint, the experience of designing and testing them *in vivo* provided valuable feedback and motivation for the in depth study of the contact problem that culminated into the bulk of this dissertation.

This first efforts of the research project (c. 2008) resulted in several small prototypes that were evaluated *in vivo*, in a live anesthetized porcine. None of the early prototypes successfully mobilized due to low friction between the robot-tissue interface and small locomotion contact area.

The early failed devices motivated a thorough literature review which revealed micro-patterning surfaces for friction enhancement, a technique that has been implemented in several fields. The following months were dedicated to learning how to fabricate micro-patterned PDMS using the photolithography technique presented in Chapter 2. Upon mastering a fabrication technique that yielded repeatable micro-patterned PDMS, a qualitative study was performed to confirm that the micro-patterned PDMS provided enhanced friction on tissue when compared to smooth PDMS. The study was performed using simple two-wheeled

robots. One wheel was equipped with a micro-patterned PDMS tread, while the other was equipped with a smooth PDMS tread. The study revealed a definite enhanced performed from the micro-patterned PDMS wheel.

Although the *in vivo* two-wheeled robot study revealed definite qualitative results in favor of the micro-patterned PDMS, it provided no insight into the mechanics of the problem. At this point in the research project three main aims were defined to direct the effort towards an efficient path. The overarching goal was to develop a deep understanding of the contact problem. Although some aspects of the contact problem had been studied previously, the majority of the contact problem was unknown. In an attempt to simplify the contact problem, it was approached from two different perspectives: 1) a global perspective and 2) a local perspective. The global perspective looked at the overall wheel-tissue interface and the associated variables, including dynamic motion (rotational speed, translational speed, vertical displacement, horizontal displacement) and forces (translational force, and normal force). The global perspective was studied experimentally and with models (empirical, finite element, and analytical). The local perspective focused on the interaction between a single micro-pattern pillar and the underlying/surrounding tissue. This perspective was primarily studied with modeling (finite element and analytical).

One of the major challenges of the project was recreating the real contact problem in a laboratory setting. The real contact problem (tread-*in vivo* tissue interaction) is a complex scenario including live tissue with its own micro-structured surface and a mucous layer. The tissue has dynamic material properties that are not isotropic or homogeneous (*i.e.*, the tissue properties are directionally dependent), and change drastically when excised from the live animal. Furthermore, the mucous layer also has dynamic material properties and secretion ceases once the tissue is excised. Although some of the studies in the dissertation use excised tissue, most of the models and related experimental studies were developed using a synthetic biological tissue, which was fabricated in an attempt to simplify the problem and improve repeatability of the results. In a further attempt to improve repeatability and reduce human error, the automated traction measurement (ATM) platform was developed to evaluate the traction force of robotic wheels on soft substrates. The platform enabled for direct control of several variables, including wheel translational speed, wheel rotational speed, wheel normal force, wheel tread pattern (*e.g.*, size, geometry, material, material modulus, etc.), and

substrate (*e.g.*, material, surface lubrication, material stiffness, etc.).

Identifying all of the parameters in the robot-tissue contact problem is an extremely difficult task, let alone studying them all. It was decided to study the effect of only certain parameters, with the goal of studying all identifiable and controllable parameters in future work. Parameters that were studied include robot translational speed, wheel rotational speed, robot weight, tread pillar geometry, tread pillar size, tread material modulus, substrate material (*e.g.*, excised bovine liver, excised porcine intestinal tissue, *in vivo* porcine intestinal tissue, synthetic tissue), substrate stiffness and lubrication (with only one material, PBS). Parameters that were identified but not studied in this dissertation include substrate surface structure (*e.g.*, to mimic intestinal villi), substrate material properties (*e.g.*, elastic modulus, viscoelastic time constants, etc.), lubrication material (*e.g.*, mucous, oil, etc.), lubrication properties (*e.g.*, viscosity, etc.), substrate surface properties (*e.g.*, hydrophobicity).

There are advantages and disadvantages to using a synthetic tissue instead of biological tissue. It is possible to approximate the material properties of biological tissue with a synthetic tissue, but it is difficult to exactly match them. It is relatively easy to make a homogeneous and isotropic synthetic tissue, but this is not a great approximation to biological tissue. For example, most synthetic tissue is made out of rubber, which is manufactured by mixing a base and a curing agent, creating a homogeneous material. This is not an excellent approximation for intestinal tissue due to its structure. Intestinal tissue is composed of both longitudinally and circumferentially oriented muscle fibers, creating a non homogeneous and non isotropic material. Once tissue is excised from a living body, its material properties immediately start to change. Furthermore, it is common to see errors of $> 10\%$ when using biological tissue. When using synthetic tissue, errors are consistently $< 5\%$. When attempting to understand a contact problem, reducing error is crucial to the experimental study. Although the synthetic tissue is not an exact replication of the biological tissue, understanding the simplified but repeatable contact problem with synthetic tissue still yields results that can be applied to the actual contact problem with biological tissue. Furthermore, using synthetic tissue eliminates some of the identified parameters (*e.g.*, surface structure) that are hard to control when using biological tissue.

9.2   Future Recommendations

Future recommendations are divided into to sections: 1) Robot wheel-tissue contact problem, and 2) Capsule housing-tissue contact problem. Chapters 2-6 were dedicated to the wheel-tissue contact problem, and the work was completed at the University of Colorado Boulder. Chapter 7 was dedicated to the capsule housing-tissue contact problem, and the work was completed at the BioRobotics Institute of Scuola Superiore Sant'Anna in Pisa, Italy.

9.2.1   Robot wheel-tissue contact problem

The most significant results from Chapters 2-6 were the ATM platform development (Chapter 4), the finite element model (Chapter 5), and the robotic capsule colonoscope (RCC) prototype (Chapter 6).

The ATM platform has been calibrated and characterized to produce repeatable and reliable traction force results. Normal forces between 5 mN and 500 mN can be induced, but wider ranges are obtainable by changing out the counter weight. The ATM platform was valuable for this dissertation work for producing experimental results that were used to identify trends, develop empirical models, and validate finite element and analytical models. Future recommendations for this device include studying the effects of additional identified parameters such as substrate surface structure (*e.g.*, to mimic intestinal villi), substrate material properties (*e.g.*, elastic modulus, viscoelastic time constants, etc.), lubrication material (*e.g.*, mucous, oil, etc.), lubrication properties (*e.g.*, viscosity, etc.), substrate surface properties (*e.g.*, hydrophobicity). Priority would be given to lubrication properties and hydrophobicity (both substrate and tread), followed by substrate surface structure. It is important to isolate the effect of each of these properties and study typical *in vivo* ranges. For example, when studying lubrication properties, it would be important to first characterize the properties (*e.g.*, viscosity) of mucous at body temperature (37° C). Then, using either biological or synthetic mucous, it would be important to study its effect on traction force generation at body temperature using the characterized range and the ATM platform. PDMS is naturally very hydrophobic, however the hydrophobicity can be temporarily reduced (become more hydrophilic) by exposing it to oxygen plasma. The hydrophilic effect wears off over time. Hydrophobicity is typically characterized by measuring the contact

angle of a water droplet on the surface of the material. In order to study the effects of hydrophobicity on traction force, it would be necessary to characterize the hydrophobicity of PDMS after exposure to oxygen plasma over time. Then, after treating a PDMS wheel (or substrate) with oxygen plasma, run continuous traction force tests on the ATM platform over the time that it takes the PDMS to revert to its original hydrophobicity.

The finite element model that was developed in Chapter 5 has exhibited promising results thus far, and therefore a future recommendation would be to further develop and validate this model. The model takes into account the viscoelastic and hyperelastic material properties of the synthetic tissue, and a velocity dependent coefficient of friction. The model has been characterized with respect to traction force and vertical displacements for a smooth wheel on a synthetic tissue substrate using both experimental data and analytical solutions. The model has also been developed to examine the effects of a micro-pattern. To date, the micro-pattern finite element model has been validated experimentally with respect to traction force and global vertical displacement, but not local displacements (u_z in Chapter 5) due to the inability to empirically measure bulging displacements between pillars. Immediate future recommendations include validating the finite element model for a micro-patterned wheel on synthetic tissue substrate with respect to local displacements using the analytical solution. Long-term future recommendations include validating the model experimentally with respect to substrate height (*i.e.*, stiffness) and tread size. If the model proves to be reliable for all stiffnesses and sizes, then an optimization algorithm could be executed to determine the optimum tread size to substrate stiffness ratio. This optimum value could be validated with existing experimental data.

The third significant result from the dissertation work was the RCC described in Chapter 6. The RCC developed in Chapter 6 was the result of several prototypes. The RCC consisted of a housing with a centrally located DC motor that actuated a worm. A gear train transferred power from the motor to 8 externally located and circumferentially oriented PDMS micro-patterned treads. These treads interfaced with the surrounding tissue, providing traction and propulsion. The RCC was capable of locomotion on both planar and tubular surfaces. The RCC featured two types of lighting (white and infrared) and an analog camera. The device was tethered for power and video transmission. One of the largest drawbacks

of the RCC was its large size and power loss due to the multi-tiered gear train. Future recommendations for the RCC include higher quality video (*e.g.*, high definition), and smaller size. To implement a power transmission solution with enough torque, the speed output had to be reduced significantly, resulting in a maximum speed of 3 mm/s. Future RCCs should have a higher maximum speed (*e.g.*, 5 mm/s). Long-term recommendations include implementation of a localization system, so that the position and orientation of the RCC can be known in real-time. Accurate real-time position and orientation could lead to a fully autonomous colonoscopy.

9.2.2   Capsule housing-tissue contact problem

The most significant results from Chapter 7 were the analytical model development and the resulting capsule endoscope design application for MATLAB. Chapter 7 focused on the interaction between the capsule housing and the surrounding tissue. This contact problem is important to understand regardless of the capsule endoscope mobility method. An analytical model was developed to predict the force necessary to drag a capsule endoscope through the entire GI tract. The model was validated experimentally with respect to capsule design parameters (*e.g.*, length, diameter, edge radius, weight, and velocity), and tissue properties (viscoelastic properties, coefficient of friction, and surface topography). The model and experimental results agreed with an average NRMSE of 6%.

The model was used to develop a capsule endoscope design application for use with MATLAB. The application allowed for capsule endoscope design parameter inputs along with tissue properties (experimental data or manual entry). Although the model agrees with data well for all regions of the GI tract, it is too computationally expensive for real-time application. Future recommendations include tuning the model solution algorithm so that it could be used for a real-time control algorithm. This algorithm would be dependent on real-time feedback for material properties, something that has yet to be development. Therefore, a parallel project could be to develop a device that is capable of instantaneous *in vivo* material properties measurement.

The end goal for the project is to develop an RCC that is capable of a fully autonomous colonoscopy. Before an autonomous robot can be produced, several subsystems have to be developed. The work presented

in this dissertation contributes to the locomotion system of the robot, focusing on enhancing friction through the use of micro-patterns.

Bibliography

[1] M. Moshkowitz, Y. Hirsch, I. Carmel, T. Duvdevany, I. Fabian, E. Willenz, and J. Cohen. A novel device for rapid cleaning of poorly prepared colons. Endoscopy, 42(10):834–836, October 2010.

[2] R. Kiesslich, N. Schuster, A. Hoffman, M. Goetz, P. Galle, E. Santo, and Z. Halpern. Medjet - a new co2-based disposable cleaning device allows safe and effective bowel cleansing during colonoscopy: a pilot study. Endoscopy, 44(8):767–771, August 2012.

[3] G. Ciuti, A. Menciassi, and P. Dario. Capsule endoscopy: From current achievements to open challenges. IEEE Reviews in Biomedical Engineering, 4:59–72, October 2011.

[4] Given Imaging Ltd. PillCam® Capsule Endoscopy User Manual, March 2013.

[5] S. N. Adler and Y. C. Metzger. Pillcam colon capsule endoscopy: recent advances and new insights. Therapeutic Advances in Gastroenterology, 4(4):265–268, July 2011.

[6] B. R. Mateescu, A. Bengus, M. Marinescu, F. Staniceanu, G. Micu, and L. Negreanu. First pillcam colon 2 capsule images of whipples disease: Case report and review of the literature. World Journal of Gastrointestinal Endoscopy, 4(12):575–578, December 2012.

[7] M. Keane, M. Shariff, J. Stocks, P. Trembling, P. Cohen, and G. Smith. Imaging of the small bowel by capsule endoscopy in whipples disease. Endoscopy, 41(S 02):E139, June 2009.

[8] K. Friedrich, S. Gehrke, W. Stremmel, and A. Sieg. First clinical trial of a newly developed capsule endoscope with panoramic side view for small bowel: A pilot study. Journal of Gastroenterology and Hepatology, 28(9):1496–1501, September 2013.

[9] S. Bang, J. Y. Park, S. Jeong, Y. H. Kim, H. B. Shim, T. S. Kim, D. H. Lee, and S. Y. Song. First clinical trial of the miro capsule endoscope by using a novel transmission technology: electric-field propagation. astrointestinal Endoscopy, 69(2):253–259, February 2009.

[10] S. G. Shah, J. C. Brooker, C. Thapar, C. B. Williams, and B. P. Saunders. Patient pain during colonoscopy: An analysis using real-time magnetic endoscope imaging. Endoscopy, 34(6):435–440, June 2002.

[11] A. K. Shergill, K. R. McQuaid, and D. Rempel. Ergonomics and gi endoscopy. Gastrointestinal Endoscopy, 70(1):145–153, July 2009.

[12] P. Valdastri, G. Ciuti, A. Verbeni, A. Menciassi, P. Dario, A. Arezzo, and M. Morino. Magnetic air capsule robotic system: proof of concept of a novel approach for painless colonoscopy. Surgical Endoscopy, 26(5):1238–1246, May 2012.

[13] G. Long, A. Fritscher-Ravens, C. A. Mosse, T. Mills, and P. Swain. The cath-cam: a new concept in colonoscopy. Gastrointestinal Endoscopy, 64(6):997–1001, December 2006.

[14] S. Groth, D. K. Rex, T. Rosch, and N. Hoepffner. High cecal intubation rates with a new computer-assisted colonoscope: A feasibility study. The American Journal of Gastroenterology, 106(6):1075–1080, June 2011.

[15] J. Striegel, R. Jakobs, J. V. Dam, U. Weickert, J. F. Riemann, and A. Eickhoff. Determining scope position during colonoscopy without use of ionizing radiation or magnetic imaging: the enhanced mapping ability of the neoguide endoscopy system. Surgical Endoscopy, 25(2):636–640, February 2011.

[16] Y. Chen, J. M. Oliveira, and I. W. Hunter. Sensor architecture for a two-actuator robotic endoscope tip. In 2011 Annual International Conference of the IEEE Engineering in Medicine and Biology Society, pages 8340–8343, 2011.

[17] L. Sliker, M. Kern, J. Schoen, and M. Rentschler. Surgical evaluation of a novel tethered robotic capsule endoscope using micro-patterned treads. Surgical Endoscopy, 26(10):2862–2869, October 2012.

[18] P. Valdastri, R. J. Webster, C. Quaglia, M. Quirini, A. Menciassi, and P. Dario. A new mechanism for mesoscale legged locomotion in compliant tubular environments. IEEE Transactions on Robotics, 25(5):1047–1057, October 2009.

[19] D. Gu and Y. Zhou. An approach to the capsule endoscopic robot with active drive motion. Journal of Zhejiang University SCIENCE A, 12(3):223–231, March 2011.

[20] W. Lin. A study on anchoring ability of three-leg micro intestinal robot. Engineering, 4(8):477–483, August 2012.

[21] H. M. Kim, S. Yang, J. Kim, S. Park, J. H. Cho, J. Y. Park, T. S. Kim, E.-S. Yoon, S. Y. Song, and S. Bang. Active locomotion of a paddling-based capsule endoscope in an in vitro and in vivo experiment (with videos). Gastrointestinal Endoscopy, 72(2):381–387, August 2010.

[22] I. De Falco, G. Tortora, P. Dario, and A. Menciassi. An integrated system for wireless capsule endoscopy in a liquid-distended stomach. IEEE Transactions on Biomedical Engineering, 61(3):794–804, March 2014.

[23] S. H. Woo, T. W. Kim, Z. Mohy-Ud-Din, I. Y. Park, and J.-H. Cho. Small intestinal model for electrically propelled capsule endoscopy. Biomedical Engineering OnLine, 10(108):1–20, December 2011.

[24] M. Simi, P. Valdastri, C. Quaglia, A. Menciassi, and P. Dario. Design, fabrication, and testing of a capsule with hybrid locomotion for gastrointestinal tract exploration. IEEE/ASME Transactions on Mechatronics, 15(2):170–180, April 2010.

[25] G. Tortora, S. Caccavaro, P. Valdastri, A. Menciassi, and P. Dario. Design of an autonomous swimming miniature robot based on a novel concept of magnetic actuation. In 2010 IEEE International Conference on Robotics and Automation (ICRA), pages 1592–1597, 2010.

[26] W. Chen, G. Yan, S. He, Q. Ke, Z. Wang, H. Liu, and P. Jiang. Wireless powered capsule endoscopy for colon diagnosis and treatment. Physiological Measurement, 34(11):1545–1561, November 2013.

[27] A. W. Mahoney, S. E. Wright, and J. J. Abbott. Managing the attractive magnetic force between an untethered magnetically actuated tool and a rotating permanent magnet. In 2013 IEEE International Conference on Robotics and Automation (ICRA), pages 5366–5371, 2013.

[28] G. Ciuti, N. Pateromichelakis, M. Sfakiotakis, P. Valdastri, A. Menciassi, D. P. Tsakiris, and P. Dario. A wireless module for vibratory motor control and inertial sensing in capsule endoscopy. Sensors and Actuators A: Physical, 186:270–276, October 2012.

[29] F. Cosentino, E. Tumino, G. Rubis Passoni, E. Morandi, and A. Capria. Functional evaluation of the endotics system, a new disposable self-propelled robotic colonoscope: in vitro tests and clinical trial. The International Journal of Artificial Organs, 32(8):517–527, October 2009.

[30] E. Tumino, R. Sacco, M. Bertini, M. Bertoni, G. Parisi, and A. Capria. Endotics system vs colonoscopy for the detection of polyps. World Journal of Gastroenterology, 16(43):5452–5456, November 2010.

[31] K. L. Obstein and P. Valdastri. Advanced endoscopic technologies for colorectal cancer screening. World Journal of Gastroenterology, 19(4):431–439, January 2013.

[32] S. Ramcharitar, M. S. Patterson, R. J. van Geuns, C. van Meighem, and P. W. Serruys. Technology insight: magnetic navigation in coronary interventions. Nature Clinical Practice Cardiovascular Medicine, 5(3):148–156, February 2008.

[33] P. Miloro, M. K. Llewellyn, S. Tognarelli, G. Ciuti, E. Sinibaldi, P. Dario, and A. Menciassi. An innovative platform for treatment of vascular obstructions: System design and preliminary results. In 2012 4th IEEE RAS EMBS International Conference on Biomedical Robotics and Biomechatronics (BioRob), pages 731–736, 2012.

[34] J.-F. Rey, H. Ogata, N. Hosoe, K. Ohtsuka, N. Ogata, K. Ikeda, H. Aihara, I. Pangtay, T. Hibi, S.-E. Kudo, and H. Tajiri. Blinded nonrandomized comparative study of gastric examination with a magnetically guided capsule endoscope and standard videoendoscope. Gastrointestinal Endoscopy, 75(2):373–381, February 2012.

[35] J. Keller, C. Fibbe, F. Volke, J. Gerber, A. C. Mosse, M. Reimann-Zawadzki, E. Rabinovitz, P. Layer, D. Schmitt, V. Andresen, U. Rosien, and P. Swain. Inspection of the human stomach using remote-controlled capsule endoscopy: a feasibility study in healthy volunteers (with videos). Gastrointestinal Endoscopy, 73(1):22–28, January 2011.

[36] F. Carpi, N. Kastelein, M. Talcott, and C. Pappone. Magnetically controllable gastrointestinal steering of video capsules. IEEE Transactions on Biomedical Engineering, 58(2):231–234, February 2011.

[37] F. Carpi and C. Pappone. Magnetic maneuvering of endoscopic capsules by means of a robotic navigation system. IEEE Transactions on Biomedical Engineering, 56(5):1482–1490, May 2009.

[38] G. Ciuti, P. Valdastri, A. Menciassi, and P. Dario. Robotic magnetic steering and locomotion of capsule endoscope for diagnostic and surgical endoluminal procedures. Robotica, 28(2):199–207, October 2009.

[39] G. Lucarini. Electromagnetic design for capsule endoscope navigation: a preliminary study. In The 3rd Joint Workshop on New Technologies for Computer/Robot Assisted Surgery, September 2013.

[40] E. Morita, N. Ohtsuka, Y. Shindo, S. Nouda, T. Kuramoto, T. Inoue, M. Murano, E. Umegaki, and K. Higuchi. In vivo trial of a driving system for a self-propelling capsule endoscope using a magnetic field (with video). Gastrointestinal Endoscopy, 72(4):836–840, October 2010.

[41] J. L. Gorlewicz, S. Battaglia, B. F. Smith, G. Ciuti, J. Gerding, A. Menciassi, K. L. Obstein, P. Valdastri, and R. J. Webster. Wireless insufflation of the gastrointestinal tract. IEEE Transactions on Biomedical Engineering, 60(5):1225–1233, May 2013.

[42] J. G. Albert, M. Friedrich-Rust, G. Woeste, C. Strey, W. O. Bechstein, S. Zeuzem, and C. Sarrazin. Benefit of a clipping device in use in intestinal bleeding and intestinal leakage. Gastrointestinal Endoscopy, 74(2):389–397, August 2011.

[43] D. von Renteln, H.-U. Rudolph, A. Schmidt, M. C. Vassiliou, and K. Caca. Endoscopic closure of duodenal perforations by using an over-the-scope clip: a randomized, controlled porcine study. Gastrointestinal Endoscopy, 71(1):131–138, January 2010.

[44] F. Junquera, E. Martnez-Bauer, M. Miquel, M. Fort, M. Gallach, E. Brullet, and R. Campo. [ovesco: a promising system for endoscopic closure of gastrointestinal tract perforations]. Journal of Gastroenterology and Hepatology, 34(8):568–572, October 2011.

[45] P. D. Siersema, A. Rastogi, A. M. Leufkens, P. A. Akerman, K. Azzouzi, R. I. Rothstein, F. P. Vleggaar, A. Repici, G. Rando, P. I. Okolo, O. Dewit, A. Ignjatovic, E. Odstrcil, J. East, P. H. Deprez, B. P. Saunders, A. N. Kalloo, B. Creel, V. Singh, A. M. Lennon, and D. C. DeMarco. Retrograde-viewing device improves adenoma detection rate in colonoscopies for surveillance and diagnostic workup. World J. Gastroenterol., 18(26):3400–3408, July 2012.

[46] I. M. Gralnek, P. D. Siersema, Z. Halpern, O. Segol, A. Melhem, A. Suissa, E. Santo, A. Sloyer, J. Fenster, L. M. G. Moons, V. K. Dik, R. B. DAgostino Jr, and D. K. Rex. Standard forward-viewing colonoscopy versus full-spectrum endoscopy: an international, multicentre, randomised, tandem colonoscopy trial. The Lancet Oncology, 15(3):353–360, March 2014.

[47] T. Uraoka, S. Tanaka, T. Matsumoto, T. Matsuda, S. Oka, T. Moriyama, R. Higashi, and Y. Saito. A novel extra-wide-angleview colonoscope: a simulated pilot study using anatomic colorectal models. Gastrointestinal Endoscopy, 77(3):480–483, March 2013.

[48] C. Cavallotti, M. Piccigallo, E. Susilo, P. Valdastri, A. Menciassi, and P. Dario. An integrated vision system with autofocus for wireless capsular endoscopy. Sensors and Actuators A: Physical, 156(1):72–78, November 2009.

[49] S. W. Seo, S. Han, J. H. Seo, Y. M. Kim, M. S. Kang, N. K. Min, W. B. Choi, and M. Y. Sung. Microelectromechanical-system-based variable-focus liquid lens for capsule endoscopes. Japanese Journal of Applied Physics, 48(5):052404–1–052404–4, May 2009.

[50] R. Haidry and L. Lovat. Medical Imaging in Clinical Practice. InTech.

[51] R. Singh, Y. M. Bhat, P. H. Thurairajah, M. P. Shetti, M. Jayanna, G. Nind, W. Tam, R. Walmsey, M. Bourke, A. Moss, R. Chen, P. Bampton, I. Roberts-Thomson, M. Schoeman, and G. Tucker. Is narrow band imaging superior to high-definition white light endoscopy in the assessment of diminutive colorectal polyps? Journal of Gastroenterology and Hepatology, 28(3):472–478, March 2013.

[52] P. Sharma, R. H. Hawes, A. Bansal, N. Gupta, W. Curvers, A. Rastogi, M. Singh, M. Hall, S. C. Mathur, S. B. Wani, B. Hoffman, S. Gaddam, P. Fockens, and J. J. Bergman. Standard endoscopy with random biopsies versus narrow band imaging targeted biopsies in barretts oesophagus: a prospective, international, randomised controlled trial. Gut, 62(1):15–21, January 2013.

[53] Lan-Rong Dung and Yin-Yi Wu. A wireless narrowband imaging chip for capsule endoscope. IEEE Transactions on Biomedical Circuits and Systems, 4(6):462–468, December 2010.

[54] M. A. Al-Rawhani, D. Chitnis, J. Beeley, S. Collins, and D. R. S. Cumming. Design and implementation of a wireless capsule suitable for autofluorescence intensity detection in biological tissues. IEEE Transactions on Biomedical Engineering, 60(1):55–62, January 2013.

[55] B. Li and M. Q.-H. Meng. Computer-aided detection of bleeding regions for capsule endoscopy images. IEEE Transactions on Biomedical Engineering, 56(4):1032–1039, April 2009.

[56] G. Pan, G. Yan, X. Qiu, and J. Cui. Bleeding detection in wireless capsule endoscopy based on probabilistic neural network. Journal of Medical Systems, 35(6):1477–1484, December 2011.

[57] C. K. Poh, T. M. Htwe, L. Li, W. Shen, J. Liu, J. H. Lim, K.-L. Chan, and P. C. Tan. Multi-level local feature classification for bleeding detection in wireless capsule endoscopy images. In IEEE Conference on Cybernetics and Intelligent Systems (CIS), pages 76–81, 2010.

[58] L. Crespo-Pérez and E. Vázquez-Sequeiros. Virtual chromoendoscopy as an adjuvant to capsule endoscopy: a step ahead? Rev. Esp. Enfermedades Dig. Organo Of. Soc. Esp. Patol. Dig., 104(5):227–230, May 2012.

[59] P. Valdastri, C. Quaglia, E. Susilo, A. Menciassi, P. Dario, C. Ho, G. Anhoeck, and M. Schurr. Wireless therapeutic endoscopic capsule: in vivo experiment. Endoscopy, 40(12):979–982, December 2008.

[60] K. Kong, J. Cha, D. Jeon, and D. Cho. A rotational micro biopsy device for the capsule endoscope. In IEEE/RSJ International Conference on Intelligent Robots and Systems (IROS), pages 1839–1843, 2005.

[61] K. Kong, D. Jeon, S. Yim, and S. Choi. A robotic biopsy device for capsule endoscopy. Journal of Medical Devices, 6(3):031004–1–031004–9, July 2012.

[62] M. Simi, G. Gerboni, A. Menciassi, and P. Valdastri. Magnetic torsion spring mechanism for a wireless biopsy capsule. Journal of Medical Devices, 7(4):041009–1–041009–9, September 2013.

[63] S. Yim, E. Gultepe, D. H. Gracias, and M. Sitti. Biopsy using a magnetic capsule endoscope carrying, releasing and retrieving untethered micro-grippers. IEEE Transactions on Biomedical Engineering, 61(2):513–521, February 2014.

[64] C. Quaglia, S. Tognarelli, E. Sinibaldi, N. Funaro, P. Dario, and A. Menciassi. Wireless robotic capsule for releasing bioadhesive patches in the gastrointestinal tract. Journal of Medical Devices, 8(1):014503–1–014503–6, December 2013.

[65] S. P. Woods and T. G. Constandinou. Wireless capsule endoscope for targeted drug delivery: Mechanics and design considerations. IEEE Transactions on Biomedical Engineering, 60(4):945–953, April 2013.

[66] S. Yim, K. Goyal, and M. Sitti. Magnetically actuated soft capsule with the multimodal drug release function. IEEE/ASME Transactions on Mechatronics, 18(4):1413–1418, August 2013.

[67] B. Chander, N. Hanley-Williams, Y. Deng, and A. Sheth. 24 versus 48-hour bravo ph monitoring. Journal of Clinical Gastroenterology, 46(3):197–200, March 2012.

[68] A. de Hoyos and E. A. Esparza. Technical problems produced by the bravo ph test in nonerosive reflux disease patients. World Journal of Gastroenterology, 16(25):3183–3186, July 2010.

[69] D. Ang, E. K. Teo, T. L. Ang, J. Ong, C. H. Poh, J. Tan, and K. M. Fock. To bravo or not? a comparison of wireless esophageal ph monitoring and conventional ph catheter to evaluate non-erosive gastroesophageal reflux disease in a multiracial asian cohort. Journal of Digestive Diseases, 11(1):19–27, February 2010.

[70] S. S. C. Rao, M. Camilleri, W. L. Hasler, A. H. Maurer, H. P. Parkman, R. Saad, M. S. Scott, M. Simren, E. Soffer, , and L. Szarka. Evaluation of gastrointestinal transit in clinical practice: position paper of the american and european neurogastroenterology and motility societies. Neurogastroenterology and Motility, 23(1):8–23, January 2011.

[71] A. D. Ruddock, G. A. Tew, and A. J. Purvis. Reliability of intestinal temperature using an ingestible telemetry pill system during exercise in a hot environment. The Journal of Strength and Conditioning Research, 28(3):861–869, March 2014.

[72] R. Niedermann, E. Wyss, S. Annaheim, A. Psikuta, S. Davey, and R. M. Rossi. Prediction of human core body temperature using non-invasive measurement methods. International Journal of Biometeorology, 58(1):7–15, January 2014.

[73] C. M. C. Jacquot, L. Schellen, B. R. Kingma, M. A. van Baak, and W. D. van Marken Lichtenbelt. Influence of thermophysiology on thermal behavior: the essentials of categorization. Physiology and Behavior, 128:180–187, April 2014.

[74] A. P. Hunt, A. W. Parker, and I. B. Stewart. Heat strain and hydration status of surface mine blast crew workers. Journal of Occupational and Environmental Medicine, 56(4):409–414, April 2014.

[75] I. B. Stewart, K. L. Stewart, C. J. Worringham, and J. T. Costello. Physiological tolerance times while wearing explosive ordnance disposal protective clothing in simulated environmental extremes. Plos One, 9(2):e83740–1–e83740–7, February 2014.

[76] H. Chatrath and D. K. Rex. Potential screening benefit of a colorectal imaging capsule that does not require bowel preparation. Journal of Clinical Gastroenterology, 48(1):52–54, January 2014.

[77] M. J. Gora, J. S. Sauk, R. W. Carruth, K. A. Gallagher, M. J. Suter, N. S. Nishioka, L. E. Kava, M. Rosenberg, B. E. Bouma, and G. J. Tearney. Tethered capsule endomicroscopy enables less invasive imaging of gastrointestinal tract microstructure. Nature Medicine, 19(2):238–240, February 2013.

[78] Z. Dubravcsik A. Szepes P. Pák, G. Balogh and L. Madácsy. Magnetic maneuvering of capsule endoscopy: Preliminary phantom tests in an experimental colonic model. Zeitschrift für Gastroenterologie, 51(5):51–A49, May 2013.

[79] J. H. Pikul, H. Gang Zhang, J. Cho, P. V. Braun, and W. P. King. High-power lithium ion microbatteries from interdigitated three-dimensional bicontinuous nanoporous electrodes. Nature Communications, 4:1732, April 2013.

[80] N. Singh, C. Galande, A. Miranda, A. Mathkar, W. Gao, A. L. M. Reddy, A. Vlad, and P. M. Ajayan. Paintable battery. Scientific Reports, 2:481–1–481–5, June 2012.

[81] S. Yu, Y. guozheng, J. Zhiwei, and Z. Bingquan. The design and implementation of the wireless power transmission system of video capsule endoscopy. In International Conference on Biomedical Engineering and Biotechnology (iCBEB), pages 578–581, 2012.

[82] G.F. Dakin and M. Gagner. Comparison of laparoscopic skills performance between standard instruments and two surgical robotic systems. Surgical Endoscopy And Other Interventional Techniques, 17(4):574–579, 2003.

[83] D. Nio, W.A. Bemelman, K.T. Boer, M.S. Dunker, D.J. Gouma, and T.M. Gulik. Efficiency of manual versus robotical (zeus) assisted laparoscopic surgery in the performance of standardized tasks. Surgical Endoscopy And Other Interventional Techniques, 16(3):412–415, 2002.

[84] M. Cenk Çavuşoğlu, Winthrop Williams, Frank Tendick, and S. Shankar Sastry. Robotics for telesurgery: second generation berkeley/ucsf laparoscopic telesurgical workstation and looking towards the future applications. Industrial Robot: An International Journal, 30(1):22–29, 2003.

[85] M. Cenk Çavuşoğlu and S. Shankar Sastry. Telesurgery and surgical simulation: Haptic interfaces to real and virtual surgical environments. In in Touch in Virtual Environments, Ser, IMSC Series in Multimedia, pages 217–237, 2001.

[86] Wei-Tech Ang. Active Tremor Compensation in Handheld Instrument for Microsurgery. PhD thesis, Robotics Institute, Carnegie Mellon University, Pittsburgh, PA, May 2004.

[87] C.N. Riviere, Wei Tech Ang, and P.K. Khosla. Toward active tremor canceling in handheld microsurgical instruments. IEEE Transactions on Robotics and Automation, 19(5):793–800, Oct 2003.

[88] Jacob Rosen, Mitch Lum, Denny Trimble, Blake Hannaford, and Mika Sinanan. Spherical mechanism analysis of a surgical robot for minimally invasive surgery – analytical and experimental approaches. Studies in Health Technology and Informatics, 111:422–428, 2005.

[89] Andrew Miller, Peter Allen, and Dennis Fowler. In-vivo stereoscopic imaging system with 5 degrees-of-freedom for minimal access surgery. Studies in Health Technology and Informatics, 98:234–240, 2004.

[90] Tie Hu, Peter K. Allen, Roger Goldman, Nancy J. Hogle, and Dennis L. Fowler. In vivo pan/tilt endoscope with integrated light source, zoom and auto-focusing. Studies in Health Technology and Informatics, 132:174–179, 2008.

[91] N. A. Patronik, M. A. Zenati, and C. N. Riviere. Preliminary evaluation of a mobile robotic device for navigation and intervention on the beating heart. Computer Aided Surgery, 10(4):225–232, 2005.

[92] Nicholas A. Patronik, Marco A. Zenati, and Cameron N. Riviere. Crawling on the heart: A mobile robotic device for minimally invasive cardiac interventions. In Christian Barillot, DavidR. Haynor, and Pierre Hellier, editors, Medical Image Computing and Computer-Assisted Intervention MICCAI 2004, volume 3217 of Lecture Notes in Computer Science, pages 9–16. Springer Berlin Heidelberg, 2004.

[93] Mark E. Rentschler, Shane M. Farritor, and Karl D. Iagnemma. Mechanical design of robotic in vivo wheeled mobility. Journal of Mechanical Design, 129(10):1037–1045, Oct 2007.

[94] Mark E. Rentschler, Adnan Hadzialic, Jason Dumpert, Stephen R. Platt, Shane Farritor, and Dmitry Oleynikov. In vivo robots for laparoscopic surgery. Studies in Health Technology and Informatics, 98:316–322, 2004.

[95] M. Rentschler, J. Dumpert, S. Platt, S. Farritor, and D. Oleynikov. Mobile in vivo robots can assist in abdominal exploration, Apr 2005.

[96] Mark E. Rentschler, Jason Dumpert, Stephen R. Platt, Karl Iagnemma, Dmitry Oleynikov, and Shane M. Farritor. An in vivo mobile robot for surgical vision and task assistance. Journal of Medical Devices, 1(1):23–29, Mar 2007.

[97] T. Fukuda, Shuxiang Guo, K. Kosuge, F. Arai, M. Negoro, and K. Nakabayashi. Micro active catheter system with multi degrees of freedom. In Proceedings of the 1994 IEEE International Conference on Robotics and Automation (ICRA), volume 3, pages 2290–2295, May 1994.

[98] K. Suzumori, S. Iikura, and H. Tanaka. Development of flexible microactuator and its applications to robotic mechanisms. In Proceedings of the 1991 IEEE International Conference on Robotics and Automation (ICRA), volume 2, pages 1622–1627, Apr 1991.

[99] L. Phee, D. Accoto, A. Menciassi, C. Stefanini, M.C. Carrozza, and P. Dario. Analysis and development of locomotion devices for the gastrointestinal tract. Biomedical Engineering, IEEE Transactions on, 49(6):613–616, June 2002.

[100] A. M. Flynn, K. R. Udayakumar, D. S. Barrett, J. D. McLurkin, D. L. Franck, and A. N. Shectman. Tomorrow's surgery: Micromotors and microrobots for minimally invasive procedures. Minimally Invasive Therapy & Allied Technologies, 7(4):343–352, 1998.

[101] Paul Breedveld, Danielle E. van der Kouwe, and Maria A. J. van Gorp. Locomotion through the intestine by means of rolling stents. In Procedings of the ASME 2004 International Design Engineering Technical Conferences and Computers and Information in Engineering Conference, volume 2, pages 963–969, Salt Lake City, Utah, USA, Jan 2004. ASME.

[102] Young-Tae Kim and Dae-Eun Kim. A novel propelling mechanism based on frictional interaction for endoscope robot. In Jianbin Luo, Yonggang Meng, Tianmin Shao, and Qian Zhao, editors, Advanced Tribology, pages 859–860. Springer Berlin Heidelberg, 2010.

[103] Cesare Stefanini, Arianna Menciassi, and Paolo Dario. Modeling and experiments on a legged microrobot locomoting in a tubular, compliant and slippery environment. The International Journal of Robotics Research, 25(5-6):551–560, 2006.

[104] A. Menciassi, C. Stefanini, S. Gorini, G. Pernorio, B. Kim, J.O. Park, and P. Dario. Locomotion of a legged capsule in the gastrointestinal tract: theoretical study and preliminary technological results. In Proceedings of the 26th Annual International Conference of the IEEE Engineering in Medicine and Biology Society (IEMBS), volume 1, pages 2767–2770, Sept 2004.

[105] A. Menciassi, A. Moglia, S. Gorini, G. Pernorio, C. Stefanini, and P. Dario. Shape memory alloy clamping devices of a capsule for monitoring tasks in the gastrointestinal tract. Journal of Micromechanics and Microengineering, 15(11):2045–2055, 2005.

[106] Kanako Harada, Denny Oetomo, Ekawahyu Susilo, Arianna Menciassi, David Daney, Jean-Pierre Merlet, and Paolo Dario. A reconfigurable modular robotic endoluminal surgical system: vision and preliminary results. Robotica, 28:171–183, Mar 2010.

[107] M.E. Karagozler, E. Cheung, Jiwoon Kwon, and M. Sitti. Miniature endoscopic capsule robot using biomimetic micro-patterned adhesives. In The First IEEE/RAS-EMBS International Conference on Biomedical Robotics and Biomechatronics (BioRob), pages 105–111, Feb 2006.

[108] E. Cheung, M.E. Karagozler, Sukho Park, Byungkyu Kim, and M. Sitti. A new endoscopic microcapsule robot using beetle inspired microfibrillar adhesives. In Proceedings of the 2005 IEEE/ASME International Conference on Advanced Intelligent Mechatronics, pages 551–557, July 2005.

[109] P. Glass, E. Cheung, and M. Sitti. A legged anchoring mechanism for capsule endoscopes using micropatterned adhesives. IEEE Transactions on Biomedical Engineering, 55(12):2759–2767, Dec 2008.

[110] Mark E. Rentschler and John D. Reid. The development of a material model and wheeltissue interaction for simulating wheeled surgical robot mobility. Computer Methods in Biomechanics and Biomedical Engineering, 12(2):239–248, 2009. PMID: 19012064.

[111] Daniel Blero and Jacques Deviere. Endoscopic complications-avoidance and management. Nature Reviews Gastroenterology & Hepatology, 9(3):162–172, Mar 2012.

[112] D. Cave, P. Legnani, R. de Franchis, and B. S. Lewis. Icce consensus for capsule retention. Endoscopy, 37(10):1065–1067, Oct 2005.

[113] Zhuan Liao, Rui Gao, Can Xu, and Zhao-Shen Li. Indications and detection, completion, and retention rates of small-bowel capsule endoscopy: a systematic review. Gastrointestinal Endoscopy, 71(2):280–286, Feb 2010.

[114] Levin J. Sliker, Jonathan A. Schoen, Mark E. Rentschler, and Xin Wang. Micropatterned treads for in vivo robotic mobility. Journal of Medical Devices, 4(4):041006–1–041006–8, Dec 2010.

[115] R. G. Beutel and S. N. Gorb. Ultrastructure of attachment specializations of hexapods (arthropoda): evolutionary patterns inferred from a revised ordinal phylogeny. Journal of Zoological Systematics and Evolutionary Research, 39(4):177–207, 2001.

[116] Rolf G. Beutel and Stanislav N. Gorb. A revised interpretation of the evolution of attachment structures in hexapoda with special emphasis on mantophasmatodea. Arthropod Systematics & Phylogeny, 64(1):3–25, Oct 2006.

[117] Stanislav N. Gorb and Matthias Scherge. Biological microtribology: anisotropy in frictional forces of orthopteran attachment pads reflects the ultrastructure of a highly deformable material. Proceedings of the Royal Society of London. Series B: Biological Sciences, 267(1449):1239–1244, 2000.

[118] B. N. J. Persson and S. Gorb. The effect of surface roughness on the adhesion of elastic plates with application to biological systems. The Journal of Chemical Physics, 119(21):11437–11444, 2003.

[119] Elisa Buselli, Virginia Pensabene, Piero Castrataro, Pietro Valdastri, Arianna Menciassi, and Paolo Dario. Evaluation of friction enhancement through soft polymer micro-patterns in active capsule endoscopy. Measurement Science and Technology, 21(10):105802–1–105802–7, 2010.

[120] Benjamin S. Terry, Allison B. Lyle, Jonathan A. Schoen, and Mark E. Rentschler. Preliminary mechanical characterization of the small bowel for in vivo robotic mobility. Journal of Biomechanical Engineering, 133(9):091010–1–091010–7, Oct 2011.

[121] American Cancer Society. Cancer facts & figures 2014, 2014. Atlanta: American Cancer Society. www.cancer.org.

[122] Freddie Bray, Jian-Song Ren, Eric Masuyer, and Jacques Ferlay. Global estimates of cancer prevalence for 27 sites in the adult population in 2008. International Journal of Cancer, 132(5):1133–1145, 2013.

[123] Cancer Research UK. Bowel cancer (colorectal cancer), 2009. www.cancerresearchuk.org.

[124] Oralia Garcia Dominic, Thomas McGarrity, Mark Dignan, and Eugene J Lengerich. American college of gastroenterology guidelines for colorectal cancer screening 2008. The American journal of gastroenterology, 104(10):2626–2629, Oct 2009.

[125] Sidney Winawer, Robert Fletcher, Douglas Rex, John Bond, Randall Burt, Joseph Ferrucci, Theodore Ganiats, Theodore Levin, Steven Woolf, David Johnson, Lynne Kirk, Scott Litin, Clifford Simmang, and Gastrointestinal Consortium Panel. Colorectal cancer screening and surveillance: clinical guidelines and rationale-update based on new evidence. Gastroenterology, 124(2):544–560, Feb 2003.

[126] Wendy S Atkin, Rob Edwards, Ines Kralj-Hans, Kate Wooldrage, Andrew R Hart, John MA Northover, D Max Parkin, Jane Wardle, Stephen W Duffy, and Jack Cuzick. Once-only flexible sigmoidoscopy screening in prevention of colorectal cancer: a multicentre randomised controlled trial. The Lancet, 375(9726):1624–1633, May 2010.

[127] Luis Bujanda, Cristina Sarasqueta, Leire Zubiaurre, Angel Cosme, Carmen Muoz, Araceli Snchez, Cristina Martn, Llucia Tito, Virginia Piol, Antoni Castells, Xavier Llor, Rosa M Xicola, Elisenda Pons, Juan Clofent, Mara L de Castro, Jaime Cuquerella, Enrique Medina, Ana Gutierrez, Juan I Arenas, and Rodrigo Jover. Low adherence to colonoscopy in the screening of first-degree relatives of patients with colorectal cancer. Gut, 56(12):1714–1718, 2007.

[128] L.J. Sliker, M.D. Kern, and M.E. Rentschler. Preliminary experimental results and modeling for a four degree of freedom automated traction measurement platform for quantitative evaluation of in vivo robotic capsule colonoscopy mobility effectiveness. In Proceedings of the 2013 IEEE International Conference on Robotics and Automation (ICRA), pages 4875–4880, May 2013.

[129] Sung Hoon Kim and K. Ishiyama. Magnetic robot and manipulation for active-locomotion with targeted drug release. IEEE/ASME Transactions on Mechatronics, 19(5):1651–1659, Oct 2014.

[130] Benjamin S. Terry, Anna C. Passernig, Morgan L. Hill, Jonathan A. Schoen, and Mark E. Rentschler. Small intestine mucosal adhesivity to in vivo capsule robot materials. Journal of the Mechanical Behavior of Biomedical Materials, 15:24–32, 2012.

[131] Stanislav N. Gorb. Attachment Devices of Insect Cuticle. Springer, New York, NY, 2001.

[132] Jiwoon Kwon, Eugene Cheung, Sukho Park, and Metin Sitti. Friction enhancement via micro-patterned wet elastomer adhesives on small intestinal surfaces. Biomedical Materials, 1(4):216–220, 2006.

[133] Allison B. Lyle, Jeffrey T. Luftig, and Mark E. Rentschler. A tribological investigation of the small bowel lumen surface. Tribology International, 62:171–176, 2013.

[134] L.J. Sliker and M.E. Rentschler. The design and characterization of a testing platform for quantitative evaluation of tread performance on multiple biological substrates. IEEE Transactions on Biomedical Engineering, 59(9):2524–2530, Sept 2012.

[135] Xin Wang, Jonathan A. Schoen, and Mark E. Rentschler. A quantitative comparison of soft tissue compressive viscoelastic model accuracy. Journal of the Mechanical Behavior of Biomedical Materials, 20:126–136, 2013.

[136] Benjamin S. Terry, Jonathan A. Schoen, and Mark E. Rentschler. Measurements of the contact force from myenteric contractions on a solid bolus. Journal of Robotic Surgery, 7(1):53–57, 2013.

[137] C. Canudas de Wit and P. Tsiotras. Dynamic tire friction models for vehicle traction control. In Proceedings of the 38th IEEE Conference on Decision and Control, volume 4, 1999.

[138] J.S. Kim, I.H. Sung, Y.T. Kim, E.Y. Kwon, D.E. Kim, and Y.H. Jang. Experimental investigation of frictional and viscoelastic properties of intestine for microendoscope application. Tribology Letters, 22(2):143–149, 2006.

[139] J.S. Kim, I.H. Sung, Y.T. Kim, D.E. Kim, and Y.H. Jang. Analytical model development for the prediction of the frictional resistance of a capsule endoscope inside an intestine. Proceedings of the Institution of Mechanical Engineers, Part H: Journal of Engineering in Medicine, 221(8):837–845, 2007.

[140] X. Wang and M.Q. Meng. An experimental study of resistant properties of the small intestine for an active capsule endoscope. Proceedings of the Institution of Mechanical Engineers, Part H: Journal of Engineering in Medicine, 224(1):107–118, 2010.

[141] Cheng Zhang, Hao Liu, Renjia Tan, and Hongyi Li. Modeling of velocity-dependent frictional resistance of a capsule robot inside an intestine. Tribology Letters, 47(2):295–301, 2012.

[142] Allison B. Lyle, Benjamin S. Terry, Jonathan A. Schoen, and Mark E. Rentschler. Preliminary friction force measurements on small bowel lumen when eliminating sled edge effects. Tribology Letters, 51(3):377–383, 2013.

[143] Ze Wang, Xia Ye, and Ming Zhou. Frictional resistance model of capsule endoscope in the intestine. Tribology Letters, 51(3):409–418, 2013.

[144] Thomas K. Wu. Occult injuries during colonoscopy: Measurement of forces required to injure the colon and report of cases. Gastrointestinal Endoscopy, 24(5):236–238, 1978.

[145] Viacheslav I. Egorov, Ilia V. Schastlivtsev, Edward V. Prut, Andrey O. Baranov, and Robert A. Turusov. Mechanical properties of the human gastrointestinal tract. Journal of Biomechanics, 35(10):1417–1425, Oct 2002.

[146] Mert Sedef, Evren Samur, and C. Basdogan. Real-time finite-element simulation of linear viscoelastic tissue behavior based on experimental data. IEEE Computer Graphics and Applications, 26(6):58–68, Nov 2006.

[147] Pietro Valdastri, Massimiliano Simi, and Robert J. Webster. Advanced technologies for gastrointestinal endoscopy. Annual Review of Biomedical Engineering, 14(1):397–429, 2012.

[148] Gerhard A. Holzapfel. Nonlinear solid mechanics : a continuum approach for engineering. Wiley, Chichester, New York, 2000.

[149] R. W. Ogden. Large deformation isotropic elasticity - on the correlation of theory and experiment for incompressible rubberlike solids. Proceedings of the Royal Society of London. Series A, Mathematical and Physical Sciences, 326(1567):565–584, Feb 1972.

[150] M. F. Beatty and D. O. Stalnaker. The poisson function of finite elasticity. Journal of Applied Mechanics, 53(4):807–813, Dec 1986.

[151] B. Nordon. On the compression of a cylinder in contact with a plane surface. NBS Internal Report, pages 1–67, July 1973.

[152] V. Popov. Contact Mechanics and Friction: Physical Principles and Applications. Springer Berlin Heidelberg, 2010.

[153] K. L. Johnson. Contact Mechanics. Cambridge University Press, 1985. Cambridge Books Online.

[154] Given Imaging Ltd. Overview of products, 2011. www.givenimaging.com.

[155] Vasilis Ntziachristos and Britton Chance. Probing physiology and molecular function using optical imaging - applications to breast cancer. Breast Cancer Research, 3(1):41–46, Nov 2000.

[156] World Health Organization. Cancer mortality and morbidity, 2014.

[157] Cancer Research UK. Bowel cancer survival statistics, 2014.

[158] Levin Sliker and Gastone Ciuti. Flexible and capsule endoscopy for screening, diagnosis and treatment. Expert Review of Medical Devices, 11(6):649–666, 2014.

[159] G. Ciuti, R. Donlin, P. Valdastri, A. Arezzo, A. Menciassi, M. Morino, and P. Dario. Robotic versus manual control in magnetic steering of an endoscopic capsule. Endoscopy, 42(2):148–152, February 2010.

[160] A. Uehara and K. Hoshina. Capsule endoscope norika system. Minimally Invasive Therapy & Allied Technologies, 12(5):227–234, 2003.

[161] Yoshihiro Kusuda. A further step beyond wireless capsule endoscopy. Sensor Review, 25(4):259–260, 2005.

[162] Chungseon Yu, Juhyun Kim, Hyunchul Choi, Jongho Choi, Semi Jeong, Kyoungrae Cha, Jong oh Park, and Sukho Park. Novel electromagnetic actuation system for three-dimensional locomotion and drilling of intravascular microrobot. Sensors and Actuators A: Physical, 161(1-2):297–304, 2010.

[163] Edpard P. Furlani. Permanent magnet and electromechanical devices: materials, analysis, and applications. Academic Press, 2001.

[164] Jiwoon Kwon, Sukho Park, Byungkyu Kim, and Jong-Oh Park. Bio-material property measurement system for locomotive mechanism in gastro-intestinal tract. In Proceedings of the 2005 IEEE International Conference on Robotics and Automation (ICRA), pages 1303–1308. IEEE, 2005. doi: 10.1109/ROBOT.2005.1570295.

[165] Cheng Zhang, Hao Liu, and Hongyi Li. Modeling of frictional resistance of a capsule robot moving in the intestine at a constant velocity. Tribology Letters, 53(1):71–78, 2014.

[166] Cheng Zhang, Hao Liu, and Hongyi Li. Experimental investigation of intestinal frictional resistance in the starting process of the capsule robot. Tribology International, 70(0):11 – 17, 2014.

[167] N.K. Baek, I.H. Sung, and D.E. Kim. Frictional resistance characteristics of a capsule inside the intestine for microendoscope design. Proceedings of the Institution of Mechanical Engineers, Part H: Journal of Engineering in Medicine, 218(3):193–201, 2004.

[168] Cheng Zhang, Hao Liu, Renjia Tan, and Hongyi Li. Interaction model between capsule robot and intestine based on nonlinear viscoelasticity. Proceedings of the Institution of Mechanical Engineers, Part H: Journal of Engineering in Medicine, 228(3):287–296, 2014.

[169] Suck-Ho Lee, Il-Kwun Chung, Sun-Joo Kim, Jin-Oh Kim, Bong-Min Ko, Young Hwangbo, Won Ho Kim, Dong Hun Park, Sang Kil Lee, Cheol Hee Park, Il-Hyun Baek, Dong Il Park, Seun-Ja Park, Jeong-Seon Ji, Byung-Ik Jang, Yoon-Tae Jeen, Jeong Eun Shin, Jeong-Sik Byeon, Chang-Soo Eun, and Dong Soo Han. An adequate level of training for technical competence in screening and diagnostic colonoscopy: a prospective multicenter evaluation of the learning curve. Gastrointestinal Endoscopy, 67(4):683–689, 2008.

[170] Hong-Jun Park, Jin-Heon Hong, Hyun-Soo Kim, Bo-Ra Kim, So-Yeon Park, Ki-Won Jo, and Jae-Woo Kim. Predictive factors affecting cecal intubation failure in colonoscopy trainees. BMC Medical Education, 13(5):1–7, 2013.

[171] C. Di Natali, M. Beccani, K. L. Obstein, and P. Valdastri. A wireless platform for in vivo measurement of resistance properties of the gastrointestinal tract. Physiological Measurement, 35(7):1197–1214, 2014.

Appendix A

Derivation of N

Advantages of magnetic actuation systems include minimal, if any, capsule size increase to accommodate the IPM and no increase in capsule complexity from the addition of onboard actuators. Drawbacks of the magnetic actuation systems include large external platform (*i.e.*, magnet, robotic arm, and controller) size, electromagnetic interference with other devices in the operating room, and actuation failure if the drag force imposed on the capsule is not large enough to overcome the frictional resistance.

The magnetic capsule locomotion system described in [38] demonstrated a reliable empirical control of a capsule, and is therefore used here as a basis to experimentally determine N. A capsule mockup (Fig. A.1) was fabricated to mimic a PillCam Colon 2 capsule ($D = 11.6 \; mm$, $R = D/2$, $L = 31.5 \; mm$, $m = 3.22 \; g$) with respect to size and hold 3 cylindrical (diameter $d_{Nd} = 3.1 \; mm$ and length $l_{Nd} = 19 \; mm$) neodymium (Nd) magnets which occupied 15% of the capsule volume. The capsule was fixed to a load cell (Nano17, ATI Industrial Automation, Apex, NC, USA) and the load cell was tared. A cylindrical magnet (NdFeB 1.38T magnet, Magnetworld AG, Jena, Germany) was fixed to the end effector of a 6 DOF robotic arm (Melfa RV-6SL, Mitsubishi, Tokyo, Japan), and was centered (by minimizing x- and z- forces) 150 mm (d_y) above the capsule mockup. Dynamic vertical attraction force due to the magnet ($F_{\vec{B}_y}$) was measured (at a rate of 10 kHz) as the magnet was lowered at a rate of 5 mm/s until $d_y = 10 \; mm$. Then, static vertical attraction force was measured at 5 mm increments from $d_y = 10 \; mm$ to $d_y = 150 \; mm$. The static and dynamic attraction forces are displayed in Fig. A.2. The experimental setup to measure attraction force is shown in Fig. A.1.

The volume of the capsule mockup is:

$$V_{capsule} = \pi \left(D/2 \right)^2 \left(L - D \right) + \frac{4\pi}{3} \left(D/2 \right)^3 = 2920.4 \ mm^3 \tag{A.1}$$

The volume of the 3 cylindrical neodymium internal permanent magnets (IPMs) is:

$$V_{Nd} = \frac{3\pi}{4} l_{Nd} d_{Nd}{}^2 = 430.2 \ mm^3 \tag{A.2}$$

The percent volume of the capsule occupied by neodymium magnets is

$$pv_{Nd} = 100 \frac{V_{Nd}}{V_{capsule}} = 14.73\% \tag{A.3}$$

The total weight of the capsule mockup with 15% of its volume occupied by neodymium magnets is

$$F_W = (m + V_{Nd}\rho_{Nd})g = 63.2 \ mN \tag{A.4}$$

where ρ_{Nd} is the density of neodymium ($7.5 g/cm^3$), m is the mass of the PillCam Colon 2 ($3.22 \ g$) and g is the acceleration due to gravity. A typical, reasonable operating distance for the robot is between $d_y = 100$ mm and $d_y = 120 \ mm$. Resulting attraction forces can be looked up using Fig. A.2, and the related values of N can be computed using equation (A.5).

$$N = \frac{F_{\vec{B}_x}}{F_W} \tag{A.5}$$

For operating distances (d_y) between 100 mm and 120 mm, N ranges between 2.25 and 1.25, respectively. For the purposes of this work, N was set to 2, corresponding to an operating distance of $d_y = 105 \ mm$.

Figure A.1: Experimental setup for measuring attraction force $\left(F_{\vec{B}_y}\right)$ of a typical permanent magnetic capsule locomotion system. Attraction force is then used to determine the N value for a typical magnetic capsule locomotion system.
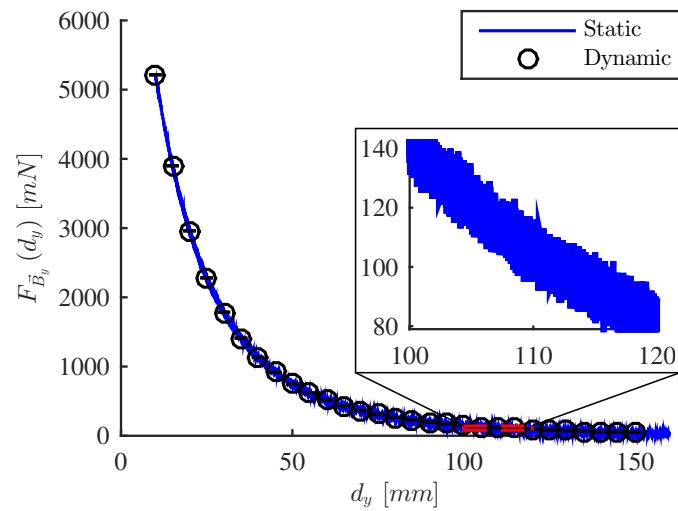
Figure A.2: Attraction force $\left(F_{\vec{B}_y}\right)$ as a function of distance (d_y) between a capsule endoscope with an internal permanent magnet (IPM) and an external permanent magnet (EPM). The IPM inside the capsule consumes 15% of the total capsule volume and is made of neodymium.

Appendix B

MATLAB GUI

A graphical user interface (GUI) was designed using the MATLAB programming environment. The purpose of the GUI is to provide the end-user with a tool to help during the design process of an *in vivo* capsular device where a prediction of the force required to drag the capsule through the GI tract is needed. This can be applied to RCEs, RCCs, and other cylindrical probes. The GUI uses the analytical model developed in Chapter 7 to predict the drag force needed to move a capsule endoscope given the fact that the capsule is in contact with the inside of an insufflated GI lumen (*i.e.*, in contact with one side).

The GUI consists of two main screens, shown in Fig. B.1. The first screen that appears when the GUI is launched is the model input screen (Fig. B.1a). The image in the top left corner of Fig. B.1a provides the user with a diagram of the problem setup, including labeled pertinent capsule dimensions and forces acting on the capsule. The block in Fig. B.1a labeled "Capsule Design Inputs" is where the user enters the size (R, L, and D), weight (F_W), and velocity (v) of the capsule. One of these parameters can be varied at a time by clicking on the associated radio button. The parameter being varied is highlighted in red in the problem setup image. The varied parameter requires minimum and maximum values as well as the number (N) of capsules within the specified range. The software creates N number of capsule variations with equally spaced iterations between the specified minimum and maximum values. Once the capsule design parameters have been set, the user should click on the "Build Capsules" button. This action populates the section titled "Capsule Design Outputs". There are 9 output displays, Volume, Area, $L - 2R$ (contact length), R, L, D, v, F_w, and N. i is the capsule index and can be adjusted by clicking on the arrows to the left and right of the output field. The ← button decreases the index by 1. The → button increases the index by 1. The

⬅ button set the index to 1. The ➡ button advances the index to the N. i can also be manually typed into the output field. The values displayed in the output fields correspond to the i index. In the top right corner of Fig. B.1a is a set of axes, which displays 1 of 4 graphs. The default plot is a 2D shape function of the capsule mid-line profile. The user can select between plots using the drop down menu. The second option displays capsule volume as a function of the varied parameter (volume is on the y-axis while the varied parameter is on the x-axis). The third option displays capsule surface area as a function of the varied parameter (surface area is on the y-axis while the varied parameter is on the x-axis). The fourth option displays a 3D rendering of the capsule surface. The display changes when the index is changed. The "Plot Hold?" check box is only active for the 2D shape function option. If the "Plot Hold?" check box is checked, then shape functions will stack as the index i is changed. Figures from the axes in the upper right corner of Fig. B.1a can be exported individually by clicking on the "Export Fig" button below the axes. If at anytime the use would like to start over, the "Reset" button can be clicked.

The lower half of Fig. B.1a is for entering tissue property data. There are three subsections on the lower left, lower center and and lower right corresponding to "Coefficient of Friction", "Tissue Topography", and "Compressive Tissue Properties", respectively. Any of these properties can be either entered manually or populated using data by toggling the radio buttons in the top left corner of each subsection. Sample data is supplied with the GUI for all three subsections. To add data, click the corresponding "Choose file(s)" button and select the data. The "Coefficient of Friction" subsection takes multiple files, one for each drag test trial, while the "Tissue Topography" and "Compressive Tissue Properties" subsections only take 1 input file. If data is being used to calculate the Coefficient of Friction, it is important to enter the correct weight of the capsule mockup that was used when performing the drag tests. Likewise, for the Compressive Tissue Properties, it is important to enter the indentation depth as well as the indenter radius used during the indentation tests, and the number of indentation trials. For the Coefficient of Friction and Tissue Topography subsections, the program automatically calculates the values and populates the corresponding output fields once the files are selected. For the Compressive Tissue Properties, the "Calculate" button must be clicked after the file is selected. The output field will populate with values once the program computes the solution. All of the input parameters can be exported to a MATLAB data (.mat) file once all of the
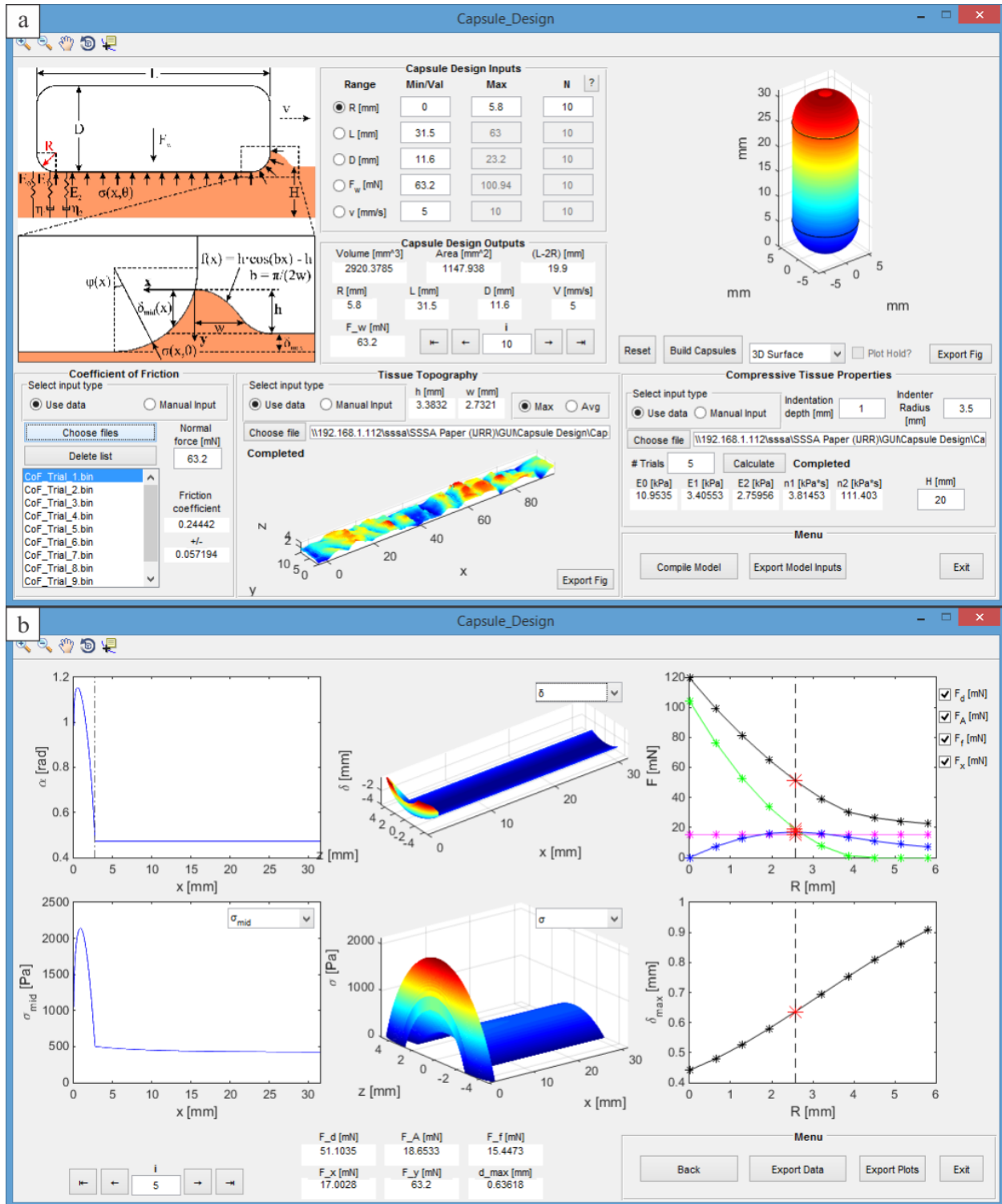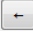
Figure B.1: Screenshots of the input window (a) and the model solution window (b) for the graphical user interface (GUI) of the capsule designer software. The GUI takes manual inputs for the capsule design parameters (R, L, D, and F_W), and takes either manual or data entry for tissue properties (E_0, E_1, E_2, η_1, η_2, μ, h, and w)

fields have been populated. Additionally, the model can be compiled by clicking on the "Compile Model" button. If either the "Compile Model" or "Export Model Inputs" buttons are clicked before all field have been populated, an error message is generated describing which fields need populated.

Once the "Compile Model" button is clicked and all input field have been populated, the program starts computing the solution and switched to an intermediate screen (not shown in Fig. B.1). The intermediate screen displays a row for each capsule index with a total of N rows, along with the time (in s) that is takes to compute each solution as the solution is found. Once all solutions have been computed, the program displays the model output screen (Fig. B.1b). The window contains 6 axes, control buttons for navigating between capsule indexes, and populated output fields on the bottom center of the screen. The ⬅ and ➡ buttons can be used to navigate sequentially between capsule indexes in reverse and forward order, respectively. The ⏮ and ⏭ buttons can be used to navigate to the beginning and end indexes, respectively. Output fields include drag force (F_d), resistance force due to contact between the tissue and the vertical leading end of the capsule (F_A), frictional force (F_f), and force due to the horizontal component of the stress integrated over the contact area (F_x).

The axes in the top-left of Fig. B.1b display $\alpha(x)$ (in rad). $\alpha(x)$ is the angle of integration with respect to θ as a function of location along the capsule length.

The axes in the bottom-left of Fig. B.1b display one of three options, σ_{mid}, $\sigma_{mid,x}$, or $\sigma_{mid,y}$. The σ_{mid} option is the overall stress at the mid-line of the capsule as a function of location along the length of the capsule (in Pa). The $\sigma_{mid,x}$ option is the horizontal component of the stress at the mid-line of the capsule as a function of location along the length of the capsule (in Pa). The $\sigma_{mid,y}$ option is the vertical component of the stress at the mid-line of the capsule as a function of location along the length of the capsule (in Pa).

The axes in the top-center of Fig. B.1b display one of four options, ε, δ, "Tissue Profile 3D", or "Tissue Profile 2D". The ε option displays a 3D rendering of the strain in the tissue substrate. The x- and y-axes represent dimensions of the contact area (in mm), while the z-axis represents the strain (in %). The δ option displays the 3D vertical deflection of the tissue substrate on z-axis (in mm) as a function of contact area dimension on the x- and y-axes (in mm). The "Tissue Profile 3D" option displays a 3D rendering of the tissue shape function prior to contact with the capsule. Each axis represents the dimension of the tissue

in mm. The "Tissue Profile 2D" options displays a tissue shape function profile. The y-axis displays the height of the profile (in mm) while the x-axis displays the length of the profile (in mm).

The axes in the bottom center of Fig. B.1b display one of three options, σ, σ_x, or σ_y. The σ option displays a 3D rendering of the total stress on the capsule over the contact area. The z-axis represents stress (in Pa) while the x- and y-axes represent contact area dimensions (in mm). The σ_x option displays a 3D rendering of the horizontal component of the stress on the capsule over the contact area. The z-axis represents stress (in Pa) while the x- and y-axes represent contact area dimensions (in mm). The σ_y option displays a 3D rendering of the vertical component of the stress on the capsule over the contact area. The z-axis represents stress (in Pa) while the x- and y-axes represent contact area dimensions (in mm).

The axes in the upper right of Fig. B.1b display the output force as a function of the varied variable, which is R in Fig. B.1b. Each component of the total drag force can be displayed by toggling the corresponding check box on the right side of the axes. F_d is the total drag force (in mN), F_A is the force due to the contact between tissue and the vertical leading end of the capsule (in mN), F_f is the frictional force (in mN), and F_x is the horizontal component of the stress on the capsule integrated over the contact area (in mN).

The axes in the lower right of Fig. B.1b display the maximum vertical deflection of the capsule into the tissue (δ_{max}) as a function of the varied parameter. The vertical axis represents δ_{max} (in mm) while the horizontal axis represents the varied parameter.

The output data can be exported to a MATLAB data file (.mat) by clicking on the "Export Data" button, and the plots can be exported to MATLAB figure files (.fig) by clicking on the "Export Plots" button. If the user would like to go back to the input screen (Fig. B.1a), the "Back" button can be clicked. To exit the program, the user can click the "Exit" button.